Crafting magnetic skyrmions at room temperature : size, stability and dynamics in multilayers

William Legrand

Crafting magnetic skyrmions at room temperature: size, stability and dynamics in multilayers

Thèse de doctorat de l'Université Paris-Saclay
préparée à Université Paris-Sud

École doctorale n°564 Physique en Île-de-France (PIF)
Spécialité de doctorat: Physique

Thèse présentée et soutenue à Palaiseau, le 29/03/2019, par

William Legrand

Composition du Jury :

M. Pietro Gambardella   Rapporteur
Professeur, D-MATL
Eidgenössische Technische Hochschule (ETH) Zürich

Mme Stefania Pizzini   Rapportrice
Directrice de recherche, Institut Néel (UPR2940)
Université Grenoble Alpes

M. Claude Chappert   Président
Directeur de recherche, C2N (UMR9001)
Université Paris-Saclay

M. Russell Cowburn   Examinateur
Professeur, Cavendish Laboratory
University of Cambridge

M. Stéphane Mangin   Examinateur
Professeur, Institut Jean Lamour (UMR7198)
Université de Lorraine

M. Vincent Cros   Directeur de thèse
Directeur de recherche, UMPhy CNRS/Thales (UMR0137)
Université Paris-Saclay

M. Nicolas Reyren   Invité
Chargé de recherche, UMPhy CNRS/Thales (UMR0137)   Co-encadrant de thèse
Université Paris-Saclay

M. Albert Fert   Invité
Professeur, UMPhy CNRS/Thales (UMR0137)
Université Paris-Saclay

À mon grand-père, Michel Legrand, qui le premier m'a appris l'intérêt de ce que l'on ne peut pas voir de ses yeux.

Résumé étendu

Les skyrmions magnétiques sont des enroulements bidimensionnels et nanométriques de la configuration de spin, pouvant être stabilisés au sein de certains matériaux magnétiques soumis à une interaction d'échange antisymétrique, l'interaction Dzyaloshinskii-Moriya. Les skyrmions présentent une topologie non triviale et s'annoncent peut-être comme étant les plus petites configurations magnétiques pouvant être réalisées. Par ailleurs, ces configurations magnétiques peuvent être manipulées efficacement par des courants électriques. Juste avant le début de cette thèse, des skyrmions magnétiques ont pu être stabilisés à température ambiante grâce à la conception de multicouches magnétiques brisant la symétrie d'inversion selon la direction verticale. Suite à cette avancée, l'objectif central de cette thèse est la compréhension et la maîtrise des multiples propriétés physiques des skyrmions hébergés dans ces systèmes multicouches. Nous nous intéressons dans le cadre de cette thèse aux skyrmions les plus simples, dont la topologie est définie par le nombre de skyrmion topologique N_{sk}, un entier défini suivant

$$N_{\mathrm{sk}} = \frac{1}{4\pi} \iint \mathbf{m} \cdot \left(\frac{\partial \mathbf{m}}{\partial x} \times \frac{\partial \mathbf{m}}{\partial y} \right) dxdy,$$

valant ici ± 1, $\mathbf{m}(x,y)$ étant l'orientation locale de l'aimantation. Ces objets posssèdent également, dans le cadre de ce travail, une symétrie cylindrique lorsqu'un milieu uniforme est considéré.

Tout d'abord, la nature des cinq interactions physiques donnant naissance aux skyrmions dans les multicouches magnétiques est décrite: interaction d'échange symétrique, interaction d'échange antisymétrique Dzyaloshinskii-Moriya, anisotropie magnétique perpendiculaire, interaction dipolaire et interaction Zeeman avec un champ magnétique extérieur. Par le contrôle de la composition des systèmes multicouches, il est possible d'ajuster simultanément les intensités de ces différentes interactions. Les connaissances actuelles concernant leur ajustement dans les multicouches sont passées en revue, ainsi que leurs valeurs expérimentales attendues, leurs éventuelles corrélations, et les conditions dans lesquelles leur équilibre peut stabiliser les skyrmions. Il est montré numériquement que ces cinq interactions jouent un rôle majeur dans la stabilisation des skyrmions et qu'aucun de ces termes ne peut être négligé. Suivant la stabilité ou la metastabilitié des skyrmions relativement aux autres configurations magnétiques possibles (uniforme, domaines étendus, etc.), des skyrmions isolés ou sous la forme de réseaux périodiques de skyrmions peuvent être obtenus. Cette thèse porte essentiellement sur l'obtention et la manipulation des skyrmions isolés.

Pour aborder ensuite l'objectif de maîtriser les interactions physiques influançant les skyrmions,

un bref état de l'art de la modélisation des skyrmions révèle que les différents modèles existant jusqu'alors sont insuffisants pour décrire de façon satisfaisante les skyrmions hébergés dans les systèmes multicouches. Un modèle original a ainsi été conçu au cours de cette thèse, permettant la prédiction des profils d'aimantation adoptés par les skyrmions multicouches. Il est tout d'abord décrit de façon générale, les exemples d'applications de ce modèle apparaissant par la suite, lorsqu'il sera employé afin d'apporter un éclairage théorique sur les diverses problématiques abordées au cours cette thèse. Ce modèle numérique est très générique, n'utilisant que la symétrie cylindrique des skyrmions afin de simplifier la détermination des interactions magnétostatiques. La validité de ce modèle est établie par comparaison avec un outil micromagnétique standard et très commun, MuMax^3, utilisant quant à lui une géométrie prismatique. Ce nouveau modèle constitue un outil de modélisation polyvalent, permettant de décrire tout à la fois la taille, la chiralité et l'énergie des skyrmions. Cette description des skyrmions permet également de faire la distinction entre "bulles skyrmioniques" et "skyrmions compacts". Ce modèle est ensuite étendu afin de pouvoir approximer d'une part la stabilité des skyrmions vis-à-vis des élongations anisotropes, et d'autre part la stabilité thermique des skyrmions vis-à-vis de leur annihilation, ce qui constitue un élément clé vers leur obtention expérimentale.

Une seconde dimension de ce travail de thèse consiste en l'étude expérimentale de la manipulation électrique des skyrmions dans les systèmes multicouches, démontrant la possibilité de trois fonctionnalités centrales que sont leur nucléation par courants locaux, leur déplacement sous courant de spin et leur détection électrique individuelle par tension transverse. L'étude de la nucléation dans des pistes lithographiées de taille micrométrique montre qu'elle peut se produire par échauffement local ou sous l'influence du champ d'Oersted dans les coins de structures rectangulaires, agissant comme des constrictions. Les densités de courant nécessaires à la nucléation sont de l'ordre de $2 \times 10^{11}\,\mathrm{A\,m^{-2}}$. Le rôle joué dans la répartition spatiale des skyrmions nucléés par la non-uniformité des systèmes est décrit. Les mécanismes de couple induit par le couplage spin-orbite dans les multicouches, permettant la dynamique induite par courant des skyrmions, sont ensuite passés en revue, et les descriptions des mouvements des skyrmions dans les systèmes étendus et confinés sont comparées. Le déplacement de skyrmions induit par un courant électrique est observé dans des expériences types de microscopie à force magnétique couplée à l'injection d'impulsions de courant sub-µs. Ces premiers résultats indiquent bien un mécanisme de couple induit par le couplage spin-orbite, mais le mouvement se révèle être très peu efficace, limité à des vitesses en deçà du $\mathrm{m\,s^{-1}}$. La compréhension de ce phénomène fait l'objet d'une étude à part entière, qui est présentée par la suite. Enfin, la détection des skyrmions repose sur l'effet Hall anomal et ne permet pas d'identifier de contribution de l'effet Hall topologique. Il est montré par des mesures de microscopie à force magnétique couplées à des mesures de transport que l'optimisation de la taille des structures lithographiées permet une détection électrique individuelle des skyrmions, dans des pistes lithographiées de $400\,\mathrm{nm}$ de largeur.

Le troisième aspect de cette thèse porte sur l'étude des propriétés physiques influençant le déplacement des skyrmions dans les multicouches magnétiques. Un comportement d'ancrage sur

des défauts est mis en évidence expérimentalement et est analysé à l'aide d'une modélisation micromagnétique de la dynamique des skyrmions hébergés dans un système inhomogène. Les rôles de différents types de défauts sont évalués et comparés quantitativement, ce qui permet d'établir un lien direct entre l'importance de l'ancrage et la taille relative des skyrmions par rapport à l'échelle caractéristique des inhomogénéités magnétiques. Un des résultats importants de ce travail est l'identification de deux voies distinctes permettant d'éviter ce comportement d'ancrage nuisant au déplacement des skyrmions, aboutissant à une alternative entre l'utilisation de couches épitaxiées (comportant donc des grains extrêmement étendus) et l'utilisation de couches de matériaux amorphes (approchant donc un régime de grains de taille nulle). Un autre résultat obtenu au cours de cette thèse est la prédiction de l'existence d'une chiralité hybride dans les configurations magnétiques de certaines multicouches, trouvant son origine dans une compétition entre les interactions Dzyaloshinskii-Moriya et dipolaire. En raison de la forme des champs dipolaires créés entre le cœur de skyrmion et son environnement, la chiralité uniforme favorisée par l'interaction Dzyaloshinskii-Moriya peut être perdue au profit d'une chiralité variant dans l'épaisseur afin de mieux coïncider avec les champs dipolaires. Ce phénomène nouveau est décrit en détail à l'aide du modèle de skyrmion dans les multicouches. La formation de textures magnétiques présentant une telle chiralité hybride est ensuite confirmée expérimentalement par des mesures de dichroïsme circulaire de diffraction magnétique résonante de rayons X au synchrotron, effectuées sur une série de multicouches présentant différents nombres de couches magnétiques et des valeurs opposées de l'interaction Dzyaloshinskii-Moriya obtenues en renversant l'ordre de dépôt des structures. Les conditions dans lesquelles se forment ces structures hybrides sont étudiées en détail, notamment en fonction de l'aimantation à saturation et du nombre de couches magnétiques. Les conséquences attendues de cette chiralité hybride sur le déplacement des skyrmions sont étudiées de façon prédictive, en considérant plusieurs structures de multicouches possibles en ce qui concerne les couples induits par le couplage spin-orbite et l'injection des courants de spin associés. Il convient soit de s'assurer d'une chiralité uniforme, soit d'induire des injections de spin opposes de part et d'autre de la multicouche. Ces résultats ont permis l'optimisation progressive des multicouches au long de la thèse, en lien avec l'étude du déplacement de skyrmions induit par courant électrique dans une succession de structures, aboutissant à l'observation expérimentale de la propagation de skyrmions de $50\,\text{nm}$ de rayon à des vitesses atteignant environ $40\,\text{m}\,\text{s}^{-1}$. Par ailleurs, l'effet Hall de skyrmion, qui est une déflexion de la trajectoire des skyrmions due à leur topologie particulière, est observé avec des angles évoluant autour de 15–$25°$ environ entre la direction du courant et les trajectoires des skyrmions. L'observation d'un effet Hall de skyrmion est une indication de l'efficacité accrue de la dynamique de skyrmions sous courant dans ces multicouches optimisées. Il est proposé, par ailleurs, d'employer des skyrmions présentant une chiralité hybride afin de compenser l'effet Hall de skyrmion dans des structures spécifiques.

La dernière partie de cette thèse vise à mettre à profit ces avancées théoriques et expérimentales afin de parvenir à réduire la taille des skyrmions à température ambiante. Après avoir analysé, avec l'aide du modèle numérique précédemment établi, le lien direct entre taille et stabilité ainsi

que l'impact des interactions dipolaires sur la stabilité des skyrmions, il est entrepris d'optimiser le choix des matériaux et la périodicité des couches. Le modèle indique que la réduction de l'anisotropie perpendiculaire effective ainsi que de l'aimantation à saturation permet de réduire la taille du plus petit skyrmion stable pour un jeu de paramètres optimisés. Il apparaît que l'insertion de Ni dans les couches de Co ne permet pas d'améliorer, a priori, la stabilité des skyrmions à température ambiante. En revanche, la conception de multicouches Pt/Co/Ni dans lesquelles chaque couche déposée est très fine (d'une épaisseur de l'ordre de 0.4 nm) semble prometteuse. Je m'intéresse pour finir à la conception expérimentale de textures magnétiques chirales dont l'aimantation est compensée, au sein de structures multicouches appelées antiferromagnétiques synthétiques. Ces développements sont basés sur une structure Pt/Co/Ru dont les possiblités d'ingénierie de multicouche sont exemplaires, combinant une anisotropie perpendiculaire modulable, une interaction Dzyaloshinskii-Moriya significative et un fort couplage antiferromagnétique de type Ruderman-Kittel-Kasuya-Yoshida entre les couches magnétiques. L'influence des épaisseurs individuelles de chaque couche est étudiée en détail. Je montre que ces structures peuvent héberger des textures magnétiques chirales appelées spirales de spin lorsque leur anisotropie perpendiculaire effective est ajustée à une valeur proche de zéro, ainsi que des skyrmions antiferromagnétiques, lorsque de plus une multicouche extérieure Pt/Co à aimantation perpendiculaire agit comme biais magnétique sur la structure antiferromagnétique synthétique. Les profils et la stabilité des skyrmions antiferromagnétiques dans les systèmes antiferromagnétiques synthétiques sont modélisés numériquement, indiquant la possibilité d'obtenir des tailles de skyrmions en deçà de 10 nm de rayon, néanmoins stables à température ambiante. Cette modélisation révèle que les champs dipolaires sont, comme attendu, largement compensés, bien que le décalage vertical nanométrique entre les skyrmions hébergés dans chaque couche permette leur observation par un faible champ de fuite. La présence de spirales de spin et de skyrmions antiferromagnétiques dans ces structures à température ambiante et en l'absence de champ extérieur est ainsi mise en évidence expérimentalement, par des mesures de microscopie à force magnétique sous vide. La périodicité des spirales de spin correspond à la valeur attendue. Il est montré que les skyrmions antiferromagnétiques restent stables dans une large plage de champs extérieurs couvrant 0–60 mT, pour lesquels l'évolution des images de microscopie à force magnétique reflète l'évolution des profils d'aimantation au sein des skyrmions antiferromagnétiques hébergés dans le système antiferromagnétiques synthétiques.

Différentes directions sont proposées afin de poursuivre au delà de ce résultat final, qui ouvre de nouvelles perspectives vers la réalisation, à température ambiante, de skyrmions à la fois mesurant moins de 10 nm et très mobiles, qui pourraient être utilisés dans la conception de composants de calcul et de stockage d'information plus compacts et plus efficaces.

Trois annexes complètent cette thèse. La première porte sur les efforts expérimentaux permettant l'ingénierie et l'optimisation des multicouches magnétiques, au travers de l'exemple typique offert par la structure Pt/Co/Ru. Les conditions dans lesquelles les dépôts par pulvérisation cathodique sont effectués sont détaillées. Les techniques expérimentales de mesure de l'anisotropie magnétique perpendiculaire, de l'interaction Dzyaloshinskii-Moriya et du couplage électronique in-

tercouche sont ensuites décrites, ainsi que l'évolution de leurs valeurs en fonction des épaisseurs respectives des différentes couches. Les deux autres annexes sont plus courtes et portent, respectivement, sur les conditions permettant l'observation de skyrmions en microscopie à force magnétique et sur un protocole permettant l'estimation de l'interaction Dzyaloshinskii-Moriya, à partir de l'observation de la périodicité des domaines magnétiques alignés dans des multicouches désaimantées.

Abstract

Magnetic skyrmions are nanoscale two-dimensional windings in the spin configuration of some magnetic materials subject to the Dzyaloshinskii-Moriya antisymmetric exchange interaction. They feature a non-trivial topology and show promise to be the smallest achievable magnetic textures. Very recently, magnetic skyrmions have been successfully stabilised up to room temperature by leveraging on the design of magnetic multilayer systems breaking the vertical inversion symmetry. Following up on this achievement, the main objective of this thesis is the understanding and the control of the various physical properties of skyrmions hosted by such multilayer systems. As a first approach to this objective, an original model allowing to predict the profiles adopted by multilayer skyrmions is described and then employed. This numerical model is very generic, as it exploits only the cylindrical symmetry of multilayer skyrmions, in order to determine the magnetostatic interactions with less effort. This model is further extended in order to approximate the thermal stability of multilayer skyrmions, which is key to their experimental realisation. The next aspect of this thesis consists in the experimental study of the electrical manipulation of multilayer skyrmions, demonstrating three main functionalities that are nucleation by local currents, displacement under spin currents and individual detection by transverse voltage. The third aspect of my thesis is the study of the physical properties influencing the current-induced motion of skyrmions in magnetic multilayers. A pinning behaviour is evidenced experimentally and analysed relying on micromagnetic modelling. One of the important results of this work is also the prediction of hybrid chirality for some multilayer magnetic configurations, which is then demonstrated experimentally using a synchrotron technique. The impact of hybrid chirality on current-induced skyrmion motion is discussed and leads to the optimisation of the multilayer design, resulting in the experimental observation of motion for skyrmions below 50 nm in radius at velocities reaching around 40 m/s. The last part of this thesis aims at leveraging on these theoretical and experimental advances in order to reduce the size of skyrmions at room temperature. After the analysis of the impact of dipolar interactions on skyrmion stability, the engineering of the materials and of the layers periodicity is attempted. I also investigate experimentally the conception of magnetic textures with compensated magnetization in multilayer structures known as synthetic antiferromagnets, and show that they can host antiferromagnetic skyrmions at room temperature. This last result opens up new prospects for achieving room-temperature skyrmions combining size in the single-digit nm range and high mobility, potentially allowing applications towards energy-efficient computation and storage devices with a very dense integration.

Acknowledgments

La préparation de cette thèse m'a donné l'occasion de côtoyer nombre de personnes incroyablement chaleureuses. On s'attache bien vite ... Aussi ai-je la joie d'entamer cette monographie par les remerciements, dont j'espère qu'ils témoignent, aussi fidèlement que possible, de tous ceux qui m'ont entouré, de très près ou d'un peu plus loin, durant toute cette période.

Naturellement, mes premiers remerciements vont à mes deux encadrants de thèse, Vincent et Nicolas. Vous avez été présents tout au long de ces trois ans ... Vincent, ta confiance, le partage de tes avis, tout comme ta philosophie, ont de toute évidence contribué à mon grand bien-être au cours de ce bout de chemin parcouru ensemble, alors merci. Qui plus est, tu sais être quelqu'un avec qui il est agréable non seulement d'être d'accord, mais aussi d'être en désaccord, une qualité bien utile pour avancer ensemble. Nicolas, ton calme olympien, ta patience semble-t-il sans limites pour aider sans compter, ainsi que ta grande humilité, pour ne citer ici que ces trois qualités, m'ont inspiré pendant tout le temps de la thèse, et resteront pour moi une source d'inspiration longtemps encore, tu le sais. Merci à toi. Enfin, merci à Albert pour les excellents conseils disséminés de part et d'autre au long de la thèse. Je ne dois pas être le premier à remarquer que l'idée de ce que l'on veut faire semble systématiquement bien plus claire en sortant de ton bureau, bien que tout aussi systématiquement augmentée de nouvelles questions.

Je remercie l'ensemble des membres du jury d'avoir pris le temps de relire avec tant d'attention les pages qui suivent, ainsi que d'être venus nous rendre visite à Palaiseau pour permettre nos échanges lors de la soutenance.

Je veux désormais faire ici mention spéciale de toute l'équipe de l'Unité Mixte de Physique CNRS/Thales, qui a été si agréable à découvrir puis fréquenter au quotidien. Merci à Cyrile pour ses conseils éclairants (les plus brillants au monde, même) et pour m'avoir laissé user aussi intensément le bâti de pulvérisation sous ses yeux sans se récrier; à Éric pour son humour jamais émoussé par ses passages obligés devant mon bureau pour rejoindre le sien, toujours muni d'une plaisanterie bien sentie à disposition ; aux 2 directeurs Frédéric et Frédéric toujours au top et sur le pont malgré la tâche titanesque qui leur incombe de mettre de l'ordre au milieu de toutes les autres personnes mentionnées ici ; au flegmatique Jean-Marie pour le partage de sa curiosité circonspecte (par exemple autour des mesures d'AHE, série-feuilleton que j'ai suivie tout au long de ma thèse et dont les rebondissements ne tarissent pas), pour ses questions concises en tendant le cou ("alors ?"), et pour n'avoir jamais laissé entrevoir la moindre pointe d'agacement alors que mes questions se résumaient souvent à des "tu ne saurais pas où est Vincent ?", dont il partage le bureau. Merci à Madjid pour ses conseils aigres-doux (je suis bien désolé de n'avoir trouvé aucun autre terme aussi

précis pour décrire ta bienveillance envers moi) et ses talents de psychologue inversé ; à Olivier pour sa curiosité intellectuelle rafraîchissante et ses talents d'infographiste fourbement employés à manipuler mon identité ; à l'inégalable Pierre, et pas seulement pour avoir suggéré le titre de cette thèse, mais aussi pour tout le reste : tous ses "petits côtés", allant par exemple des retours en voiture à la place du siège enfant, jusqu'au suivi quotidien du prix de mon admission à la cantine ; à Richard, le fin connaisseur de beaucoup de choses importantes autour des bouteilles et de la pression, pour n'avoir néanmoins jamais fait remarquer que je lui ai demandé au moins dix fois de m'apprendre à transférer l'Hélium dans le SQUID ; à Vincent, toujours bienveillant et attentif notamment par ses appréciations sur la qualité artistique de mes images MFM à chacun de ses passages en salle de manip, et accessoirement pour avoir été mon parrain de thèse. J'éprouve aussi beaucoup de gratitude envers Anne, Christine et Nathalie, pour nous avoir rendu la vie si simple, à nous tous les doctorants, pour nous avoir choyés, avertis de mille choses importantes, ou encore aidés à préparer nos incessants déplacements, avec le seul inconvénient qu'en comparaison toute démarche en dehors du labo semblait insurmontable puisque sans leur aide. Merci également à Agnès, Anke, Brunos, Cécile, Denis, Fayçal, Florence, Henri, les Javier, Juan, Julie, Manu, Paolo, Steef et Yves, qui pour les coups de main, qui pour les conseils, qui pour les expériences culinaires et les avis sur les recettes, et tous pour les bons moments partagés.

Plus en particulier, merci à Sophie, reine de l'élaboration et de la lithographie. Je serais bien incapable de compter le temps que nous avons passé ensemble à échanger autour de choses du labo et surtout du reste. Merci de m'avoir aidé dans quasiment tout ce que j'ai fait de mes mains au cours de cette thèse, merci pour ton écoute et tes questions, pour ton soutien et tes encouragements.

Tout aussi particulièrement, merci à Karim, archiduc des AFMs réunis, mais aussi mentor de chaque instant. Tu es un homme vrai, et un bien bon camarade avec qui partager de longues heures passées en salle de manip ("chuuuuuuut ! ..."), des discussions enflammées sur la thèse, les labos, le monde, ou encore des pots (ou alors un simple sandwich).

Les autres, ce sont les précaires (selon le bon mot de Nicolas). Ceux qui ont quotidiennement besoin des équipements; or, c'est dans le besoin que l'on reconnait ses amis. Avant tous les autres, je ne peux pas m'imaginer ce que cette thèse aurait été sans toi, Lucile. Compagnons de fortune et d'infortune, nous sommes allés partout ensemble, avons affronté les machines rebelles, les intempéries, le RER, les alligators, nous avons tenté toutes les expériences et même les plus *worthless*, et nous avons progressé (parce que nous le voulions). Tack tack et à bientôt à Stockholm ! Merci Florian pour ton empathie et ton attention toute particulière. Tu as rehaussé toutes mes journées au labo et toutes les très bonnes soirées hors du labo ! Regina, merci de m'avoir permis de rencontrer en toi une amie aux qualités innombrables, une si belle voix et une si bonne oreille ; merci aussi pour m'avoir fait découvrir toute l'étendue de la culture catalane. Davide, c'était très chouette de travailler avec toi aussi longtemps ; merci de m'avoir appris la patience de la recherche, et à rester motivé quand le 50 Hz est de retour. J'ai aussi beaucoup profité de ton accent délicatement cultivé et de tes bons conseils en vue de l'agrandissement de la famille. Benoît, merci pour ces 3 ans d'hilarité grâce à ton trash-talk et ton auto-dérision. Ta diligence pour accélérer notre départ

collectif à la cantine n'aura jamais d'égale que ta rigueur pour retarder notre départ des bars du 5e un tour de cadran plus tard. Sérieusement pour une fois, tu vas me manquer ! Sophie, même si j'ai dû faire mauvaise impression en débranchant ton PC à peine 2 minutes après avoir été installé à mon bureau, tu n'as pas semblé m'en vouloir C'était au top de partager le bureau et de se cuire au soleil pour des pique-nique, merci pour ton franc-parler dont j'ai beaucoup appris, les conseils de montagnarde, et vive l'Aubrac (et Grenoble un peu aussi) ! Merci aussi à la vieille garde : David pour nous avoir appris tous les secrets du labo, et Martin pour nous avoir montré l'exemple de comment être un mec *sympa*. Merci Quentin d'avoir aussi régulièrement visité mon bureau afin de partager tes réjouissances autour de la litho, de l'optique géométrique, du solitaire et du démineur, des crêpes, des campings des Côtes-d'Armor, de la bibliométrie ; grâce à toi j'en sais plus. Merci à Steffen pour avoir toujours été au rendez-vous au labo et le soir après les conférences. Merci à Karin pour toutes les lithos et aussi pour avoir supporté la confusion éternelle, devenue blague récurrente, entre Karin/Karim. Bonne chance pour la suite ! Merci Fernando de nous avoir rejoints dans la quête des 10 nm, et pour être toujours resté enthousiaste malgré les revers de fortune. Merci André, ça faisait du bien d'avoir un gars un peu plus posé et mûr parmi nous au labo et au contraire plus ardent et enthousiaste dès qu'on était en dehors ! Merci aussi de m'avoir partagé le résultat de ta quête de la pizza parfaite, j'ai bien profité de tes adresses. Hugo, merci pour les soupirs échangés au sujet de Mumax, ça faisait beaucoup de bien de parler à quelqu'un qui comprenait à quel point on peut s'arracher les cheveux, quelle idée aussi de travailler en salle café ? Merci surtout *thanks buddy* pour le basket, le fromage et les crêpes ! Merci à Johanna pour les déjeuners à toute heure, pour les courses à toute heure aussi, avant ou après le déjeuner donc, et pour le super soutien moral pendant la période où je ne pouvais plus courir. J'espère que l'on va bientôt pouvoir marier nos échantillons comme prévu mais il est vrai que la préparation au mariage est un long processus ! Merci Eloïse pour avoir rejoint le bureau le temps du stage, c'était très agréable de partager ton énergie et ta bonne humeur et du coup c'était trop court. Heureusement que tu continues de nous voir souvent ! Merci Victor pour toujours avoir le smile, qui suffit à remettre d'aplomb même les pires journées. Alice, merci pour ton enthousiasme de tous les jours et toutes les anecdotes qui vont avec ; j'ai préféré te mettre ici plutôt qu'au paragraphe du dessus car pour moi tu resteras à jamais la doctorante avenante qui m'a dit de foncer pour venir à l'UMR car c'était top ! Merci Maëlis pour les ballades à midi sous le soleil et l'exemple impressionnant de la maman docteure en toute simplicité, on va tâcher de s'en inspirer. Merci à Philippe, pour avoir pris le parti tout à fait fortuit de participer exactement aux mêmes conférences que moi, et pour tous les bons moments qui en ont découlé ; heureusement, j'ai déjà oublié que tu as lâchement cessé de voyager au moment de la rédaction de ta thèse. Merci aussi à Aymeric, Danijela, Eliana, Erick, Hiro, Lisa, Marta, Mathieu, Salvatore, Samh, Sophie, Thi Huong, Ralph, Raphaël, aux nombreux Victor, et Xavier, qui avez été d'une si bonne compagnie. Enfin, Yanis, je te souhaite le meilleur pour toute la suite, et pardon d'avoir tout laissé en cet état ; mais après ces quelques excellents mois passés ensemble je suis certain que tu t'en sortiras et que je vais regretter que tu ne sois pas arrivé plus tôt parmi nous !

Évidemment vient maintenant Maxence, ni collègue ni ami mais les deux à la fois car ami de toujours que j'ai eu la joie immense de voir nous rejoindre au labo ! Rien de plus particulier à dire ici qu'à notre excellente habitude, je regrette simplement que tu aies finalement passé beaucoup plus de temps au C2N qu'avec nous, même s'ils ont dû bien en profiter.

Je tiens à remercier chaleureusement et avec une jovialité aussi communicative que les leur Jean-Yves Chauleau et Nicolas Jaouen ; en premier lieu, pour la confiance qu'ils m'ont accordée en m'associant dès la première heure aux projets autour de la chiralité magnétique observée aux X ; qui plus est, j'ai passé de vraiment bons moments à Soleil en votre compagnie, tandis que vous m'appreniez une foule de choses indispensables !

Un grand merci également à Bernd, qui a poussé son intérêt pour collaborer avec nous autour de l'ab-initio jusqu'à nous rendre une agréable visite de quelques mois au labo en acceptant de quitter momentanément Jülich. Ce fût à n'en pas douter une période très enrichissante pour nous tous, et je garde un excellent souvenir de tout l'à côté ni expérimental ni théorique.

J'ai une pensée très particulière à adresser à toute ma famille et aux amis, qui m'ont toujours soutenu sans relâche dans mes projets, parmi lesquels ce travail de thèse a constitué une étape riche de sens. En ce qui concerne la bande à Amaury, Léa, Mathieu, Quentin, Romain, Sylvain, Sophie, et Sophie, vous êtes tous incroyables autant les uns que les autres et c'est grâce à vous que j'ai autant confiance dans ce que l'on peut accomplir. Merci aux poulets du basket qui font comme moi l'effort de ne pas trop changer malgré les affres de la thèse ou de leur vie professionnelle. Un autre merci particulier à mes colocs de Vercin au début de la thèse, Amaury, Jéjé, Momo, Guillaume (heureusement pas tous en même temps), ainsi qu'à Pierrot, qui ont partagé (à moins qu'on ne dise subi ?) en filigrane beaucoup d'histoires autour de cette thèse.

Merci à vous tous qui êtes venus assister à la soutenance pour joindre votre enthousiasme au mien à l'occasion de cette journée.

Merci à vous qui lisez ces lignes, cela me fait plaisir de savoir que vous allez peut-être lire quelques pages parmi celles qui suivent, alors n'hésitez pas à me contacter si le cœur vous en dit.

Enfin, surtout et par-dessous tout, mes remerciements les plus profonds et exaltés vont à la femme de ma vie, à ma Mathilde, pour son soutien de tous les jours et sa présence dans ma vie, ma vie scientifique ne faisant pas exception ! Nous avons de grandes choses à accomplir ensemble, car parmi toutes ces grandes choses du monde, il n'y a rien qui soit au-dessus de toi.

Contents

List of Abbreviations

AF   antiferromagnet.

AHE   Anomalous Hall Effect.

BL   bias layer.

CCW   counter-clockwise.

CW   clockwise.

DM interaction   Dzyaloshinskii-Moriya interaction.

DW   domain-wall.

FM   ferromagnet.

HM   heavy-metal.

IP   in-plane.

MFM   Magnetic Force Microscopy.

NM   non-magnet.

NV   nitrogen-vacancy.

OOP   out-of-plane.

RKKY   Ruderman-Kittel-Kasuya-Yoshida.

RT   room temperature.

SAF   synthetic antiferromagnet.

SHE   Spin Hall Effect.

SOT   Spin-Orbit Torque.

SQUID   Superconducting Quantum Interference Device.

STT   Spin-Transfer Torque.

TEM   Transmission Electron Microscopy.

THE   Topological Hall Effect.

XRMS   X-Ray Resonant Magnetic Scattering.

List of Symbols

The formulas and the units are according to "International System of Units" (SI).

A	Heisenberg (symmetric) exchange interaction parameter	$\mathrm{J\,m^{-1}}$
B	Magnetic induction	T
D	Dzyaloshinskii-Moriya interaction parameter	$\mathrm{J\,m^{-2}}$
$\mathcal{D}$	Thiele dissipation factor	$\mathrm{kg\,s^{-1}}$
E	Magnetic energy	J
E_{B}	Energy barrier height	J
E_{tot}	Total skyrmion energy	J
e	Electron charge (absolute value)	$1.602 \times 10^{-19}\,\mathrm{A\,s}$
$\mathbf{F}$	Thiele effective force of spin-transfer	N
$\mathbf{G}$	Thiele gyrotropic vector	$\mathrm{kg\,s^{-1}}$
$\mathbf{H}_{\mathrm{dem}}$	Demagnetizing field	$\mathrm{A\,m^{-1}}$
H_{eff}	Effective uniaxial anisotropy field	$\mathrm{A\,m^{-1}}$
$\hbar$	Reduced Planck constant	$6.626 \times 10^{-34}\,\mathrm{J\,s}$
K_{eff}	Effective perpendicular magnetic anisotropy parameter	$\mathrm{J\,m^{-3}}$
K_{u}	Uniaxial magnetic anisotropy parameter	$\mathrm{J\,m^{-3}}$
k_{B}	Boltzmann constant	$1.381 \times 10^{-23}\,\mathrm{J\,K^{-1}}$
J	(Charge) current density	$\mathrm{A\,m^{-2}}$
J_{s}	Spin current density	$(\frac{\hbar}{2e})\mathrm{A\,m^{-2}}$
M_{s}	Saturation magnetization	$\mathrm{A\,m^{-1}}$
$\mathbf{m}$	Normalised magnetization direction	
L	Multilayer repetition number	
p	Multilayer periodicity	m
r	Radius (defined from centre of skyrmion)	m
r_{sk}	Skyrmion radius	m
t_{SRT}	Spin reorientation transition thickness	m
t_{X}	Layer X thickness	m
v	Skyrmion velocity	$\mathrm{m\,s^{-1}}$
α	Gilbert damping parameter	
γ	(Electron) gyromagnetic ratio	$1.761 \times 10^{11}\,\mathrm{s^{-1}\,T^{-1}}$
δ	Domain-wall width	m
ε	Magnetic energy density	$\mathrm{J\,m^{-3}}$
η	Thiele dissipation to deflection ratio	
Θ_{sk}	Skyrmion Hall angle	
θ_{eff}	Effective spin Hall angle	
λ	Domain periodicity	m
μ_0	Vacuum magnetic permeability	$4\pi \times 10^{-7}\,\mathrm{H\,m^{-1}}$

The scientific man does not aim at an immediate result. He does not expect that his advanced ideas will be readily taken up. His work is like that of the planter — for the future. His duty is to lay the foundation for those to come, and point the way.
Nicola Tesla (in *The Problem of Increasing Human Energy*, The Century Magazine, June 1900)

Introduction: The skyrmion "bubble"

Chirality is a very general phenomenon in physics, commonly observed in a large variety of objects, such as molecules, solid and liquid crystals, or light, which manifests itself as a break of mirror symmetry for the considered objects. In magnetic materials, chirality may be found in the spin texture, that is, in the space-dependent, site-to-site variations of the local magnetization held by each atom. Generally, it is a consequence of the *Dzyaloshinskii-Moriya interaction (DM interaction)* [1, 2], a form of antisymmetric exchange interaction of relativistic origin that promotes a non-collinear alignment for neighbouring spins. The DM interaction, whose properties are further detailed in the next chapter, is central to the topic under study in this thesis.

A significant DM interaction is found in materials that lack inversion symmetry due to their crystalline structure, a typical example being the B20-class "chiral magnet" materials (including MnSi, $Fe_{0.5}Co_{0.5}Si$, FeGe, MnGe, *etc.*). Because of the DM interaction present in such materials, a rotating or spiralling magnetic order with a defined chirality is observed under varied temperature and field conditions [3–5].

For many years, magnetic thin films have been the topic of dedicated research, motivated by the unusual properties of materials that can be obtained when they are confined into two dimensions [8], in comparison to their bulk form (the bulk form designates three-dimensional materials). Notably, with reducing the thickness of the films down to the nm scale or even down to the atomic scale, interfaces begin to play a predominant role over the bulk properties. Among the interfacial properties arising in the case of thin films, a DM interaction is obtained, consequently to the lack of vertical structural inversion symmetry, as predicted already in the 90's [9, 10]. Due to the presence of interfacial DM interaction in thin ferromagnetic films, other configurations than the usual ferromagnetic domains [11–14] are promoted, with notably the onset of chiral magnetic order [15, 16]. This interfacial form of the DM interaction does not require non-centrosymmetric materials, which thus greatly expands the number of compounds that can be prone to chiral interactions. Consequently, this has largely increased the amount of studies on non-collinear spin textures. Such chiral magnetic order in low-dimensional systems has been first observed by spin-polarized scanning tunnelling microscopy, at cryogenic temperatures, in a single layer of Mn grown above a W substrate [17, 18].

The DM interaction actually takes different forms, thus exhibiting different symmetries, depending on whether it has an interfacial or a bulk origin, which results in turn in inducing different types of chiral order [6, 19]. The symmetry of the DM interaction is described by the orientation with respect to a line of magnetic atoms of the DM interaction vector, whose components are constrained by the symmetries of the system [2]. For a non-centrosymmetric material breaking the horizontal inversion symmetry in its bulk form (Fig. 1a), the DM interaction vector is aligned with the line of magnetic atoms and favours a rotation of the magnetization (red arrows) around this line. In its interfacial form (Fig. 1b), the DM interaction vector is horizontal and favours a rotation of the magnetization through the plane.

A particular type of chiral magnetization configuration stabilised by the DM interaction is the *magnetic skyrmion*. Magnetic skyrmions are two-dimensional, localised, swirling arrangements of the spin texture, obtained in an otherwise uniformly magnetized material [20–22], as shown in Fig. 2a and Fig. 3. They are intrinsically different from magnetic vortices, the later being two-dimensional magnetization textures with potentially infinite expansion (Fig. 4a). In this Ph.D. work, we focus
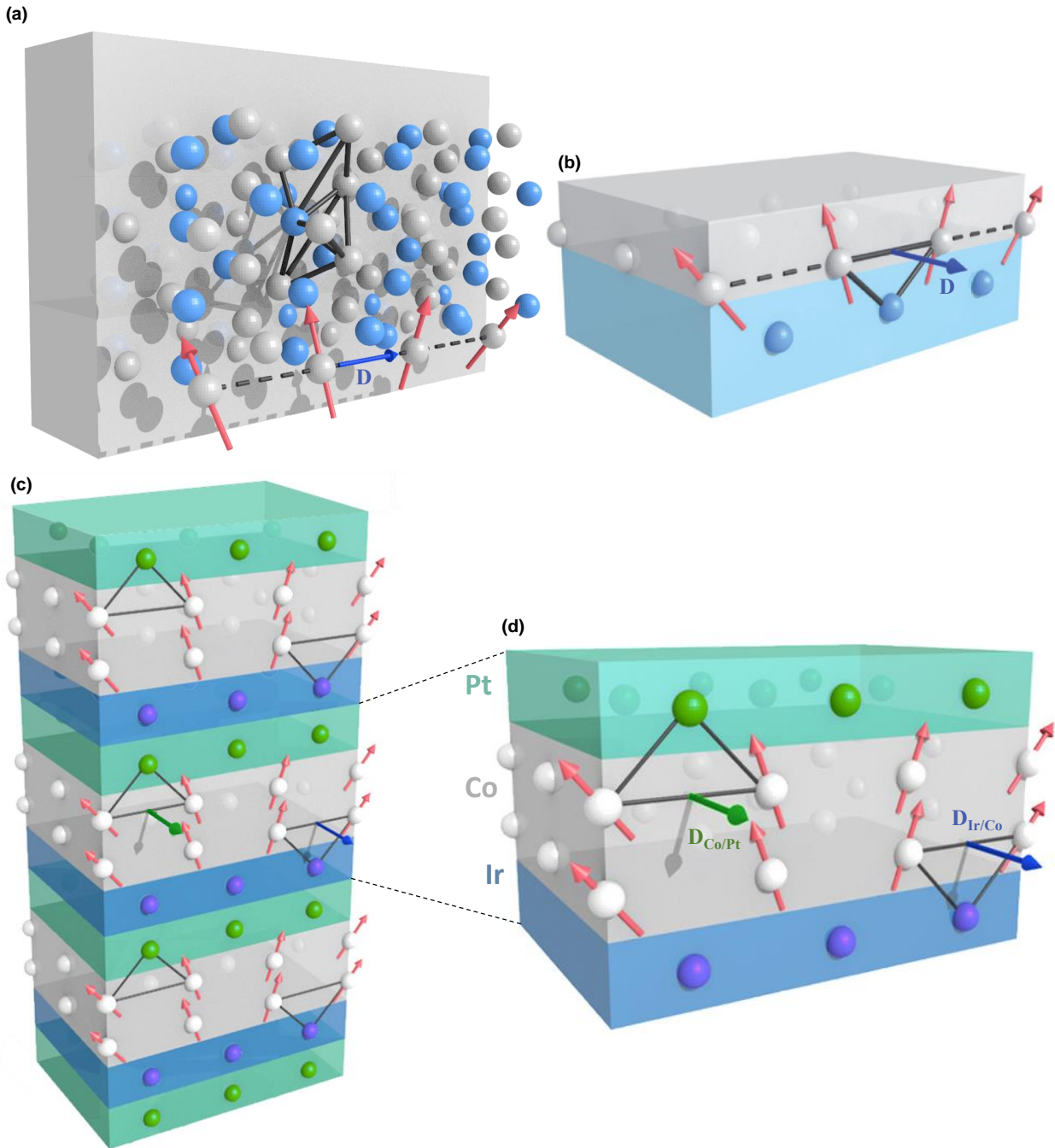
Figure 1: (a) Orientation of the DM interaction vector in a bulk non-centrosymmetric system (here a B20-class "chiral magnet" material) breaking the horizontal inversion symmetry, where the magnetization vector (in red) held by the magnetic atoms (grey spheres) rotates in a vertical plane. (b) Orientation of the DM interaction vector in a an interfacial system breaking the vertical inversion symmetry, where the magnetization vector (in red) rotates through the layers plane. Panels b is adapted from [6]. (c) Orientation of the DM interaction vectors in a multilayer system breaking the vertical inversion symmetry with (d) a detailed view of the base trilayer repetition unit, for example when it is Ir/Co/Pt. Panels c and d are adapted from [7].
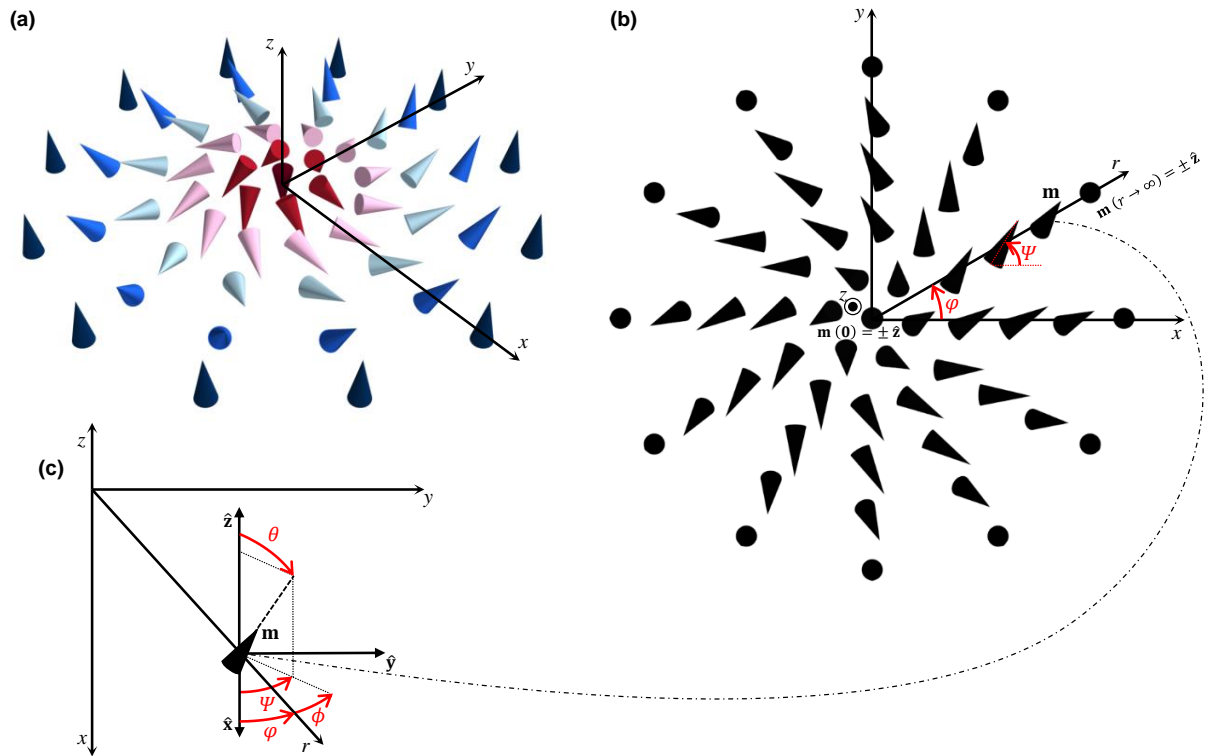
Figure 2: (a) Perspective view of the planar magnetization texture $\mathbf{m}(x,y)$ for an example of magnetic skyrmion, as represented by the coloured thick arrows. Outside the skyrmion (not represented), the magnetization is uniform and directed along $\pm\hat{\mathbf{z}}$ in general, along $+\hat{\mathbf{z}}$ in this example. (b) Top view of the magnetization texture $\mathbf{m}(x,y)$ for the same skyrmion. Polar coordinate angles are represented in red. (c) Spherical coordinates definition for $[m_{\mathrm{x}}, m_{\mathrm{y}}, m_{\mathrm{z}}] = [\sin\theta\cos\Psi, \sin\theta\sin\Psi, \cos\theta]$, for the magnetization vector located at the arrow labelled $\mathbf{m}$ in panel b.

on the most usual realisation of skyrmions, obtained in *perpendicularly magnetized* materials with uniaxial magnetic anisotropy. In the case of thin films, effectively forming two-dimensional systems, the material is perpendicularly magnetized if an anisotropic interaction promotes a direction perpendicular to the film plane for the magnetization of the atoms. Magnetic skyrmions have been first observed under lattice forms in chiral magnets with bulk DM interaction [23, 24], and later in thin films with interfacial DM interaction [25, 26]. Note that skyrmions can also be stabilised by a frustrated exchange interaction [27–30], which we do not consider further in the following as this effect does not come into play at the length scales of the skyrmions studied in this thesis.

Topological properties of skyrmions

In order to classify the different possible skyrmion textures, an analysis of their topology is most useful. The magnetization texture held by the atoms can be modelled by a space-varying function $\mathbf{m}(x,y)$ defined in the infinite plane, which corresponds to the local direction of the normalised magnetization. The topological skyrmion number (or winding number) N_{sk} of a skyrmion texture is given by integrating in space its local topological charge, that is, a

measure of the local winding of $\mathbf{m}$, as follows in [8, 19, 31]

$$N_{\text{sk}} = \frac{1}{4\pi} \iint \mathbf{m} \cdot \left(\frac{\partial \mathbf{m}}{\partial x} \times \frac{\partial \mathbf{m}}{\partial y} \right) dxdy. \tag{1}$$

The normalised vector $\mathbf{m}(x,y)$, a function of $\mathbb{R}^2$, evolves in the unit sphere S^2. Due to the limit condition that the skyrmion is hosted in an otherwise uniformly magnetized material, $\mathbf{m}(r)$ tends towards a unique value for $r = (x^2 + y^2)^{1/2} \to \infty$, making that a continuous magnetization function $\mathbb{R}^2 \mapsto S^2$ needs to map an integer number of times the whole unit sphere. In other words, the skyrmion number $N_{\text{sk}} = 0$, 1, -1, *etc.*, is quantised, which defines separate *homotopy classes* [32]. Magnetic textures from a single homotopy class can be converted into each other by continuous transformations, but not into magnetic textures belonging to an other homotopy class. For example, a skyrmion with unity topological skyrmion number $N_{\text{sk}} = \pm 1$ cannot be continuously transformed into the uniformly magnetized configuration $\mathbf{m}(x,y) = +\hat{\mathbf{z}}$ with trivial topology $N_{\text{sk}} = 0$. It is important to realise that even if topology predicts distinct and separate homotopy classes, the magnetization of physical thin film systems always remains hosted by a discrete lattice of localised atoms. Consequently, the topological properties derived from continuity of transformations are not observed, and for example, a skyrmion with unity skyrmion number $N_{\text{sk}} = +1$ can be injected into the uniformly magnetized configuration $\mathbf{m}(x,y) = +\hat{\mathbf{z}}$. However, this transformation cannot be realised easily: the different topology will be associated to a sizeable energy cost, due to exchange ferromagnetic interactions favouring parallel alignment of the magnetization of neighbouring atoms, which has been often referred as a *topological protection* of skyrmion textures. In this context, the tools of topology remain nevertheless useful to classify magnetization textures. For a proper definition of skyrmions in this thesis, it is also imposed that they exhibit cylindrical symmetry, which constitutes a personal choice, thus dropping more complex objects that could also be analysed with the tools of topology. We can then describe $\mathbf{m}$ as a function of the position in polar coordinates (r, φ). The values of $\mathbf{m}$ evolve in the unit sphere with spherical coordinates (θ, Ψ), providing $[m_x, m_y, m_z] = [\sin\theta\cos\Psi, \sin\theta\sin\Psi, \cos\theta]$, see Fig. 2b. Assuming at this point, for simplicity, that Ψ is constant with respect to r — which in itself does not change the result, and which is no longer assumed later in this thesis — we can then rewrite (1) into

$$N_{\text{sk}} = \frac{1}{4\pi} \int_{r=0}^{\infty} \int_{\varphi=0}^{2\pi} \frac{d\theta}{dr} \sin\theta \frac{d\Psi}{d\varphi} \, drd\varphi = \frac{1}{4\pi}[-\cos\theta(r)]_{r=0}^{r=\infty}[\Psi(\varphi)]_{\varphi=0}^{\varphi=2\pi} = QV \tag{2}$$

denoting by Q the skyrmion polarity number and by V the skyrmion vorticity number

$$Q = [-\cos\theta(r)]_{r=0}^{r=\infty}/2 = [m_z(0) - m_z(\infty)]/2 \tag{3}$$

$$V = [\Psi(\varphi)]_{\varphi=0}^{\varphi=2\pi}/(2\pi). \tag{4}$$

It is thus found that the topological skyrmion number is the product of these two terms Q and V. As a consequence of the cylindrical symmetry, we have also that $\Psi = V\varphi + \phi$ with $V = 1$, where ϕ is the tilt angle of the magnetization with respect to the radial axis. On the opposite, textures for which $V = -1$ are called antiskyrmions (Fig. 4b). They can be found in materials with anisotropic DM interaction [19, 33–35], such as tetragonal Heusler compounds [36]. In the following, the term *magnetic skyrmion* actually designates skyrmions in which the magnetization wraps the unit sphere only once, thus with unit charge $Q = \pm 1$ and $V = 1$, distinguishing them from skyrmioniums, target skyrmions, *etc.* [37].

The type of winding is then determined by the value of ϕ. For $\phi = 0$ or π, cycloidal arrangements of the magnetization along a radial axis are obtained, which defines *Néel skyrmions*
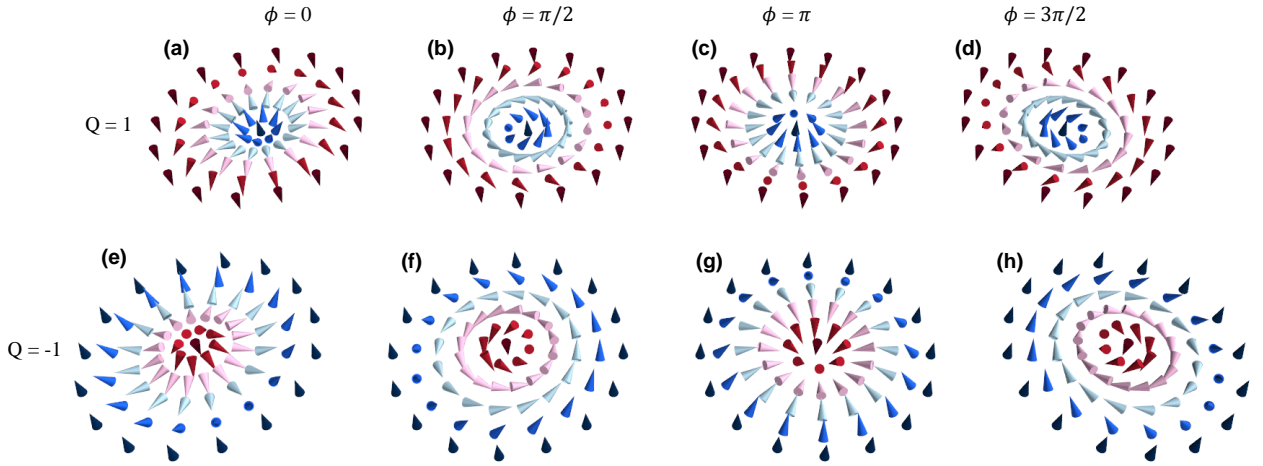
Figure 3: Classification of skyrmions: Skyrmion texture for $Q = 1$ and (a) $\phi = 0$; (b) $\phi = \pi/2$; (c) $\phi = \pi$; (d) $\phi = 3\pi/2$, and skyrmion texture for $Q = -1$ and (e) $\phi = 0$; (f) $\phi = \pi/2$; (g) $\phi = \pi$; (h) $\phi = 3\pi/2$.

(Figs. 3a,c,e,g). For $\phi = \pi/2$ or $3\pi/2$, helicoidal arrangements of the magnetization along a radial axis are obtained, which defines *Bloch skyrmions* (Figs. 3b,d,f,h). The value of ϕ also allows to define the *chirality* of the textures. For a given type of arrangement (Bloch or Néel), there can be two opposite chiralities, counter-clockwise (CCW) and clockwise (CW), given by the direction of rotation of **m** along the direction of propagation. We thus get CW Néel (Figs. 3a,g), CCW Néel (Figs. 3c,e), CW Bloch (Figs. 3d,f), CCW Bloch (Figs. 3b,h) types of skyrmions.

Due to the orientations of their DM interaction vectors **D**, a DM interaction of a bulk origin tends to stabilise helicoidal magnetic textures and Bloch skyrmions[1], while a DM interaction of interfacial origin tends to stabilise cycloidal magnetic textures and Néel skyrmions. The chirality, CW or CCW, is selected by the sign of the DM interaction. Magnetic skyrmions thus constitute a new class of magnetization textures, beyond previously studied "bubbles", which are also objects

---

[1]There are a few exceptions, *e.g.*, in the lacunar spinel GaV_4S_8 [38].
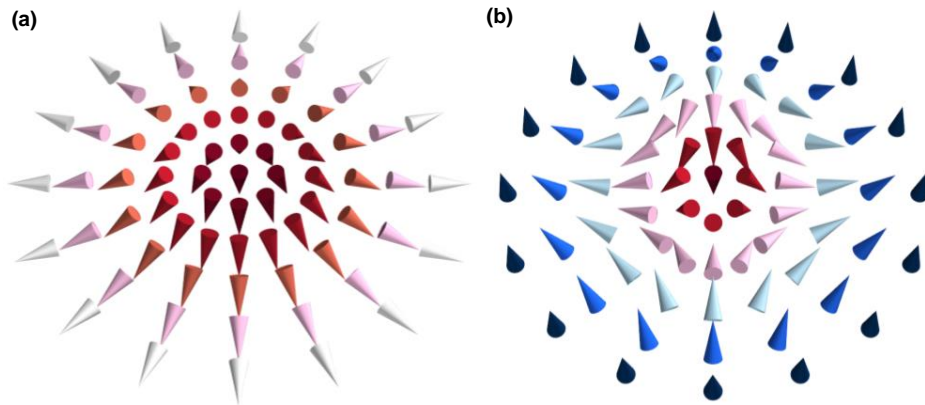
Figure 4: What a skyrmion is not: (a) Vortex texture for $Q = -1/2$ and $V = 1$; (b) Antiskyrmion texture for $Q = -1$ and $V = -1$.

with cylindrical symmetry and which are also stabilised in perpendicularly magnetized materials [39–43], but which generally lack the particular chiral and topological properties of skyrmions. As seen later, it is possible to stabilise circular, magnetic bubble domains which possess a Néel chiral domain-wall (DW), called *skyrmionic bubbles* [44, 45]. They have the same topology than magnetic skyrmions but their properties are not equivalent, especially their size that can differ by more than one order of magnitude, being in the µm range for bubbles rather than around 100 nm and below for skyrmions (see Fig. 5 and in particular panel f for bubbles). As is further detailed in the following of this work, magnetic skyrmions experience a greater stability and can indeed be much further reduced in size than magnetic bubbles in perpendicularly magnetized materials, motivating intense research efforts towards achieving the stabilisation of magnetic skyrmions as small as possible.

All the early observations of magnetic skyrmions referenced above, for both chiral magnet systems and interfacial thin film systems, report their stabilisation in cryogenic environments at low temperatures. This is because the chiral magnetic order can be destroyed by the thermal fluctuations of the magnetization under ambient conditions, and also because the precise values of the magnetic parameters stabilising skyrmion lattices may vary with temperature. To envisage applications of skyrmions in common electronic devices however, their stabilisation at *room temperature (RT)* and above is a crucial requirement. Therefore, a major breakthrough came with the successful stabilisation of isolated magnetic skyrmions at RT in *magnetic multilayer systems*, which are composed of several very thin magnetic layers (≈ 1 nm) stacked on top of each other [7, 46–49], see Fig. 1c. In such structures, the thin magnetic layers have to alternate with other materials in an asymmetric fashion, in order to allow structural inversion asymmetry and provide a significant interfacial DM interaction, the prototypical example being the combination Pt/Co/Ir [7], see Fig. 1d. The skyrmion texture is replicated vertically inside all the stacked magnetic layers, which increases the total volume of the skyrmions and allows them to better resist against thermal fluctuations. Longer efforts for investigating different compositions of non-centrosymmetric materials [50, 51] also allowed the stabilisation of RT skyrmions in bulk compounds [52, 53]. The ability to obtain stable magnetic skyrmions at RT greatly expands the field of their possible applications. This has boosted the interest for magnetic skyrmions and has recently promoted research on skyrmions to become a very active field. The study of skyrmions notably constitutes an interesting and challenging topic for fundamental research. As is detailed in the following, the need to observe extremely small spin configurations motivates advances in microscopy and imaging techniques, and the need to understand the collective behaviour of somewhat large ensembles of spins at very different timescales pushes forwards the understanding of the involved dynamical processes.

Related to the observation and characterisation of magnetic configurations as small as skyrmions, various techniques can be employed, which has also contributed to the very fast development of this field of study. The detection of skyrmions has first been achieved in the reciprocal space, by the study of skyrmion lattice phases using neutron scattering [23]. Reciprocal space studies can also be performed with X-ray scattering [54, 55], as is done later in this thesis for studying the chirality of magnetic textures. Not limited to reciprocal space studies, different imaging techniques allow the observation of the skyrmion magnetic texture in real space. For skyrmions stabilised by bulk DM interaction, a technique based on the deflection of an electron beam by the local magnetization, Lorentz transmission electron microscopy, is most often used [24], which can also be used for interfacial DM interaction systems deposited on membranes, by tilting the imaged membrane [49, 56, 57]. Scanning local probe techniques, including spin-polarized tunnelling microscopy [26, 58] or Magnetic Force Microscopy (MFM) [59], are also very suitable to study several kinds of magnetic textures and skyrmions. In particular, the precise measurement of skyrmion profiles [60] by spin-polarized tunnelling microscopy (Fig. 5a) has allowed to validate the models of physical interactions stabilising magnetic skyrmions in interfacial systems [61]. The direct detection of the magnetic order in interfacial DM interaction systems can also be performed, not exhaustively, with spin-polarized low-energy electron microscopy ([62–64], Fig. 5b), scanning transmission X-ray microscopy ([7, 46], Figs. 5c,d) or photoemission electron microscopy ([65], Fig. 5e). Among all these
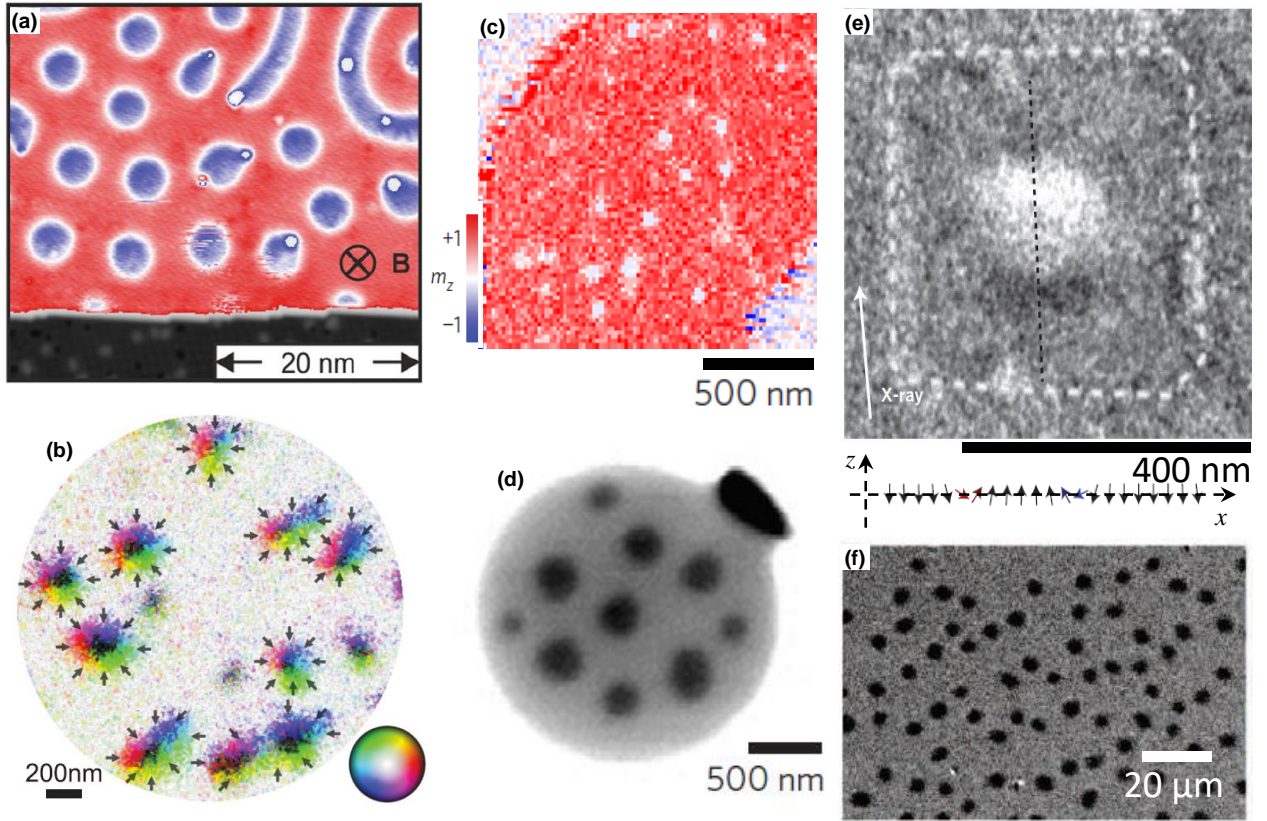
Figure 5: (a) Skyrmion lattice and stripe domains observed by spin-polarized scanning tunnelling microscopy. From [60]. (b) Isolated skyrmions observed by spin-polarized low-energy electron microscopy. Colours from the colour wheel indicates the orientation of the planar component of the magnetization. From [64]. (c) Isolated skyrmions observed in an extended film by scanning transmission X-ray microscopy. The colour scale indicates m_z. From [7]. (d) Skyrmion imperfect lattice observed in a confined structure by scanning transmission X-ray microscopy. From [46]. (e) Skyrmion stabilised by confinement in a lithographed structure observed by photoemission electron microscopy. The magnetization along a cut (dashed line) is represented below. From [65]. (f) Skyrmionic bubbles observed by Kerr microscopy. As it is a visible light microscopy technique, it cannot be used to observe skyrmions, which have a size often far below 400 nm. From [44].

possibilities, MFM constitutes a technique of choice because it can routinely be performed at the laboratory, and therefore it has been very often used in the work of this thesis.

Related to the understanding of skyrmion dynamical processes, much attention has been drawn by the experimental observation in chiral magnet systems of skyrmion motion at very low current-densities (four to five orders of magnitude smaller than those typically applied in experiments of current-driven motion of magnetic textures), induced by direct spin-transfer torques [66, 67]. This achievement contributed to raise even more the expectations that magnetic skyrmions, either stabilised in bulk chiral magnets or in interfacial systems, could be used for technological applications [6, 68]. In the case of skyrmions hosted in interfacial systems especially, prospects for reducing their size down to the nm scale [69, 70], predictions of their efficient current-induced displacement with spin-orbit torques rather than with spin-transfer torques [71], proposals of methods for their nucleation and detection [44, 71–75], allow to envisage that individual skyrmions could serve as information bits inside storage devices and even inside logic processing units. A very popular idea that has emerged from these theoretical and numerical studies is the feasibility of using magnetic skyrmions as mobile bits inside shift-register lines, known as *skyrmion racetracks*, similar to the

DW racetracks introduced a few years earlier [76, 77]. A foreseen advantage of skyrmions over DWs is their potentially very small, nm scale sizes, which could provide denser memory bits integration.

A clear parallel can be drawn between the working concepts of skyrmions-based and DWs-based racetracks, which both rely on spin-orbit torque-induced motion. The study of chiral DW motion in one-dimensional tracks [78–82] has revealed the essential role of vertical spin currents for inducing interfacial torques, and of the interfacial DM interaction for conforming the magnetization texture to the symmetry of these torques [83, 84]. These works have allowed a much better understanding of the mechanisms inducing spin-orbit torque motion of DWs, but also of skyrmions, whose motion is identically supported by the fixed chirality induced by the DM interaction (see also 3.2). Subsequently, current-induced motion of skyrmions has been evidenced in magnetic multilayers, albeit significantly hindered by a pinning behaviour [46]. Different than for DWs however, the non-trivial topology of skyrmions has an important consequence on their motion, by causing a transverse motion that deflects the trajectory of skyrmions away from the direction of the spin-orbit torque-induced driving force [19]. This effect, known as the *skyrmion Hall effect*, has recently been evidenced experimentally [44, 47], and refines the potential of current-induced skyrmion motion into tracks.

Another consequence of the particular topology of the magnetization texture of skyrmions is that they affects electron transport around them, giving rise to the *Topological Hall Effect (THE)* [19]. The THE contributes to the accumulation of a transverse voltage when an electronic current flows across skyrmions, which has been evidenced in bulk chiral magnet materials [85, 86]. In some cases, the magnitude of this effect allows to detect the presence of individual skyrmions, not relying on microscopy imaging techniques, but on electrical currents at the device level [87].

Considered together, these various properties of skyrmions, especially those of skyrmions stabilised in magnetic multilayers, appear very promising for the realisation of a new generation of common electronic devices operating at RT. They would possibly combine storage and logical operations with a much higher integration density [6, 68] that what can be achieved using present, conventional semiconductor technologies. Plenty of studies interested in potential applications of skyrmions have been triggered, alimenting what could appear as a "technological bubble", about which one can read different review articles [88–91]. The expectations are high, however, many questions remain open with regard to the practical feasibility of achieving all the functionalities promised by skyrmions. In such a context, further studies focusing on the fundamental properties of skyrmions: size, dynamics, *etc.* in real experimental systems are necessary before that the proposed advanced concepts of applications of skyrmions can be realistically and legitimately further developed. This constitutes a gap that brought the initial motivation for all the studies presented in this thesis. Several questions detailed below have been addressed, on the more fundamental or on the more applied levels, in order to contribute to the attempts towards filling this gap. Answering these questions constitutes the core of this thesis, as they appeared timely in the continued developments of the field of skyrmion physics and materials.

Not only physics but also materials, because chiral magnetism is no exception to the rule that all recent and less recent progresses in leveraging on the properties of magnetic thin films have been made possible by advances in their fabrication methods. The processes used to deposit thin films of nm and sub-nm thicknesses have a crucial influence on their magnetic properties. As it is detailed in Chapter 1, sputter deposition at RT has been privileged for the preparation of the experimental multilayer systems of this thesis. As a consequence, this work will also notably focus on the study of Néel skyrmions, as they are those obtained in magnetic thin films and multilayers. In this first chapter, some essential knowledge that is necessary to understand the formation of magnetic skyrmions and other types of magnetic textures in multilayer systems is summarised.

Based on a set of theoretical and experimental studies of skyrmions in atomically-thin systems, a good physical description of their properties has been devised [58, 60]. In contrast, many properties of skyrmions stabilised in magnetic multilayers remained imprecisely known at the beginning of this thesis, and no model was available for describing skyrmions hosted in multilayers properly. All

along my Ph.D., several observations triggered, and several aims required, the elaboration of such a model. As this tool proves crucial in the understanding of the specific properties of skyrmions hosted in multilayers, compared to atomically-thin systems or bulk compounds, this thesis then proceeds with the presentation of this new model of skyrmions in multilayers, in Chapter 2. A numerical representation going beyond previous analytical approximations is developed, which provides a versatile tool for the study of various properties of multilayered skyrmions.

Summarising the different state-of-the-art results reminded above, three complementary, main functionalities for skyrmions, including nucleation, motion and detection, have been proposed. In Chapter 3, we shortly review these concepts and their realisations in atomically-thin systems, before to establish how these three basic and essential functions can be achieved concurrently for skyrmions hosted in multilayers. Importantly, the exhibited schemes are compatible and are demonstrated in similar (but still not strictly identical) multilayers. In the particular case of the detection, no clear evidence of a topological Hall effect in interfacial DM interaction systems has been found, which we discuss as it remains an open question up to now.

While the motion of magnetic DWs has been shown to reach velocities of the order of the $\mathrm{km\,s^{-1}}$ [92–94], the motion of skyrmions remains hindered by large depinning threshold current densities and lower current-induced velocities [46]. In Chapter 4, we unveil several reasons that can harm the effectiveness of skyrmion motion and investigate how the issues of pinning and mobility could be solved in order to obtain very fast skyrmions. Several optimised multilayer structures are fabricated and are evaluated in experimental studies of current-induced motion.

Moreover, despite the fact that skyrmions hold promise to constitute the smallest magnetic objects that can be conceived in a magnetic thin film, experimental observations of RT-stable skyrmions exhibiting such small sizes has remained elusive. Chapter 5 exposes the interplay between skyrmion size and stability, and is devoted to different approaches aiming at obtaining very small skyrmions. The possibilities for combining different materials inside ferromagnetic layers are explored. Ultimately, we see how advanced multilayer structures can be designed in order to obtain antiferromagnetic skyrmions in systems of antiferromagnetically coupled layers, which is expected to allow the stabilisation of very small skyrmions stable at RT.

The engineering of magnetic multilayers, and in particular of their interfacial properties, constituted an important component of this thesis, essential notably to realise the studies presented in Chapters 4 and 5, even if this does not always directly appears in the discussion of the related experiments. In order to illustrate the kind of approach that has been followed to obtain the desired magnetic properties in our experimental systems, an archetypal example of multilayer development is presented into more details in Appendix A.

Beyond summarising the main results of this thesis, Chapter 6 provides an outlook by attempting to address the two objectives of enhanced mobility and compressed size for skyrmions all at once. The system last developed in Chapter 5 appears particularly suitable to combine progresses in these two directions. A few concluding remarks finally describe unfinished works, partial results and unexplored research, left for future studies.

The essential physics of chiral magnetism

The variety and the complexity of the magnetic configurations that can be observed in magnetic ultrathin films and multilayers arise primarily from the coexistence of five competing interactions affecting the magnetic moments held by the atoms: the Heisenberg exchange interaction, the DM interaction, the perpendicular magnetic anisotropy, the dipolar interactions and finally the Zeeman interaction with any external magnetic field applied to the system. As it will appear along their description below, it is remarkable that they are all of similar magnitude in the systems studied in this thesis. Therefore, none of these interactions can be neglected or treated within a perturbation approach —as is often done in physics— but, on the contrary, all terms need to be carefully considered as any of them may completely modify the resulting magnetic configurations.

The magnitude of these interactions, except the Zeeman interaction, are constant[1] magnetic properties in a given multilayer (which are thus determined by their composition and structure) at a given temperature (which is the RT in our case). However, they can be quite independently controlled and adjusted at the time of the fabrication of the films. The external magnetic field then constitutes an additional control parameter acting on the system, which allows the manipulation of the magnetization and the modification of the (meta)stable state(s) of the system. The study of magnetic skyrmions in multilayers actually follow a different approach, in comparison to skyrmions in bulk compounds. In films prepared by thinning of single bulk crystals ([24], [50], *etc.*), one has to rely on what Nature provides us as stable crystalline compounds, and may thus often be limited when aiming at controlling extensively all magnetic interactions. On the contrary, for the price of obtaining less perfect structures (which may not always be desirable, as shown later on in Chapter 4), multilayers allow a very flexible synthesis of compounds. In other words, being able to successively deposit sub-nm layers of different elements and alloys enables more control on their arrangement and on the bonds between the atoms composing the systems. A choice then arises with regard to the fabrication of the multilayers. On the one side, *epitaxy* methods aim at depositing films of crystalline quality as clean as possible, which can provide almost perfect crystalline order over large areas but often results in low yields and more constraints for the choice of composition and for the preparation of the substrates. On the other side, a more versatile and convenient approach is found in *out-of-equilibrium* methods (as opposed to epitaxy), which aim at depositing atoms in a disordered fashion. In the case of *sputtering* at RT, the deposition occurs by interaction of the atoms with a low-pressure plasma gas, not requiring specific substrates for the deposition of different layers. This method often results in amorphous or only partially ordered layers, that can however be more easily combined and stacked on top of each other. The more combinations and better deposition rates that can be achieved by sputtering made it one of the favourite deposition techniques for industrial applications. As it is widely used in industry, any physical system whose fabrication is based on sputtering can directly be employed for applications. These advantages motivate the choice made in this thesis of relying on sputtering for the fabrication of multilayer systems. Under the constraint that the arrangement of the atoms in the layers is only controlled along the vertical

---

[1]Actually, the magnitude of some interactions may also be controlled by electrostatic field effects [95] or by post-deposition ion-irradiation [96], which could constitute additional controls beyond what is described in this chapter

direction, while very difficult to control in the planar directions (and thus forbidding bulk DM interaction), the direct positioning of the atoms by non-epitaxial sputtering in a multilayer structure lifts the requirement of studying stable compounds, as long as they are simply metastable at RT. Adjusting between different thicknesses in the nm-range for each individual layer not only leads to infinite combinations of parameters, but also results in more complex behaviours, due to the role of the interfaces that become predominant when reaching the few atoms limit. In the perspective of targeting particular magnetic parameters, which is necessary to achieve the desired properties for skyrmions, this flexibility constitutes a great help. This point is probably well illustrated by the study presented in Appendix A, which shows how the DM interaction, the perpendicular magnetic anisotropy, *etc.*, can be precisely tuned by varying individual layer thicknesses, allowing its application to the stabilisation of antiferromagnetic skyrmions in §5.4.

In the following, I introduce into more details the five magnetic interactions of chiral systems listed above. They are essential in order to understand the properties of the varied magnetic textures that are to be studied in this thesis. Subsequent to their introduction, I discuss how and to what extent these interactions can be controlled by adjusting the composition of the multilayers. I provide typical values for each term, in order to explain how these interactions affect magnetic skyrmions and contribute to their stabilisation under particular anisotropy and field conditions.

1.1 Energy terms in magnetic thin films and multilayer systems

In order to build a physical description of the magnetic moments of atoms and their interactions for large systems (such as layers of several atoms of thickness or magnetic multilayers), it is suitable to define the magnetic order within a continuous approximation. As the length scale for the variations of the magnetic moments of atoms, typically the exchange length ≈ 10 nm, is orders of magnitudes larger than the interatomic distance, ≈ 2–3 Å, the magnetization can be described by the real-space reduced magnetization function $\mathbf{m}(x, y, z)$, a continuously varying unit vector indicating the local direction of the magnetization. By convention, x and y are orthogonal directions contained in the plane of the layers, while the z direction is directed along the normal of the films. This constitutes the *micromagnetic approach*. It is based on the argument that in the ferromagnetic transition-metals studied here —Co, Fe, Ni or their alloys— the magnetic moment of atoms does not significantly vary in magnitude but is only free to rotate. The strength of these moments is given by the saturation (volume) magnetization M_{s}. Moreover, the small thickness of the magnetic layers, around 1 nm, allows to neglect any variations of $\mathbf{m}$ in the vertical dimension of a single layer, thus allowing to simplify it into $\mathbf{m}(x, y)$. For a multilayered system comprising L magnetic layers separated by non-magnetic ones, the magnetization is defined in all the individual magnetic layers, denoted by l_i (i ranging 1–L from bottom to top), as individual functions $\mathbf{m}_i(x, y)$ that are not necessarily identical.

The magnetic energy density terms can be subsequently expressed as functions of the components of $\mathbf{m}$ and their derivatives, obtained by starting from the initial Hamiltonian description of the interactions and through summation over all magnetic moments or pairs of moments. Therefore, the micromagnetic description employed here differs completely from atomistic models used, *e.g.*, for describing atomically thin layers of magnetic systems grown epitaxially, in which case a complete Hamiltonian description taking into account several levels of neighbours is kept. The micromagnetic description actually neglects any possible consequence of having a varying value or sign for the different neighbour terms, such as in the case exchange frustration [29], by averaging all terms to effective quantities. Such an approximation is perfectly suitable for studying the equilibrium state of magnetic skyrmions hosted in disordered thin films and multilayers, ranging 10–100 nm in size, but it shall fail to provide an accurate description of smaller skyrmions as is required, for example, in analysing their stability against collapse [97, 98], an issue that is addressed into more details in §2.6 and §5.1 when dealing with the thermal stability of skyrmions.

Heisenberg exchange

In ferromagnetic materials, the Heisenberg (symmetric) exchange interaction promotes the alignment of neighbouring magnetic moments, and thus it tends to form domains of uniform magnetization. In the micromagnetic approach, for films uniform across their thickness, the Heisenberg exchange energy density ε_A is expressed as

$$\varepsilon_A = A \triangle \mathbf{m} = A \sum_{i=x,y,z} \left(\frac{\partial^2 m_i}{\partial x^2} + \frac{\partial^2 m_i}{\partial y^2} \right) \tag{1.1}$$

with A the Heisenberg exchange magnetic parameter.

In transition metal ferromagnets (FMs), A usually ranges 5–$30\,\mathrm{pJ\,m^{-1}}$. This exchange stiffness parameter progressively builds up upon increasing the thickness of the magnetic layers, because atoms acquire more and more neighbours that all couple together, before it saturates due to the fast decay of the magnetic orbitals overlap with the distance separating the atoms. This behaviour is more or less pronounced depending on the type of FM, and the bulk value is reached at thicknesses of 3–4 atoms typically [99]. In the bulk limit, $A \approx 30\,\mathrm{pJ\,m^{-1}}$ for Co, $20\,\mathrm{pJ\,m^{-1}}$ for Fe and $10\,\mathrm{pJ\,m^{-1}}$ for Ni [100, 101]. In principle, the exchange stiffness parameter can thus be controlled experimentally by reducing the magnetic layer thickness around $1\,\mathrm{nm}$ and below, or by varying the transition metal FMs. However, this also affects all other magnetic parameters, so that this approach is not used in practice. Exchange can rather be tuned by alloying transition metal FMs together [102, 103], or can be reduced by up to half when alloying them with several atomic percent of a non-magnetic element such as Pt, Ni, Pd, Cr or Ru [104, 105].

Dzyaloshinskii-Moriya interaction

The DM interaction [1, 2] can be seen as the antisymmetric counterpart of the Heisenberg exchange interaction. Due to symmetry rules, DM interaction terms are only allowed in systems which breaks the inversion symmetry along some direction. The DM interaction favours a perpendicular alignment of neighbouring magnetic moments with a preference for one direction of rotation of the magnetic moments, either $\uparrow\rightarrow\downarrow$ or $\uparrow\leftarrow\downarrow$ depending on its sign [106]. Combined with the influence of the Heisenberg exchange, it results in the formation of spiralling, non-collinear configurations of the magnetization featuring a unique chirality of the magnetic textures, which constitutes a crucial feature for the present work. As mentioned in the introduction, the inversion symmetry in multilayer systems is usually not broken due to the crystalline structure, except for a few epitaxial multilayers [107], but by the change of type of atoms found at the interfaces between layers [9, 10]. The direction of symmetry breaking is thus perpendicular to the interfaces of the layers. The DM interaction energy density ε_D is expressed as [83]

$$\varepsilon_D = D[m_z \operatorname{div} \mathbf{m} - (\mathbf{m} \cdot \nabla) m_z] = D \sum_{i=x,y} \left(m_z \frac{\partial m_i}{\partial i} - m_i \frac{\partial m_z}{\partial i} \right) \tag{1.2}$$

with D the norm of the effective DM interaction vector (contained in the interfacial plane, see Fig. 1b) and that we call DM interaction parameter.

The interfacial DM interaction appears as the key ingredient for obtaining chiral textures in magnetic thin film systems and multilayers. We might therefore now devote some attention to its origins and to the means of controlling its magnitude. The consideration of the DM interaction at interfaces of not atomically-thin systems has emerged very recently — arguably, with the results of Chen *et al.* in 2013 [62, 63] — and at present it only offers a partial understanding of its mechanisms. Guidelines can nonetheless be drawn from the several theoretical and experimental results available.

The Fert-Levy mechanism for the DM interaction involves a pair of magnetic moments plus a third atom, subject to a three-site interaction [108]. It is due to the spin-orbit scattering of the conduction electrons by the nonmagnetic impurities [108], and is thus a consequence of the spin-orbit interaction, that would naively scale with Z^4, where Z is the atomic number of the third atom

element. In metals, spin-orbit coupling effects instead scale with Z^2, and the DM interaction evolves linearly with respect to spin-orbit coupling [109]. This causes that a DM interaction significant enough to impose a specific chirality is found in FM interfaced with heavy-metal (HM) layers such as Pt, Ta to a lower extent, *etc.* [82, 110, 111]. The interfacial DM interaction can also be significant in the absence of HM elements, in the case of FM layers adjacent to insulating oxides [65, 112] as is done in this thesis, or graphene [113], due to a different, Rashba type spin-orbit coupling mechanism [114–116]. The DM interaction Hamiltonian parameters in thin film systems reach energy values at most one order of magnitude below that of the Heisenberg exchange. The strength of the micromagnetic DM interaction parameter $|D|$ thus belongs to the $mJ\,m^{-2}$ range, whose sign and magnitude depend on the nature of the interfaces with the FM layer.

As it is necessary to break the inversion symmetry of the multilayer structure in order to obtain a significant DM interaction, it means in practice that it is required to alternate between at least three different materials. In multilayers composed of two materials only, *e.g.* [Pt/Co], the inversion symmetry is not significantly broken in the vertical direction. As similar —yet not necessarily equivalent, due to growth conditions— interfaces are formed at the bottom and at the top of the FM, a very weak interfacial DM interaction results, because the local DM interactions at bottom Pt/Co and top Co/Pt interfaces compensate each other almost completely. On the contrary, a significant DM interaction can be achieved by combining different bottom and top interfaces enclosing the FM, *e.g.*, in [Pt/Co/Ir] multilayers, see Fig. 1c [7, 110]. By definition of the DM interaction vector, a reversed sign of the DM interaction is obtained upon reversing the stacking order, *i.e.*, by depositing [Ir/Co/Pt] in the present example [7]. Because it is an effect of interfacial origin, the effective DM interaction parameter D obeys to an inverse dependence with the thickness of the FM layer [112, 117]. We can identify an interfacial DM interaction parameter D_s such $D = D_s/t_{FM}$. Experimentally, D can mostly be controlled by selecting different materials and/or reversing the stacking order. Nevertheless, only Pt/Co interfaces and Co/oxide interfaces have been recognised as good platforms to obtain a significant $|D| > 1\,mJ\,m^{-2}$, up to $|D| \approx 2\,mJ\,m^{-2}$ when combining both, such as in [Pt/Co/Al$_2$O$_3$] or [Pt/Co/MgO] structures [65, 112]. All other interfaces combinations are found to provide only moderate or very moderate DM interaction, with $|D| < 0.5\,mJ\,m^{-2}$ [118].

A work conducted in collaboration with the team of ab-initio calculations lead by S. Blügel in Jülich allowed to verify during this thesis that the DM interaction is expected to be quite robust against intermixing [119], so that obtaining clean interfaces should not be critical in achieving large DM interaction strengths. A definition of what is called intermixing here is represented in Fig. 1.1a, in which x is the proportion of atoms 1 and 2 that are swapped at the interface. A couple of examples are shown in Fig. 1.1b, with the limit cases x = 0 and x = 1, as well as x = 0.25. The evolution of the calculated DM interaction parameter D_s is shown as a function of x in Fig. 1.1c, which reveals that the DM interaction only drops by up to 20–25 percent for a maximal intermixing[2] at x = 0.5. This point further **justifies our choice of relying on sputter deposition**.

In contrast, the DM interaction has been found to be sensitive to the crystalline order, notably in W/CoFeB/MgO [120]. This is further confirmed by the progressive reinforcement of the DM interaction at the Pt/Co interface with the thickening of its buffer layer [121], as it promotes a (111) texture[3] for the interfaces. This sensitivity to the crystalline texture may explain the dependence of the DM interaction on the interfacial quality in Pt/Co/Pt [122]. A different mechanism explains the variation of the DM interaction with HM layer thickness when it is not a buffer affecting the crystallinity, but for example a Pt capping layer [123]. Even if the DM interaction is strongly located at the first atomic plane of Pt adjacent to the FM layer, there is a greater number of farther Pt atoms, which are thus expected to also contribute, albeit with a reduced magnitude, to the overall DM interaction. Consequently, the DM interaction is found to rise as a function of Pt layer

---

[2]The maximal intermixing is indeed reached at x = 0.5 and not at x = 1, for which a Pt/Co (1 ML)/Pt(1 ML)/Co system is formed, where ML designates a single atomic layer.

[3]The texture designates the orientation of atom planes at the surface of a layer. Here, (111) refers to the crystallographic axis obtained perpendicular to the surface. With an increasing amount of Pt atoms deposited in a layer, the originally disordered atoms at the surface progressively arrange themselves so that a flat (111) plane is formed.
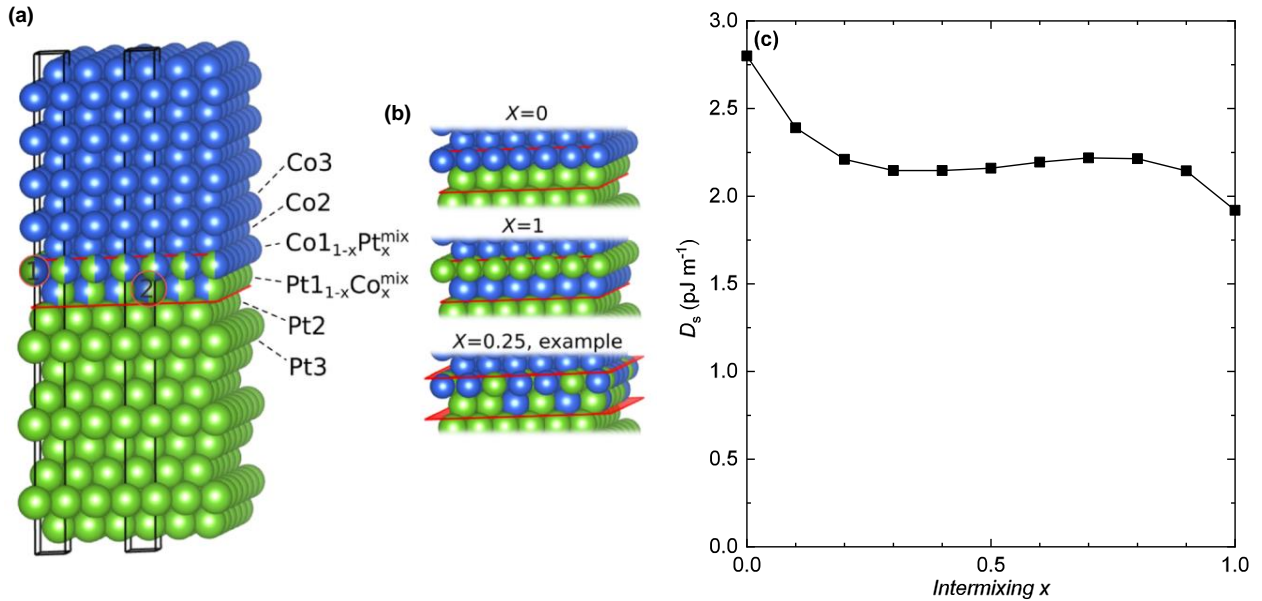
Figure 1.1: (a) Definition of disorder for a crystalline Pt/Co interface. Green atoms are Pt, blue atoms are Co. In case of disorder, for example, atom 1 that is initially a Co atom can be swapped with atom 2 that is initially a Pt atom. The proportion of swapped atoms is measured by x, as shown in the examples of (b) x = 0, x = 1 and x = 0.25. (c) Theoretical evolution of D_s with x.

thickness, before it rapidly saturates below 2 nm. Finally, the DM interaction is expected to be tunable through the dusting of the FM interfaces with HM elements [119], as well as by combining different FM into adjacent layers [48], or even into alloys.

Note that almost all multilayers reported so far to show a significant DM interaction are composed of amorphous or (111)-textured layers exhibiting C3v symmetry, for which the DM interaction is isotropic. However, a non-isotropic DM interaction could be obtained in Au/Co/W(110) [34], which may allow to stabilise antiskyrmions [33, 35].

Magnetic anisotropy

The interfacial magnetic anisotropy existing in magnetic thin films and multilayers mainly originates from the lower symmetry of the environment of magnetic moments located close to the interfaces [9]. Contributions to the magnetic anisotropy can include magnetocrystalline effects being reinforced at the interfaces between different materials, interfacial chemical bonds with adjacent layers and/or strain effects due to the action of adjacent layers. All these mechanisms can favour either easy-axis (uniaxial) perpendicular anisotropy or easy-plane magnetic anisotropy. In general, the anisotropy energy density ε_K is expressed as

$$\varepsilon_K = -K_u m_z^2 \qquad (1.3)$$

where the magnetic anisotropy parameter $K_u > 0 \; (< 0)$, corresponding to perpendicular (in-plane) magnetic anisotropy, can be decomposed into

$$K_u = \frac{K_s}{t_{FM}} + K_v \qquad (1.4)$$

with K_v the volume (thickness independent) term, and K_s the surfaces anisotropy term (including contributions from top and bottom interfaces) thus causing an inverse dependence of the magnetic anisotropy on t_{FM}, the thickness of the FM layer. In most FM thin films, notably including those under consideration in this thesis, K_v is negligible. However, the planar geometry of thin films makes them subject to an additional contribution of the dipolar interactions between moments,

which causes an effective reduction of the anisotropy. In the case of a uniformly magnetized layer (the case of dipolar interactions occurring in non-uniformly magnetized films is described after), an effective magnetic anisotropy

$$K_{\text{eff}} = K_{\text{u}} - \frac{\mu_0 M_{\text{s}}^2}{2} \qquad (1.5)$$

needs to be considered, replacing K_{u} in (1.3), in order to take into account the reduction of anisotropy due to dipolar interactions.

Contrary to what is the case for the DM interaction, the topic of magnetic anisotropy in metallic multilayers has received enormous attention for nearly three decades. It thus seems reasonable to say that its mechanisms are well understood, with the support of a myriad of experimental observations. It is certainly not possible to summarise all these results here while keeping enough conciseness, but the interested reader can refer to several extended reviews on the topic [124, 125]. Nevertheless, a very large majority of studies has been focused on multilayers made of two repeated layers, thus requiring new studies towards characterising magnetic anisotropy in multilayers with a trilayered repetition unit, as is required for obtaining a significant DM interaction. An important aspect of the work conducted along the three years of preparation of this thesis consisted in the characterisation and the systematic investigation of perpendicular magnetic anisotropy in multilayers with such trilayered repetition units. Several examples such as Pt/Co/Ir, Pt/CoFeB/Al$_2$O$_3$, Pt/Co/Ru, Pt/Co/Ni, *etc.*, appear in the following chapters, and were inspired by the literature results on binary compounds.

In the case of metallic FMs that are Co, Fe, Ni and their alloys, the surfaces anisotropy term can be large enough to ensure perpendicular magnetic anisotropy in nm-thick layers, but not for more than a few nm [124]. The FM layer thickness at which the effective magnetic anisotropy K_{eff} changes sign from perpendicular to easy-plane anisotropy is called spin-reorientation transition thickness, t_{SRT}. For example, it can vary in the window 0.2-2.5 nm for Co, depending on the material of adjacent layers. The value of K_{s} is indeed strongly modulated by the type of non-magnet (NM) elements the FM layers are interfaced with. Due to the dipolar-related term $-\mu_0 M_{\text{s}}^2/2$ in the effective anisotropy, the spin-reorientation thickness is also strongly influenced by M_{s}. Consequently, the observed spin-reorientation thicknesses observed in Fe-based systems are generally smaller than in Co-based systems, despite their larger surfaces anisotropy K_{s}, due to their higher saturation magnetization. In figures, $-\mu_0 M_{\text{s}}^2/2 = 1.86$, 1.27 and 0.14 MJ m^{-3} for bulk Fe, Co and Ni, respectively [124]. Different binary multilayered systems are known to provide a robust perpendicular magnetic anisotropy, notably Pt/Co [126], Pd/Co [127], Pt/Ni [128]; or also Pd/Fe [127], Ag/Fe [129], for which the origin of the perpendicular magnetization is less understood. A particular case is Co/Ni [130], in which case no FM/NM interfaces are formed but only FM/FM interfaces. Nevertheless, the strain effects building up in the Co/Ni superlattice are sufficient to create perpendicular magnetic anisotropy. As for the DM interaction, the magnetic anisotropy often strongly depends on the texture of the interfaces as well [124].

The perpendicular magnetic anisotropy can thus be varied experimentally by the choice of the nature of the FM and of its interfaces, by adjustment of the FM layer thickness and by tuning its M_{s} [104, 105]. The use of varied buffer layers, preparing the growth of the multilayers differently, allows to select an orientation and a degree of texture [such as as the (111) texture for Pt/Co] and thus to control the perpendicular magnetic anisotropy of the interfaces [131]. These considerations are crucial for realising the systems described later in this thesis.

Dipolar interactions

The magnetization of thin films and multilayers might also be affected by the dipolar interactions, which correspond to the dipole-dipole interactions between the magnetic moments hold by all FM atoms. Contrary to the three interactions already described, which are local, *i.e.*, limited to the neighbouring moments, dipolar interactions are distant and may thus give rise to long-range order over lengths of hundreds of nm to hundreds of µm. In the micromagnetic framework, the

dipolar interactions are described not by considering all moments individually but by defining a demagnetizing field $\mathbf{H}_{\text{dem}}$, originating from the distribution of the magnetization inside the system, and acting on the magnetization. It is thus a self-demagnetizing field, as the generated field continuously evolves with the changes of the magnetization configuration towards reaching the lowest energy configuration. The demagnetizing field is obtained as $\mathbf{H}_{\text{dem}} = -\nabla\psi$, where the magnetostatic potential ψ satisfies Poisson's equation and usual boundary conditions, with regard to the contributions of volume and surface magnetic charges [132]

$$
\begin{aligned}
&\text{(i) } \nabla^2\psi = \begin{cases} M_{\text{s}}\operatorname{div}\mathbf{m}, & |z| \leq t_{\text{FM}}/2 \\ 0, & |z| > t_{\text{FM}}/2 \end{cases} \\
&\text{(ii) } \nabla\psi \xrightarrow[z\to\pm\infty]{} 0 \\
&\text{(iii) } \psi \text{ continuous at } z = \pm t_{\text{FM}}/2 \\
&\text{(iv) } \left.\frac{\partial\psi}{\partial z}\right|_{z=\left(\pm\frac{t_{\text{FM}}}{2}\right)^-} \pm (-M_{\text{s}}\mathbf{m}\cdot\hat{\mathbf{z}}) = \left.\frac{\partial\psi}{\partial z}\right|_{z=\left(\pm\frac{t_{\text{FM}}}{2}\right)^+}
\end{aligned}
\tag{1.6}
$$

for a ferromagnetic layer of thickness t_{FM}. The demagnetizing energy density ε_{dem} is then obtained as

$$
\varepsilon_{\text{dem}} = -\frac{\mu_0 M_{\text{s}}}{2}(\mathbf{H}_{\text{dem}}\cdot\mathbf{m}).
\tag{1.7}
$$

In general, this part of the magnetic energy is difficult to treat accurately because of the computationally expensive resolution of (1.6), which has a simple analytical solution in only very few cases, or with restrictive simplifications. As mentioned above, in the case of a uniformly magnetized layer, the dipolar interactions are equivalent to a rescaling of the perpendicular magnetic anisotropy into an effective magnetic anisotropy. However, a more general case occurring in ferromagnetic layers is the formation and stabilisation of alternate uniform domains separated by DWs [12]. We focus here on the case of perpendicular magnetic anisotropy, as perpendicular order is required to host skyrmions. Inside a domain, the magnetization is then either $\mathbf{m} = +\hat{\mathbf{z}}$ or $\mathbf{m} = -\hat{\mathbf{z}}$, and the magnetization continuously rotates through the DWs to connect these domains. In multilayers, the energy of magnetic stripe patterns can be derived [13, 14, 133], allowing to explain the different magnetic configurations (phases) that can be obtained in a ferromagnetic film with perpendicular anisotropy, upon varying the applied field and the magnetic anisotropy [134]. The dipolar interactions are then no longer equivalent to a rescaling of the perpendicular magnetic anisotropy as soon as non-uniform magnetic configurations are formed.

Experimentally, the strength of the dipolar field generated by a given configuration cannot be directly controlled. However, the influence of the dipolar interactions on the magnetization can be controlled varying M_{s}, by using different FM elements or alloying them as described above, which is important for the considerations of Chapter 5. Small variations of M_{s} have large effects on dipolar interactions, as the generated field is proportional to M_{s}, and is multiplied again by M_{s} to obtain the demagnetizing energy ε_{dem}. In magnetic multilayers, changing the vertical geometry, $i.e.$, either the FM layer thickness t_{FM}, the repetition periodicity p between FM layers or the repetition number L dramatically modifies the strength of the dipolar field. The separation between the different FM layers can be seen as a vertical dilution of the magnetization through the thickness, in which the average magnetization is only $(t_{\text{FM}}/p)M_{\text{s}}$ [46].

External field

Due to Zeeman splitting, the magnetization tends to align with any external magnetic field applied to the films. The Zeeman energy density ε_{ext} due to an external field is

$$
\varepsilon_{\text{ext}} = -\mu_0 M_{\text{s}}(\mathbf{H}_{\text{ext}}\cdot\mathbf{m}),
\tag{1.8}
$$

and its effect is thus proportional to M_{s}. It provides an external control on the magnetic configurations present in the system. Notably, when a non-uniform configuration is stabilised, applying

	t_{FM}	p	L	FM material	HM/NM material	Stack order	Texture
A	↕†	·	·	↕	·*	·	↕
D	1/	·	·	↕	↕	±	↕
K_{eff}	1/	·	·	↕	↕	·	↕
ε_{dem}	↕	↕	↕	↕	·*	·	↕
ε_{ext}	↕‡	·	·	↕	·*	·	↕

Table 1.1: Dependences of A, D, K_{eff}, ε_{dem} and ε_{ext} (lines) with controllable experimental parameters (columns). "↕": varies with. "±": changes sign with. "1/": inversely proportional to. "·": independent. †until $\approx 1\,\text{nm}$. ‡if changes in M_{s}. *actually not perfectly true, because of the possibility of induced moments.

magnetic fields favours the parts of the magnetic configuration where **m** is aligned with the field, and disfavours the parts where **m** is opposed to the field. For large enough fields, a uniform magnetic configuration with **m** aligned along the field is obtained.

Decorrelating the magnetic parameters

It appears from the considerations above that A (Heisenberg exchange), D (DM interaction), K_{u} (anisotropy) and M_{s} (for effective anisotropy, dipolar interactions and magnitude of Zeeman interaction with respect to the applied field) necessarily show some correlations, because they often depend on the same experimental parameters that are t_{FM}, type of FM/NM interfaces, crystallinity of the layers, *etc.* This actually constitutes a key issue in the engineering of skyrmion multilayer properties, for which it would be desirable to be able to control each magnetic energy term independently. For example, parameters D and K_{u} depend similarly on t_{FM}. It is therefore difficult to modify one parameter among D and K_{u} without modifying the other. In order to obtain an overview of how independently the magnetic parameters can be controlled with multilayer design, their relations are summarised in Table 1.1. Note that growth conditions and hence texture of the interfaces may potentially vary with any of t_{FM}, p, L, materials and stacking order, affecting in turn all magnetic energies. For example, the variation of texture that may result of an inversion of the stacking order limits in practice the possibility of reversing the sign of D by reversing the stack, without changing the values of $|D|$, K_{u} and M_{s}. Likewise, variations of texture of the interfaces related to changes in the thicknesses of the non-magnetic layers (in the case of Ta, W, *etc.*) or to the accumulation of layers (increasing L) may render all these considerations even more complicated.

Because D and K_{u} depend similarly on whether (111)-oriented or completely amorphous interfaces are formed, it has been found experimentally that there is some correlation between them in Pt/Co systems [120]. An open question remains, however, related to the origin of a correlation between Heisenberg exchange and DM interaction [135, 136]. These effects hinder the possibilities for independent tuning of all the magnetic parameters in a single system defined by its combination of layers (*e.g.*, Pt/Co/Ir or MgO/CoFeB/Pt), but make necessary to use several different systems in order to be able to reach more sets of magnetic parameters. For example in §5.3, a strategy is developed to allow independent tuning of M_{s} without affecting D_{s} and K_{s}, by insertion of an additional Ni layer in the Pt/Co/Ru system.

1.2 Balance between magnetic interactions inside skyrmions

From the expressions of the five magnetic energy densities, it is possible to evaluate their different contributions to the total energy of a magnetic skyrmion. Several attempts have been made to derive either more accurate or more simplified analytical models grasping the essential features of these five interactions inside isolated ferromagnetic skyrmions [61, 68, 137–139], which is discussed in the

next chapter. Rather than showing any convoluted equations at this point, we can first simply evaluate orders of magnitude for each energy density term. The characteristic size of DWs in perpendicularly magnetized materials is about $10\,\text{nm}$. The variations of the magnetization inside a skyrmion occur on the same length scale. The exchange energy density scales with the square of the gradient of magnetization, so that $\varepsilon_\text{A} \approx 10\,\text{pJ}\,\text{m}^{-1} \times (10\,\text{nm})^{-2} \approx 0.1\,\text{MJ}\,\text{m}^{-3}$. Likewise the DM interaction energy density scales with the gradient, so that $\varepsilon_\text{D} \approx 1\,\text{mJ}\,\text{m}^{-2} \times (10\,\text{nm})^{-1} \approx 0.1\,\text{MJ}\,\text{m}^{-3}$. The competition between perpendicular magnetic anisotropy and dipolar interactions often result in an effective perpendicular magnetic anisotropy $\varepsilon_\text{K} + \varepsilon_\text{dem} \approx 0.1\,\text{MJ}\,\text{m}^{-3}$. Finally, for a field of $\mu_0 H_\text{ext} = 0.1\,\text{T}$, typical among the perpendicular field values employed to stabilise skyrmions in magnetic multilayers, and $M_\text{s} = 1\,\text{MA}\,\text{m}^{-1}$, within the average range of saturation magnetization values for Co, Fe, Ni and their alloys, $\varepsilon_\text{ext} \approx 0.1\,\text{T} \times 1\,\text{MA}\,\text{m}^{-1} \approx 0.1\,\text{MJ}\,\text{m}^{-3}$. This simple point illustrates well why all magnetic interactions are important in understanding the formation of skyrmion magnetic configurations in multilayer systems.

Beyond simply showing similar order of magnitude, it appears that the integration of the different magnetic energy density terms, over the whole volume of an isolated multilayered skyrmion, leads to comparable energies. Moreover, they all exhibit a similar evolution with the size of the skyrmion. In order to obtain a more precise evaluation of each energy contribution for a skyrmion, we can use here a widely available micromagnetic simulation software, MuMax[3] [140]. Such a numerical simulation tool allows, among other functionalities, to analyse the time-evolution of a magnetic configuration and of its energies in a magnetic system of arbitrary geometry. Let us choose a set of very usual magnetic parameters, similar to the ones determined in standard Pt/Co/NM-based skyrmion multilayers [7, 46]: $A = 10\,\text{pJ}\,\text{m}^{-1}$, $D = 1.35\,\text{mJ}\,\text{m}^{-2}$, $M_\text{s} = 1\,\text{MA}\,\text{m}^{-1}$, $K_\text{u} = 0.8\,\text{MJ}\,\text{m}^{-3}$ (which corresponds to $K_\text{eff} = 0.172\,\text{MJ}\,\text{m}^{-3}$), in a multilayer geometry given by $t_\text{FM} = 1\,\text{nm}$ and $p = 3\,\text{nm}$ for $L = 5$ magnetic layers. The variations of the different energy terms are analysed as a function of the skyrmion radius r_sk in Fig. 1.2, for different external magnetic fields applied perpendicular to the multilayer, ranging $\mu_0 H_\text{ext} = 25\text{–}50\,\text{mT}$. The skyrmion radius r_sk is defined as the distance from the centre of the skyrmion at which the magnetization crosses the plane of the layer, $i.e.$, $m_\text{z} = 0$ at a distance r_sk from the centre. The evolution of the skyrmion energy is analysed for initial radii either larger or smaller than the equilibrium radius, which both converge towards the equilibrium radius over simulation time[4]. As can be seen in Figs. 1.2a,d,g, all energy terms are comparable in magnitude. This is even further verified when E_K is rescaled into E_Keff, thus rather taking into account the effective anisotropy, while the difference between them is added to E_dem, in order to obtain the distant dipolar interaction part only, referred to here as E_lr (see Figs. 1.2b,e,h). In other words, we define $E_\text{Keff} = -K_\text{eff} m_\text{z}^2$ and $E_\text{lr} = -(\mu_0 M_\text{s}/2)(\mathbf{H}_\text{dem} \cdot \mathbf{m} + M_\text{s} m_\text{z}^2)$. Consistent with the definition of the dipolar fields, $E_\text{lr} = 0$ for a uniform magnetization. Note that the total energy is conserved as $E_\text{K} + E_\text{dem} = E_\text{Keff} + E_\text{lr}$. By performing this transformation, some parts of the energy components are simply combined under different labels. It also appears that all energy terms increase monotonically with the skyrmion size. However, a particular equilibrium skyrmion size r_sk is obtained at a minimum of the total energy E_tot (Figs. 1.2c,f,i). It is only the small deviations from linearity of the evolution of E_A, E_D, E_ext, E_Keff and E_lr with r_sk that explain the formation of a minimum of energy, which is a very shallow minimum if compared to the magnitude of the different energy terms that compete to create it. This supports even further the statement that all magnetic interactions are of comparable magnitude, by adding the fact that they vary by similar amounts with skyrmion size. Consequently, it appears that all terms must be evaluated precisely in order to model satisfactorily a magnetic skyrmion in magnetic multilayers.

---

[4]The present $E(r_\text{sk})$ curves have been corrected for an artefact due to the dynamical evolution of $\mathbf{m}$ that shifts the curves, because of the on-going contraction or expansion of the profiles. The displayed energies are corrected by shifting each half curve (r_sk larger than equilibrium and r_sk smaller than equilibrium) by half their vertical gap.
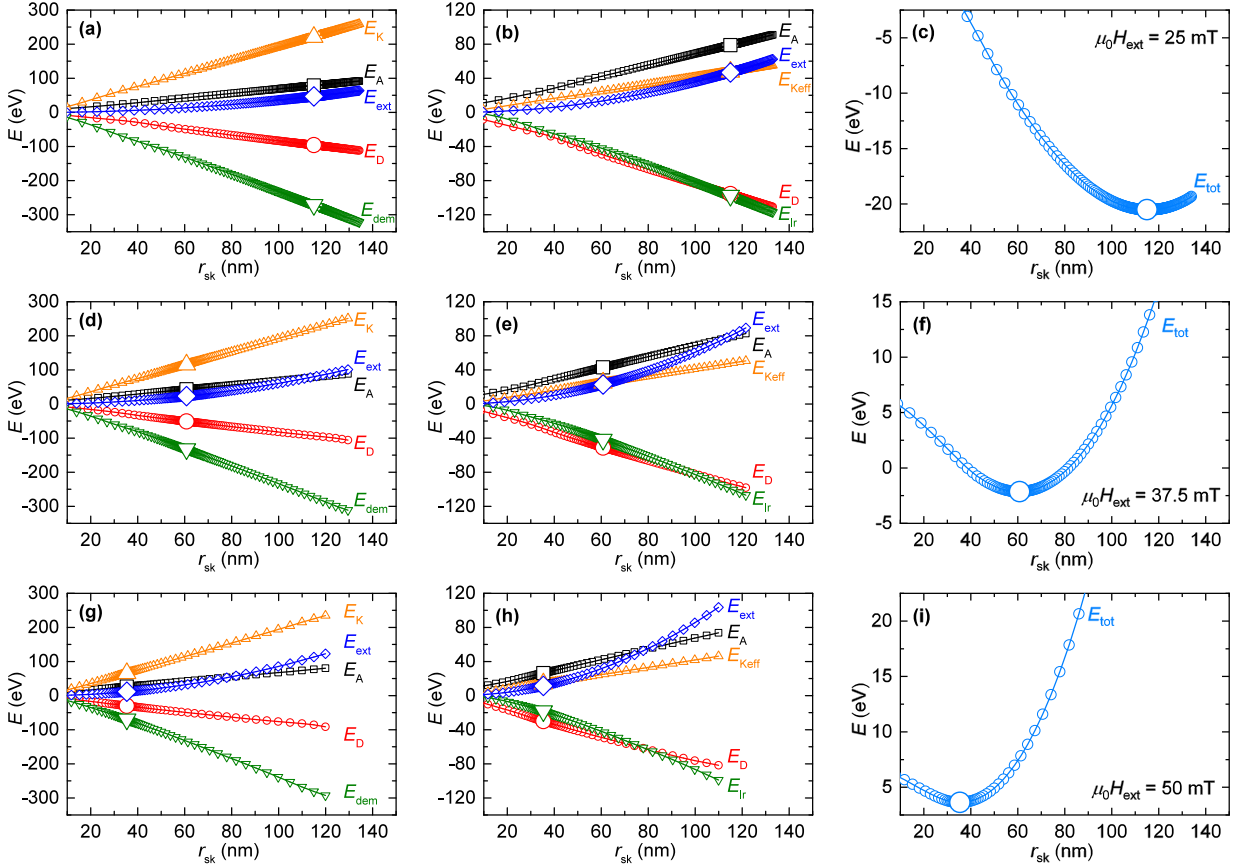
Figure 1.2: (a,d,g) Integrated energies over the multilayer skyrmion E_A (exchange, black squares), E_D (DM interaction, red circles), E_K (uniaxial anisotropy, gold up triangles), E_{dem} (demagnetizing field, green down triangles) and E_{ext} (external field, blue diamonds), as a function of skyrmion radius r_{sk}. (b,e,h) Same with replacing E_K by E_{Keff} and E_{dem} by E_{lr}. (c,f,i) Total skyrmion energy E_{tot} as a function of skyrmion radius. External field is set at (a–c) $\mu_0 H_{ext} = 25\,\text{mT}$, (d–f) $37.5\,\text{mT}$ and (g–i) $50\,\text{mT}$. The larger symbols indicate the values at the minimum of the total energy E_{tot}, located at the equilibrium skyrmion radius.

1.3 Phase diagrams for skyrmion systems

It is important to understand that even in magnetic systems with strong DM interaction, magnetic skyrmions are not necessarily the most stable magnetic configuration. The usual situation in magnetic multilayers with infinite extension in the plane is that in the absence of any external field applied to the system, alternate up ($m_z = 1$) and down ($m_z = -1$) stripe domains, separated by DWs, are formed [14]. The formation of such stripe domains may occur in the presence or in the absence of DM interaction, as it originates from distant dipolar interactions. In a perpendicularly magnetized material, the magnetic anisotropy disfavours the formation of alternate domains by associating an additional cost to the formation of DWs. However, distant dipolar interactions are increasingly stabilising when increasingly tight alternate domains are formed. Their balance defines the periodicity of the stripe domains. In the presence of DM interaction, the energy cost of DWs is drastically reduced, which favours even more the stripe domains configuration.

For this reason notably, even if a skyrmion solution is found, *i.e.*, even if there exists a cylindrically symmetric magnetization profile with a reversed core that constitutes a minimum of energy for the system, this solution can almost always lower its energy by breaking its cylindrical symmetry and expanding into a stripe (elliptical instability). Even if stabilising skyrmions in the absence of external field is theoretically possible in simulations, it requires a very careful control of

the magnetic parameters, which may be very difficult to achieve in experiments. In the presence of an external magnetic field opposed to the core magnetization of the skyrmion however, which thus acts as a confinement field, axisymmetric skyrmion solutions can be more easily stabilised (and therefore resist to perturbations) [22, 68, 137]. On the opposite, when the applied magnetic field is too large, skyrmion configurations may reduce in size until they collapse and vanish.

In order to evidence the role played by the external field into controlling the magnetic configuration of the system, the energy of the skyrmion lattice configuration [141] can be analysed with respect to the two other possible phases, namely, ferromagnetic stripe domains and uniform configuration [68, 69, 142]. The stable phase is the configuration which results in the lower total energy for the system. It was found by Monte-Carlo simulations and temperature-dependent simulations that in systems with infinite extension, stripe domains and uniform phases compete with a skyrmion crystal phase, in which circular or deformed skyrmions condense into the form of an hexagonal lattice [69, 143, 144]. Consequently, isolated skyrmions, which constitute the object of interest in this thesis, are only metastable solutions in uniform systems, but do not constitute the ground state of the system. If the skyrmion energy is lower than those of both uniform and stripe configurations, a skyrmion crystal is favoured; otherwise, isolated skyrmions can only be metastable and constitute defects in the magnetic configuration. Note that as there exists a given energy barrier separating the locally uniform magnetization from the skyrmion configuration and the opposite — constituting a skyrmion nucleation barrier and a skyrmion annihilation barrier, respectively — isolated skyrmions can be stabilised in a uniform magnetization background for parameters favouring either the skyrmion crystal or the uniform phase. However, for parameters favouring the stripe phase, the energy barrier between a skyrmion and a stripe domain is either absent or very low, which prevents the stabilisation of isolated skyrmions in RT systems, as they immediately expand into stripes (see §2.5).

It is possible to determine numerically the stable phase by determining the energies of the stripe, skyrmion crystal and uniform phases within micromagnetic simulations (here performed with MuMax[3]), instead of performing Monte-Carlo simulations, which are too complex for our simply explanatory needs here. To this effect, an approach is to vary the periodicity of both stripe and skyrmion crystal phases in order to retain the resulting minimum energy for each phase. For each applied field value, a minimum energy search is thus performed by rescaling the stripe and skyrmion phases and letting these configurations converge to their stable state at each value of imposed periodicity. An example of resulting energy densities for such simulations is displayed in Fig. 1.3a for an applied field varying in the range $\mu_0 H_{\text{ext}} = 0$–40 mT. Parameters are: $A = 14$ pJ m^{-1}, $D = 1.4$ mJ m^{-2}, $M_{\text{s}} = 1.3$ MA m^{-1}, $K_{\text{u}} = 1.06$ MJ m^{-3}. In this example, a single layer of thickness 1 nm is considered, for which dipolar interactions are directly included into the uniaxial anisotropy by transforming K_{u} into K_{eff} (thus neglecting its distant effects). By performing this operation for various values of the anisotropy, it is possible to obtain a $(\mu_0 H_{\text{ext}}, K)$ phase diagram of the system, as displayed in Fig. 1.3b, which summarises the essential role of the external field in controlling the magnetic configuration of the system. Notice that the skyrmion phase cannot be obtained in multilayers with a too large anisotropy (top of Fig. 1.3b), unless strong dipolar interactions are present. Such phase diagrams match with experimental observations [145]. Further optimisation of this simulation technique would be required to extend its results to multilayers in the presence of dipolar interactions, which has not been performed in this thesis as it would require to further optimise the micromagnetic code itself.

In practice, the different magnetic phases can be directly observed, for example, using MFM (see Appendix B), a technique which records maps of the local magnetization at the nm-scale through detecting the dipolar field gradients generated by the imaged system. In Figs. 1.4a–c, different MFM images are shown, similar to maps of $m_{\text{z}}(x, y)$, which have been recorded for different values of the field $\mu_0 H_{\text{z}}$ applied perpendicular[5] to a multilayer of composition [Pt(2.4 nm)/ Co$_{10}$Fe$_{70}$B$_{20}$(0.8 nm)/

---

[5]In the following of this thesis, $\mu_0 H_{\text{ext}}$ continues to be used for modelling, while $\mu_0 H_{\text{z}}$ is used to describe experiments, in order to facilitate the understanding of what results are theoretical and what results are experimental.
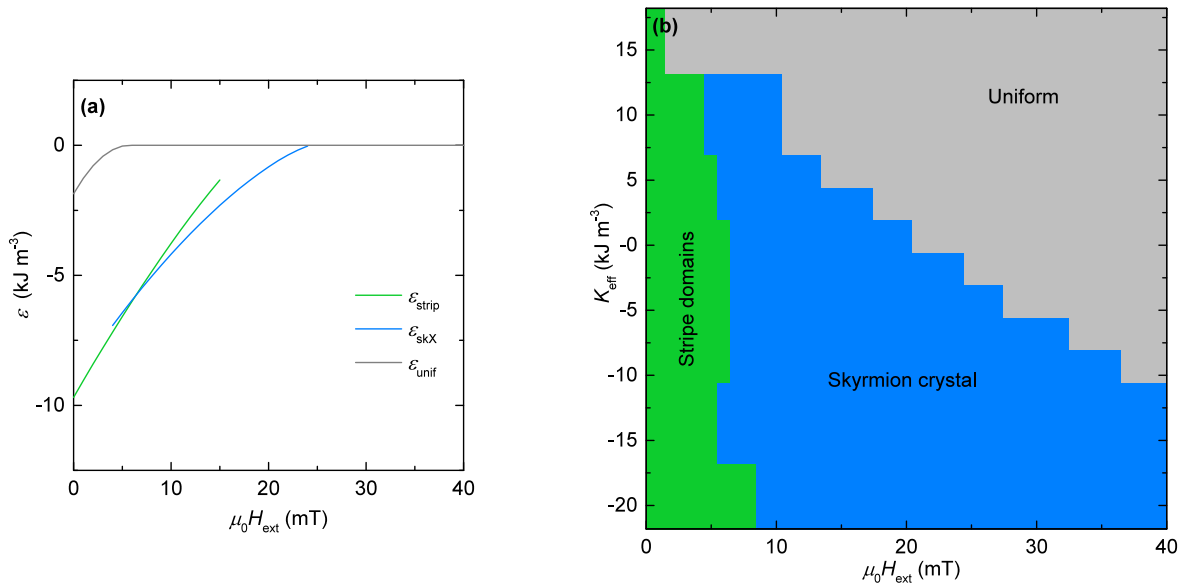
Figure 1.3: (a) Energies of the stripe ($\varepsilon_{\text{strip}}$), skyrmion crystal ($\varepsilon_{\text{skX}}$) and uniform ($\varepsilon_{\text{unif}}$) phases as a function of the external field $\mu_0 H_{\text{ext}}$ for $K_{\text{u}} = 1.06\,\text{MJ m}^{-3}$. (b) Phase diagram of the magnetic system with interfacial DM interaction (but neglecting distant effects of dipolar interactions), for varying field $\mu_0 H_{\text{ext}}$ (controllable parameter) and anisotropy K_{u} (system parameter).

Al_2O_3 (1.0 nm)]$_{20}$, with a very weak anisotropy ($|\mu_0 H_{\text{eff}}| = |2 K_{\text{eff}}/M_{\text{s}}| < 100\,\text{mT}$) and large dipolar interactions due to the many layers. They reveal stripe domains in the absence of external fields or at low fields (Figs. 1.4a,b, here at $\mu_0 H_{\text{z}} = 10\,\text{mT}$), a skyrmion crystal at intermediate fields (Fig. 1.4b, here at $\mu_0 H_{\text{z}} = 70\,\text{mT}$) and a uniform saturated magnetization with no contrast above a given saturation field (not shown, here at $\mu_0 H_{\text{z}} \geq 150\,\text{mT}$).

Beyond being controlled by the instantaneous value of the applied field, the magnetic configuration is actually also dependent on the field history applied to the system, exhibiting an hysteretic behaviour that is a general characteristic of many magnetic systems. This is apparent in Figs. 1.4a,b, for which one system has been demagnetized by applying in-plane (IP) fields, aligning the stripe domains along a particular direction, while the other one has been demagnetized with out-of-plane (OOP) fields, resulting in labyrinthine stripe domains. Both configurations are metastable at zero field. This hysteretic behaviour explains the frequent coexistence of different magnetic phases in multilayer systems, and also allows the stabilisation of metastable isolated skyrmions, even when their energy is higher than that of the uniform state.

When the anisotropy is more significant and the dipolar interactions less effective than in the previous example, for example here with a multilayer of composition [Pt (1.2 nm)/Co (1.4 nm)/Ru (1.4 nm)]$_3$, indeed the energy of the skyrmion phase may be higher than those of the stripe and uniform states for all field values. In Figs. 1.5a–c, MFM images at different field values $\mu_0 H_{\text{z}} = 12\,\text{mT}$, 18 mT and 30 mT are shown, which reveal a gradual transition from stripes to isolated skyrmions. When a magnetic stripe domain shortens in length under the progressive increase of the external field, both ends of the stripe join each other and an isolated skyrmion state is obtained, at which point an energy barrier needs to be overcome for skyrmion annihilation. In multilayers such as the present one, the metastability of skyrmion states allows their observation as isolated objects rather than in a lattice form, which proves crucial in order to envisage the manipulation of individual skyrmions.

Note that in the particular case of geometric confinement, skyrmions can be more easily sta-

---

However, they correspond to the same quantity.
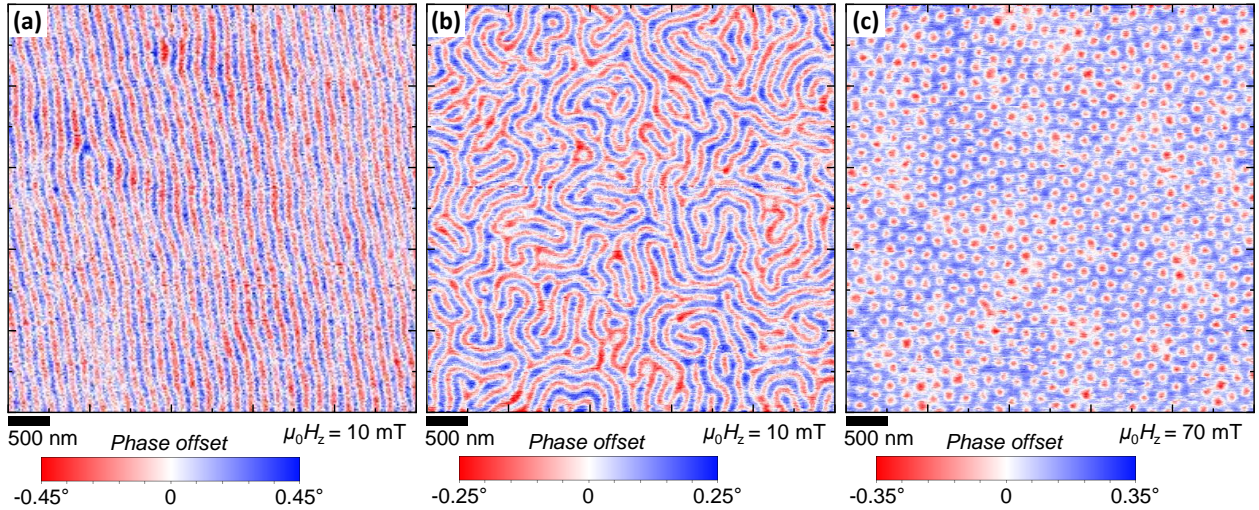
Figure 1.4: Magnetic configurations observed by MFM in a multilayer of base unit composition [Pt (2.4 nm)/ $Co_{10}Fe_{70}B_{20}$ (0.8 nm)/ Al_2O_3 (1.0 nm)] with 20 ferromagnetic layers at $\mu_0 H_z =$ (a) 10 mT after an IP demagnetization procedure, (b) 10 mT after an OOP demagnetization procedure, and (c) 70 mT.

bilised, and even without external fields, if the geometry of the system matches the one of the skyrmions [7, 61, 65, 71, 146]. According to the explanations given above however, in ferromagnetic multilayer systems with infinite extension and therefore no confinement that are studied in this thesis, **the application of an external field is essential** to stabilise (isolated) skyrmions. Note also that the question of the stability of isolated skyrmions (actually, metastability) is slightly different from the question of determining the stable phase as discussed just above. In the example of Fig. 1.5, a large anisotropy prevents from obtaining a skyrmion crystal as being the stable phase of the system, but once an isolated skyrmion is created as a defect, it may remain stable in spite of this large anisotropy if the unwinding of the magnetic texture of the skyrmion costs more energy than what thermal agitation can provide. The question of the stability of isolated skyrmions is further discussed in §2.5–2.6, after a more extensive modelling of skyrmion profiles in multilayers.
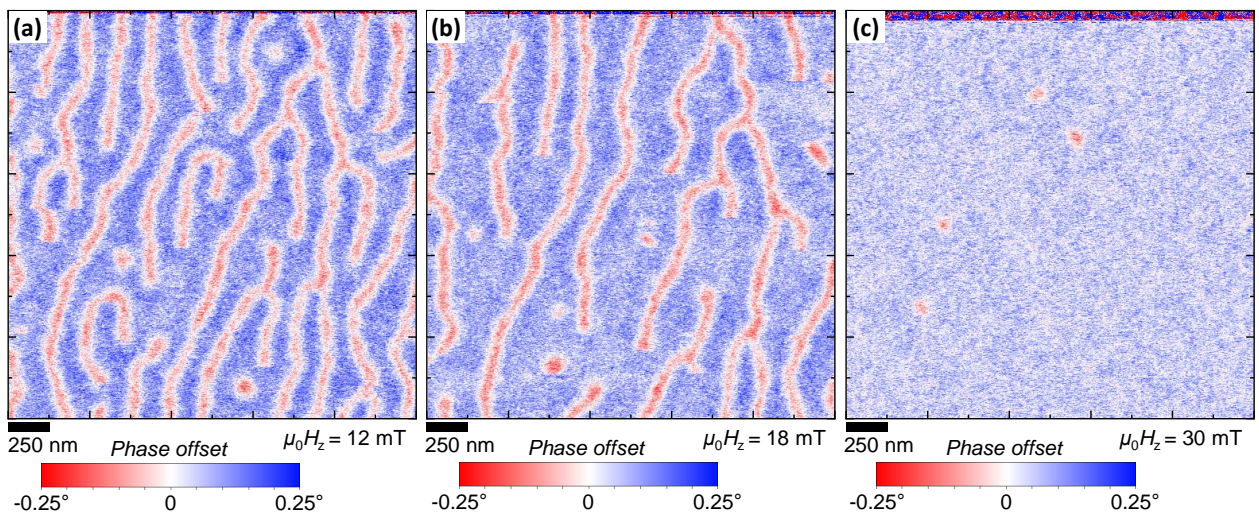
Figure 1.5: Magnetic configurations observed by MFM in a multilayer of base unit composition [Pt (1.2 nm)/Co (1.4 nm)/Ru (1.4 nm)] with 3 ferromagnetic layers at $\mu_0 H_z =$ (a) 12 mT, (b) 18 mT, and (c) 30 mT.

<div align="right">

Chapter 2

</div>

A numerical model of magnetic skyrmions

To achieve the goal of controlling skyrmion properties in multilayers, such as their size, chirality or stability, a first and natural step is to construct a predictive model for the skyrmion profiles. The knowledge of the expected behaviours for idealised multilayers constitutes a great help in understanding experimental observations and further adjusting the design of skyrmion multilayers.

In the following, I first briefly review the progresses made in the modelling of magnetic skyrmions before this work, which eventually are not sufficient to describe the multilayers of interest in this thesis (§2.1). As a new approach is required in the case of magnetic multilayers, I introduce a fully numerical model allowing to obtain the profile of axisymmetric skyrmions in magnetic multilayers (§2.2). The predictions of this numerical model are verified by comparison against the standard micromagnetic software MuMax³ (§2.3). By avoiding to make assumptions about the magnetization profiles as is often done in analytical models, the present solver proves to be reliable for the large diversity of skyrmion profiles that can be stabilised in RT multilayers, including "skyrmionic bubbles" as well as "compact skyrmions", in single magnetic layers or in multilayers with many repetitions, either with or without strong DM interaction (§2.4). A criterion is defined, which allows to assess the stability of skyrmions against elliptical deformations into stripe domains (§2.5). Finally, even if the present modelling cannot not provide the lifetime of the skyrmions, it allows for an estimation of the energy barrier protecting skyrmions against their isotropic collapse, which is crucial for achieving sufficient RT stability (§2.6).

This chapter is therefore restrained to the introduction of a numerical model for multilayered skyrmions, while its usages are found in several later sections of the following chapters. The appropriateness of this model in the perspective of studying the properties of multilayered skyrmions appears at several occasions, as it notably proves able to explain hybrid chiralities of skyrmions in multilayers, §4.4 and §4.7, allows to predict current-induced skyrmion dynamics, §4.6 and §4.9, illustrates the relation between skyrmion size and stability, §5.1 and §5.3, is able to quantify the properties of antiferromagnetic skyrmions in synthetic antiferromagnet (SAF) systems, §5.5, and allows the analysis of the relation between size and mobility, §6.2.

2.1 The need to go beyond analytical ansatz

The aim of this section is to summarise previous efforts in modelling magnetic skyrmions, prior to the model developed in this thesis. We have seen in the previous chapter that when they are stable, ferromagnetic skyrmions in magnetic multilayers exhibit a cylindrical symmetry around an axis aligned along $\hat{\mathbf{z}}$, which also defines their centre. It is then convenient to consider their radial profiles only, which are invariant upon rotation around this vertical symmetry axis. Based on the five energy density terms introduced in Chapter 1, the skyrmion energy in a single magnetic layer

of thickness t can be written as [137]

$$E_{\text{sk}} = t \int_{r=0}^{\infty} \int_{\varphi=0}^{2\pi} \left\{ A(\nabla\mathbf{m})^2 + D(m_{\text{z}} \operatorname{div} \mathbf{m} - \mathbf{m}\nabla m_{\text{z}}) + K_{\text{u}}\left(1 - m_{\text{z}}^2\right) \right.$$
$$\left. + \mu_0 H_{\text{ext}} M_{\text{s}}(1 - m_{\text{z}}) - \frac{\mu_0 M_{\text{s}}}{2}(M_{\text{s}} + \mathbf{H}_{\text{dem}} \cdot \mathbf{m}) \right\} r\,dr\,d\varphi \quad (2.1)$$

where r is then radial distance from the centre of the isolated skyrmion, φ the angle referring to cylindrical coordinates, as in the introduction, and H_{ext} the value of an external field pointing towards $+\hat{\mathbf{z}}$. Note that using the definition in (2.1), all energies are worth zero in the uniform perpendicular state $\mathbf{m} = +\hat{\mathbf{z}}$, which is the reference for this energy functional. In particular this is the reason why an additional M_{s} constant is introduced in the dipolar energy term.

Because the norm of $\mathbf{m}$ is fixed, it is customary to express $\mathbf{m}$ in spherical coordinates using polar and azimuthal angles (θ, ϕ) as defined in Fig. 2 (now ϕ is a function of r), which gives

$$E_{\text{sk}} = 2\pi t \int_{r=0}^{\infty} \left\{ A\left[\left(\frac{d\theta}{dr}\right)^2 + \left(\frac{d\phi}{dr}\right)^2 \sin^2\theta + \frac{\sin^2\theta}{r^2} \right] \right.$$
$$+ D\left[\frac{d\theta}{dr}\cos\phi + \frac{\cos\theta\sin\theta}{r}\cos\phi - \frac{d\phi}{dr}\cos\theta\sin\theta\sin\phi \right] + K_{\text{u}}\sin^2\theta \quad (2.2)$$
$$\left. + \mu_0 H_{\text{ext}} M_{\text{s}}(1 - \cos\theta) - \frac{\mu_0 M_{\text{s}}}{2}(M_{\text{s}} + H_{\text{dem,r}}\sin\theta\cos\phi + H_{\text{dem,z}}\cos\theta) \right\} r\,dr$$

when taking into account the radial symmetry of the skyrmion. By introducing the dimensionless radius $\rho = r/\sqrt{A/K_{\text{eff}}}$, we get a dimensionless energy integral [21, 147]

$$\frac{E_{\text{sk}}}{2\pi t} = A \int_{\rho=0}^{\infty} \left\{ \left[\left(\frac{d\theta}{d\rho}\right)^2 + \left(\frac{d\phi}{d\rho}\right)^2 \sin^2\theta + \frac{\sin^2\theta}{\rho^2} \right] \right.$$
$$+ \frac{4D}{\pi D_{\text{c}}}\left[\frac{d\theta}{d\rho}\cos\phi + \frac{\cos\theta\sin\theta}{\rho}\cos\phi - \frac{d\phi}{d\rho}\cos\theta\sin\theta\sin\phi \right] + \frac{K_{\text{u}}}{K_{\text{eff}}}\sin^2\theta \quad (2.3)$$
$$\left. + \frac{\mu_0 H_{\text{ext}} M_{\text{s}}}{K_{\text{eff}}}(1 - \cos\theta) - \frac{\mu_0 M_{\text{s}}^2}{2K_{\text{eff}}}\left(1 + \frac{H_{\text{dem,r}}}{M_{\text{s}}}\sin\theta\cos\phi + \frac{H_{\text{dem,z}}}{M_{\text{s}}}\cos\theta \right) \right\} \rho\,d\rho$$

where $D_{\text{c}} = 4\sqrt{AK_{\text{eff}}}/\pi$ is the critical DM interaction for the onset of spin-spirals at zero field in a single thin layer [61, 106].

Variational approach

The stable skyrmion profile is the solution $[\theta(\rho), \phi(\rho)]$ that minimises the energy functional (2.3). Let us first perform an intuitive and simple analysis of the skyrmion energy. Only Néel skyrmions are considered, which is ensured only when $|D|$ is large enough. Further, D is supposed positive (for example), which results in a CCW Néel configuration and thus $\phi(\rho) = 0$ for a core pointing down, *i.e.*, for $m_{\text{z}}(0) = -1$. Finally, the effects of the demagnetizing field can be simplified into an effective perpendicular anisotropy model [21], which is necessarily inaccurate but convenient for our present qualitative analysis. In this case (2.3) simplifies to

$$\frac{E_{\text{sk}}}{2\pi t} = A \int_{\rho=0}^{\infty} \left\{ \left(\frac{d\theta}{d\rho}\right)^2 + \frac{\sin^2\theta}{\rho^2} + \frac{4D}{\pi D_{\text{c}}}\left(\frac{d\theta}{d\rho} + \frac{\cos\theta\sin\theta}{\rho} \right) + \sin^2\theta + \frac{B_{\text{z}} M_{\text{s}}}{K_{\text{eff}}}(1 - \cos\theta) \right\} \rho\,d\rho$$
$$(2.4)$$

where $B_{\text{z}} = \mu_0 H_{\text{ext}}$. It is illustrative to analyse qualitatively the dependence of the different energy terms with skyrmion size through the use of ansatz functions and scaling transforma-

tions [68, 137]. Without expressing its form, let us consider that the skyrmion profile follows a given $\theta(\rho)$ profile function $f(\rho)$ with $m_z = 0$ at $\rho = 1$. It can then be simply rescaled by ρ_{sk}, without change of shape. This constitutes a good approximation in the case of compact enough skyrmions. Defining $\rho_{sk} = r_{sk}/\sqrt{A/K_{eff}}$, we get the scaling relation for the profiles $f(\rho/\rho_{sk})$

$$\frac{E_{sk}(\rho_{sk})}{2\pi t} = A\left[I_1 - I_2\frac{4D}{\pi D_c}\rho_{sk} + \left(I_3 + I_4\frac{B_z M_s}{K_{eff}}\right)\rho_{sk}^2\right] \tag{2.5}$$

or, equivalently,

$$\frac{E_{sk}(r_{sk})}{2\pi t} = AI_1 - DI_2 r_{sk} + (K_{eff}I_3 + B_z M_s I_4)r_{sk}^2 \tag{2.6}$$

with I_1, I_2, I_3, I_4 the integrals of $\{(df/d\rho)^2 + \sin^2 f/\rho^2\}$, $\{-df/d\rho - \sin f \cos f/\rho\}$, $\{\sin^2 f\}$ and $\{1 - \cos f\}$, respectively, which depend on the shape of the profile, but not on its scale. A modelling of the stable skyrmion size and its energy as a function of the magnetic parameters can be obtained from either (2.5) or (2.6). By minimising the second order polynomial with r_{sk} once the numerical values of I_1, I_2, I_3, I_4 are obtained [138, 147], the skyrmion radius and energy are found as

$$r_{sk}^{(stab)} = \frac{DI_2}{2(K_{eff}I_3 + B_z M_s I_4)} \tag{2.7}$$

$$\frac{E_{sk}^{(stab)}}{2\pi t} = AI_1 - \frac{D^2 I_2^2}{4(K_{eff}I_3 + B_z M_s I_4)}. \tag{2.8}$$

Note that minimising E_{sk} for different shapes of ansatz functions allows to find the most suitable profile function under defined conditions.

Atomically thin systems — The expressions of (2.5) and (2.6) suggest that in the absence of DM interaction, no stable skyrmion solution can be found. The case of Néel skyrmions was supposed above, thus requiring a large enough D. A similar treatment can be performed in the case of Bloch skyrmions for low DM interaction values [137], only affecting I_1, I_2, I_3, I_4, which is not presented here for conciseness. In the case of Bloch skyrmions, for $D = 0$, the energy always increases with ρ_{sk} due to I_3 and I_4 terms. Consequently, starting from any initial size, the skyrmion always evolves towards smaller radii and eventually collapses, known as collapse instability. The DM interaction thus plays the essential role of stabilising magnetic skyrmions against collapse. On the contrary, the combination of anisotropy and external field, appearing in the energy term proportional to ρ_{sk}^2 in (2.5) and (2.6), plays the role of confining the skyrmion and preventing its infinite expansion. In practice, this expansion in the absence of sufficient confinement does not occur radially but forms stripe domains, known as elliptical instability [22]. Upon increasing the applied field, in the present continuous micromagnetic model, the energy minimum remains present for any arbitrarily strong confinement, but it may be shifted to sizes below the validity of the micromagnetic limit, under which conditions the skyrmion may not be stable in an atomistic model. As described already qualitatively in the previous chapter, it appears here into equations that the external magnetic field plays the role of an adjustable parameter, controlling skyrmion size and phase transitions of the system between stripe domains, skyrmion states and saturated state. Finally, it appears from the present qualitative analysis that the Heisenberg exchange does not play a significant role in the stabilisation or destabilisation of the skyrmions, apart from ensuring the ferromagnetic order, that is, the continuity of **m** from the micromagnetic point of view. As the term proportional to A in the energy is found independent on ρ_{sk}, the Heisenberg exchange simply determines the skyrmion energy relative to the ferromagnetic state, but has no link with the size (as will appear below in our more elaborate model, A actually has an influence on the size, but it is limited compared to other terms). In other words, once a skyrmion is formed, the exchange interaction does not play

a particular role in its stability. Nevertheless, the exchange interaction constitutes the principal component of the barrier preventing the nucleation of a skyrmion from the uniform state, by raising the energy of a single isolated skyrmion above the energy of the uniform state [97, 137].

Some indicative (but approximate) rules can be drawn from (2.5)–(2.8), even if they are obtained within a simple model. In first approximation, both skyrmion size and skyrmion energy should be unchanged if varying K_{eff} and B_{z} while keeping $K_{\mathrm{eff}}I_3 + B_{\mathrm{z}}M_{\mathrm{s}}I_4$ constant, as appears in (2.6). In other words, varying the external field allows to compensate for the different K_{eff} in order to provide identical skyrmion size in systems with different anisotropy values. It also appears from (2.6) and (2.8) that scaling all parameters by a unique factor multiplies the skyrmion energy by the same factor, without affecting its size. Varying parameters independently, (2.7) shows that the size of a skyrmion is proportional to D, but inversely proportional to $K_{\mathrm{eff}}I_3 + B_{\mathrm{z}}M_{\mathrm{s}}I_4$. As a general property of second order polynomials[1], at the equilibrium skyrmion size $r_{sk}^{(\mathrm{stab})}$ the energy contribution of the DM interaction, E_{D}, is twice the opposite of that of the effective anisotropy and external field combined, $E_{\mathrm{K}} + E_{\mathrm{dem}} + E_{\mathrm{ext}}$. This is a quite good approximation, as can be verified by looking again at the energy terms determined micromagnetically in Fig. 1.2. We may keep in mind these intuitive rules when attempting to control the properties of skyrmions in thicker layers or multilayers, as is done later in this work, even if controlling case by case the validity of these rules is highly recommended, given that the complexity of multilayered systems may not be entirely captured by this rough model. Beyond the variational approach with radius as a unique parameter, a more quantitative description of skyrmions profiles can be obtained for ansatz functions with two free parameters: the skyrmion radius, that we have been using until here in this work, and the width of the profile at its perimeter δ_{sk}, which can be defined by analogy with the usual DW width as [60]

$$\delta_{\mathrm{sk}} = \left. \frac{1}{(dm_{\mathrm{z}}/dr)} \right|_{r=r_{\mathrm{sk}}}. \tag{2.9}$$

However, in this case the energy needs to be numerically minimised.

Single magnetic layers — The simplification performed above concerning the dipolar energy allows a clear qualitative understanding of the basic role played by each magnetic parameter, but it is quantitative only for extremely thin magnetic systems. It becomes largely insufficient to obtain accurate results as soon as the thickness of the magnetic systems reaches the nm scale, as it notably fails to predict the existence of "skyrmionic bubbles" [44, 68, 148], which are stabilised by the distant effects of the dipolar interactions. In this case, distant contributions can be included as a correction to the effective magnetic anisotropy approximation [138], which allows to treat "compact skyrmions" (usual size in the range of 50–200 nm) and "skyrmionic bubbles" (usual size in the range of 0.2–2 µm) on the same grounds. Notably, the transition from bubble solutions to skyrmion solutions can be approximatively determined within this approach, as done recently by A. Bernand-Mantel *et al.* [138]. The definitions for "compact skyrmions" and "skyrmionic bubbles" are more extensively described in §2.4.

Magnetic multilayers — This treatment is no longer valid for magnetic multilayers, in which the dipolar interactions are determined by both surface and volume magnetic charges and result in a complex energy behaviour with respect to the skyrmion profiles. It is possible to derive a model of all energy terms even in the complex geometry of a multilayer by using ansatz functions and analytically solving the Poisson equation (1.6) to find the dipolar contribution, as done by Büttner *et al.* [139]. In this case, the ansatz function cannot be simply rescaled but it requires to have three free parameters: radius, width of the profile at the perimeter and chirality (magnetization angle ϕ in the plane) [139]. In this model, the skyrmion profile is identical in all layers. The skyrmion energy can eventually be minimised numerically as a function of these three free parameters, which provides the equilibrium size (and energy) of the skyrmion for any set of magnetic parameters.

However, at this point the validity of this approach can be questioned for two reasons: first,

---

[1]It can be found back by injecting (2.7) in (2.6).

because the ansatz function may be varying for different magnetic parameters or multilayer geometries, and may be altered if a new magnetic interaction is taken into account in the model, thereby limiting the flexibility of the modelling; second, because such an analytical resolution does not allow to determine whether the determined solutions are stable against anisotropic deformations into stripe domains. In addition, it will appear later in this thesis that due to dipolar interactions, magnetic skyrmions in multilayers may form complex textures in which the size, chirality and shape of the profiles are not unique through the thickness of the system (see §4.4). This constitutes clear evidence that a more extensive model is required. For all these reasons, building a fully numerical micromagnetic model, which requires a minimal number of assumptions about the skyrmion profiles, is most useful in order to understand the properties and behaviours of skyrmions in magnetic multilayers. This issue has therefore been tackled as a part of the work of this thesis.

2.2 A (not so) new micromagnetic model

I now present this numerical model and some basic results it can provide. Being entirely numerical, it differs from the previous analytical models by leading to more general and robust results, despite requiring much more computation effort. A key advantage is that any isotropic interaction can be added to the interactions presented here, as will be done in §5.4. Note that the description given here focuses on the case of interfacial DM interaction, as we are interested in magnetic multilayers, but it can be adapted to describe bulk DM interaction in non-centrosymmetric crystalline compounds, by simply changing the term related to D in the energy functional.

From all previous efforts of modelling reviewed above, it appears that the dipolar interactions energy term is at the origin of most of the complexity in evaluating the energy functional (2.1). Whereas all other terms are local and depend on the local magnetization and its derivatives only, the dipolar interactions constitute a long range interaction that couples all magnetic moments with the magnetization everywhere. As a consequence, evaluating the dipolar interactions in tridimensional systems for arbitrary magnetic configurations is a difficult task, which requires to be repeatedly performed as the solution for the equilibrium magnetization $\mathbf{m}(x, y, z)$ needs to be found iteratively. Fortunately, ferromagnetic skyrmions in magnetic multilayers exhibit a cylindrical axial symmetry. The ambition here is therefore to build a model exploiting this rotational invariance in order to simplify the computation of the demagnetizing field. This approach has been successfully applied in the past to the description of cylindrical magnetic domains (magnetic bubbles) in thick magnetic layers [39, 40]. In this thesis, such approach has been extended by the consideration of the DM interaction and of the multilayered nature of the systems, as detailed below, in order to describe skyrmions in magnetic multilayers.

Let us first develop the energy functional (2.1) for a vector $\mathbf{m}$ described by its Cartesian components, in a mobile system rotating with the cylindrical coordinates, which proves more convenient for numerical computations. Moreover, this avoids the issue of coordinates singularity that occurs along the axis chosen to define spherical coordinates. This provides for a single layer

$$\frac{E_{\mathrm{sk}}}{2\pi t} = A \int_{\rho=0}^{\infty} \left\{ \frac{1-m_{\mathrm{z}}^2}{\rho^2} + \left(\frac{dm_{\mathrm{r}}}{d\rho}\right)^2 + \left(\frac{dm_{\varphi}}{d\rho}\right)^2 + \left(\frac{dm_{\mathrm{z}}}{d\rho}\right)^2 + \frac{4D}{\pi D_{\mathrm{c}}}\left(\frac{m_{\mathrm{r}}m_{\mathrm{z}}}{\rho} + m_{\mathrm{z}}\frac{dm_{\mathrm{r}}}{d\rho} - m_{\mathrm{r}}\frac{dm_{\mathrm{z}}}{d\rho}\right) \right.$$
$$\left. + \frac{K_{\mathrm{u}}}{K_{\mathrm{eff}}}(1-m_{\mathrm{z}}^2) + \frac{\mu_0 H_{\mathrm{ext}} M_{\mathrm{s}}}{K_{\mathrm{eff}}}(1-m_{\mathrm{z}}) - \frac{\mu_0 M_{\mathrm{s}}^2}{2K_{\mathrm{eff}}}\left(1 + \frac{\mathbf{H}_{\mathrm{dem}}}{M_{\mathrm{s}}}\cdot\mathbf{m}\right) \right\} \rho d\rho \quad (2.10)$$

in which all three components of the magnetization profile at any ρ are taken into account: $m_{\mathrm{r}}(\rho)$ (along the radial direction), $m_{\varphi}(\rho)$ (perpendicular to the radial direction) and $m_{\mathrm{z}}(\rho)$ (perpendicular to the plane of the layer), as defined in Fig. 2.1. The total skyrmion energy in the multilayer, E_{tot}, is given by the sum of $E_{\mathrm{sk,i}}$ in all layers i ranging 1 to L. In order to minimise the energy functional and find the equilibrium skyrmion profile, the present model relies on a straightforward minimisation technique. The quasi-static time evolution of the magnetic configuration is computed using the

Landau-Lifshitz equation, omitting the precession term, which causes the magnetization profile to converge directly to its closest energy minimum. This technique has the advantage of providing a quite realistic evolution of the system towards the equilibrium states, which should allow to distinguish between them if different minima are present. To this end, the magnetic configuration is initialised with an arbitrary initial configuration, which simply constitutes an initial guess but not at all an ansatz function, as this profile is let entirely free to evolve. The minimisation is then performed iteratively. A step increment $\delta_{\mathbf{m}}(\rho)$ is determined at each iteration, thus representing the fixed time-step evolution of $\mathbf{m}(\rho)$, obtained from the Landau-Lifshitz equation as

$$
\begin{aligned}
\delta_{\mathbf{m}} &= -\beta\, \mathbf{m} \times (\mathbf{m} \times \mathbf{H}_{\text{tot}}) \\
&= \beta \begin{bmatrix} H_{\text{r}}\big(1 - m_{\text{r}}^2\big) - H_{\varphi}m_{\text{r}}m_{\varphi} - H_{\text{z}}m_{\text{r}}m_{\text{z}} \\ H_{\varphi}\big(1 - m_{\varphi}^2\big) - H_{\text{z}}m_{\varphi}m_{\text{z}} - H_{\text{r}}m_{\varphi}m_{\text{r}} \\ H_{\text{z}}\big(1 - m_{\text{z}}^2\big) - H_{\text{r}}m_{\text{z}}m_{\text{r}} - H_{\varphi}m_{\text{z}}m_{\varphi} \end{bmatrix}
\end{aligned}
\tag{2.11}
$$

where relaxation β is a constant small enough to ensure convergence. H_{r}, H_{φ} and H_{z} are the three Cartesian components of the total effective magnetic field $\mathbf{H}_{\text{tot}}$, obtained as the sum of the effective field contributions deriving from the different energy terms in the energy functional, which are given below. By adding successively the step increments $\delta_{\mathbf{m}}(\rho)$ to $\mathbf{m}(\rho)$, the profile evolves following the direction given by the sum of all effective field components, and the magnetic configuration converges to its closest minimum of energy, thus minimising E_{tot}.

The effective field $\mathbf{H}_{\text{tot}}$ is given by the sum of

$$
\begin{aligned}
\mathbf{H}_{\text{A}} &= \frac{2A}{\mu_0 M_{\text{s}}} \nabla^2 \mathbf{m} \\
&= \frac{2A}{\mu_0 M_{\text{s}}} \begin{bmatrix} \frac{d^2 m_{\text{r}}}{dr^2} + \frac{1}{r}\frac{dm_{\text{r}}}{dr} - \frac{m_{\text{r}}}{r^2} \\ \frac{d^2 m_{\varphi}}{dr^2} + \frac{1}{r}\frac{dm_{\varphi}}{dr} - \frac{m_{\varphi}}{r^2} \\ \frac{d^2 m_{\text{z}}}{dr^2} + \frac{1}{r}\frac{dm_{\text{z}}}{dr} \end{bmatrix}
\end{aligned}
\tag{2.12}
$$

$$
\begin{aligned}
\mathbf{H}_{\text{D}} &= \frac{2D}{\mu_0 M_{\text{s}}} \left[(\text{div}\,\mathbf{m})\hat{\mathbf{z}} - \nabla m_{\text{z}} \right] \\
&= \frac{2D}{\mu_0 M_{\text{s}}} \left[\frac{dm_{\text{z}}}{dr}\hat{\mathbf{r}} - \left(\frac{m_{\text{r}}}{r} + \frac{dm_{\text{r}}}{dr} \right)\hat{\mathbf{z}} \right]
\end{aligned}
\tag{2.13}
$$

$$
\mathbf{H}_{\text{K}} = \frac{2K_{\text{u}}}{\mu_0 M_{\text{s}}} \left[m_{\text{z}}\hat{\mathbf{z}} \right]
\tag{2.14}
$$
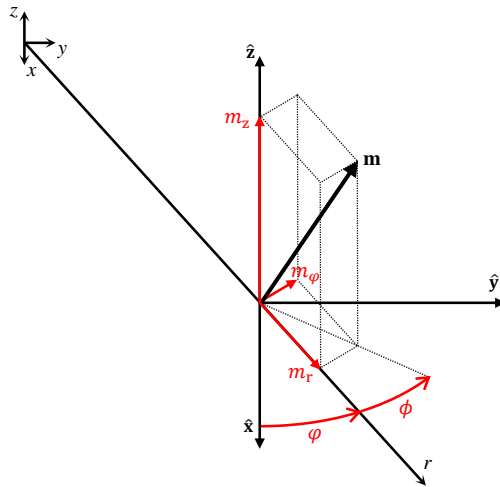
Figure 2.1: (a) Mobile Cartesian coordinates system definition for m_{r}, m_{φ} and m_{z}, in red.

$\mathbf{H}_{\mathrm{dem}}$ and $H_{\mathrm{ext}}\hat{\mathbf{z}}$, being the effective exchange field, effective DM interaction field, effective anisotropy field, demagnetizing field and external field. All terms are thus straightforward to obtain from $\mathbf{m}(\rho)$, at the exception of the demagnetizing field that is obtained by solving Poisson's equation (1.6) in the cylindrical geometry [39, 40]. Note that in the present model without electronic interlayer couplings, the demagnetizing field is the only term that couples the different magnetic layers together.

By applying the superposition principle of magnetostatics in order to find $\mathbf{H}_{\mathrm{dem}}$, the volume charges of (1.6)(i), denoted $f(r) = M_{\mathrm{s}}\operatorname{div}\mathbf{m}$, and surface charges of (1.6)(iv), denoted $h(r) = -M_{\mathrm{s}}\mathbf{m}\cdot\hat{\mathbf{z}}$, are treated separately. Let us define ψ_{f} the potential part associated to f keeping $h = 0$, and ψ_{h} the potential part associated to h keeping $f = 0$.

In the present case of cylindrical coordinates and invariant functions upon rotation around $\hat{\mathbf{z}}$, Poisson's equation (1.6) is solved into reciprocal space, through the use of Hankel transforms. Selecting the Bessel function of the first kind, order 0, denoted J_0, let us define for any function g its Hankel transform

$$\bar{g}(k) = \int_{r=0}^{\infty} r J_0(kr)g(r)dr \tag{2.15}$$

in reciprocal space. As the magnetic potential $\psi(r,z)$ satisfies $\triangle\psi = f$ or 0, in turn its Hankel transform $\bar{\psi}(k,z)$ verifies for any k,z

$$\frac{\partial^2\bar{\psi}(k,z)}{\partial z^2} - k^2\bar{\psi}(k,z) = \bar{f} \text{ or } 0. \tag{2.16}$$

The potential in reciprocal space $\bar{\psi}$ is found by solving the partial differential equation (2.16) with the boundary conditions obtained from Poisson's equation (1.6)(i–iv). For $\bar{\psi}_{\mathrm{f}}$, a general solution is

$$\bar{\psi}_{\mathrm{f}} = \begin{cases} B_1\cosh(kz) + B_2\sinh(kz) + B_0, \text{ inside} \\ A_1\exp(kz) + A_2\exp(-kz) + A_0, z > t/2 \end{cases} \tag{2.17}$$

for the inside and outside parts, respectively, where $A_{0,1,2}, B_{0,1,2}$ are real constants. Using (i), $B_0 = -\bar{f}(k)/k^2$ and $A_0 = 0$. Using (ii), $A_1 = 0$. The symmetry with respect to z of volume charges yields $\bar{\psi}_{\mathrm{f}} = A_2\exp(kz), z < -t/2$, and $B_2 = 0$. Combining (iii) and (iv) at $z = t/2$ leads to

$$\begin{cases} B_1\cosh(kt/2) - \bar{f}(k)/k^2 = A_2\exp(-kt/2) \\ kB_1\sinh(kt/2) = -kA_2\exp(-kt/2) \end{cases} \tag{2.18}$$

which finally solves A_2 and B_1. For $\bar{\psi}_{\mathrm{h}}$, a general solution is

$$\bar{\psi}_{\mathrm{h}} = \begin{cases} B_1\cosh(kz) + B_2\sinh(kz) + B_0, \text{ inside} \\ A_1\exp(kz) + A_2\exp(-kz) + A_0, z > t/2 \end{cases} \tag{2.19}$$

for the inside and outside parts, respectively, where $A_{0,1,2}, B_{0,1,2}$ are real constants. Using (i), $B_0 = 0$ and $A_0 = 0$. Using (ii), $A_1 = 0$. The antisymmetry with respect to z of surface charges yields $\bar{\psi}_{\mathrm{h}} = -A_2\exp(kz), z < -t/2$, and $B_1 = 0$. Combining (iii) and (iv) at $z = t/2$ leads to

$$\begin{cases} B_2\sinh(kt/2) = A_2\exp(-kt/2) \\ kB_2\cosh(kt/2) + \bar{h}(k) = -kA_2\exp(-kt/2) \end{cases} \tag{2.20}$$

which finally solves A_2 and B_1. The potentials created by volume charges f and surface charges h

are

$$\bar{\psi}_{\mathrm{f}} = \begin{cases} \dfrac{\bar{f}}{k^2} \exp\left(-kt/2\right)\cosh\left(kz\right) - \dfrac{\bar{f}}{k^2}, & 0 \le z \le t/2 \\[2ex] \dfrac{-\bar{f}}{k^2}\sinh\left(kt/2\right)\exp\left(-kz\right), & z > t/2 \end{cases}$$

$$\bar{\psi}_{\mathrm{h}} = \begin{cases} \dfrac{-\bar{h}}{k}\exp\left(-kt/2\right)\sinh\left(kz\right), & 0 \le z \le t/2 \\[2ex] \dfrac{-\bar{h}}{k}\sinh\left(kt/2\right)\exp\left(-kz\right), & z > t/2 \end{cases} \tag{2.21}$$

and can be completed by symmetry. Volume charges are symmetric with respect to z while surface charges are antisymmetric with respect to z, which results in

$$\begin{aligned} \bar{\psi}_{\mathrm{f}}(k,z) &= +\bar{\psi}_{\mathrm{f}}(k,-z) \\ \bar{\psi}_{\mathrm{h}}(k,z) &= -\bar{\psi}_{\mathrm{h}}(k,-z). \end{aligned} \tag{2.22}$$

These two parts of the potential in reciprocal space $\bar{\psi}_{\mathrm{f,h}}$ then need to be transformed back into real space potentials $\psi_{\mathrm{f,h}}$, whose gradients $\partial\psi_{\mathrm{f,h}}/\partial r$ and $\partial\psi_{\mathrm{f,h}}/\partial z$ are averaged over the thickness of the layers in order to finally find the demagnetizing field components along r and z. Note that due to the cylindrical symmetry of the problem, there is no demagnetizing field along φ. Let us consider that the magnetic layer l_j, of thickness t' and position z', is affected by a source magnetization distribution located in layer l_i (either l_j itself or any other magnetic layer), of thickness t and at position $z = 0$. Therefore

$$\begin{aligned} H_{\mathrm{dem,r}}^{i,j}(r) &= -\frac{1}{t'}\int_{z=z'-t'/2}^{z'+t'/2}\left(\frac{\partial\psi_{\mathrm{f}}}{\partial r} + \frac{\partial\psi_{\mathrm{h}}}{\partial r}\right)dz \\ H_{\mathrm{dem,z}}^{i,j}(r) &= \frac{(\psi_{\mathrm{f}} + \psi_{\mathrm{h}})|_{z'-t'/2} - (\psi_{\mathrm{f}} + \psi_{\mathrm{h}})|_{z'+t'/2}}{t'}. \end{aligned} \tag{2.23}$$

allows to define for any couple (i,j) the field contribution $\mathbf{H}_{\mathrm{dem}}(\mathbf{m}_i(r), t, t', \Delta z)$ that depends on the source magnetization configuration $\mathbf{m}_i(r)$, on the source layer thickness $t = t_i$, on the affected layer thickness $t' = t_j$ and on the interlayer spacing $\Delta z = z_j - z_i$. Layer positions and thicknesses can be chosen arbitrarily to reproduce any multilayer geometry, either periodic or not.

The geometry of the system hosting an isolated magnetic skyrmion is actually infinite, so that a cut-off position r_N for the discretisation of r into N points, associated to a position $\rho_N = r_N/\sqrt{A/K}$ in (2.10), needs to be introduced in order to perform computations. For a large enough value of r_N, it is a very good approximation to consider $m_{\mathrm{z}} = 1$ for $r > r_N$ (in the case of a core magnetization of the skyrmion pointing down) as a boundary condition. Consequently $f(r > r_N) = 0$, but $h(r > r_N) = -M_{\mathrm{s}}$, so that h requires a transformation in order to take into account the demagnetizing field originating from outside the simulation environment at $r > r_N$, and in order to get a well defined Hankel transform for h. In the aim of making h integrable, it needs to undergo a transformation in order to have a compact support, ensuring that $h(r > r_N) = 0$.

Let us define $\tilde{h} = M_{\mathrm{s}}(1 - \mathbf{m}\cdot\hat{\mathbf{z}})$, the surface charges associated to the difference $\mathbf{m}(r) - \mathbf{m}_{\mathrm{unif}}(r)$, for $\mathbf{m}_{\mathrm{unif}}(r) = \hat{\mathbf{z}}$ the uniform up-pointing magnetization. $\tilde{h}(r > r_N) = 0$ and thus $\tilde{h}$ has a properly defined transform. The demagnetizing field associated to a source $\mathbf{m}_{\mathrm{unif}}(r)$ is confined inside the layer itself and is equal to $-M_{\mathrm{s}}\hat{\mathbf{z}}$. By summing the two source terms $\mathbf{m}(r) - \mathbf{m}_{\mathrm{unif}}$ and $\mathbf{m}_{\mathrm{unif}}(r)$, the distribution of magnetization $\mathbf{m}(r)$ generates a field

$$\mathbf{H}_{\mathrm{dem}} = \begin{cases} \tilde{\mathbf{H}}_{\mathrm{dem}} - M_{\mathrm{s}}\hat{\mathbf{z}}, & -t/2 \le z \le t/2 \\ \tilde{\mathbf{H}}_{\mathrm{dem}}, & |z| > t/2 \end{cases} \tag{2.24}$$

with $\tilde{\mathbf{H}}_{\mathrm{dem}}$ the partial field obtained by replacing h by $\tilde{h}$. Now considering separately the interior environment (with a variable $\mathbf{m}$, for $r \le r_N$) and the exterior environment (with a fixed $\mathbf{m}$, for

$r > r_N$), the integrated dipolar energy becomes

$$\mathbf{E}_{\text{dem}} = \left(\int_{int} + \int_{ext} \right) \frac{-\mu_0 M_{\text{s}}}{2} (\mathbf{H}_{\text{var}} + \mathbf{H}_{\text{fix}}) \cdot \mathbf{m} \qquad (2.25)$$

where $\mathbf{H}_{\text{var}}$ is the field generated by the interior part and $\mathbf{H}_{\text{fix}}$ is the field generated by the exterior part. In the exterior part, both $\mathbf{m}$ and $\mathbf{H}_{\text{fix}}$ are fixed, their constant scalar product can be dropped. Keeping only

$$\mathbf{E}_{\text{dem}} = \frac{-\mu_0 M_{\text{s}}}{2} \left[\int_{int} (\mathbf{H}_{\text{var}} + \mathbf{H}_{\text{fix}}) \cdot \mathbf{m} + \int_{ext} \mathbf{H}_{\text{var}} \cdot \mathbf{m} \right] \qquad (2.26)$$

and noticing that it contains twice a symmetrical interaction between two sub-systems verifying

$$\int_{ext} \mathbf{H}_{\text{var}} \cdot \mathbf{m} = \int_{int} \mathbf{H}_{\text{fix}} \cdot \mathbf{m} \qquad (2.27)$$

allows to rewrite

$$\mathbf{E}_{\text{dem}} = \frac{-\mu_0 M_{\text{s}}}{2} \int_{int} \mathbf{H}_{\text{dem}} \cdot \mathbf{m} + \mathbf{H}_{\text{fix}} \cdot \mathbf{m} \qquad (2.28)$$

where $\mathbf{H}_{\text{dem}} = \mathbf{H}_{\text{var}} + \mathbf{H}_{\text{fix}}$ reappears and for which the integration only concerns the interior environment. In other words, $\mathbf{H}_{\text{fix}}$ is the field generated by the saturated outer part inside the interior part. The saturated outer part being the complementary of a saturated disk to form a saturated infinite plane, $\mathbf{H}_{\text{fix}}$ is equal to $-M_{\text{s}}\hat{\mathbf{z}} - \mathbf{H}_{\text{var}}(h = 1)$, where $\mathbf{H}_{\text{var}}(h = 1)$ is the field generated by a saturated inner part ($h = 1$ for $r < r_N$). The final fields are equivalently written as functions of ρ. Eventually, (2.10) is redefined as an integral between 0 and ρ_N with all terms unchanged except the dipolar part, for which the integrand becomes

$$\frac{-\mu_0 M_{\text{s}}}{2K_{\text{eff}}} (M_{\text{s}} + \mathbf{H}_{\text{dem}} \cdot \mathbf{m} + \mathbf{H}_{\text{fix}} \cdot (\mathbf{m} - \hat{\mathbf{z}})) \qquad (2.29)$$

which is indeed worth zero in the uniform, up-pointing state.

Note that both forward and backward Hankel transforms, as well as the different mathematical operations required in (2.21) and (2.23) to find the field of each layer acting on each layer, are extremely costly in terms of computation as compared to what is required for the four other field terms. However most of these steps are redundant and need not to be performed at each evolution step. The Hankel transforms can be implemented as matrices multiplications, and can thus be factorised with the formulas of (2.21) and stored for the different layer spacing combinations. Finally and most importantly, because magnetostatic problems can be solved by superposing simpler problems, it can also be done with respect to the source terms $\mathbf{m}(r)$ at each r. For a given sampling of r points $r_1, r_2, \ldots, r_N$, four demagnetizing field kernels can be precomputed and kept to determine the demagnetizing field due to any f and h distributions, along r and z. They constitute $L \times L \times N \times N$ arrays, referred to as $K_{\text{h,f}}^{r,z}(j, i, r_j, r_i)$, which store the magnetic field components created in layer j at point r_j by a unit (surface or volume) charge located in layer i at point r_i. By superposition of each elementary source, the fields in each layer j are obtained as

$$
\begin{bmatrix} H_{\text{dem}}^{r,z}(r_1) \\ H_{\text{dem}}^{r,z}(r_2) \\ \vdots \\ H_{\text{dem}}^{r,z}(r_N) \end{bmatrix} = \sum_{i=1}^{L} K_f^{r,z}(j, i, r_1 \cdots r_N, r_1 \cdots r_N) \begin{bmatrix} f_i(r_1) \\ f_i(r_2) \\ \vdots \\ f_i(r_N) \end{bmatrix}
$$
$$
+ \sum_{i=1}^{L} K_h^{r,z}(j, i, r_1 \cdots r_N, r_1 \cdots r_N) \begin{bmatrix} h_i(r_1) \\ h_i(r_2) \\ \vdots \\ h_i(r_N) \end{bmatrix} \qquad (2.30)
$$

and provide the self-interacting term (if $i = j$), or interaction term between two layers (if $i \neq j$), $\mathbf{H}_{\text{dem}}$, within four matrices multiplications. This treatment greatly accelerates the computation of $\mathbf{H}_{\text{dem}}$ at the cost of some more initialisation time, but at no precision cost. The initially tridimensional problem is effectively reduced into a bidimensional problem, as the only geometric variables are layers $l_1, l_2, \ldots, l_L$ and radial positions $r_1, r_2, \ldots, r_N$.

2.3   Validation of the model

In order to check the validity of the implementation of this numerical model, its results are compared with the ones provided by the standard micromagnetic simulation software MuMax[3]. For simplicity, let us focus here on standard multilayers with fixed magnetic layer thickness ($t_i = t_{\text{FM}}$ for all layers) and periodicity p between layers. Magnetic parameters are $A = 10\,\text{pJ}\,\text{m}^{-1}$, $D = 1.35\,\text{mJ}\,\text{m}^{-2}$, $M_{\text{s}} = 1\,\text{MA}\,\text{m}^{-1}$, $K_{\text{u}} = 0.8\,\text{MJ}\,\text{m}^{-3}$, in a multilayer geometry given by $t = 1\,\text{nm}$ and $p = 3\,\text{nm}$, typical for the type of systems studied in this thesis. Two cases are analysed here : $L = 3$ and $L = 5$, which correspond to some of our experimental systems.

The initial guess of the magnetization before minimisation is chosen to be identical in all layers and is given by a usual approximation [60] of the skyrmion profiles

$$\mathbf{m} = [\sin\theta\cos\phi, \sin\theta\sin\phi, \cos\theta]$$
$$\theta(\rho) = \frac{\pi}{2} - \arcsin\left[\tanh\left(\rho - 4\right)\right], \phi(\rho) = \pi/4, \tag{2.31}$$

thus defining an initial skyrmion radius $\rho_{\text{sk}} = 4$ ($r_{\text{sk}} = 4\delta$) and an initial skyrmion-bounding profile width unity in reduced units ($\delta_{\text{sk}} = \delta$) that matches the linear DW width $\delta = \sqrt{A/K_{\text{eff}}}$. The initial ϕ is chosen on-purpose between Bloch ($\phi = \pm\pi/2$) and Néel ($\phi = 0, \pi$) configurations, in order to let the system relax to its most stable state. Note that in the absence of bulk DM interaction, if a partly or fully Bloch solution exists, having a final $\phi(\rho) \neq 0, \pi$ in any layer, then the two symmetrical solutions $\pm\phi(\rho)$ are degenerate in energy and constitute two different solutions with opposite Bloch component for that layer. Due to the choice made for the initial guess, a Bloch component of the magnetization texture with $\phi > 0$ is selected if any, but the solution with an opposite Bloch component with $\phi < 0$ is equally valid. The present numerical model, called $\mathbf{m}(r, z)$ model, and MuMax magnetic profiles are evolved until $|\delta_{\mathbf{m}}| < 10^{-9}$.

It is to be noticed that the system modelled in MuMax is not strictly equivalent to the one in our $\mathbf{m}(r, z)$ solver. As described above, the $\mathbf{m}(r, z)$ solver models an isolated skyrmion within an infinite, otherwise uniformly magnetized layer. In contrast, the systems simulated with MuMax always possess a finite size. Any magnetization outside the simulation volume can only be mimicked using periodic boundary conditions. In order to verify the quantitative agreement between the two tools, it is therefore necessary to check that both agree in the limit of very large MuMax simulation sizes (that is, with a number of cells along one edge of the simulated square area $N_{\text{mumax}} \to \infty$). Different runs of MuMax have been performed with increasing simulation sizes $N_{\text{mumax}} = 256, 512, 768$, with cell size kept fixed at $1 \times 1 \times 1\,\text{nm}^3$.

The obtained skyrmion profiles are displayed and compared in Figs. 2.2a,b for the two geometries with $L = 3$ and $L = 5$ layers, respectively. In both cases, the $\mathbf{m}(r, z)$ solver and MuMax show a very good agreement. Due to the large value of D in the present example, skyrmions are Néel with $\phi = 0$ in all layers. The increasingly large hollow squares correspond to plots of layer-resolved profiles $\theta(r)$ with increasing sizes of the simulation grid $N_{\text{mumax}} = 256, 512, 768$. It can be seen that the skyrmion profiles in the finite geometry of MuMax progressively converge to the solutions determined by the $\mathbf{m}(r, z)$ solver in an infinite geometry (line plots). As the cylindrical geometry of the $\mathbf{m}(r, z)$ solver matches better the geometry of the skyrmions than the prismatic space of MuMax, notably at small radii, a small difference between profiles may remain in the limit of $N_{\text{mumax}} \to \infty$ for equivalent discretisation sizes (here $1\,\text{nm}^3$), in favour of the $\mathbf{m}(r, z)$ solver. Beyond comparing
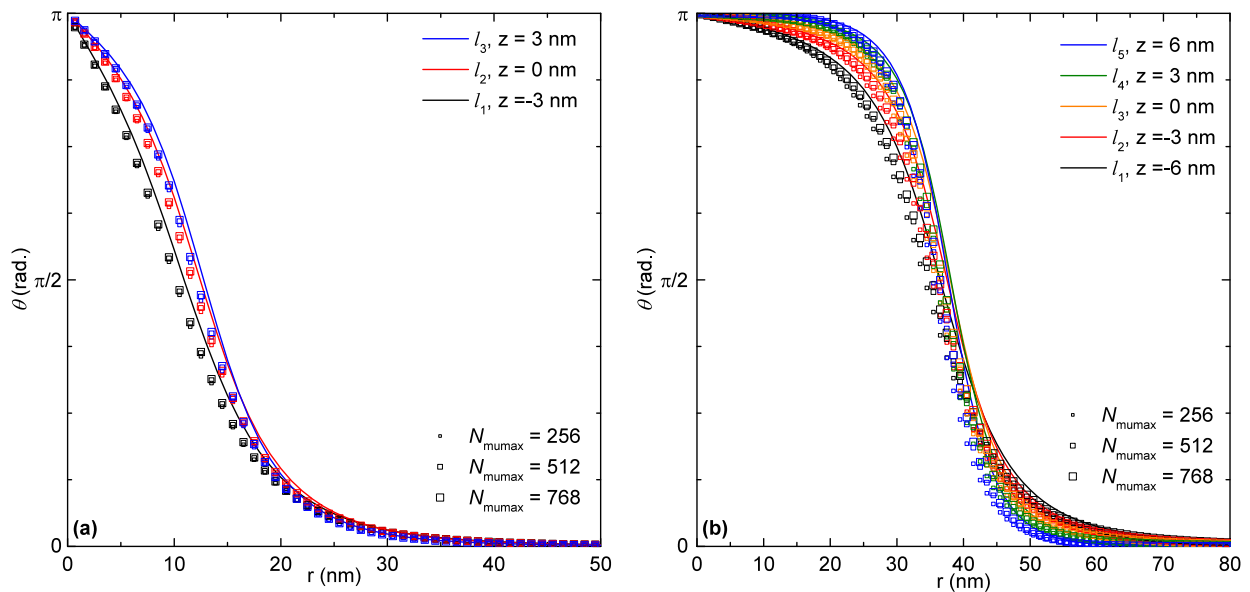
Figure 2.2: Comparison of results provided by profile solver for $\mathbf{m}(r, z)$ (colored lines) and MuMax[3] (hollow squares) for both (a) $L = 3$ and (b) $L = 5$ layers. Layers are referred to as l_i with i increasing from bottom to top. The increasing sizes of the hollow squares correspond to $N_{\mathrm{mumax}} = 256, 512, 768$.

the solutions in these two example cases, it has been verified that the values of the effective fields found by both models were equal, for $L = 3$ up to $L = 20$, at several different values of $\phi(r)$.

2.4 Discriminating between skyrmions and bubbles

Based on this numerical model of axisymmetric skyrmion profiles, a clarification of the definition for what a skyrmion is can be attempted. Our aim here is to try not to overlay more considerations about a long-standing scholastic debate, but to identify some essential characteristics of skyrmions for the following of this thesis. Two main types of axially symmetric solutions exist in interfacial DM interaction systems, often referred to as "compact skyrmions" and "skyrmionic bubbles" [68, 138, 139]. The difference between these two types of solutions can be seen as a difference of stabilising mechanism. Contrasting with most analytical models introduced in §2.1, the present model allows the distinction between "compact skyrmions" and "skyrmionic bubbles" in arbitrary system geometries without requiring any assumptions, as detailed below.

Historically, a "bubble" in a perpendicularly magnetized material is, as mentioned in the introduction, a circular magnetic domain with a reversed core and surrounded by a DW separating it from an otherwise uniformly magnetized environment. They have been studied over decades without considering any DM interaction and thus do not necessarily rely on chiral interactions to be stabilised [41–43]. We have seen in Chapter 1 that what defines the stability of a skyrmion solution is (i) the existence of an axially symmetric profile of minimal energy at a given radius and (ii) the stability of this profile against anisotropic perturbations. In the absence of DM interaction, the stabilisation of a bubble relies on dipolar interactions [39, 40] to create such a minimum, and on a confinement field to prevent its extension into a stripe domain. The addition of some interfacial DM interaction into the system simply provides a fixed Néel chirality to the DW surrounding the bubble, which also affects its energetics. The reduction of the DW energy causes the stabilisation of bubbles at higher external fields or for weaker dipolar interactions.

The other type of solutions in the infinite plane are localised magnetic objects, which do not rely on distant dipolar interactions for their stabilisation. They are predicted as metastable states in
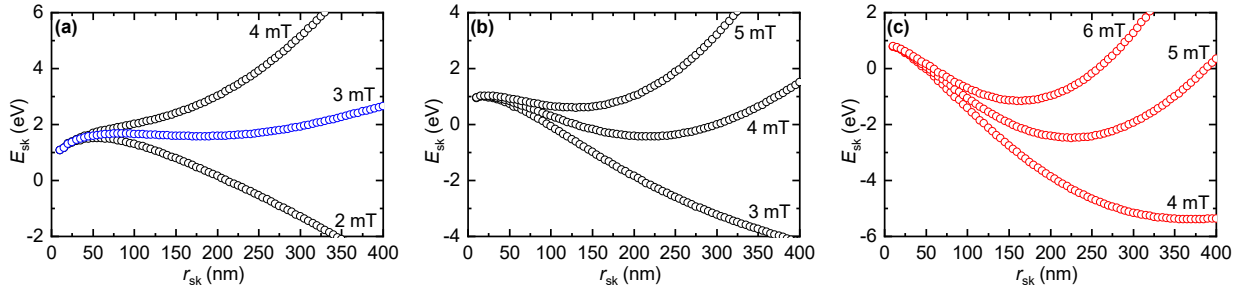
Figure 2.3: Skyrmion energy E_{sk} as a function of r_{sk} for different field values and (a) $D = 0.4\,\mathrm{mJ\,m^{-2}}$, (b) $D = 0.6\,\mathrm{mJ\,m^{-2}}$ and (c) $D = 0.8\,\mathrm{mJ\,m^{-2}}$. The blue curve in (b) for $\mu_0 H_{ext} = 5\,\mathrm{mT}$ exhibits a "skyrmionic bubble" solution with positive dE_{sk}/dr_{sk} at $r_{sk} = 0$, while the red curves in (c) exhibit each a "compact skyrmion" solution with negative dE_{sk}/dr_{sk} at $r_{sk} = 0$.

the continuous approximation of FMs layers [31], because the uniformly magnetized state cannot be reached following a continuous transformation starting from a skyrmion state. Looking again at the simplified energy functional (2.6), a skyrmion solution f exists in the absence of D only for $K_{eff} = 0$ and $B_z = 0$, in which case the energy curve (resulting in $E_{sk} = 8\pi tA$) is a flat energy minimum without a well defined size [31]. Consequent to the absence of significant dipolar interactions, the stabilisation of "compact skyrmions" in realistic systems thus requires the presence of some DM interaction to prevent them from isotropic collapse [21, 22].

Because dipolar interactions usually favour a uniform central part, with a size of the order of the characteristic dipolar length, while the core of a skyrmions is usually considered punctual, the radius is often linked with the type of solution. However, the size does not constitute a good criterion, as small "skyrmionic bubbles" and large "compact skyrmions" may exist [138]. Moreover, most often in magnetic multilayers both dipolar interactions and DM interaction are present, and they jointly shape the function $E_{sk}(r_{sk})$ that determines the skyrmion solutions. Another criterion than size or strength of the DM interaction is then used to distinguish between "skyrmionic bubbles" and "compact skyrmions" in this thesis. With our model described in §2.2, E_{sk} can be calculated as a function of r_{sk}, similar to what was done in Chapter 1, by imposing an additional condition $m_z(r_{sk}) = 0$ to the minimiser, and varying the value of r_{sk} for different runs. The results are shown in Figs. 2.3a–c for parameters: $A = 10\,\mathrm{pJ\,m^{-1}}$, $M_s = 1.3\,\mathrm{MA\,m^{-1}}$, $K_u = 1.14\,\mathrm{MJ\,m^{-3}}$, $D = 0.4$, 0.6 and $0.8\,\mathrm{mJ\,m^{-2}}$, respectively and $\mu_0 H_{ext} = 2\text{–}6\,\mathrm{mT}$ in each case. In the presence of both dipolar interactions and DM interaction, our definition relies on the sign of dE_{sk}/dr_{sk} towards $r_{sk} = 0$.[2] For positive initial dE_{sk}/dr_{sk}, the object is called a "skyrmionic bubble"; **for negative initial** dE_{sk}/dr_{sk}, it is called a "compact skyrmion". Examples are highlighted in Figs. 2.3a,c, with the blue curve corresponding to a "skyrmionic bubble" (here with a shallow energy minimum) and the red curves corresponding to "compact skyrmions".

As it appears from the analysis of the link between skyrmion size and the different energy terms conducted in the previous chapter (see Fig. 1.2), reaching "compact skyrmions" is favoured by increasing D and the external field $\mu_0 H_{ext}$ together, by reducing effective perpendicular magnetic anisotropy K_{eff}, and by reducing distant dipolar interactions, that is, by reducing number of layers L, their thickness t_{FM} and their M_s.

This distinction allows us to determine that our interest within this thesis resides in the study of "compact skyrmions" according to our definition, for the following reasons: (i) in case of a positive initial dE_{sk}/dr_{sk} a skyrmion compressed by an external field or thermal fluctuations until the saddle point cannot remain stable and will collapse towards $r_{sk} = 0$. In contrast, in case of a negative initial dE_{sk}/dr_{sk}, a skyrmion of low radius remains stable, even for large applied fields, as long as the micromagnetic limit is not reached ($r_{sk} \approx 3\,\mathrm{nm}$). As will appear in Chapter 5, this type of minimum is easily conserved upon increasing D (and compensating by increasing $\mu_0 H_{ext}$), which provides a

---

[2]In practice towards $r_{sk} \approx 3\,\mathrm{nm}$, below which the micromagnetic model becomes less reliable.

systematic way to enhance the thermal stability of skyrmions. (ii) The size can in principle be further reduced for "compact skyrmions" than for "skyrmionic bubbles", which are influenced by the characteristic size of the dipolar interactions, by layer thicknesses, etc. (iii) Compact skyrmions are less easily deformable and thus better described by the Thiele equation, which considers rigid textures (see §3.2 and §6.2).

2.5 Radial stability of skyrmion profiles

To ensure the stability of skyrmion solutions against elliptical elongation into stripe domains, it is not sufficient that the skyrmion state be the minimum energy solution in the space of cylindrically symmetric profiles, but it needs to remain also a minimum of energy when this symmetry constraint is relaxed [137]. The straightforward method of studying numerically the stability against small perturbations to $\mathbf{m}(x, y, z)$ in its full, three-dimensional Cartesian micromagnetic description is unfortunately computationally expensive. An alternative approach is to simply compare the linear energy of a stripe domain to the energy of the saturated ferromagnetic configuration. If the resulting stripe has a total energy lower than the one of the saturated state, the system can actually decrease its energy through splitting the skyrmion configuration into two half-skyrmions (also called merons) connected by a stripe domain, and thus the skyrmion will be unstable. Let us consider initially a stripe domain, uniform along y, as being a profile $\mathbf{m}(x, z)$, matching the skyrmion cut radial profile $\mathbf{m}(r, z)$ for $x > 0$ and its symmetric for $x < 0$. This initial profile is influenced by the cylindrical geometry of the skyrmion, so that we need to let it relax to its more stable stripe form, proceeding with a similar energy minimisation as described above, but assuming instead a linear geometry uniform along y. The terms associated to Heisenberg exchange interaction, DM interaction, anisotropy, and Zeeman fields are straightforward, while the dipolar field can be found as in §2.2, using the usual Fourier transform instead of the Hankel transform, with $h(x) = -M_s m_z(x)$ and $f(x) = M_s \partial m_x(x)/\partial x$. In the k-space, all expressions are unchanged. We get, now using $\chi = x/\sqrt{A/K_{\mathrm{eff}}}$,

$$
E_{\mathrm{st}} = t\sqrt{AK_{\mathrm{eff}}} \int_{-\infty}^{\infty} \left\{ \left(\frac{dm_x}{d\chi}\right)^2 + \left(\frac{dm_y}{d\chi}\right)^2 + \left(\frac{dm_z}{d\chi}\right)^2 + \frac{4D}{\pi D_c}\left(m_z \frac{dm_x}{d\chi} - m_x \frac{dm_z}{d\chi}\right) \right.
$$
$$
\left. + \frac{K_u}{K_{\mathrm{eff}}}\left(1 - m_z^2\right) + \frac{\mu_0 H_{\mathrm{ext}} M_s}{K_{\mathrm{eff}}}\left(1 - m_z\right) - \frac{\mu_0 M_s^2}{2K_{\mathrm{eff}}}\left(1 + \frac{\mathbf{H}_{\mathrm{dem}}}{M_s} \cdot \mathbf{m}\right) \right\} d\chi. \quad (2.32)
$$

The energy E'_{tot} (sum of E_{st} in all layers) of the stripe domains is displayed as a function of $\mu_0 H_{\mathrm{ext}}$ in Figs. 2.4a,b for $M_s = 1.0\,\mathrm{MA\,m^{-1}}$; $K_u = 0.8\,\mathrm{MJ\,m^{-3}}$ and $M_s = 1.3\,\mathrm{MA\,m^{-1}}$; $K_u = 1.2\,\mathrm{MJ\,m^{-3}}$, respectively. Geometries with $L = 3$, 5 and 10 are considered. In a usual single magnetic layer, a single DW possesses an energy per surface unit $4\sqrt{AK_{\mathrm{eff}}}$, not including the DM interaction and distant dipolar interactions contribution. For stripe domains in multilayers, composed of two DWs, a natural scale for the stripe energy per unit length is thus $8Lt\sqrt{AK_{\mathrm{eff}}}$. When the DM interaction and dipolar interactions compensate for the DWs energy and Zeeman energy cost then $E'_{\mathrm{tot}} < 0$, in which case the stripe configuration is favoured over the saturated uniform state. In this case, the skyrmion is unstable as it decreases its energy by elongating into a stripe domain. The results of this simplified method are compared to the results of the perturbation method in the full, tridimensional micromagnetic simulations performed with MuMax[3] in order to verify the validity of the present approach. An excellent agreement is found, as the unstable configurations found from the perturbation method are also the ones with $E'_{\mathrm{tot}} < 0$ after minimisation, except for two cases only, $L = 5$; $\mu_0 H_{\mathrm{ext}} = 80\,\mathrm{mT}$ and $L = 5$; $\mu_0 H_{\mathrm{ext}} = 150\,\mathrm{mT}$, for $M_s = 1.3\,\mathrm{MA\,m^{-1}}$. This simple modelling of linear stripe domains therefore provides a robust mean of assessing the thermodynamical stability of skyrmions against elongation into stripe domains.
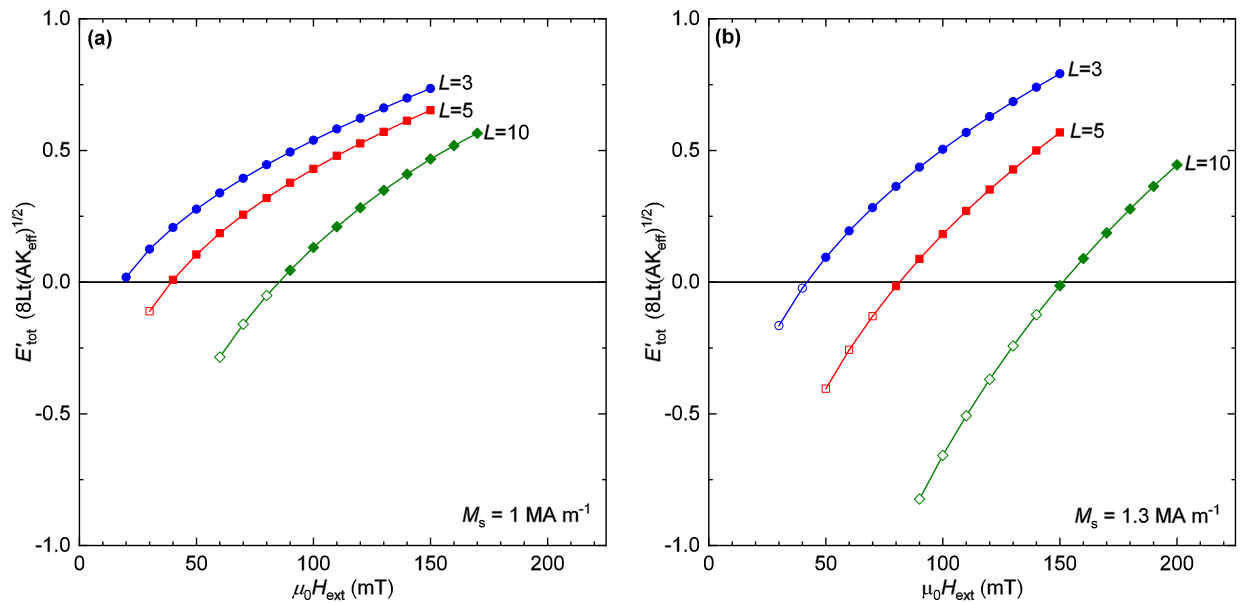
Figure 2.4: Energy of the stripe domain as a function of $\mu_0 H_{\text{ext}}$, for $L = 3, 5, 10$, in the cases of (a) $M_s = 1.0\,\text{MA m}^{-1}$ and (b) $M_s = 1.3\,\text{MA m}^{-1}$. Circles correspond to $L = 3$, squares to $L = 5$, and diamonds to $L = 10$. The filled symbols correspond to stable skyrmions in full, tridimensional simulations, while hollow symbols correspond to unstable skyrmions (subject to elliptical instability) in these full, tridimensionnal micromagnetic simulations, performed with MuMax^3 .

2.6 Thermal stability of energy barrier against collapse

The micromagnetic approach is no longer valid for the description of magnetic textures down to very small sizes, which hence requires an atomistic model. In such a discrete model, due to the relaxed continuity constraint, the isotropic collapse of skyrmions can occur. At zero temperature, collapse conditions are reached as soon as the external field is strong enough to overcome the exchange interaction of a very small ensemble of atoms, above a threshold value (in the 1–10 T range) that can be found by dynamic atomistic simulations [29, 137]. At finite temperatures, the path towards skyrmion collapse can also be induced by thermal fluctuations. Such thermally activated annihilation is a stochastic process, and determining quantitatively the thermal stability of magnetic skyrmions constitutes a rather complex task. This can be achieved by Nudged Elastic Band calculations, which allow to determine the minimum energy path between a skyrmion state and the uniform magnetization state (thus necessarily within an atomistic model for skyrmions [29, 97, 98, 149–152]). From this minimum energy path, two values are deduced: the height of the energy barrier separating the skyrmion energy minimum from the saddle point along the minimal energy path, E_{B}, and the prefactor transition rate, $k(T)$, which depends on the configurations of the magnetization in the different states, obtained from Harmonic Transition State Theory. The characteristic lifetime τ of skyrmions regarding collapse induced by thermal fluctuations is then linked to the energy barrier height E_{B} and to the temperature T by an Arrhenius law

$$1/\tau = k(T)e^{-E_{\text{B}}/(k_{\text{B}}T)}. \tag{2.33}$$

Knowing the thermal stability of the skyrmions is crucial to control their stabilisation at RT. However, a first difficulty in finding the skyrmion lifetime τ for skyrmions in magnetic multilayers, such as the skyrmions considered in this thesis, is that Nudged Elastic Band atomistic calculations have been applied only to two-dimensional systems so far, mainly because the scale of the calculations becomes unreasonably large for multilayers. Attempts have been given for systems with a thickness of 3 atomic layers, but not more [153]. Another difficulty is that in multilayers the details
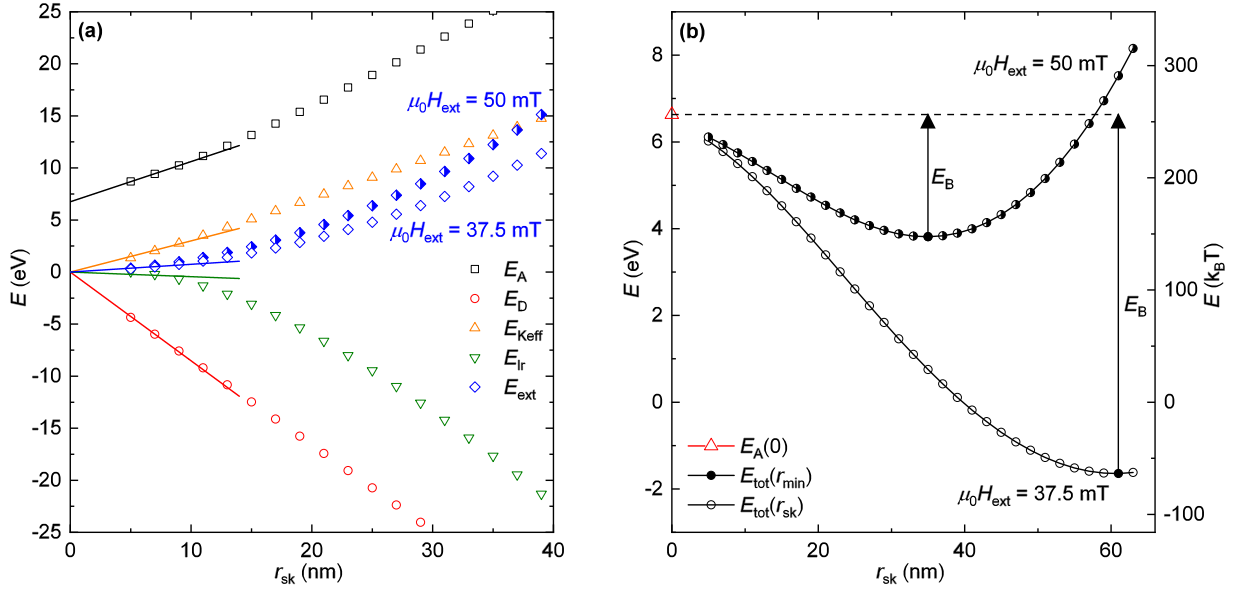
Figure 2.5: (a) Dependence of the different energy terms on r_{sk} for exchange E_A (black squares), DM interaction E_D (red circles), effective anisotropy E_{Keff} (gold up triangles), distant dipolar interactions E_{lr} (green down triangles) and Zeeman E_{ext} (blue diamonds). Two field values are represented for E_{ext}, $\mu_0 H_{ext} = 37.5\,\text{mT}$ (open symbols) and $50\,\text{mT}$ (half-filled symbols). Lines are only guides. (b) Skyrmion energy E_{tot} as a function of r_{sk} for two field values $\mu_0 H_{ext} = 37.5\,\text{mT}$ and $50\,\text{mT}$. The energy barrier E_B is found in both cases as the energy difference between the energy minimum (filled symbol) and the collapse radius ($r_{sk} \to 0$) (red triangle).

of the atomic structure are often unknown, while it has been shown [29, 151] that for the isotropic annihilation of nm-scale isolated magnetic skyrmions in extended thin films, the details of the atomistic interaction parameters, beyond their micromagnetic average, are of capital importance into finding the actual skyrmion lifetimes.

Despite the inaccessibility of Nudged Elastic Band calculations at the scale of our skyrmions, our aim here is to nevertheless find a way to approximate the skyrmion stability in magnetic multilayers. It has been shown that for the isotropic collapse of skyrmions, their cylindrical symmetry is conserved until very small sizes of a few lattice constants are reached (≈ 1–$2\,\text{nm}$) [97, 149]. It is thus possible to find the essential part of the energy barrier from simple micromagnetic simulations in the cylindrical geometry by varying r_{sk} as above: indeed, the collapse radius is at most $2\,\text{nm}$ smaller than the limit of the micromagnetic validity. In contrast, the attempt frequency $k(T)$, which can only be calculated from a precise knowledge of the minimum energy path, cannot be easily accessed by micromagnetic calculations. For the isotropic annihilation of isolated magnetic skyrmions, the attempt frequency has been found around 10^8–$10^{10}\ \text{s}^{-1}$ [97, 150]. Note that the attempt frequency is also dependent on temperature, and may change by orders of magnitudes for different annihilation processes, or for skyrmions stabilised in different compounds such as chiral magnets [154]. Assuming however this value of 10^8–$10^{10}\ \text{s}^{-1}$ for the attempt frequency, our considerations can focus on the barrier height. Owing to the exponential dependence of τ with E_B, any misestimation of the attempt frequency would simply shift the required barriers for RT stability by several $k_B T$. A RT thermal stability sufficient for experimental studies of skyrmions is reached for $E_B > 40 k_B T$, providing an average thermal stability of several years, while $55 k_B T$ is generally required for reliable long-term data retention [155]. Let us now detail how E_B can be found, adapting a recent work of Büttner *et al.* [139] to our model.

In Fig. 2.5a, the dependence of the different energy terms constituting E_{sk} are shown as a function of r_{sk} for a magnetic multilayer with $t = 1\,\text{nm}$, $p = 3\,\text{nm}$, $N = 5$, $A = 10\,\text{pJ m}^{-1}$, $D =$

$1.35\,\mathrm{mJ\,m^{-2}}$, $M_\mathrm{s} = 1.0\,\mathrm{MA\,m^{-1}}$, $K_\mathrm{u} = 0.8\,\mathrm{MJ\,m^{-3}}$ and $\mu_0 H_\mathrm{ext} = 37.5\,\mathrm{mT}$ or $50\,\mathrm{mT}$. As highlighted by the lines at low r_sk, it appears that all terms tend towards zero when $r_\mathrm{sk} \to 0$, except E_A, which converges to a finite value at low radii. As expected, the value for $E_\mathrm{A}(0)$ is $\approx 8\pi ALt$, the minimal exchange energy for a skyrmion of integer topological charge in the continuous description [31], assumed by the micromagnetic approach. This value falls in between the value of $27\,ALt$, found by Büttner *et al.* [139] using a skyrmion profile ansatz, and the value of $22\,ALt$, found by Rohart *et al.* [97] in an atomistic Nudged Elastic Band model. Indeed, the radial magnetization profile is not restrained to a class of ansatz functions in our case, which relaxes partly the exchange energy below $27\,ALt$, but it remains an axially symmetric and continuous profile without any deformations and which neglects the atomistic nature of the interactions, resulting in a value above $22\,ALt$. The precise value of the exchange energy at annihilation depends also anyway on the atomic structure of the layers and/or on any potential inhomogeneity in the materials. Therefore, the value of E_B that can be determined within the present method remains in any case an approximation by a couple ALt, that is, a few $k_\mathrm{B}T$ at RT. The energy barrier E_B can be deduced as the difference between the minimum of energy and $E_\mathrm{sk}(0) = E_\mathrm{A}(0)$, which is displayed in Fig. 2.5b. This method thus allows to obtain an approximation of the thermal stability of magnetic skyrmions in multilayers. An immediate observation that we can make at this point is that, in a simple view, E_B scales proportionally with number of layers L, justifying the choice of relying on multilayers for the RT stabilisation of skyrmions [7]. However, this reasoning has some limits, which is further discussed in Chapter 5.

Chapter 3

Essential functionalities for skyrmions: Nucleation, motion, detection

Studies of magnetic skyrmions in epitaxial, atomically thin systems have already demonstrated the stabilisation [25], controllable creation [26, 156], detection [74, 75], and deletion [26, 156] of nm-scale skyrmions, which can together achieve the goal of offering a large degree of control over the skyrmion states. In addition, the measurement of atom-resolved profiles of skyrmions in the same epitaxial systems has demonstrated the high accuracy of the description offered by atomistic models [60]. Various theoretical results and experimental observations have been gathered in these epitaxial ultrathin systems, which have allowed building a sound understanding of chiral magnetism in interfacial systems, well summarised in a recent review covering this topic [58]. These results constitute, in some sense, a proof of concept demonstrating that beyond the fundamental properties of skyrmions, they may perfectly find applications in electronic devices which could harness their rich behaviours. Unfortunately, RT stability of magnetic skyrmions in atomically thin systems could not be obtained so far, a situation which probably has to persist in the near future due to the intrinsic limitations of the energetics of atomically thin skyrmions compared to the thermal agitation energy. After the demonstration of RT stabilisation of skyrmions in magnetic multilayers, shortly before the beginning of the work of this thesis, the natural continuation was to investigate how to realise all these essential operations of skyrmion manipulation at RT in simple tabletop experiments and, hopefully, in prototype devices. Different means of achieving skyrmion manipulation in nm-thick thin films and multilayers had been proposed based on simulation works [6, 71] and indicated a possible path towards skyrmion based technologies. At this point, physics also meet materials engineering, as the objective is to reproduce and harness in larger, inevitably more complex and imperfect systems the interesting properties that were observed in atomically thin systems. After the works conducted over three years by several research groups, it remains at present a difficult task, even if very significant progresses have been achieved combining investigations in different directions. Several extensive reviews on the issue have been recently published [88–91]. In the following, I address this topic with a personal view, on the basis of experiments that were conducted in the course of my Ph.D. work.

3.1 Nucleation of skyrmions

The entry point towards many applications of skyrmions is the possibility of achieving their current-induced nucleation, thus allowing to obtain them at specific positions rather than distributed all over the structures, as it occurs with field sweeping (see Chapter 1). One scheme that has been studied as part of the work of this thesis was to inject homogeneous current-pulses into µm-scale tracks. This choice was motivated by the simplicity of the experiment compared to other techniques detailed later. A series of three multilayers $[\mathrm{Ir}(1.0\,\mathrm{nm})/\mathrm{Co}(t_{\mathrm{Co}})/\mathrm{Pt}(1.0\,\mathrm{nm})]_{11}$ with $t_{\mathrm{Co}} = 0.6\,\mathrm{nm}$, $0.8\,\mathrm{nm}$ and $1.0\,\mathrm{nm}$, similar to the ones that have been shown to stabilise magnetic skyrmions at RT [7], has been selected to be patterned into track-shaped devices of different widths, allowing the injection of the pulses. Some basic characterisation of the three unpatterned multilayers is provided
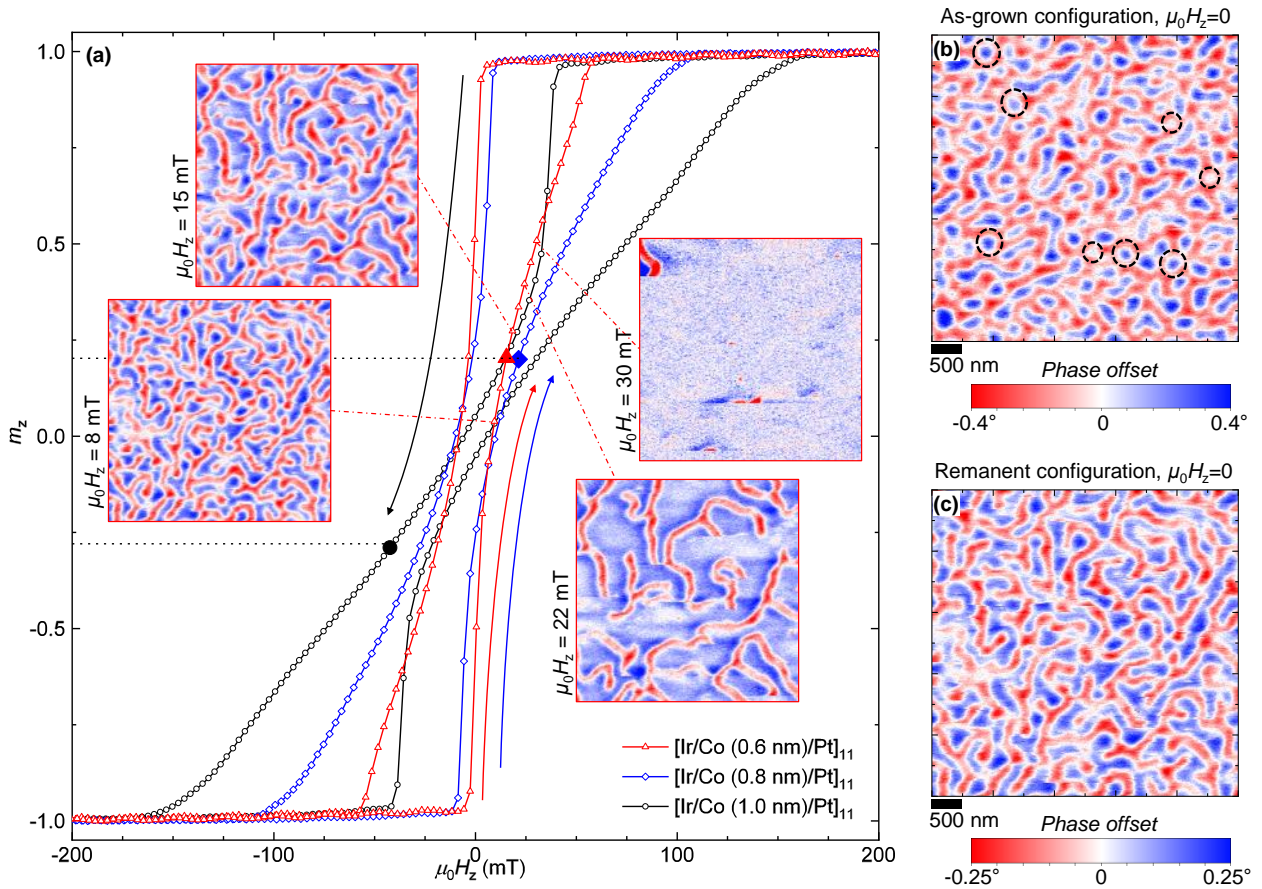
Figure 3.1: (a) OOP magnetization curves for three multilayer compositions in a series of $[\text{Ir}(1.0\,\text{nm})/\text{Co}(t_{\text{Co}})/\text{Pt}(1.0\,\text{nm})]_{11}$ multilayers, with $t_{\text{Co}} = 0.6\,\text{nm}$ (red triangles), $0.8\,\text{nm}$ (blue diamonds) and $1.0\,\text{nm}$ (black circles), respectively. Inset MFM images ($5\,\mu\text{m} \times 5\,\mu\text{m}$, colour scale as in c) show the configurations imaged in the Co ($0.6\,\text{nm}$) multilayer under applied fields of $\mu_0 H_z = 8\,\text{mT}$, $15\,\text{mT}$, $22\,\text{mT}$ and $30\,\text{mT}$, respectively. Arrows leading to the filled symbols indicate the preparation procedure before pulse experiments. (b) MFM image of the as-grown configuration in the Co ($0.6\,\text{nm}$) multilayer, at $\mu_0 H_z = 0\,\text{mT}$ before any field has been applied. The circles highlight some isolated skyrmions. (c) MFM image of the remanent configuration in the Co ($0.6\,\text{nm}$) multilayer after a field loop has been applied to saturate the magnetization before returning to zero field. The phase shift in lift mode is given by the colour scale below each image.

in Fig. 3.1a: it displays their OOP magnetization curves as a function of a perpendicular applied field, and some MFM images at different applied field values of $8\,\text{mT}$, $15\,\text{mT}$, $22\,\text{mT}$ and $30\,\text{mT}$, for the multilayer with $t_{\text{Co}} = 0.6\,\text{nm}$. The magnetic configuration is either made of labyrinthine stripe domains or saturated, due to the significant anisotropy present in these multilayers (see §1.3). However, some isolated skyrmions (indicated by the circles) are present among the labyrinthine stripe domains in the initial magnetic configuration, obtained just after deposition of the layers but before the application of fields, usually called as-grown configuration (Fig. 3.1b). The skyrmions disappear after the application of fields and do not appear again upon field cycling (Fig. 3.1c). The fact that different magnetic configurations can be stable at a single field value suggests that they can be selected by external manipulation of the system. Let us now investigate the current-induced effects.

A first observation that is made for the current-induced nucleation scheme is that it is largely independent of the initial magnetic configuration, as appeared from the experiments summarised in
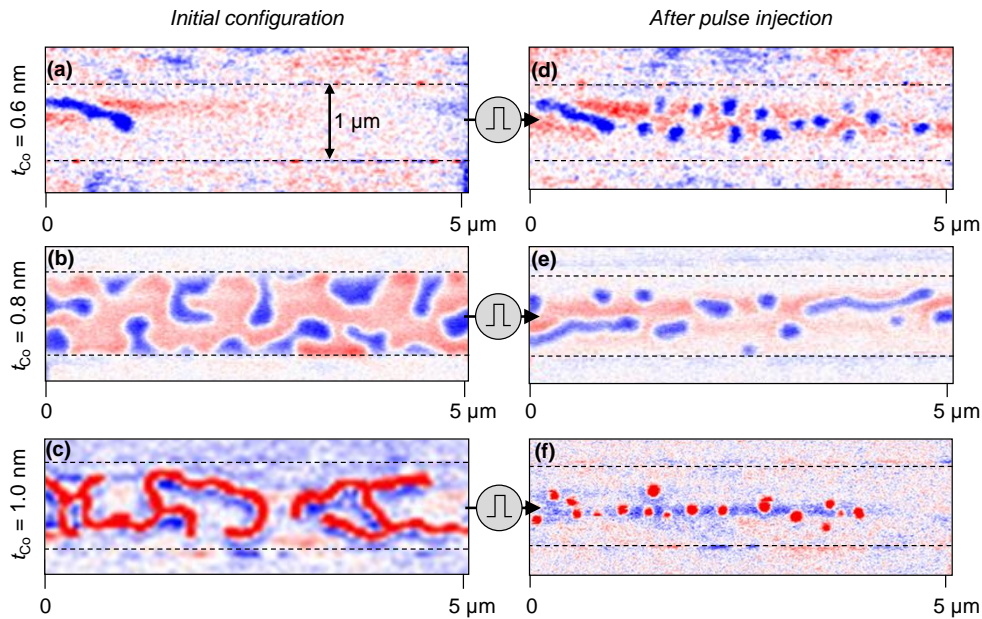
Figure 3.2: MFM images of 1 μm-wide tracks in multilayers with t_{Co} = (a) 0.6 nm, (b) 0.8 nm and (c) 1.0 nm before any pulses have been applied; and after the injection of 1000 current pulses of 200 ns each in the same multilayer tracks with t_{Co} = (d) 0.6 nm, (e) 0.8 nm and (f) 1.0 nm. The magnetic configurations are stabilised under a perpendicular field of $\mu_0 H_z = 17$ mT, 20.5 mT and -44 mT. The (threshold) pulses amplitudes are $J_n = 1.43 \times 10^{11}$ A m^{-2}, 2.38×10^{11} A m^{-2} and 2.96×10^{11} A m^{-2} for the three different Co thicknesses, respectively.

Fig. 3.2. Each track is prepared in a different initial magnetic configuration by applying different field sequences, represented by the arrows displayed in Fig. 3.1a[1]. The track with $t_{Co} = 0.6$ nm ($t_{Co} = 0.8$ nm) is saturated towards negative fields before the field is reversed to $\mu_0 H_z = 17$ mT ($\mu_0 H_z = 20.5$ mT). On the contrary, the track with $t_{Co} = 1.0$ nm is saturated towards positive fields before the field is reversed to $\mu_0 H_z = -44$ mT. Different magnetic configurations in the three tracks, saturated, with edge domains, and with labyrinthine stripe domains, result from such different field preparations, as displayed in Figs. 3.2a–c for $t_{Co} = 0.6$ nm, 0.8 nm and 1.0 nm, respectively. Whatever the initial magnetic configuration however, skyrmions can be obtained after the injection of pulses of duration 200 ns each (all pulses are separated by more than 1 ms to dissipate Joule heating between pulses), as displayed in Figs. 3.2d–f. In the present experiments, 1000 separate pulses are injected each time in order to observe even rare nucleation events, and to investigate whether the pulses damage the tracks.

The threshold current density for nucleation effects, J_n, is determined by alternatively imaging the magnetic configuration in the track and applying pulses of progressively increasing current density, until a change of magnetic configuration results in the presence of skyrmions. The threshold current density for nucleating skyrmions in the different tracks is found to be $J_n = 1.43 \times 10^{11}$ A m^{-2}, 2.38×10^{11} A m^{-2} and 2.96×10^{11} A m^{-2} for $t_{Co} = 0.6$ nm, 0.8 nm and 1.0 nm, respectively. In these experiments, J_n is also found independent on the polarity of the current pulses, as well as on the direction of the applied field, that is, of the magnetization of the domains. The square of the required current density for skyrmion formation, J_n^2, is displayed as a function of t_{Co} in Fig. 3.3a. A linear fit (including an offset due to RT thermal activation) is shown, which indicates a good correlation of J_n^2 with t_{Co}. The dissipated thermal energy per volume inside the track is thus correlated with the magnetic volume to be manipulated, suggesting a thermal origin

---

[1]All initial configurations correspond to $m_z = \pm 0.25$ on the hysteresis loops of the unpatterned films, and the use of an opposite field in the third case is to show independence on the magnetization direction.
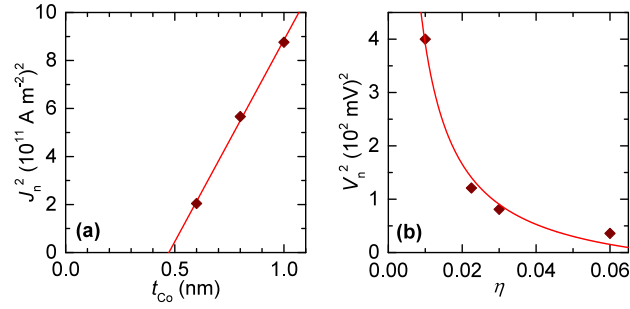
Figure 3.3: (a) Dependence of the squared threshold current density for skyrmion nucleation J_n^2 as a function of t_{Co}. The line is a linear fit to the experimental values. (b) Dependence of the squared threshold pulse amplitude V_n^2 as a function of the duty cycle of a bipolar periodic excitation. The line is an offset inverse function fit to the experimental values.

for the current-induced nucleation. In order to further confirm this observation, another experiment has been performed, in which a periodic and bipolar pulsed current excitation is applied with a frequency 2.5 MHz and varied duty cycles η, which is equivalent to tune the pulse length. The threshold pulse voltage V_n to affect the magnetic configuration is found by progressively increasing the pulse voltage until a transition towards a skyrmion configuration is observed. As appears in Fig. 3.3b, the squared voltage V_n^2 scales inversely with the duty cycle (itself being proportional to the accumulated heat), which is again consistent with Joule heating, and a probable mechanism for this observed nucleation is thus related to temperature. In contrast, this observation tends to rule out Oersted fields or spin-current related effects as possible origins (which should be insensitive to η), even if one cannot exclude minor contributions from these two effects, as they have been observed in other works [157, 158].

The application of long trains of current pulses to nucleate skyrmions is reproducible as it does not affect the multilayers or the magnetic properties of the devices, even after tens of trains of 1000 pulses. Two phenomena can be proposed to be the consequences of the temperature raise of the magnetic system during the time of the pulses, which may each, or even through a combination of both, explain the observed nucleation of skyrmions under current.

A first consequence of temperature is that it necessarily affects the magnetic parameters. A good knowledge of the temperature-dependent variations of K_u, M_s and A has been obtained over recent times, with the study of perpendicularly magnetized magnetic films for magnetic random access memory applications. Notably, it appears in various compounds that M_s follows a $(1 - T/T_c)^{1/3}$ power law (with T_c the Curie temperature) over an extended temperature range from RT to T_c, that the interfacial anisotropy K_s varies proportionally to $M_s^{2.5\pm0.3}$, independent of the materials combination, and that A varies following $A(T) = A_0(M_s/M_0)^2$ with A_0 and M_0 the values of A and M_s at $T = 0$ K, respectively [159]. Upon variations of temperature, the stable (or metastable) magnetic phase (stripes, skyrmions lattice, uniform) can be then converted into an other one, which may explain the transition of the system to an other phase. If metastable at RT, this phase can be conserved after the pulse during the temperature decrease down to RT again, and the new phase, *e.g.* skyrmions, can be obtained. This mechanism is very similar to the observed stabilisation of skyrmion lattices in field-cool experiments for bulk chiral magnets [53, 160].

In addition to this effect, the increase of temperature also reinforces thermal fluctuations, which may assist the activation of skyrmion nucleation paths. For example, in a uniformly magnetized system, there is a given barrier height for the skyrmion nucleation process, $E_{B,n}$, which mainly originates in the exchange energy that needs to be overcome to create a locally non-uniform magnetization. Neglecting variations of the attempt frequency in a simple explanation here, the nucleation rate increases exponentially with temperature, following an Arrhenius law $\propto \exp[-E_{B,n}/(k_B T)]$, and can become high enough to generate skyrmions. In principle, this nucleation should occur at
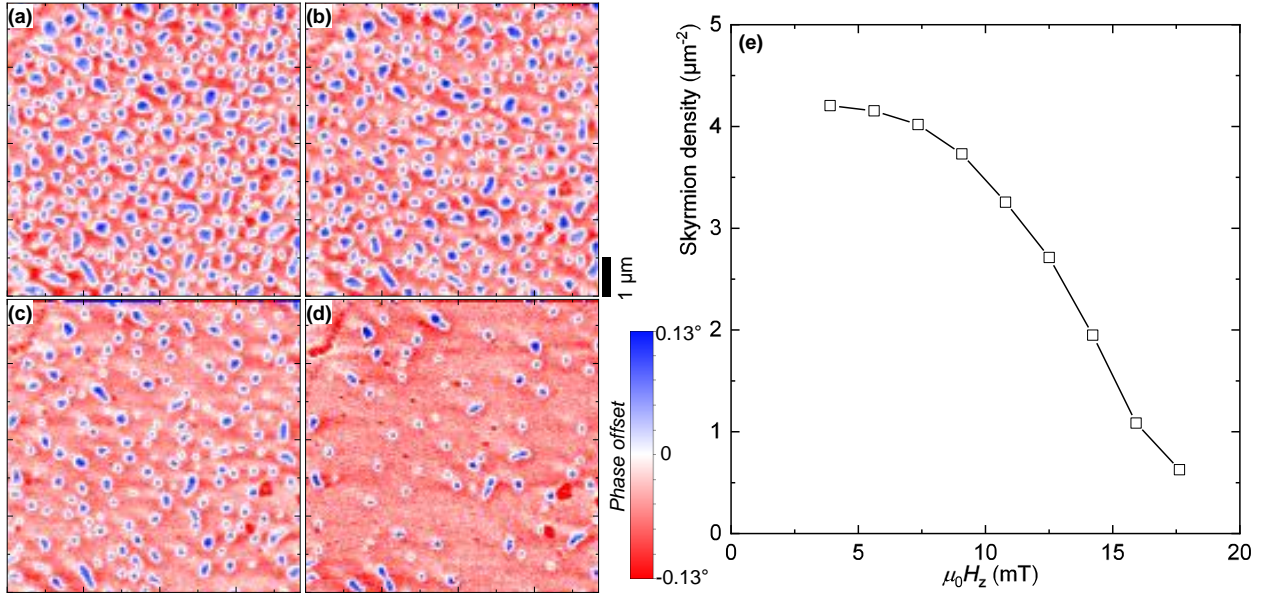
Figure 3.4: (a-d) MFM images ($7.68\,\mu m \times 7.68\,\mu m$) of the magnetic configuration in a multilayer $[\text{Pt}(1.0\,\text{nm})/\text{Co}(0.8\,\text{nm})/\text{Ir}(1.0\,\text{nm})]_5$ under applied fields of $\mu_0 H_z = 6\,\text{mT}$, $9\,\text{mT}$, $12.5\,\text{mT}$ and $16\,\text{mT}$, respectively. The phase shift in lift mode is given by the colour scale on the side. (e) Evolution of the skyrmion density with applied field.

all locations at which temperature increases enough, generating dense lattices of skyrmions after pulsed-current heating.

Following this explanation, a dense and uniform lattice of skyrmions should be nucleated everywhere in our tracks, which are subject to a uniform current density. However, skyrmions are non-uniformly nucleated, at some apparently disordered locations, which can be understood from the study of the field-dependent density of skyrmions obtained in the tracks upon field cycling. A study of the density of skyrmions obtained in a (larger, $10\,\mu m$) track at different applied perpendicular fields has been done, here for a multilayer $[\text{Pt}(1.0\,\text{nm})/\text{Co}(0.8\,\text{nm})/\text{Ir}(1.0\,\text{nm})]_5$, in which skyrmions have been initially nucleated by current pulses, under a field of a couple of mT. The recorded MFM images under applied fields of $\mu_0 H_z = 6\,\text{mT}$, $9\,\text{mT}$, $12.5\,\text{mT}$ and $16\,\text{mT}$ are shown in Figs. 3.4a–d, respectively. The evolution of the skyrmion density with $\mu_0 H_z$ is displayed in Fig. 3.4e, which demonstrates that the skyrmions are progressively annihilated with increasing fields. An explanation for such a large distribution of annihilation fields for skyrmions located at different locations of the track is the spatial variation of the magnetic parameters (*i.e.*, A, D, K_u, M_s, *etc.*) due to inhomogeneities and grains in the materials of the multilayer. Similarly, it is because of the inhomogeneity of the magnetic parameters that skyrmions can be nucleated only at apparently random locations, around each of which the magnetic properties allow to obtain skyrmions under current. However, no evident preference for particular sites of nucleation could be observed, resulting in random positions for the created skyrmions after each train of pulses. This is in contrast to other works conducted shortly after in different types of multilayers, in which favoured — but uncontrolled — nucleations sites are observed [157, 158]. Beyond these results, a controlled positioning of intended defects, for example by ion irradiation [96], should allow the nucleation of skyrmions at defined and controllable locations, as demonstrated in simulations [161].

Despite the inhomogeneities and the randomness of the nucleation locations, these experiments demonstrate the possibility of nucleating skyrmions in tracks using homogeneous current pulses. It constitutes a simple and controllable means of nucleating skyrmions as desired, even if not fully deterministic. In contrast, the alteration of magnetic textures with spin-currents relies on more complex mechanisms. For example, it has been proposed and demonstrated that the diverging current lines after a constriction allow for the non-isotropic deformation of stripe domains, leading
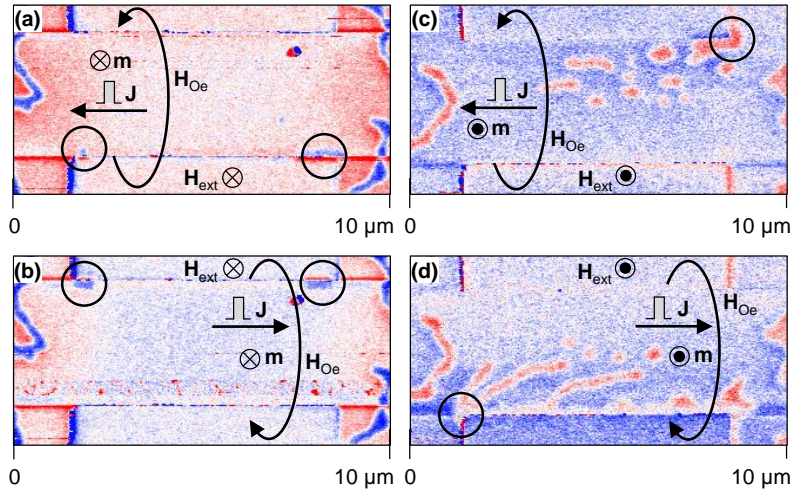
Figure 3.5: MFM images of localised skyrmion nucleation at corners of a track in a multilayer $[\text{Ir}(1.0\,\text{nm})/\text{Co}(0.8\,\text{nm})/\text{Pt}(3.0\,\text{nm})]_6$ (a) for down-pointing background magnetization ($\mathbf{m} = -\hat{\mathbf{z}}$), obtained after a negative pulse ($J < 0$, charge current from right to left), of duration $300\,\text{ns}$ and nominal current density $J = -2.0 \times 10^{11}\,\text{A}\,\text{m}^{-2}$; (b) background $\mathbf{m} = -\hat{\mathbf{z}}$, obtained after a positive pulse ($J > 0$, charge current from left to right), of duration $300\,\text{ns}$ and nominal current density $J = 2.0 \times 10^{11}\,\text{A}\,\text{m}^{-2}$; (c) background $\mathbf{m} = +\hat{\mathbf{z}}$, obtained after a negative pulse ($J < 0$), of duration $200\,\text{ns}$ and nominal current density $J = -1.9 \times 10^{11}\,\text{A}\,\text{m}^{-2}$; (d) background $\mathbf{m} = +\hat{\mathbf{z}}$, obtained after a positive pulse ($J > 0$), of duration $200\,\text{ns}$ and nominal current density $J = 1.9 \times 10^{11}\,\text{A}\,\text{m}^{-2}$. The directions of J, $\mathbf{m}$ and H_{Oe} are indicated by the arrows. Nucleation corners are circled in each panel.

to the generation of skyrmions [44, 73]. Such manipulation of stripes is significantly more complex than our method based on homogeneous heating.

However, it might not be desirable to rely on a nucleation technique based on Joule heating only, as it is arguably not the most energy efficient scheme that can be designed. Several other approaches can be considered, combining inhomogeneous current densities and/or spin-orbit torque effects [72]. In the presence of a geometric constriction, such as a corner, a notch, or a narrow electrode, the current-density is locally increased. In multilayers containing HM layers adjacent to the FM layers, the locally larger current-density at the constriction can generate large torques, which are prone to excite magnetization dynamics and induce skyrmion nucleation. It has been shown that corners are efficient skyrmion generators on the basis of numerical simulations in chiral magnets [72]. In order to verify the suitability of this approach in magnetic multilayers, the effect of current pulses has been studied also in constricted geometries, obtained by patterning multilayers into track-shaped devices now including corners and notches.

In the case of corner constrictions (see Fig. 3.5), the nucleation is found to be largely assisted by the Oersted field. Different cases are presented in Figs. 3.5a–d, displaying in each case an MFM image that has been recorded after the injection of a single (now we are looking for systematic nucleation events) current pulse into a track that was initially saturated. The two first images, corresponding to Figs. 3.5a,b, are both obtained under an external field $\mu_0 H_z = -12.5\,\text{mT}$, but for opposite current polarities. Either for $J < 0$ or $J > 0$, which thus generate opposite Oersted fields H_{Oe}, the nucleation occurs exclusively at the circled corners where the total perpendicular field, combining external and Oersted fields, is reduced during the pulse, see Figs. 3.5a,b. The nucleation corners also change side when the external field is reversed, see between Fig. 3.5a and Fig. 3.5c ($J < 0$), and between Fig. 3.5b and Fig. 3.5d ($J > 0$), again consistent with the mechanism of nucleation facilitated by the Oersted field. The directions of the Oersted field and of the corresponding background magnetization are sketched in each panel. For the case of Figs.

3.5c,d, nucleation is obtained under a weaker external field, $\mu_0 H_z = 8\,\mathrm{mT}$, compared to Figs. 3.5a,b. Due to the reduced applied field (in absolute value), skyrmions and stripes domains can be stabilised not only at the corners but also inside the track. Consequently, after nucleation they propagate away from the corner under the action of current-induced torques. Such current-induced motion of skyrmions is further discussed in the next section. Also, between the situation of Figs. 3.5a,b and the one of Figs. 3.5c,d, the pulse amplitude is reduced from $2.0 \times 10^{11}\,\mathrm{A\,m^{-2}}$ to $1.9 \times 10^{11}\,\mathrm{A\,m^{-2}}$ and its duration from 300 ns to 200 ns. Such reduction of the required nucleation pulse duration and amplitude are related to the reduced absolute value of the external field, which then creates a lower energy barrier preventing the nucleation of the skyrmions. A weaker excitation is therefore sufficient to nucleate skyrmions. Note that in the present scheme, current-induced spin torques may also play a role in the nucleation, by destabilising the perpendicular magnetization. Overall, the present observations of current-induced nucleation located at corner constrictions are very consistent with similar results demonstrated by other research teams [157, 158].

In contrast, nucleation in tracks with notches (where a triangle-shaped opening is cut at an edge of the track) was not found to be as effective, maybe because of the absence of much stronger local Oersted fields. The locally increased heat dissipation around the notches diffuses far away from them and does not result in a localised nucleation, but in a distributed nucleation everywhere in the track, exactly as it was already the case above in the standard tracks without notches. More experiments would be required to design tracks with notches geometry suitable to obtain localised nucleation.

3.2 Motion of skyrmions

Because they are magnetic solitons, skyrmions can naturally be shifted in space without affecting their texture. Two main types of current-induced motion for nanoscale magnetic textures have been largely studied in the recent years: direct transfer of angular momentum (Spin-Transfer Torque (STT) [162]) and injection of spin currents originating in spin-orbit coupling phenomena (Spin-Orbit Torque (SOT) [163, 164]). These two possible driving mechanisms have been conceptually compared in the perspective of displacing magnetic skyrmions hosted in an in-plane current-injection track [71], which has revealed that the efficiency of the motion (defined by the velocity of the moving skyrmion over the required current-density) is expected to be at least one order of magnitude larger for SOT than for STT. Such current-induced motion allows to fulfil another functionality required by most applications that are foreseen for magnetic skyrmions, controlled skyrmion displacement, which appears necessary to be able to perform memory-shift or computation operations using the information bits carried by the skyrmions, without mechanical motion (contrary to the way hard-disk drives operate, for example). Focusing the discussion on the more efficient SOT driving scheme, let us first review the essential principles allowing the motion of chiral structures, and in particular of magnetic skyrmions, in magnetic nm-thick films and magnetic multilayers. Then I present some initial results demonstrating skyrmion motion, which have been obtained in experiments using a non-optimised multilayer geometry. Chapter 4 will be devoted to modelling and further experiments of current-induced skyrmion motion, aiming at the objective, central to this work, of determining the most favourable conditions to increase its efficiency.

In the case of SOTs obtained in thin films and multilayers, the magnetization dynamics in the FM layers are generated by the injection of a vertical pure spin-current, originating from other layers. Most notably, in the case of an HM layer being adjacent to an FM layer, a vertical spin-current (of in-plane polarization orthogonal to the electrical current flow direction) can be generated inside the HM layer due to the presence of the Spin Hall Effect (SHE) [165]. The spin-current may also originate from interfacial effects, such as spin-dependent interfacial scattering, or Rashba spin-orbit coupling field located at the HM/FM interfaces [166–168]. In general, all effects may be present, even though SHE is expected to constitute the dominant mechanism for the Pt/Co-based systems studied in this work. Note that a spin-current does not carry charge: it can be seen as a

superposition of equal electron flows towards opposite directions, each carrying opposite spins. The sign and magnitude of the produced spin-current $\mathbf{J}_s$ is determined by the spin Hall angle θ_{SHE} of the material, which quantifies the charge-to-spin conversion efficiency in

$$\mathbf{J}_s = \theta_{\mathrm{SHE}} \left(-\frac{\hbar}{2e} \right) \mathbf{J} \times \hat{\mathbf{s}} \tag{3.1}$$

where $\mathbf{J}$ is the in-plane charge current vector and $\hat{\mathbf{s}}$ indicates the polarization direction of the spin current. This spin-current is then transmitted to the FM layer and interacts with the local magnetization by relaxing along it, transferring angular momentum that thus creates a torque on the magnetization. The sign and magnitude of the injected spin-current depends on the combination of HM and FM materials, and is quantified by the effective spin Hall angle θ_{eff}. It differs from the inherent spin Hall angle of the HM layer, θ_{SHE}, due to the partial reflection or dissipation of the spin-current at the HM/FM interface before it acts on the magnetization [169–171]. Moreover, as the spin current is defined for a given direction (here towards $+\hat{\mathbf{z}}$), θ_{eff} changes sign with respect to θ_{SHE} if the HM layer is located above the FM rather than below. The values of θ_{eff} are found broadly distributed depending on the HM/FM material combination, with $|\theta_{\mathrm{eff}}|$ up to 0.1–0.4 using either Pt [172, 173], with $\theta_{\mathrm{SHE}} > 0$; or Ta [174], W [175], and Hf [176], with $\theta_{\mathrm{SHE}} < 0$. Similar to magnetic properties of FMs, θ_{eff} is found dependent on the crystalline structure of the materials [175]. The way the injected spin current then acts on the magnetization $\mathbf{m}$ can be described by modifying the Landau-Lifshitz-Gilbert equation for

$$\frac{d\mathbf{m}}{dt} = -\gamma\mu_0 \mathbf{m} \times \mathbf{H}_{\mathrm{tot}} + \alpha \left(\mathbf{m} \times \frac{d\mathbf{m}}{dt} \right) - \gamma \frac{\hbar}{2e} \frac{J}{\mu_0 M_s t_{\mathrm{FM}}} \theta_{\mathrm{eff}} \mathbf{m} \times (\mathbf{m} \times \hat{\mathbf{s}}) \tag{3.2}$$

with γ the electron gyromagnetic ratio, $\mathbf{H}_{\mathrm{tot}}$ the sum of all effective fields acting on the magnetization [see (2.12)–(2.14)], and α the Gilbert damping parameter, which quantifies the dissipation of magnetic energy in the system.

Thiele Formalism

A good picture to describe how the SOT is acting on a skyrmion to induce its motion is then given by the formalism of the Thiele equation. Let us analyse its results, which constitute a good introduction to the properties of current-induced motion of skyrmions, before moving towards experimental results. The central assumption in this framework is to consider that the magnetic texture of the skyrmion is rigid and cannot be deformed, but only translated. This assumption is less and less valid for increasing current-densities and for decreasing magnitudes of the magnetic interactions, because the effective field of the SOT, favouring $\mathbf{m}$ along $\pm\hat{\mathbf{y}}$, then becomes comparable in magnitude with the magnetic energy effective fields and shall affect the symmetry of skyrmion profile. By integrating the effect of the torque term $\mathbf{m} \times (\mathbf{m} \times \hat{\mathbf{s}})$ and of other terms in (3.2) over the whole magnetic texture of the skyrmion $\mathbf{m}(x, y)$, some effective forces acting on the skyrmion can be derived [71]. The components of these effective forces describe the steady-regime velocity of the skyrmion (which is reached immediately under the hypothesis of a strictly rigid skyrmion, and below the ns timescale in practice). The Thiele equation for the velocity vector $\mathbf{v} = (v_x, v_y)$ can be written as

$$\mathbf{G} \times \mathbf{v} - \alpha \left[\mathcal{D} \right] \mathbf{v} + \mathbf{F} = \mathbf{0} \tag{3.3}$$

with

$$G = -\frac{M_s t_{FM}}{\gamma} \iint \left\{ \left(\frac{\partial \mathbf{m}}{\partial x} \times \frac{\partial \mathbf{m}}{\partial y} \right) \cdot \mathbf{m} \right\} dx dy$$

$$[\mathcal{D}] = \begin{bmatrix} \mathcal{D}_{xx} & \mathcal{D}_{xy} \\ \mathcal{D}_{yx} & \mathcal{D}_{yy} \end{bmatrix}, \mathcal{D}_{ij} = \frac{M_s t_{FM}}{\gamma} \iint \left\{ \frac{\partial \mathbf{m}}{\partial i} \cdot \frac{\partial \mathbf{m}}{\partial j} \right\} dx dy \tag{3.4}$$

$$F_{x,y} = \frac{\mu_0 M_s t_{FM}}{\gamma} \iint \left\{ (\mathbf{m} \times \mathbf{\Gamma}) \cdot \frac{\partial \mathbf{m}}{\partial x, y} \right\} dx dy$$

where $\mathbf{G} = G\hat{\mathbf{z}}$ is the gyrovector, $[\mathcal{D}]$ the dissipation matrix, $\mathbf{F} = (F_x, F_y)$ the force exerted on the skyrmion magnetization by the SOT torque $\mathbf{\Gamma}$, itself defined as the last term on the right-hand side of (3.2). Exploiting the cylindrical symmetry of the skyrmion, with $\mathbf{m} = [m_r(r), m_\varphi(r), m_z(r)]$, and considering for example a skyrmion of core magnetization pointing down $[m_z(0) = -\hat{\mathbf{z}}$ and $m_z(\infty) = +\hat{\mathbf{z}}]$ with an electrical current directed along $+\hat{\mathbf{x}}$, it results that off-diagonal terms in $[\mathcal{D}]$ are zero and

$$G = 4\pi \frac{M_s t_{FM}}{\gamma}$$

$$\mathcal{D} = \mathcal{D}_{xx,yy} = \pi \frac{M_s t_{FM}}{\gamma} a \tag{3.5}$$

$$F_{x,y} = \mp \theta_{eff} J \frac{\pi \hbar}{2e} b_{x,y}$$

where a is a dimensionless coefficient related to the magnetic texture of the skyrmion, while b_x and b_y are homogeneous to different characteristic sizes of the skyrmion related to its geometry and magnetic texture, defined as

$$a = \int_{r=0}^{\infty} \left\{ \frac{1 - m_z^2}{r} + r \sum_{i=x,\varphi,z} \left(\frac{\partial m_i}{\partial r} \right)^2 \right\} dr$$

$$b_x = \int_{r=0}^{\infty} \left\{ r \left(\frac{\partial m_r}{\partial r} m_z - \frac{\partial m_z}{\partial r} m_r \right) + m_r m_z \right\} dr \tag{3.6}$$

$$b_y = \int_{r=0}^{\infty} \left\{ r \left(\frac{\partial m_\varphi}{\partial r} m_z - \frac{\partial m_z}{\partial r} m_\varphi \right) + m_\varphi m_z \right\} dr$$

It is found again that the magnetic texture of the skyrmion possesses a particular topology, as appears from the quantisation of the gyrovector, which includes the topological constant $\pm 4\pi$ determined by the polarity of the skyrmion only (4π for $m_z(0) = -\hat{\mathbf{z}}$ or -4π for $m_z(0) = \hat{\mathbf{z}}$). It is important to note that, as appears in (3.6), a Néel skyrmion ($b_x \neq 0$; $b_y = 0$) is driven along the current, while a Bloch skyrmion ($b_x = 0$; $b_y \neq 0$) is driven orthogonal to the current. However, due to the non-zero gyrovector, the motion is deflected with respect to the direction of the driving force, which is known as the skyrmion Hall effect [19]. Skyrmion motion can be described in an infinite plane (Fig. 3.6a), which is usual when the skyrmion is located far from any edge of the film; or in a confined case corresponding to a track (Fig. 3.6b). Solving (3.3) in the infinite plane geometry,

$$v_x = -\frac{1}{1+\eta^2} \frac{F_y}{G} + \frac{\eta}{1+\eta^2} \frac{F_x}{G}$$

$$v_y = +\frac{1}{1+\eta^2} \frac{F_x}{G} + \frac{\eta}{1+\eta^2} \frac{F_y}{G} \tag{3.7}$$

in which $\eta = \alpha \mathcal{D}/G = \alpha a/4$ is a dimensionless ratio quantifying the relative strengths of dissipation effects *vs.* deflection effects. The angle of deflection of the motion with respect to

the driving force, called the skyrmion Hall angle Θ_{sk}, is then

$$\Theta_{sk} = \text{atan}\, \frac{1}{\eta} \qquad (3.8)$$

while the skyrmion velocity in this direction is

$$v_{sk} = \sqrt{v_x{}^2 + v_y{}^2} = \frac{F}{\sqrt{1 + \eta^2}G} \qquad (3.9)$$

In the case of a nanostructure patterned into a track geometry, after some time the motion of the skyrmion is forced along the x direction, resulting in $v_y = 0$ (see Fig. 3.6b). The skyrmion is indeed repelled from the edges of the track by a repulsion force F_r directed along $\pm\hat{\mathbf{y}}$, due to an additional confining potential by interaction with the track edge [71, 177, 178]. For driving forces weaker than the expulsion limit, (3.3) projected along $\pm\hat{\mathbf{y}}$ writes $F_x + \eta F_y + \eta F_r = 0$, which results in $F_r = -F_x/\eta - F_y$ and in replacing (3.7) by

$$v_x = \frac{1}{\eta}\frac{F_x}{G} \qquad (3.10)$$

In the infinite case, reminding that $\hat{\mathbf{x}}$ defines the direction of the current, we can analyse the direction of motion. In the geometry of an infinite plane, a Néel skyrmion moves along $\pm\hat{\mathbf{y}}$ in the absence of dissipation ($\eta \to 0$), along $\pm\hat{\mathbf{x}}$ when dissipation dominates ($\eta \to \infty$). Conversely, a Bloch skyrmion moves along $\mp\hat{\mathbf{x}}$ in the absence of dissipation ($\eta \to 0$), along $\pm\hat{\mathbf{y}}$ when dissipation dominates ($\eta \to \infty$). Therefore, dissipation plays the role of counteracting the skyrmion Hall effect. As $F_{x,y}/G \propto \theta_{eff}J/M_s t_{FM}$, the velocity of a skyrmion is inversely proportional to saturation magnetization and FM layer thickness. It is important to note that for skyrmions of a fixed chirality, of interest in this work, the direction of motion reverses for opposite signs of the current, or for opposite signs of the effective spin Hall angle θ_{eff}. Likewise, the direction of motion of Néel skyrmions also reverses for opposite signs of the DM interaction, because it changes the sign of b_x. For $\theta_{eff} > 0$ and $D > 0$ (CCW skyrmion chirality), corresponding to the case of a Pt layer located under the FM, $b_x < 0$ and $F_x > 0$, resulting in a motion along the current direction, consistent with experimental findings [46, 47, 179]. Note that the motion then occurs opposite to the electron flow, which shall allow in the present case to distinguish between SOT- and STT-driven effects, as the STT-driven motion is expected to instead proceed in the direction of the electron flow.

However, most experiments and projected skyrmion devices are restrained to one-dimensional tracks of limited width. In tracks, Néel skyrmions can be accelerated along the edges by a factor $\sqrt{1 + \eta^2}/\eta$, comparing (3.10) to (3.9), which can be very large for small dissipation factors η. However, exploiting such edge-enhanced velocity does not appear judicious at present, as in experiments skyrmions are found to be drastically slowed down due to edge defects [45], and may also be destroyed for too large driving currents overcoming the repulsing potential. On another note, according to (3.7) it may appear beneficial, in the weak dissipation regime $\eta \to 0$, to exploit Bloch skyrmions in order to obtain large longitudinal velocities v_x. However, in any track design, this velocity drops to zero according to (3.10). Indeed, if no driving force along x is present the skyrmion stops after shifting towards the edge, under the influence of the confining potential. For this reason, ensuring a Néel chirality for the skyrmions, by reaching a large enough value for $|D|$, is necessary in order to obtain efficient current-induced motion into tracks. Understanding how to obtain a large DM interaction in thin films and multilayers thus remains a very pertinent research direction to enhance skyrmion manipulation.

Note that most often, an additional effective field builds up due to SOT and interfacial effects, sometimes referred to as a field-like torque [additional term $\propto (\mathbf{m} \times \hat{\mathbf{s}})$ in (3.2)]. However, its effect on magnetic skyrmions cancels in the case of rigid skyrmions. When the deformation of the
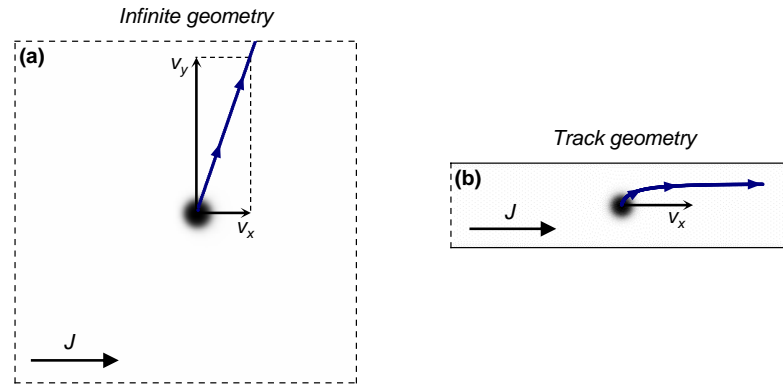
Figure 3.6: Usual geometries for skyrmion motion : (a) infinite plane and (b) track. Dashed black lines correspond to open space; in micromagnetic simulations, they correspond to periodic boundary conditions. Solid black lines correspond to physical edges; in micromagnetic simulations, they correspond to ending boundary conditions. Skyrmion trajectories are represented by the blue line with arrows in each case, with the velocity components v_x and v_y in the steady regime.

structure of the skyrmion under current is taken into account, the field-like torque is found to only moderately affect the skyrmion Hall angle [47], and is thus not essential in the analysis of skyrmion motion.

In order to observe skyrmion motion, 1.2 μm-wide tracks have been lithographed for the multilayer of composition Ta (15 nm)/Co (0.8 nm)/[Pt (1 nm)/Ir (1 nm)/Co (0.8 nm)]$_{10}$/Pt (3 nm). Initially, a few skyrmions are nucleated, as shown above, with a train of 200 ns-long current pulses in the track, under an OOP field $\mu_0 H_z = 22$ mT, which results in the magnetic configuration shown in Fig. 3.7, panel (0). To induce motion, shorter pulses of length 100 ns and current density amplitude $J = 2.85 \times 10^{11}$ A m^{-2} are injected in the track. In order to detect the skyrmion motion, the magnetic configuration and the position of the skyrmions present in the track is repeatedly imaged
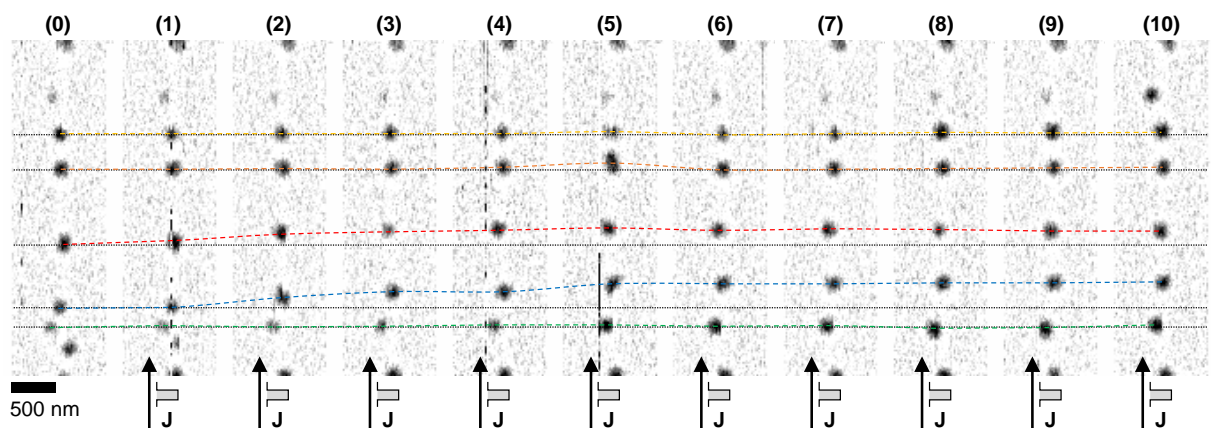
Figure 3.7: MFM images showing the initial magnetic configuration [panel (0)] and the magnetic configuration obtained after the injection of successive trains of 5 pulses [panels (1–10)]. The imaged portion of the track is 3.5 μm × 1.2 μm. The grey-tone colour scale is the MFM phase shift in lift mode, normalised between 0 and 1 in order to allow the detection and the tracking of the skyrmions. The coloured dashed lines follow the positions of the centres of the skyrmions, while the dotted lines are reference positions from the skyrmions in panel (0).

with MFM [Fig. 3.7, panels (1–10)], alternatively with the injection of trains of 5 pulses in the track between each image. It appears that the skyrmions tracked by the blue and red traces are displaced in the direction of the charge current, while the skyrmions tracked by the green, orange and gold traces remain immobile. This constitutes a pinning behaviour, causing a stochastic motion, that is discussed into more details in §4.1 and §4.2. Nevertheless, the skyrmions tracked by the blue and red traces have been shifted over 290 nm and 170 nm, respectively, between frames (0) and (5). This corresponds to skyrmion velocities $v \approx 120 \, \mathrm{mm \, s^{-1}}$ and $70 \, \mathrm{mm \, s^{-1}}$, respectively.

The fact that skyrmions are displaced in the direction of the current, opposite to the electron flow, strongly supports that the motion is caused by SOTs. The present experiment (and also similar experiments in 4.1 for both current polarities applied, which demonstrate a reversal of motion with change of current direction) thus demonstrates that skyrmion motion can be achieved under the action of current-induced torques created by the SHE in magnetic multilayers. The velocity achieved in the present initial experiment is however rather poor, as we will discuss later: Chapter 4 is devoted to the elaboration of strategies allowing to achieve more efficient current-induced motion of skyrmions.

3.3 Electrical detection of skyrmions

The experimental results presented in this section have been obtained principally by Davide Maccariello, post-doc researcher in the lab during the time of my Ph.D. I thank him for letting me closely follow his advances and sharing his results for inclusion here.

The third essential building block for any kind of skyrmion-based application is the detection of the presence of individual skyrmions at the device level. Many experiments have demonstrated the detection of skyrmions relying on direct imaging techniques [24]. Beyond imaging, it has been shown that skyrmion lattice phases in bulk B20 materials could be detected electrically, through the THE contribution to the transverse conductivity [85, 86]. In that respect, it appears interesting to attempt similar electrical detection of skyrmions in thin films and multilayers, targeting in particular the detection of individual skyrmions.

The electrical detection of individual skyrmions at RT has been demonstrated in the following experiment, combining electrical transport measurements and MFM imaging, performed on a multilayer with composition $[\mathrm{Pt}(1 \, \mathrm{nm})/\mathrm{Co}(0.8 \, \mathrm{nm})/\mathrm{Ir}(1 \, \mathrm{nm})]_{20}$. Devices including two intersecting tracks in a cross-shaped pattern (Hall configuration) have been lithographed. This design allows the injection of current-pulses along one direction, in order to nucleate skyrmion with currents, and the reading of the transverse conductivity signal at the intersection of the cross, by measuring the transverse voltage resulting from the injection of a small continuous current along the principal track. The current density injected in the main track for the electronic transport characterisation is $J = 2 \times 10^8 \, \mathrm{A \, m^{-2}}$, orders of magnitude below the skyrmion nucleation threshold.

The magnetization of the Hall cross is first saturated OOP ($m_z = 1$), by applying an OOP magnetic field $\mu_0 H_z = 140 \, \mathrm{mT}$. The applied field is then reduced to $\mu_0 H_z = 37 \, \mathrm{mT}$, at which the magnetization remains saturated. Next, in order to obtain a varying number of skyrmions in the Hall cross, trains of 20 pulses of length 200 ns at J_n are successively injected in the track, as demonstrated in §3.1. Each train of pulses allows the nucleation of one or several skyrmions that can be imaged by MFM, until the intersection is filled with the maximum number of skyrmions for the applied field value [frames (1)–(3) of Fig. 3.8a]. The variations of electrical transverse resistivity $\rho_{xy} = V_y t / I_x$ are monitored in parallel of the recording of the images, and are shown in Fig. 3.8b. Subsequent to the nucleation of the skyrmions, the reverse operation can be performed, when triggering the progressive annihilation of the skyrmions by increasing the OOP applied field against the direction of the core of the skyrmions. The field is increased in small steps, allowing the deletion of one or a couple skyrmions only at a time (similar to Fig. 3.4), which can be imaged by MFM, until the magnetization of the intersection is saturated again [frames (4)–(6) of Fig. 3.8a].
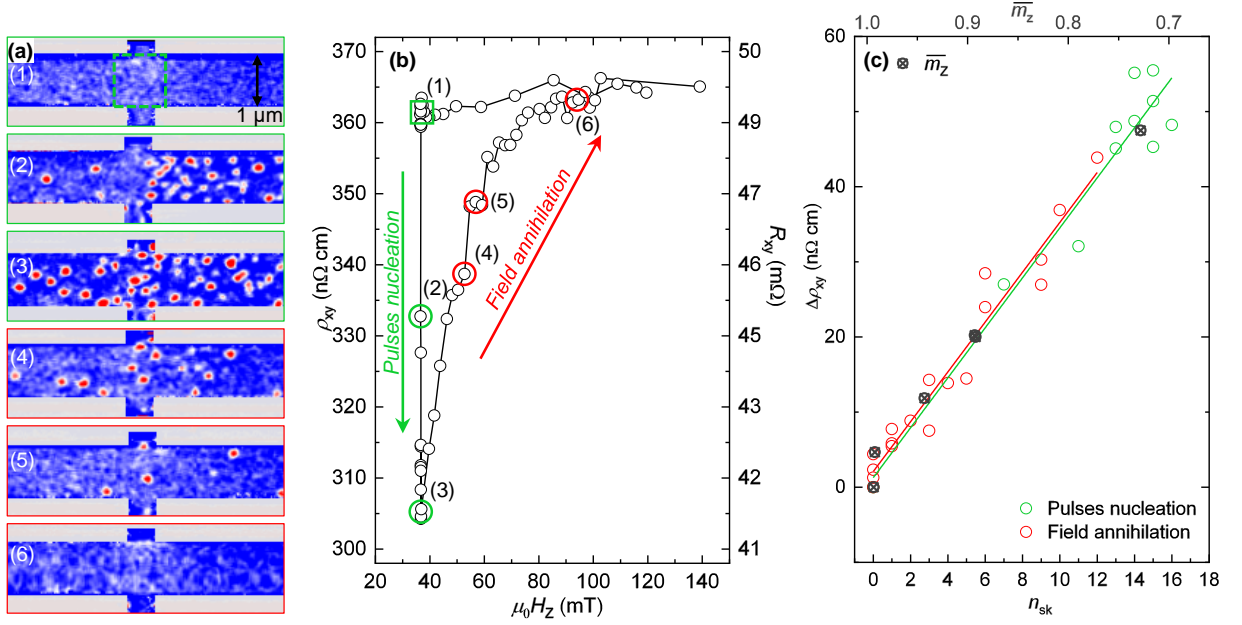
Figure 3.8: (a) MFM images at RT of the 1 µm-wide track with Hall geometry, in the initial saturated state [frame (1)], after the current-induced nucleation of skyrmions [frames (2), (3)], and during field-induced deletion of skyrmions [frames (4), (5)] until saturation [frame (6)]. The intersection area used for skyrmion counting is indicated by the dashed green box in the top frame (1). (b) Transverse resistivity ρ_{xy} as a function of the applied field $\mu_0 H_z$ upon varying the number of skyrmions with pulses (green arrow) and field (red arrow). Numbers indicate the MFM image frames corresponding to the measurement point. (c) Transverse resistivity ρ_{xy} as a function of the number of skyrmions n_{sk} in the intersection. Lines are linear fits to the measurement points for pulse nucleation (green colour) and field annihilation (red colour) of the skyrmions. The data also shows a good correlation between the average number of skyrmions n_{sk} and the average magnetization in the highlighted rectangle, $\bar{m}_z$ (black crossed circles).

Likewise, the electrical transverse resistivity ρ_{xy} is again monitored in parallel, as appears in Fig. 3.8b. Upon progressive skyrmion annihilation, ρ_{xy} increases back to its initial saturation value.

The number of skyrmions inside the intersection part of the device can be counted on each image, which allows to relate the variations of the transverse magnetoresistance signal $\Delta\rho_{xy}$ to the number of skyrmions n_{sk} (see Fig. 3.8c). According to the linear fits, the transverse resistivity is a good indication of the number of skyrmions n_{sk} present in the intersection part, independent of whether nucleation or deletion of skyrmions is analysed. A constant contribution per skyrmion $\Delta\rho_{xy}^{(sk)} \approx$ 3.5 nΩ cm can be found by determining the slope of the linear fit function. This is due to the fact that in the range of fields used in the present experiment and for this multilayer, the skyrmion radius is almost independent of the applied field, with a value $r_{sk} \approx 40$ nm, as was determined in X-ray transmission microscopy experiments [7].

The origin of this change of transverse conductivity essentially lies in the Anomalous Hall Effect (AHE), which is another consequence of spin-orbit coupling. The AHE is due to a deflection of the conduction electrons to the sides of the track, caused by the local perpendicular component of the magnetization[2] m_z. The difference of transverse resistivity is found proportional to the average $\bar{m}_z$ of the perpendicular magnetization in the intersection area. This is confirmed by looking at $\Delta\rho_{xy}$ as a function of $\bar{m}_z$ extracted from the MFM images, also displayed in Fig. 3.8c (black crossed dots). Let us assume that the magnetization of the skyrmions follow a usual profile [60], consistent with

---

[2]hence its name as it is very similar to the usual Hall effect but related to the internal magnetization instead of the external magnetic field

the results of X-ray transmission microscopy experiments [7]. The change of $\bar{m}_z$ due to the presence of one skyrmion can be numerically evaluated and provides the expected AHE contribution per skyrmion as

$$\Delta\rho_{xy}^{(sk,AHE)} \approx 2\frac{\pi r_{sk}^2}{a_{tot}}\rho_{xy}^{AHE} \tag{3.11}$$

with a_{tot} the area of the intersection of the device and ρ_{xy}^{AHE} the total change of transverse resistivity between the up-pointing ($\bar{m}_z = +1$) and down-pointing ($\bar{m}_z = -1$) saturated states. Given the dimensions of the intersection, determined from the images as $a_{tot} = 1.1\,\mu m^2$, and the skyrmion radius $r_{sk} \approx 40\,nm$, each skyrmion is expected to contribute $\Delta\rho_{xy}^{(sk,AHE)} \approx 3.3\,n\Omega\,cm$, in good agreement with the value determined from the electrical measurements. In contrast, any potential contribution of the THE appears negligible in comparison to this value. The THE contribution can be calculated as $\Delta\rho_{xy}^{(sk,THE)} = -PR_0\Phi_0/a_{tot}$ [87], in which P is spin polarization of the electrons, R_0 is the ordinary Hall coefficient and Φ_0 is the quantised magnetic flux due to a single skyrmion. This provides a value of $\Delta\rho_{xy}^{(sk,THE)} = 1.7\,p\Omega\,cm$, three orders of magnitude lower than the AHE contribution, which is an upper-bound estimate as the electron mean free path is shorter than the skyrmion size and shall further reduce this value. Therefore, we can conclude that the THE plays a negligible role in the present scheme for skyrmion detection in multilayers.

In narrower tracks, the sensitivity of transverse measurements becomes sufficient to detect unambiguously the presence of a single skyrmion. In another experiment, a track of width 400 nm is saturated, after what the OOP field is reduced to $\mu_0 H_z = 27\,mT$ and its transverse resistivity measured. A train of current pulses is then injected in order to nucleate a single skyrmion in the Hall device, and its transverse resistivity is measured again. The nucleation of a single skyrmion in the intersection is verified by MFM imaging. As appears in Fig. 3.9, the difference of resistivity due to the nucleation of a single skyrmion in the intersection is found as $\Delta\rho_{xy}^{(sk)} \approx 25\,n\Omega\,cm$, well above the noise level, given by the error bars (standard deviation determined from 20 consecutive measurements). The enhanced sensitivity is well explained by the reduction of the area of the intersection part to $a_{tot} = 0.16\,\mu m^2$ in (3.11), which results in an expected contribution of $23\,n\Omega\,cm$ per skyrmion. In conclusion, this experiment demonstrates the possibility of detecting electrically a single magnetic skyrmion in a nanodevice. Some independent studies suggest that an additional THE contribution may add to the AHE signature of skyrmions in the transverse conductivity [48, 180], despite the argumentation presented above. No definitive answer valid for all systems on the origins of the skyrmion transverse conductivity can be drawn from the different results available at present.

Following (3.11) and $\Delta V_y = \Delta\rho_{xy}Jw$, with w the width of the track and keeping a detection current density $J = 2 \times 10^8\,A\,m^{-2}$, it appears that upon scaling down the device and the skyrmion radius by a common reduction factor, the measured transverse voltage reduces by the same scaling factor, which is detrimental to the fast readout of the skyrmion state. With the value of $\rho_{xy}^{AHE} \approx 360\,n\Omega\,cm$ measured above, resulting in a voltage signal V_y of about 20 nV for $r_{sk} = 40\,nm$ and $w = 400\,nm$, V_y becomes 5 nV for $r_{sk} = 10\,nm$ and $w = 100\,nm$[3] which is below the detection threshold for our present experimental setup and calls for more sensitive techniques for the reliable detection of skyrmions.

Other means of detecting electrically magnetic skyrmions in atomically-thin layers have been demonstrated, known as the tunnelling non-collinear magnetoresistance [75] or tunnelling spin-mixing magnetoresistance [74]. The presence of an individual skyrmion can be detected as a change of the differential tunnel conductance between a metallic tip and the surface, due to the non-collinearity of the magnetic texture. This technique has only been demonstrated at low temperatures in scanning tunnelling microscopes so far, but exploiting a similar phenomenon in a skyrmion multilayer at RT, designed as a magnetic tunnel junction, may provide an alternative to the detection of skyrmions

---

[3]Having $r_{sk} \approx 1/10$ of w corresponds already to a large fraction of the track, due to DM interaction induced tilting of $\mathbf{m}$ at the edges; reducing further w would probably affect the skyrmion properties.
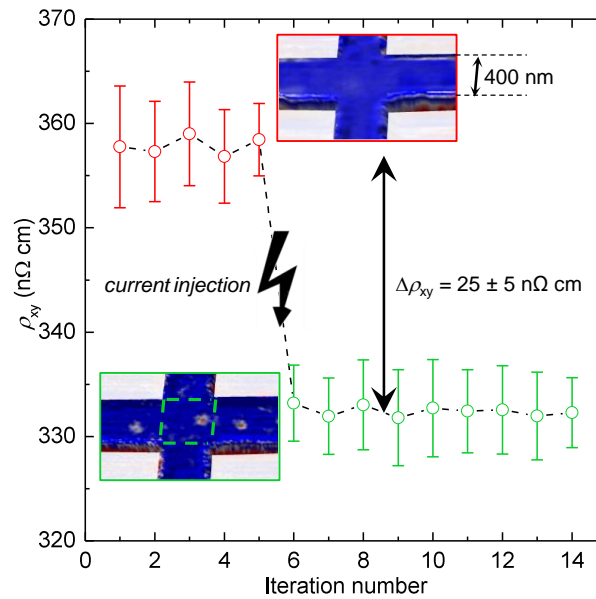
Figure 3.9: Transverse resistivity ρ_{xy} for five measurements in the saturated state (red circles), and for nine measurements after the injection of current pulses (green circles), allowing the nucleation of a single skyrmion in the intersection of the Hall cross device. Insets display the MFM images of the corresponding magnetic configurations in the intersection.

through transverse conductivity signals. It may notably provide much enhanced signal-to-noise ratios.

3.4 Towards skyrmion-based technologies

Three main features of skyrmion manipulation have thus been demonstrated here in multilayered devices: current-induced nucleation, current-induced motion and electrical detection. These three functionalities should be achievable in a same multilayer and combined, so that in principle several skyrmion-based devices could be implemented in multilayer systems. Very interesting attempts in this direction have been recently realised [181].

Further improvements remain nevertheless very desirable. The initial hope in skyrmions was based on the observation that they can be extremely compact magnetic textures, in the range of a couple nm [25]. In contrast, skyrmions are found just below the 100 nm range in the above experiments, which limits, for example, the potential density of information for memory applications or potential device scaling for logic integration. In Chapter 5, I present a study of how to further reduce the size of skyrmions. Another feature that immediately triggered an enthusiastic interest around skyrmions was the prediction of their efficient current-induced motion in nm-thick magnetic thin films at velocities in the range of 100-1000 m s^{-1}, being insensitive to track geometry [71], as well as the experimental observation of very low current density thresholds to induce skyrmion motion in B20 materials [66]. However, the motion of skyrmions demonstrated above, at RT and in multilayers, exhibits in comparison a rather high current density threshold for the motion. In the next chapter of this thesis, I discuss several studies that have been performed during my Ph.D. aiming at improving our understanding of current-induced skyrmion dynamics and at enhancing the efficiency of skyrmion motion.

How to obtain very rapid skyrmions?

In this chapter, I address the challenging task of enhancing the skyrmion velocity under current-induced motion. Beyond the fundamental interest of understanding the dynamic behaviour of magnetic skyrmions, many potential applications of skyrmions rely on the ability to manipulate them smoothly and at low currents. As will be shown below, we can define two quantities in order to characterise the efficiency of the skyrmion motion under current: the depinnning threshold current, which is of interest when skyrmion motion at very low current densities is required; and the mobility, that is, the efficiency of the current-injection once pinning is overcome, which is of interest when large skyrmion velocities are desired. I first address the pinning aspect from experiments in §4.1, and then study it quantitatively with simulations in §4.2. Then, I discuss the mobility aspect, presenting different structures that have been attempted in experiments in order to enhance spin injection and the amplitude of the SOT in multilayers. It will appear that this issue is intrinsically linked with the question of the chirality of the skyrmions in multilayers. Finally, an original consequence of the hybrid chirality building in multilayers subject to a competition between DM interaction and dipolar interactions is evidenced that is the possible cancellation of the skyrmion Hall effect.

4.1 Pinning issues

The first and most visible limitation to the efficiency of skyrmion motion observed in Chapter 3 is the presence of strong pinning effects. A more extensive observation of such pinning behaviour in current-induced motion experiments has been realised on larger ensembles of skyrmions. The nanotracks of width $1.2\,\mu m$ described in the previous chapter, of composition Ta $(15\,nm)$/Co $(0.8\,nm)$/[Pt $(1\,nm)$/Ir $(1\,nm)$/Co $(0.8\,nm)$]$_{10}$/Pt $(3\,nm)$, are now prepared in a magnetic state which exhibits denser isolated skyrmions under an OOP field $\mu_0 H_z = 18.5\,mT$. Further nucleation or deletion of skyrmions once the skyrmions have been nucleated with $200\,ns$-long pulses is avoided by relying on shorter $(100\,ns$-long) current pulses for the motion. As these shorter pulses show no effect on the magnetic configuration at the previous current density $J_n = 2.38 \times 10^{11}\,A\,m^{-2}$, it is possible to progressively increase the current density in order to get stronger SOTs, until motion is obtained. Increasing the current density to $J = 2.85 \times 10^{11}\,A\,m^{-2}$ for $100\,ns$ pulses allows to observe the motion of the skyrmions. The initial configuration in the track and the magnetic configurations observed after the injection of 50, 100 and 150 pulses are shown in Figs. 4.1a–d, respectively, for pulses of negative polarity (charge current towards the left, as indicated below panel d). The corresponding images for pulses of the opposite polarity (charge current towards the right, as indicated below panel h) are shown in Figs. 4.1e–h. In Figs. 4.1i,j for each current polarity, the positions of the centre of each domain are tracked after every injection of 10 pulses by the points evolving from black points, for the initial frame, to red points, after 50 frames.

The blue arrows in Figs. 4.1i,j highlight the motion of the moving skyrmions in each case, indicating that skyrmions are displaced towards the left in Fig. 4.1i, and towards the right in Fig. 4.1j. Again contrary to the initial expectations, only a fraction (about half) of the skyrmions
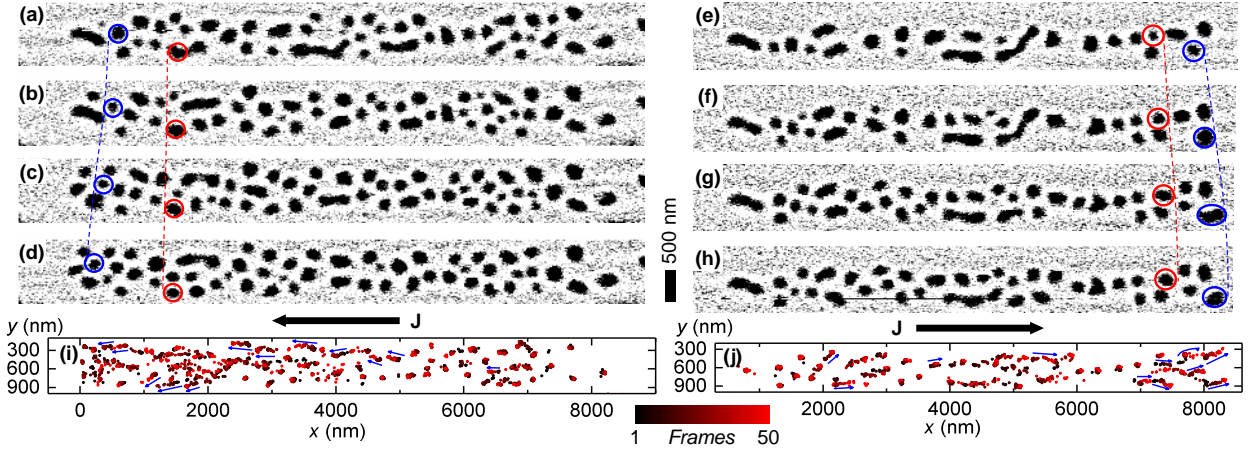
Figure 4.1: MFM images of (a) the initial magnetic configuration in the track (width 1 μm), and of the magnetic configuration observed after the injection of (b) 5, (c) 10 and (d) 15 trains of 10 pulses, respectively, for $J < 0$; of (e) the initial magnetic configuration in the track, and of the magnetic configurations observed after the injection of (f) 5, (g) 10 and (h) 15 trains of 10 pulses, respectively, for $J > 0$. All pulses are $100\,\mathrm{ns}$ long with $|J| = 2.85 \times 10^{11}\,\mathrm{A\,m^{-2}}$. The motion of some skyrmions is highlighted by the blue and red circles, linked by the dashed lines. Traces of the tracked skyrmion positions, for (i) $J < 0$ and (j) $J > 0$, with the repetition of pulses encoded by the colour, from black (initial) to red (after 50 bursts of 10 pulses) as shown on the colour scale. The motion of the most mobile skyrmions is indicated by the blue arrows.

are moving in the present experiment, while some other skyrmions appear completely pinned. This pinning behaviour can be measured by the value of depinning current, here of the order of $J_0 = 2.85 \times 10^{11}\,\mathrm{A\,m^{-2}}$, constituting the threshold below which motion is effectively cancelled. A similar behaviour has been observed in similar independent experiments by Woo *et al.* in Pt/Co/Ta multilayers [46]. From the present experiment, it is possible to extract the average velocity for the moving skyrmions, $v \approx 20\text{--}40\,\mathrm{mm\,s^{-1}}$, as well as the peak velocity of skyrmions between two frames, $v \approx 0.5\,\mathrm{m\,s^{-1}}$, much lower than theoretical expectations for motion in ideal systems, in the absence of pinning. Similar results have been obtained in the tracks with $t_{\mathrm{Co}} = 1.0\,\mathrm{nm}$, albeit at higher current-densities, for which skyrmions are found less stable under equivalent conditions. Actually, the main difficulty of such experiments is **to avoid the nucleation or the deletion of skyrmions at the current densities required to overcome the pinning** and obtain motion. A more quantitative discussion of pinning is now presented.

4.2   Understanding of pinning

Looking again to the MFM images shown in Figs. 4.1a–h, it is possible to estimate a size for each skyrmion by analysing their apparent profiles. We can define the MFM size of a skyrmion r_{MFM}, by measuring the area $\pi(r_{\mathrm{MFM}})^2$ over which the MFM signal from the skyrmion (phase shift in lift mode, proportional to the local magnetic field gradient above the multilayer) is half the full scale of the MFM data (this is the black area for each skyrmion in the images). Note that it is actually not equivalent to the skyrmion radius r_{sk}, but it is expected to be roughly similar for large skyrmions (see Appendix B). A large dispersion of skyrmions sizes appears, with a standard deviation $\sigma(r_{\mathrm{MFM}}) = 81\,\mathrm{nm}$, to be compared to the average value $<r_{\mathrm{MFM}}> = 88\,\mathrm{nm}$. The imprecisions of the MFM measurement are not sufficient to explain this large dispersion of skyrmions sizes. This demonstrates that the magnetic parameters in our systems, whose interplay define the size of the magnetic skyrmions, are not uniform at the skyrmion scale of a few tens of nm. On the atomic level, Co-based multilayers with perpendicular anisotropy, especially when they
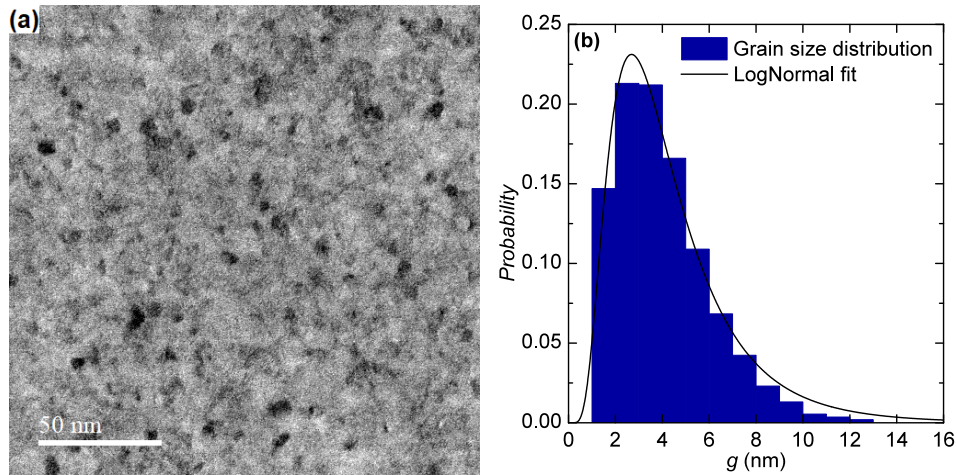
Figure 4.2: (a) TEM image obtained in dark field mode, where grains are apparent in a multilayer Pt (10 nm)/[Ir (1 nm)/Co (0.6 nm)/Pt (1 nm)]$_{10}$/Pt (3 nm). (b) Histogram of the distribution of individual grain sizes measured on 30 different images. The solid curve is a fit of the measured distribution to a LogNormal distribution. From [57].

are grown by sputtering, have an imperfect structure, and are known to exhibit local variations of the magnetic parameters due to the formation of material grains, which may lead to pinning and apparently disordered motion [99, 182, 183]. This observation of varied skyrmion sizes indicating local variations of the magnetic parameters is very consistent with Fig. 3.4 and other MFM studies [184], and is most probably the principal origin of the pinning behaviour observed in §4.1.

Some magnetic multilayers similar to those used in the motion experiments discussed above have been deposited on Si$_3$N$_4$ membranes in order to be characterised by Transmission Electron Microscopy (TEM) imaging. A typical dark field image, obtained by S. McVitie *et al.* in Glasgow [57], is shown in Fig. 4.2a, which reveals the polycrystalline structure of a multilayer of composition Pt (10 nm)/[Ir (1 nm)/Co (0.6 nm)/Pt (1 nm)]$_{10}$/Pt (3 nm), exhibiting grains of variable size and orientation. In dark field imaging, part of the grains appear with dark contrast (when away from Bragg scattering conditions), which allows to estimate their sizes by thresholding the contrast. The obtained distribution of grain sizes can be fitted to a LogNormal distribution (Fig. 4.2b), which gives an estimate of the average grain size around 4 nm. Moreover, it clearly appears that significantly larger grains, up to 10–15 nm in size, are present in the images, which may have an even larger influence on skyrmions dynamics. This result supports the idea that even in unpatterned multilayers the magnetic properties are not perfectly uniform, which is an intrinsic source of pinning effects. In addition, all lithography processes employed to fabricate the tracks used in current-injection experiments may induce additional edge damage in the devices [45].

It thus appears crucial to account for the possible local variations of the different magnetic parameters if aiming at providing a realistic picture of the current induced motion of skyrmions. This aspect can be very conveniently addressed by micromagnetic simulations of the current-induced motion with the help of the MuMax^3 package. The local variations of a magnetic parameter (either A, D, K, M_s) around its mean value are included by modelling a system with columnar grains, for which the distributions of positions and sizes of the grains, as well as the local value of the magnetic parameter inside these grains, are random. Only the average grain size g is controlled. Beyond varying one by one the magnetic parameters, small variations of thickness in the FM layers are also simulated, by varying in concert D, K_u as they follow a $1/t_{Co}$ dependence, and renormalising M_s proportionally to t_{Co}. The distribution law for grain-to-grain variations is chosen as the normal law, parametrised by its standard deviation relative to the mean value of the parameter. An example of grain distribution for $\sigma(D)/D = 10\%$ and $g = 30$ nm is shown in Fig. 4.3a, which therefore constitutes a simplified model for the type of granular multilayers observed in Fig. 4.2. As the

layers considered here have a thickness of a few atoms, any local variation of thickness by one atom only can largely affect all thickness-dependent magnetic parameters, such as anisotropy or DMI. It has been evaluated experimentally that such local variations can reach up to 75% around some grains, assuming variations of D only [184]. In that perspective, a modelling with $\sigma(D)/D = 10\%$ (maximal grain-to-grain variations up to 55% in Fig. 4.3a) appears rather realistic. Each simulated system has dimensions of $1024 \times 512\,\mathrm{nm}^2$, with periodic boundary conditions along x and y. The vertical dimension of the multilayer is also considered by introducing vacuum layers around the FM layer, and adding symmetric periodic boundary conditions along z (5 layers to the top and 5 layers to the bottom), which makes that the 10 virtually added layers are coupled to the single simulated layer by the dipolar interactions only. With this simplification, the computation of the detailed dipolar field is slightly less accurate, but the simulated system is much more compact and faster to simulate. For the present simulations, parameters [7] are $A = 10\,\mathrm{pJ\,m}^{-1}$, $D = 1.8\,\mathrm{mJ\,m}^{-2}$, $M_s = 0.956\,\mathrm{MA\,m}^{-1}$, $K_u = 0.717\,\mathrm{MJ\,m}^{-3}$, OOP field $\mu_0 H_\mathrm{ext} = 200\,\mathrm{mT}$, $\theta_\mathrm{eff} = 0.033$ and $\alpha = 0.2$, in a multilayer geometry[1] given by $t_\mathrm{FM} = 0.8\,\mathrm{nm}$, $p = 2.6\,\mathrm{nm}$ and $N = 11$. Before any simulation of current-induced dynamics, the system is first relaxed under a perpendicular magnetic field, starting from a fully randomised magnetic configuration, in order to obtain a distributed population of skyrmions. This step is very similar to the mechanism of nucleation of magnetic skyrmions due to Joule heating, which also lets the magnetization relax from a thermally-induced random configuration. An example of resulting magnetic configuration is shown in Fig. 4.3b. A broad distribution of the skyrmion sizes is obtained, very consistent with the experimental observations made in Figs. 4.1a–h.

Let us first analyse the perturbations to the ideal current-induced motion behaviour on a typical example, by comparing an ideal system and a system with grains characterised by $\sigma(D)/D = 10\%$ and $g = 30\,\mathrm{nm}$. We consider two values of applied current density, $J = 7.5 \times 10^{10}\,\mathrm{A\,m}^{-2}$ and $3.75 \times 10^{11}\,\mathrm{A\,m}^{-2}$, for which the obtained skyrmion trajectories are displayed in Figs. 4.3c,d (uniform case) and Figs. 4.3e,f ($g = 30\,\mathrm{nm}$). Note that the charge current is directed towards the left (electron flow towards the right). In the homogeneous system, all skyrmions follow closely parallel trajectories (that are only slightly perturbed due to interactions with each other), at some angle with respect to the current direction ($\Theta_\mathrm{sk} = 73.5°$) due to the skyrmion Hall effect. A much larger velocity is observed for larger currents, and as expected, the obtained average velocity v is found multiplied by five when the current density is multiplied by the same factor, from $7.5 \times 10^{10}\,\mathrm{A\,m}^{-2}$ to $3.75 \times 10^{11}\,\mathrm{A\,m}^{-2}$. In contrast, a severe pinning behaviour appears in the presence of grains, with only a few skyrmions being free to move at low current densities. At higher current densities, about half of the skyrmions are able to escape the pinning points created by the grains, however their trajectories remain largely perturbed and apparently disordered. Comparing the length and the angle of the trajectories, it appears that the local variations of D here affect both longitudinal and transverse motions. It is particularly noticeable that the global direction of the motion is affected, as most of the trajectories show a reduced angle with respect to the current direction, compared to the uniform case. This behaviour reproduces faithfully the previous observations of pinned motion in Figs. 4.1a–h: at $J = 2.85 \times 10^{11}\,\mathrm{A\,m}^{-2}$ in this case, which is in between $7.5 \times 10^{10}\,\mathrm{A\,m}^{-2}$ and $3.75 \times 10^{11}\,\mathrm{A\,m}^{-2}$, a dramatically reduced average skyrmion velocity is expected under the influence of the inhomogeneity of magnetic parameters, while motion is almost entirely impeded at lower currents. Likewise, this simulation predicts that indeed no evident skyrmion Hall angle is expected at $J = 2.85 \times 10^{11}\,\mathrm{A\,m}^{-2}$.

These different behaviours are summarised in Figs. 4.4a,b, which display the skyrmion velocity v and skyrmion Hall angle Θ_sk as a function of J ranging $0.75\text{-}9 \times 10^{11}\,\mathrm{A\,m}^{-2}$ (uniform layer: black squares; $g = 30\,\mathrm{nm}$: gold pentagons). The bars superposed to the data points indicate the standard deviation of v and Θ_sk for the whole population of about 80 skyrmions inside each simulation. In the absence of grains, straight and ideal motion is obtained, characterised by a constant mobility

---

[1] A small $\theta_\mathrm{eff} = 0.033$ is chosen as only 2 layers (bottom Ta and top Pt) contribute to the SOT, while intermediate thin Pt layers are expected to provide negligible contributions, see also §4.3.
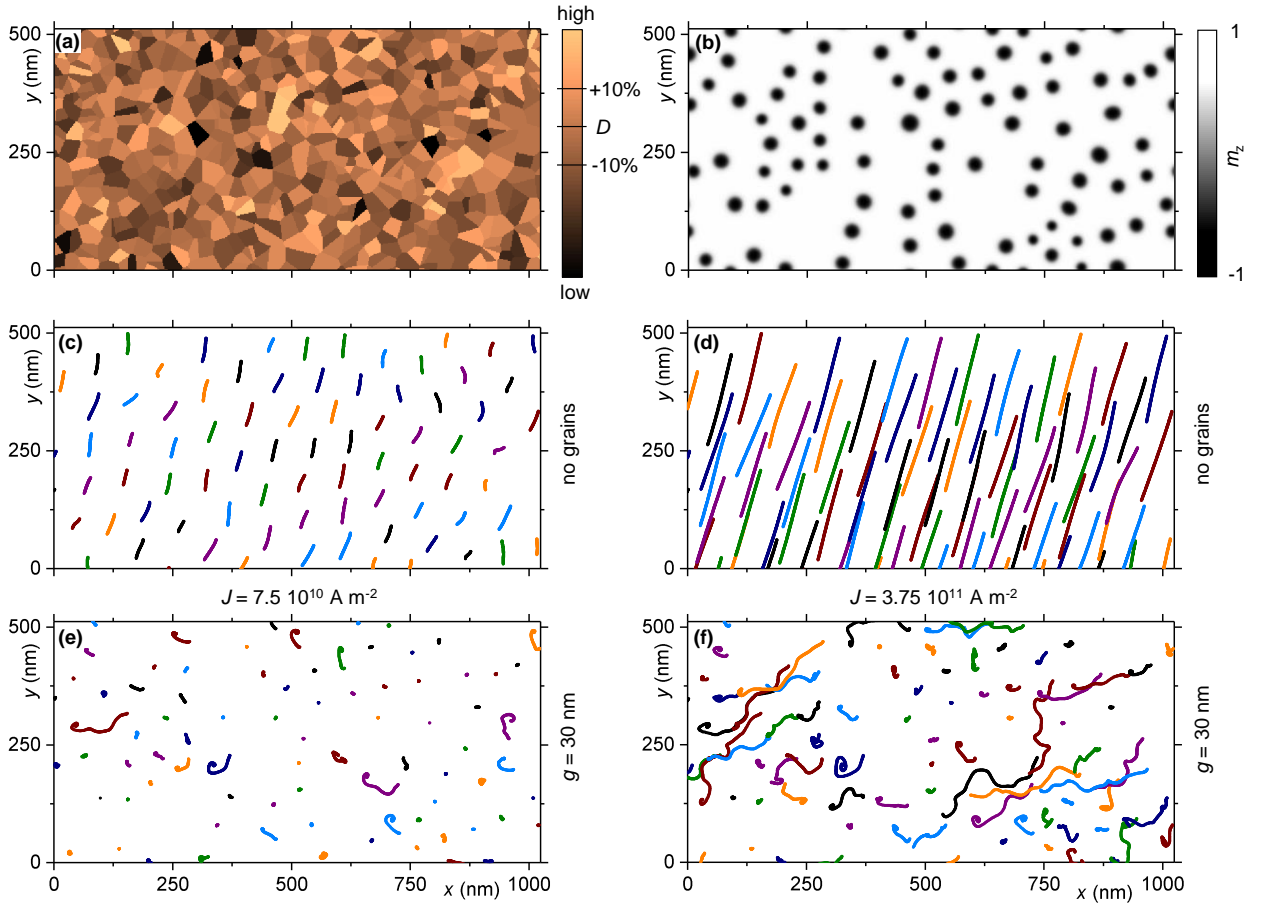
Figure 4.3: (a) Map of the local DMI parameter D in a modelled granular media, given by the colour scale of D. (b) Resulting magnetic configuration obtained after the relaxation of an initially random configuration, with skyrmions appearing from their cores with reversed magnetization $m_z = -1$. Trajectories of the simulated current-induced motion of skyrmion for (c) no grains, $J = 7.5 \times 10^{10}\,\mathrm{A\,m^{-2}}$; (d) no grains, $J = 3.75 \times 10^{11}\,\mathrm{A\,m^{-2}}$; (e) $g = 30\,\mathrm{nm}$, $J = 7.5 \times 10^{10}\,\mathrm{A\,m^{-2}}$; (f) $g = 30\,\mathrm{nm}$, $J = 3.75 \times 10^{11}\,\mathrm{A\,m^{-2}}$. Here $\sigma(D)/D = 10\,\%$.

(defined as dv/dJ) and a constant Θ_{sk}. However, in the presence of grains, the motion is almost cancelled at low current densities. The obtained v-J curve significantly differs from the expected linear current-velocity relation of the uniform case, and the mobility is only recovered at higher current densities. In link with the same pinning behaviour, the trajectories are perturbed by the presence of the grains, and tend to align with the current direction, resulting in a lower Θ_{sk}, unless large current densities are applied. In the limit of very large current densities (as shown here by the simulation for an unrealistic $J = 4.2 \times 10^{12}\,\mathrm{A\,m^{-2}}$), mobility and skyrmion Hall angle are fully recovered, but the average velocity remains lower than in the uniform case, as appears from the shift between the fitted v-J curves in Fig. 4.4a. An explanation is that some energy is dissipated in the system due to the presence of grains, which can be tentatively attributed to the breathing of skyrmions (size oscillations), excited by their displacement between areas in which the equilibrium size of skyrmions varies, due to differences of local magnetic parameters. Such dissipation is not found in other models implementing punctual defects [185–187].

The influence of the grain size has been evaluated by performing similar simulations for $g = 60\,\mathrm{nm}$ (blue hexagons), $15\,\mathrm{nm}$ (red diamonds), $10\,\mathrm{nm}$ (blue triangles) and $5\,\mathrm{nm}$ (green stars), as shown in Figs. 4.4a–d. The influence of the grains on the motion is found to first increase with reducing grain size, but to then decrease for g further reducing from 15 to 5 nm, because the spatial
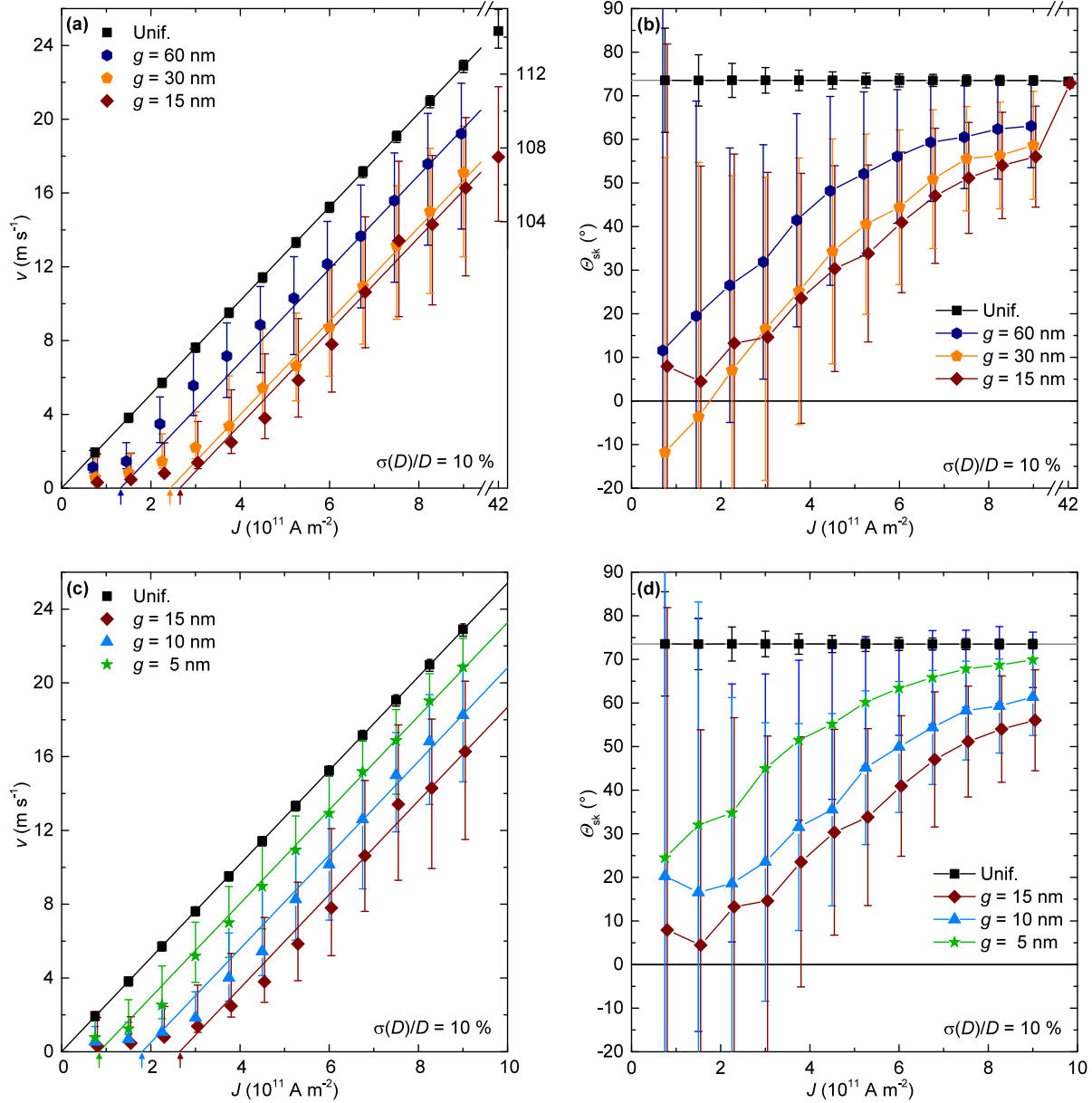
Figure 4.4: (a) Average velocity v and (b) skyrmion Hall angle Θ_{sk} of the simulated skyrmion motion as a function of applied current density J, for the uniform case ($g \to \infty$) and granular media with average grain sizes $g = 60$–15 nm. (c) v and (d) Θ_{sk} for the uniform case ($g \to 0$) and granular media with grain sizes $g = 5$–15 nm. Here $\sigma(D)/D = 10\,\%$. Lines in (a) and (c) are linear fits to the data points with fixed dv/dJ (mobility) obtained from the fit in the uniform case. The bars display the standard deviation of all values obtained for the around 80 skyrmions considered in each simulation. Coloured arrows indicate the extracted depinning current obtained for a given grain size.
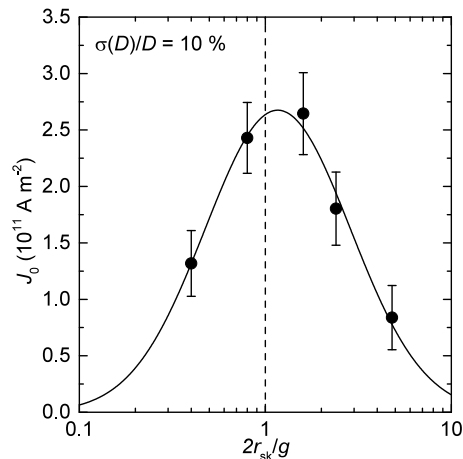
Figure 4.5: (a) Critical depinning current J_0, obtained from the fits in Figs. 4.4a,c, as a function of the ratio $2r_{sk}/g$. Errors bars are displayed, which correspond to error analysis of the fits. The solid curve is a fit of the obtained values of J_0, to the function $J_{0,m}g/(2r_{sk})\exp(-a|\log(2r_{sk}/g)|^2)$ with free parameters $J_{0,m}$ and a.

variations of parameters that affect the skyrmions are then increasingly averaged over their size. In order to quantitatively describe the pinning resulting from a size of grains, it is possible to extract a value for the critical depinning current, J_0, by determining the x-intercept of a linear fit to the v-J curve. To allow comparison between the different values of g, all fits are done at high current densities (above 6×10^{11} A m^{-2}) and are constrained to follow the same mobility dv/dJ of the uniform case, which results into very satisfying fits. The coloured arrows on the horizontal axes of Figs. 4.4a,c, indicate the determined values of critical depinning current J_0, which are displayed as a function of $2r_{sk}/g$ in Fig. 4.5. In the present case, $2r_{sk} = 24$ nm. It appears that the pinning resulting from the magnetic inhomogeneities is maximal when the size of the grains g matches the size of the skyrmions $2r_{sk}$. This is further highlighted by the consistency of a Gaussian-log fit of J_0 values to the function $J_{0,m}g/(2r_{sk})\exp(-a|\log(2r_{sk}/g)|^2)$, with free parameters a and $J_{0,m}$, where the latter represents the maximum depinning current density, found here to amount $J_{0,m} \approx 2.7 \times 10^{11}$ A m^{-2}, very close to the experimental current densities used in §4.1.

The influence of the type of inhomogeneities has also been assessed, by studying v-J and Θ_{sk}-J curves upon varying, instead of D, either A, K_u, M_s or t_{FM} inside the grains, and keeping $g = 30$ nm for different magnitudes of the standard deviation parametrising the inhomogeneity. Part of the studied curves are displayed in Figs. 4.6a,b, for A, K_u and M_s varying by 1–10 %. The values of J_0 obtained for the different types and magnitudes of inhomogeneity (indicated by coloured arrows in Fig. 4.6a) are summarised in Table 4.1. Overall, the inhomogeneities of the different magnetic parameters lead to very similar skyrmion pinning behaviours, albeit with a varying strength, depending on the type of inhomogeneity, ordered as $D < A < K_u < t_{Co} < M_s$ (at least for our system). Consequently, variations of thickness are found susceptible to cause strong pinning, as well as variations of crystallinity, which would affect either D, K_u or both.

Note that the experimental grain size is found rather small ($g \approx 4$ nm) compared to skyrmion size ($2r_{sk} \approx 80$–160 nm [7]) in the above experiments. The grain size may be slightly different on SiO$_2$ substrates and on Si$_3$N$_4$ membranes, despite the use of buffers before growth. Nevertheless, following the above models, the motion of the skyrmions should probably not appear so much affected by pinning. An hypothesis can however be formulated that once nucleated, the skyrmions naturally diffuse towards the strongest pinning points on the timescale of the experiments (after field- or pulse-induced nucleation, a few seconds or minutes elapse before the injection of current pulses) due to a thermal-driven Brownian motion. Such mechanism can be expected to largely reinforce pinning effects, and may explain why skyrmion are found largely pinned despite the small
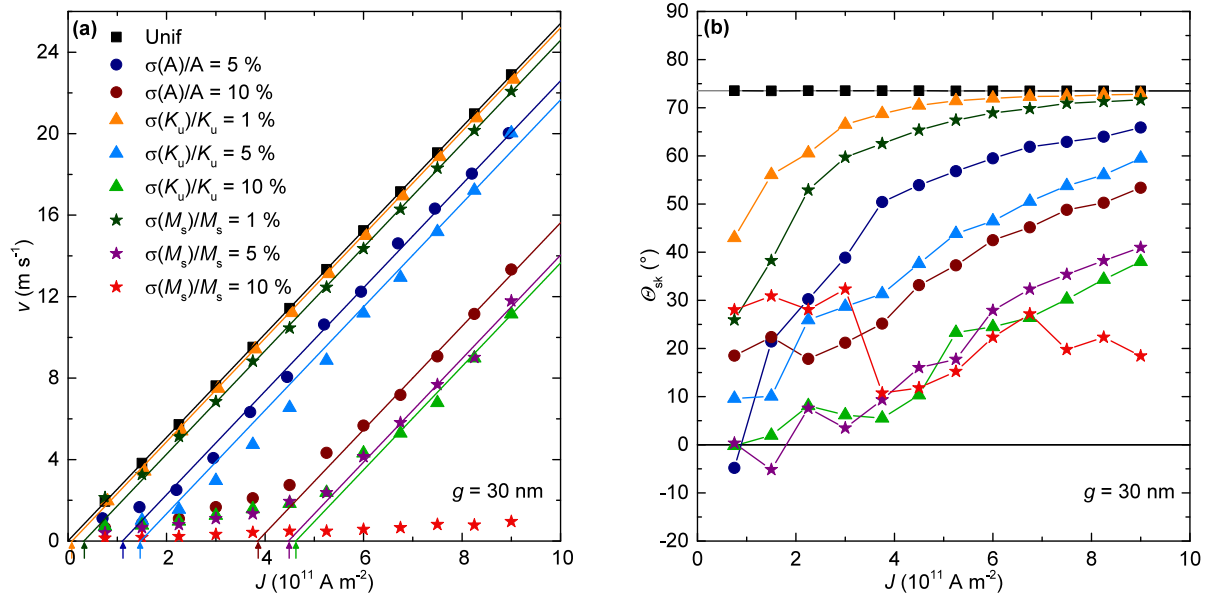
Figure 4.6: (a) Average velocity v and (b) skyrmion Hall angle Θ_{sk} of the simulated skyrmion motion as a function of applied current density J, for the uniform case ($\sigma \to 0$) and for $\sigma(A)/A = 5\%$, 10% (blue, red circles), $\sigma(K_u)/K_u = 1\%$, 5%, 10% (gold, cyan, green triangles), $\sigma(M_s)/M_s = 1\%$, 5%, 10% (dark green, purple and red stars). Here $g = 30$ nm. Lines in (a) are linear fits to the data points with fixed dv/dJ (mobility) obtained from the fit in the uniform case. Coloured arrows indicate the extracted depinning current obtained for a given grain size.

size of grains, that should cause the averaging of most effects of the pinning.

This study demonstrates that current-induced motion of skyrmions is **very sensitive to the presence of local variations of the magnetic parameters**, in particular when it originates from a granular structure of the material. It originates in the punctual nature of the skyrmions. This reality turns out to be actually quite problematic, as most solutions allowing to achieve perpendicular magnetic anisotropy in magnetic multilayers rely on the formation of (111)-oriented textured interfaces, associated with the growth of columnar grains (*e.g.*, in Pt/Co, Pd/Co, Co/Ni, ...). Two favourable directions appear from the curve shown in Fig. 4.5: one is to target epitaxial

Table 4.1: Values of the critical depinning current J_0 found for various types of magnetic inhomogeneities considering 30 nm grains.

Parameter	Amplitude of variation	J_0 (10^{11} A m^{-2})
D	10 %	2.43
A	5 %	1.10
A	10 %	3.85
K_u	1 %	0.08
K_u	5 %	1.47
K_u	10 %	4.63
M_s	1 %	0.32
M_s	5 %	4.47
M_s	10 %	>6
t_{Co}	1 %	0.22
t_{Co}	5 %	3.48
t_{Co}	10 %	>6

systems with extremely large grains in comparison to skyrmion and device sizes ($g \to \infty$), the other is to target very small grains ($g \to 0$) by optimising the deposition of the magnetic multilayers, or even the absence of grains (despite some possible thickness fluctuations) in the case of amorphous materials. For example, low depinning thresholds have been demonstrated in the case of quasi-amorphous CoFeB alloys [46, 47], combined with oxide layers in order to still obtain the required perpendicular magnetic anisotropy. To date, this probably constitutes the best material-oriented solution towards mitigating the problem of skyrmions pinning, which has allowed reaching velocities above $100 \, \mathrm{m \, s^{-1}}$ [46].

4.3 Optimisation of spin-injection in multilayers

Another lever to act on for achieving more efficient motion is to work on the spin-injection part in order to generate larger driving forces. Different spin injection geometries can be considered, depending on the positions and on the materials of the HM layers incorporated in the stack. Note that the adopted strategy here is to always keep one Pt layer adjacent to each FM layer, in order to keep perpendicular magnetic anisotropy and to enable a significant DM interaction in the stacks, as is required to promote Néel skyrmions. In order to compare different approaches, potential multilayer designs are sketched in Fig. 4.7. In this thesis, it is always assumed that the FM layers are thick enough to absorb fully the injected spin current, which thus cannot cross the FM layers. In the most straightforward experimental situation, the multilayer is grown above a Pt buffer, which results into SOT in the bottom layer only [case (I)]. Indeed, one expects negligible SOTs to be obtained in the intermediate Pt layers if they are thin compared to the spin diffusion length. When a Pt capping layer is also deposited on top of the multilayer, the SOTs from bottom and top layers tend to compensate each other, due to the opposite signs of the individual values of θ_{eff} for top and bottom spin current injection with a same material [case (II)]. In contrast, ensuring opposite DM interaction signs and θ_{eff} signs for two coupled layers in a symmetric stack (*e.g.* in Pt/Co/Au/Co/Pt, not shown here) results in enhanced stabilisation of skyrmions by dipolar interactions and their efficient motion [188]. A better choice for uniform DM interaction stacks is rather to deposit a layer of opposite spin Hall angle (for example Ta) on top of the structure, such that the SOTs in top and bottom layers work in concert to inject identical spin polarizations in the multilayer and add up [case (III)]. For all these geometries in which SOTs are only induced from the bottom and from the top, enlarging the number of magnetic layers L reduces the expected mobility of the skyrmions. In order to obtain efficient current-induced motion in multilayers with a large L, a good approach is to ensure that SOTs are generated at the interfaces of each FM layer, and not only in the bottom or top layers [case (IV)]. A suitable thickness for these intermediate layers shall be of the order of one or two times the spin diffusion length, above which increasing the HM layer thickness does not contribute to significantly reinforce the SOTs [189]. The previous thickness of $t_{\mathrm{Pt}} = 1 \, \mathrm{nm}$ could be increased to 3-8 nm, for example. The torques, and thus skyrmion mobility, should be maximised when two HM layers of opposite θ_{SHE} enclose each FM layer [case (V)], as in the case of Pt/Co/Ta [46, 190]. In principle, motion could then be of the order of L times more efficient in case (V) than in case (III).

Note that even if $|\theta_{\mathrm{SHE}}|$ is often found larger for Ta than for Pt, it is not sure whether $|\theta_{\mathrm{eff}}|$ is larger for Ta than for Pt, due to different interface transmissions [191] and/or current-shunting effects [192]. Another candidate for the second HM is naturally W, given its high θ_{SHE} in the β phase [175].

As mentioned above, another direction of improvement for enhancing skyrmion motion is the reduction of pinning, through **material optimisation, which needs to be combined with the optimisation of the spin injection geometry** [46]. An alternative strategy that I have studied in order to reduce pinning is the increase of the total number of layers L. With the above picture of thickness/grain distributions in mind, the accumulation of more FM layers is expected to reduce the standard deviation of the averaged magnetic parameters over the whole thickness,
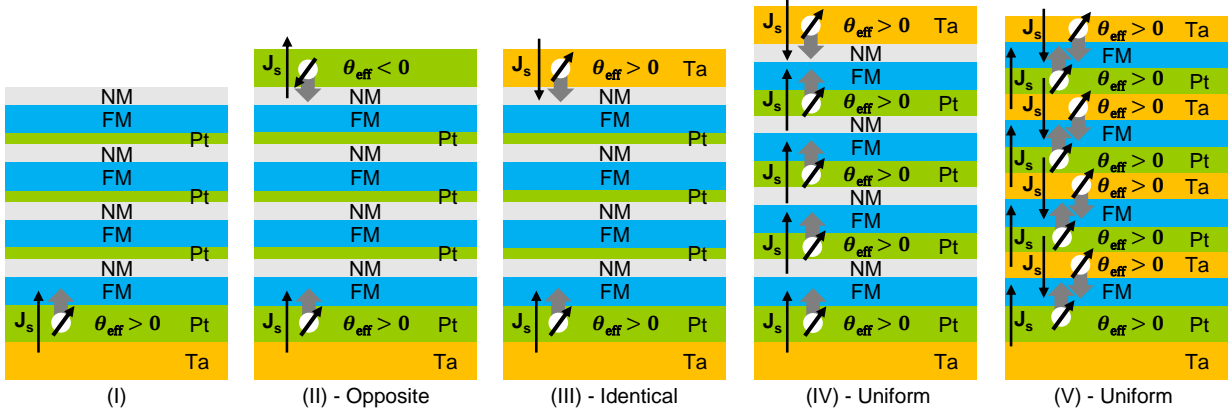
Figure 4.7: (a) Schematics of different types of multilayer injection geometry.

following $\sqrt{L}$, under the condition that the different layers present uncorrelated inhomogeneity. The fact that completely dark spots can be seen in the TEM images of Fig. 4.2 suggests that the grains in this structure are columnar and show correlation from layer to layer. The absence of correlation between grains of consecutive FM layers can on the contrary be ensured by using oxide amorphous spacers, which decouple grains, and to a lower extent, by using thick Ta spacers, which tend to form flat (111)-textured interfaces. Several series of multilayers have been fabricated to explore this direction, with the results shown in §4.8. By increasing individual layer thicknesses or total number of layers L, the total thickness of skyrmion multilayer gets larger, which increases in turn the required power to reach a given current density J. For current-induced motion, this is detrimental to the energy efficiency of the devices. Once pinning is overcome, further increasing L should be avoided.

4.4   Hybrid chiral skyrmions in magnetic multilayers

We now discuss the influence of L on the magnetic texture of chiral objects, such as Néel DWs and Néel skyrmions, with the help of the numerical model established in Chapter 2. Let us first compare the cases of skyrmions in a single magnetic layer $L = 1$ and in a multilayer with $L = 3$, for different values D. The external field can be varied concurrently with D in order to compensate for the energy dependence on skyrmion size. This allows to obtain skyrmions of comparable size (around 30–40 nm) at all the different values of D. Several skyrmion[2] profiles are displayed in Figs. 4.8a–c ($L = 1$) for $D = 0\,\mathrm{mJ\,m^{-2}}$, $0.30\,\mathrm{mJ\,m^{-2}}$ and $0.55\,\mathrm{mJ\,m^{-2}}$; and in Figs. 4.10a–f ($L = 3$) for $D = 0\,\mathrm{mJ\,m^{-2}}$, $0.30\,\mathrm{mJ\,m^{-2}}$, $0.90\,\mathrm{mJ\,m^{-2}}$, $1.20\,\mathrm{mJ\,m^{-2}}$, $1.35\,\mathrm{mJ\,m^{-2}}$ and $1.65\,\mathrm{mJ\,m^{-2}}$. Other parameters are $A = 10\,\mathrm{pJ\,m^{-1}}$, $M_\mathrm{s} = 1.3\,\mathrm{MA\,m^{-1}}$, in a multilayer geometry given by $t_\mathrm{FM} = 1.4\,\mathrm{nm}$ and $p = 3.4\,\mathrm{nm}$. K_u is chosen as $1.1\,\mathrm{MJ\,m^{-3}}$ for $L = 1$ and $1.2\,\mathrm{MJ\,m^{-3}}$ for $L = 3$.

For a single layer, the chirality evolves linearly from a Bloch profile[3] $[m_\mathrm{r}(r) = 0]$ at $D = 0$, see Fig. 4.8a, to a Néel profile $[m_\varphi(r) = 0]$ obtained for D above around $0.5\,\mathrm{mJ\,m^{-2}}$, see Fig. 4.8c. This is an expected behaviour [83, 139], due to the competition between the DM interaction, favouring Néel skyrmions, and the intralayer dipolar interactions from volume charges, favouring Bloch skyrmions.

For $L = 3$, the evolution of the magnetic texture with D is however much more complex, due to the influence of surface charge interactions, which generate a loop-closing dipolar field between the

---

[2]The magnetization textures obtained at $D = 0\,\mathrm{mJ\,m^{-2}}$ are not strictly speaking "skyrmions" but "skyrmionic bubbles", according to our definition in §2.4.

[3]As a reminder of Chapter 2, for all skyrmion solutions that include here a partially or completely Bloch-type profile in some layers, a CW Bloch component is obtained only as a result of the choice of initial conditions with $\phi > 0$. Nevertheless both signs for ϕ (CW or CCW Bloch component) are solutions for the magnetic profiles, due to the absence of DM interaction of bulk origin.
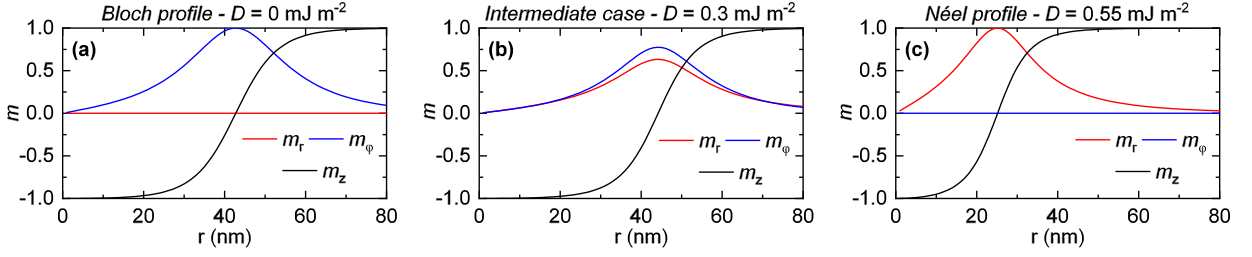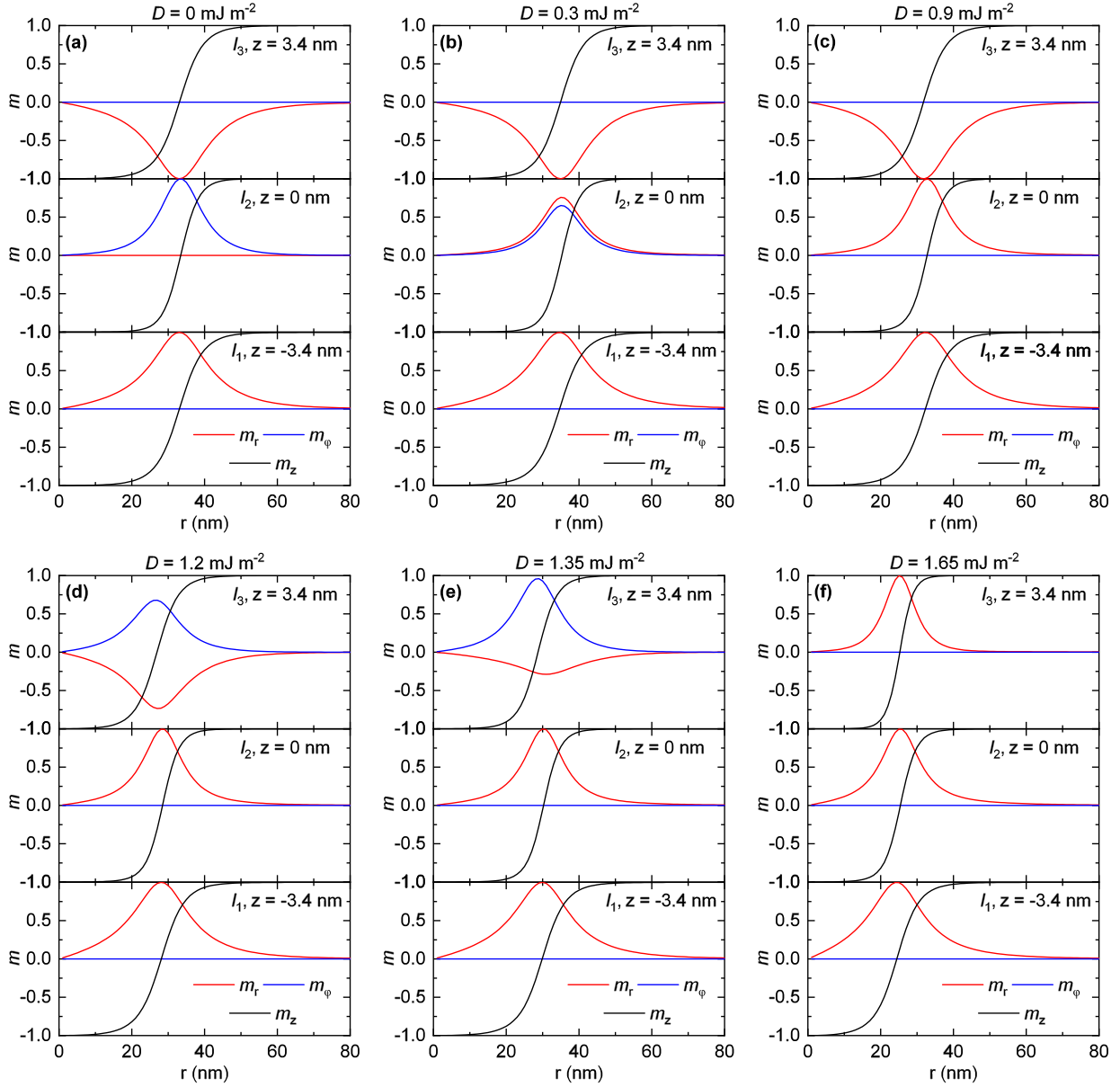
Figure 4.8: Skyrmion profiles obtained for (a) $D = 0\,\mathrm{mJ\,m^{-2}}$ and $\mu_0 H_\mathrm{ext} = 2.9\,\mathrm{mT}$, (b) $0.30\,\mathrm{mJ\,m^{-2}}$ and $5.5\,\mathrm{mT}$, (c) $0.55\,\mathrm{mJ\,m^{-2}}$ and $15\,\mathrm{mT}$. Red, blue and black lines indicate the three magnetization components m_r, m_φ and m_z as a function of radius r. Skyrmion size is kept approximatively around $r_\mathrm{sk} = 30\text{–}40\,\mathrm{nm}$.

core of the skyrmion, where **m** points down, and its environment, where **m** points up. Such surface charges cause interlayer interactions, which add to the volume charge interactions in all layers. As a consequence, the dipolar field acquires an extra radial component due to interactions with other layers, competing with the DM interaction to impose the chirality in external layers, see Fig. 4.9. The loop-closing arrangement of the interlayer dipolar field appears also clearly in the magnetic profile obtained for $D = 0$ where only dipolar interactions, but no DM interaction, are present (Fig. 4.10a): it favours a CCW Néel chirality in the bottom layer l_1 and a CW Néel chirality in the top layer l_3, while the central layer l_2 shows a Bloch-type profile, as interlayer interactions from layers above and below compensate. This indeed corresponds to the orientations of the arrows in Fig. 4.9. Consequently, the chirality of the central layer l_2 depends on D in a fashion very similar to the case of a single layer, as appears for $D = 0.3$ and $0.9\,\mathrm{mJ\,m^{-2}}$ (Figs. 4.10b,c). However, a much larger DM interaction is required to impose a unique CCW chirality in the three layers, $D \geq 1.65\,\mathrm{mJ\,m^{-2}}$ in the present case (see the evolution of the chirality in the top layer l_3 for $D = 1.2\text{–}1.65\,\mathrm{mJ\,m^{-2}}$ in Figs. 4.10d–f). For negative values of D, the roles of l_1 and l_3 are reversed upon imposing a unique CW chirality in all layers.
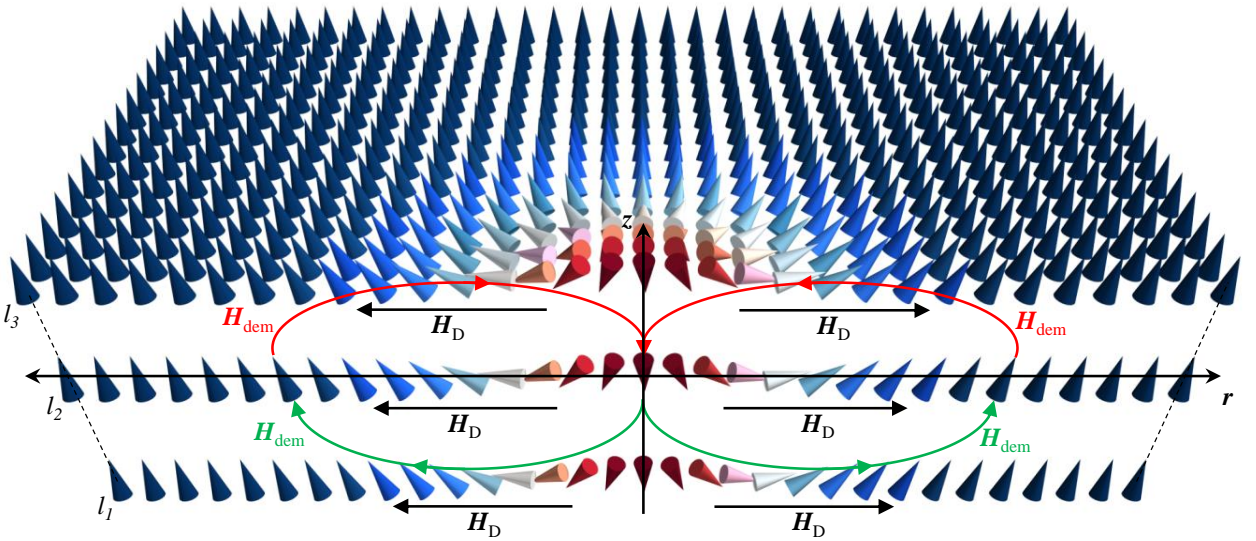
Figure 4.9: Schematic view of the dipolar and DM interactions in a skyrmion (cut view of the top layer and profile) hosted by a multilayer with $L = 3$. Black arrows represent the DM interaction field H_D. Other coloured arrows represent the demagnetizing field H_dem, in green when it stabilises the same chirality then the DM interaction (in layer l_1), in red when it opposes the chirality stabilised by the DM interaction (in layer l_3).

Figure 4.10: Skyrmion profiles obtained in layers l_1, l_2 and l_3 for (a) $D = 0\,\mathrm{mJ\,m^{-2}}$ and $\mu_0 H_\mathrm{ext} = 60\,\mathrm{mT}$, (b) $0.30\,\mathrm{mJ\,m^{-2}}$ and $60\,\mathrm{mT}$, (c) $0.90\,\mathrm{mJ\,m^{-2}}$ and $70\,\mathrm{mT}$, (d) $1.20\,\mathrm{mJ\,m^{-2}}$ and $80\,\mathrm{mT}$, (e) $1.35\,\mathrm{mJ\,m^{-2}}$ and $80\,\mathrm{mT}$, (f) $1.65\,\mathrm{mJ\,m^{-2}}$ and $100\,\mathrm{mT}$. Red, blue and black lines indicate the three magnetization components m_r, m_φ and m_z as a function of radius r. Skyrmion size is kept approximatively around $r_\mathrm{sk} = 30\text{–}40\,\mathrm{nm}$.

Such a competition occurring between the DM interaction and the dipolar interactions to impose the chirality of the skyrmion profiles in the different layers is summarised in Figs. 4.11a,b, which present respectively the size and the chirality of skyrmions hosted in l_1, l_2, l_3 for varying D and $\mu_0 H_\mathrm{ext}$. The layer-dependent size r_sk is determined from the m_z profiles, while the layer-dependent chirality $<\phi>$ is found as the polar direction of vector

$$\left[\int_{r=0}^{\infty} m_\mathrm{r} r dr, \int_{r=0}^{\infty} m_\varphi r dr\right] \tag{4.1}$$

formed by the integrated m_r and m_φ components. The evolution of equilibrium skyrmion size with both D and $\mu_0 H_\mathrm{ext}$ appears here, as well as the reversal of skyrmion chirality occurring
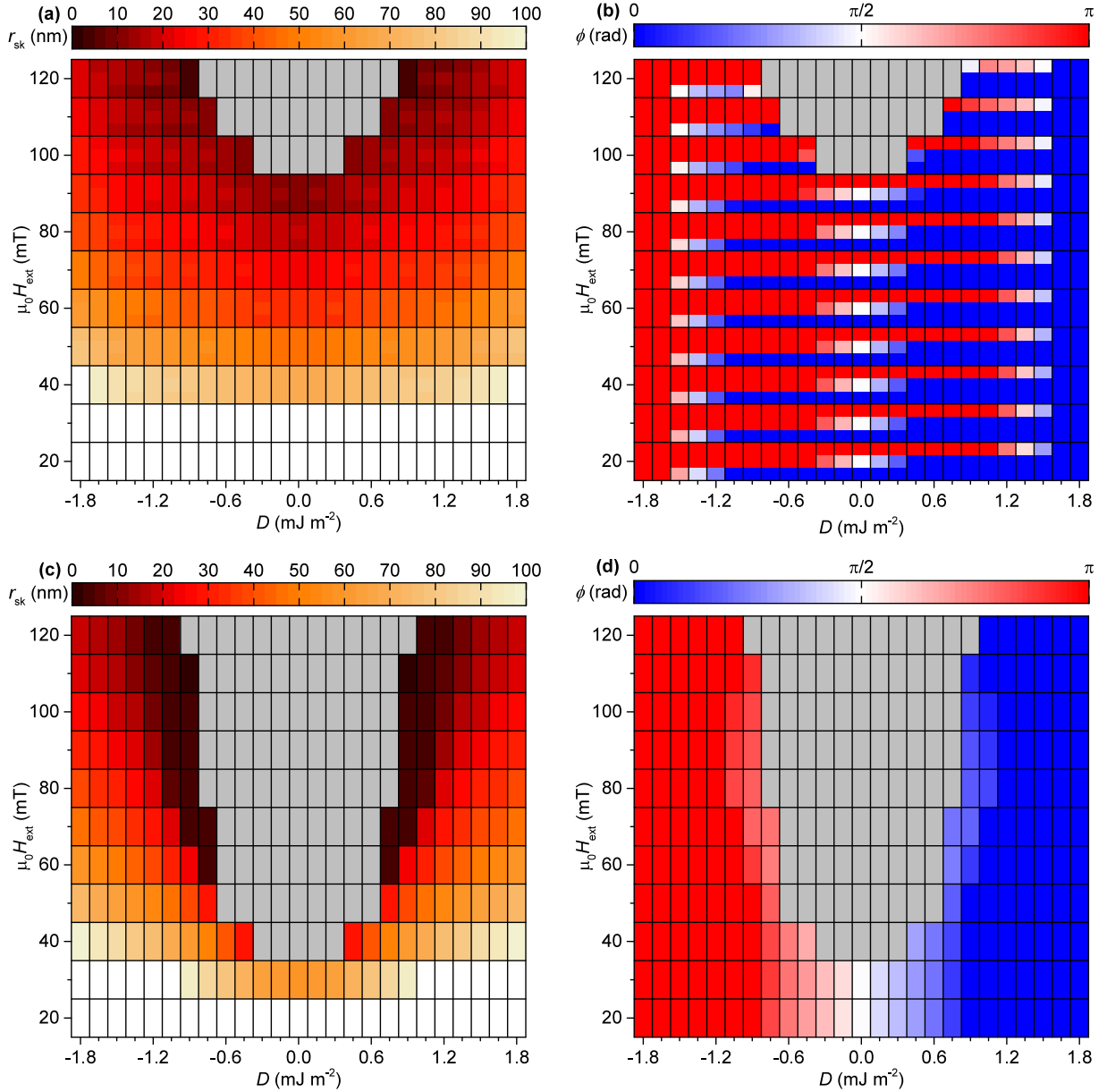
Figure 4.11: (a) Skyrmion radius r_{sk} and (b) skyrmion chirality $<\phi>$ as a function of D and $\mu_0 H_{ext}$ for $L = 3$ layers considered individually, and (c) Skyrmion radius r_{sk} and (d) skyrmion chirality $<\phi>$ as a function of D and $\mu_0 H_{ext}$ for $L = 3$ layers considered with a unique 1D profile. In the case of independent $L = 3$ layers, the three colours present in each cell indicate the values for l_1, l_2 and l_3, from bottom to top. Grey colour indicates parameters resulting in unstable skyrmion configurations that collapse.

around different values of D for the different layers, located at $D = -1.35\,\mathrm{mJ\,m^{-2}}$, $0\,\mathrm{mJ\,m^{-2}}$ and $1.35\,\mathrm{mJ\,m^{-2}}$ for l_1, l_2 and l_3, respectively.

In order to emphasise that a *layer-resolved* description of the profiles of multilayered skyrmions beyond previous analytical models is required, we now compare the results of our $\mathbf{m}(r, z)$ model to the results of a $\mathbf{m}(r)$ model in which a unique skyrmion profile is imposed in all layers, referred to here as a *1D model*, summarised in Figs. 4.11c,d. In each diagram, the grey colour indicates sets of parameters for which the skyrmion configuration is not stable and collapses down to zero radius. Comparing the two models, it appears that more sets of parameters lead to unstable configurations in the 1D case. This is due to an increased energy owing to the restrained degree of freedom for

the profile evolution. Moreover, the 1D model conveys results of size and chirality for $L = 3$ that resembles more to the results that should be obtained for $L = 1$. This is because it neglects the effects of interlayer dipolar interactions present in the $L = 3$ case. These considerations on the chirality of skyrmions in $L = 3$ multilayers show us that the vertical dimension of multilayers can dramatically modify the type of skyrmions that they host, resulting in complex structures that are neither Néel nor Bloch, and that are referred to here as **hybrid chiral skyrmions**.

4.5 Revealing hybrid chiralities with XRMS

In this thesis, an experimental clue of such hybrid chiralities has been looked after in order to confirm the predictions obtained by modelling. In the following, we study experimentally hybrid chiral structures in DWs. The explanations provided above are equally valid in the case of DWs, which were more convenient to study as they could be obtained without field inside demagnetized multilayers. An easily variable OOP field, required to stabilise skyrmion lattices, was indeed not available in the setup at the time of these experiments. The chirality of magnetic textures in metallic layers can be determined in a direct way, with the help of circular dichroism in X-Ray Resonant Magnetic Scattering (XRMS) [193], as has been established by a collaboration work with the team of the SEXTANTS beamline at the SOLEIL synchrotron [194]. In this experiment, an X-ray photon beam is set at the photon energy of a dichroic transition of the FM in order to interact with the magnetic configuration, at the Co L_3 edge (778.2 eV) in the present case. The beam reflects on the magnetic layer in resonant conditions, and is aligned with a CCD to image the diffraction pattern resulting from scattering on the magnetic texture [194]. A beamstop hides the specular reflection in order to be sensitive to the diffracted photons only and increase the sensitivity. The experiments presented here are performed with an incidence angle θ_X of about 18.5°, which corresponds to the first resonant Bragg peak of the multilayer structure. The diffraction image is recorded for both circular polarizations of the incident light, circular left (CL) and circular right (CR), as shown in Figs. 4.12a,b, respectively. These example diffractograms are obtained on a multilayer [Ir (1.0 nm)/Co (0.8 nm)/Pt (1.0 nm)]$_5$ after OOP demagnetization. A ring of variable intensity is observed, due to the diffraction on the labyrinthine magnetic stripe domains that are stabilised. The circularity of the ring indicates the planar isotropy of the multidomain state, whose periodicity λ appears here, in reciprocal space, as a ring of radius $2\pi/\lambda$. By summing both images, the polarization-independent image (CL)+(CR) is generated (Fig. 4.12c), whereas by subtraction, the dichroism image (CL)-(CR)/[(CL)+(CR)] is generated (Fig. 4.12d). In the present convention, dichroism is therefore positive when the measured intensity is larger with (CL) light. A schematic of the principle of the experiment is displayed in Fig. 4.12e. In order to analyse the dichroism of the diffraction pattern, an orthoradial projection in the (Q_x, Q_y) plane (where **Q** is the difference between incident wavevectors) is adapted, and defines the orthoradial profile with respect to angle ψ_X ranging 0–360°, as shown in Fig. 4.12f.

The interest of this technique lies in the fact that the analysis of these two (CL) and (CR) images (collected during 10 minutes only) directly provides information on both type and chirality of the magnetic configuration present in multilayers. Due to symmetry rules of magnetic scattering [194], dichroism is allowed along the Q_x (0°–180°) axis for helicoidal (or Bloch-like) windings and along the Q_y (90°–270°) axis for cycloidal (or Néel-like) windings. Moreover, the sign of the dichroism is directly related to the chirality, distinguishing between CCW and CW magnetic textures. Therefore, CW Néel, CW Bloch, CCW Néel and CCW Bloch magnetic textures cause a maximum of dichroism around 90°, 180°, 270° and 0°, respectively, as shown by the calculated profiles presented in Fig. 4.12a [194]. This allows to unambiguously assess the nature of the magnetic textures hosted by the multilayers, for example, it is CW Néel in the case presented in Fig. 4.12f, whose orthoradial profile is displayed in Fig. 4.12b. The deviation between predictions and experiments regarding the exact shapes of the orthoradial profile probably lies in the use of kinematic conditions for calculations of diffraction of the X-rays in the multilayer structure [194]. Nevertheless, the position of the
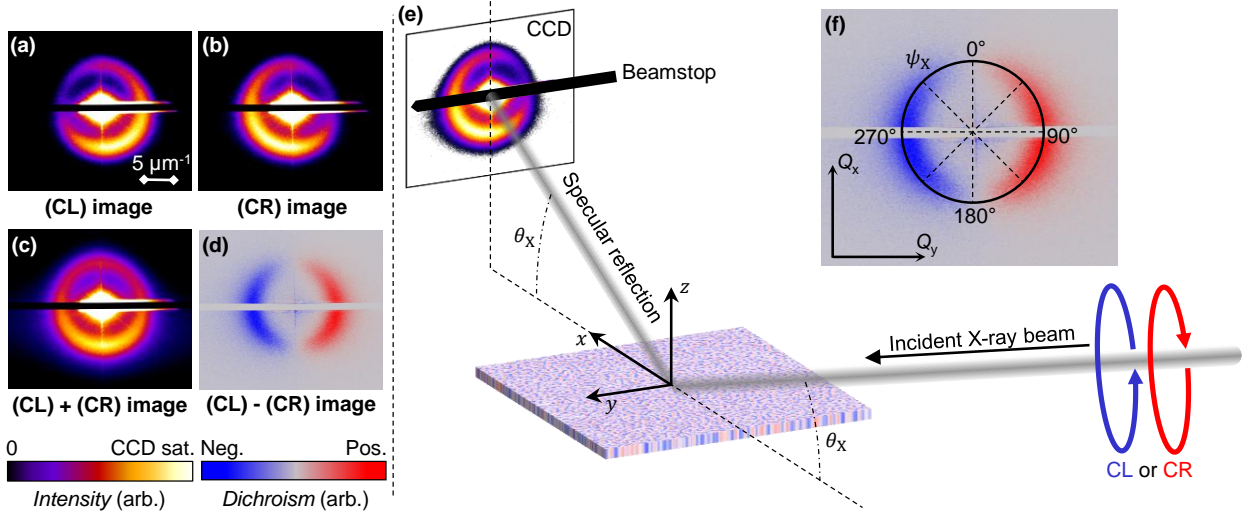
Figure 4.12: For a multilayer of composition $[\mathrm{Ir}(1.0\,\mathrm{nm})/\mathrm{Co}(0.8\,\mathrm{nm})/\mathrm{Pt}(1.0\,\mathrm{nm})]_5$, diffraction image obtained (a) for (CL) incident light and (b) for (CR) incident light, (c) sum image (CL)+(CR) and (d) normalised dichroism image (CL)-(CR)/[(CL)+(CR)]. (e) Experimental principle of the measurement of circular dichroism in XRMS, along with (f) definition of orthoradial angle in the analysis of dichroism patterns.

maximum remains sufficient to determine the type and chirality of the winding.

Circular dichroism in XRMS thus appears as a technique of choice for the experimental study of the effects of increasing the number of layers L on the magnetic configuration present in multilayers. A selection of results is reported here for six typical multilayers, labelled (ML 1)–(ML 6), whose properties are indicated in Table 4.2. The number of magnetic layers L is increased from 5 to 10 and 20, while the position of the Pt layer with respect to the Co layer is alternated, above for odd-numbered multilayers, below for even-numbered multilayers. For multilayers with $L = 20$, Ir
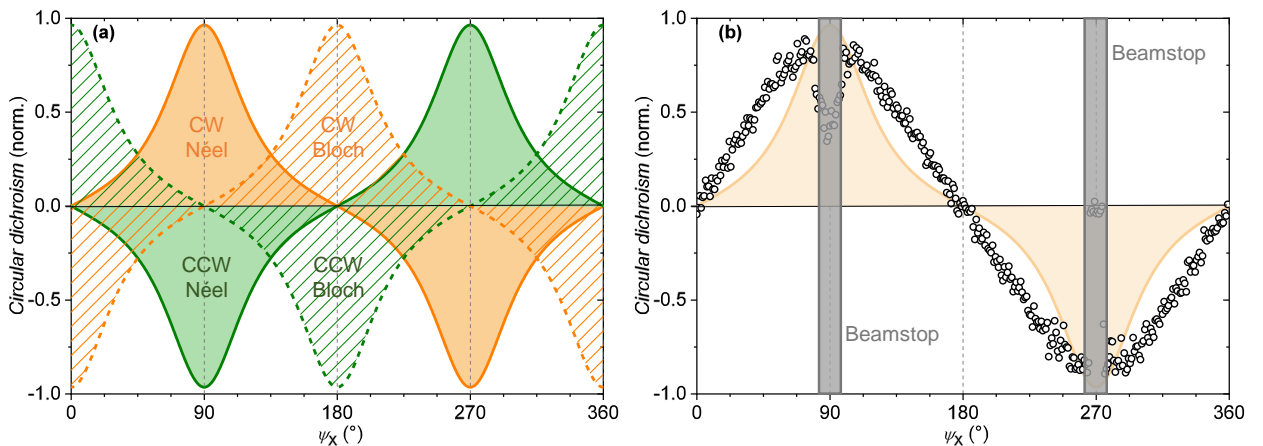
Figure 4.13: (a) Calculated (and normalised) circular dichroism orthoradial profiles for diffraction on CW Néel (solid orange line), CCW Néel (solid green line), CW Bloch (dashed orange line) and CCW Bloch (dashed green line) magnetic textures. (b) Experimental (and normalised) circular dichroism orthoradial profile for diffraction pattern of Fig. 4.12f on a multilayer of composition $[\mathrm{Ir}(1.0\,\mathrm{nm})/\mathrm{Co}(0.8\,\mathrm{nm})/\mathrm{Pt}(1.0\,\mathrm{nm})]_5$ (dots), superposed to the expected orthoradial profile corresponding to a CW Néel configuration (orange line). The position of the beamstop is indicated by the grey vertical bars.

Table 4.2: List of magnetic multilayers investigated with XRMS. The composition with thicknesses in nm starting from SiO_2 substrate side //, the saturation magnetization M_s, the effective uniaxial anisotropy field H_{eff}, the measured domains periodicity λ, and the estimated DW width δ obtained within a (δ, λ, ψ) model (see Appendix C) are given for each multilayer.

#	Multilayer stack	M_s (kA m^{-1})	H_{eff} (mT)	λ (nm)	$\delta_{\delta,\lambda,\psi}$ (nm)
(ML 1)	//Pt 10/[**Ir 1/Co 0.8/Pt 1**]$_5$/Pt 3	1229	640	150	4.13
(ML 2)	//Pt 11/[**Co 0.8/Ir 1/Pt 1**]$_5$/Pt 3	637	516	278	7.08
(ML 3)	//Ta 15/Co 0.8/[**Pt 1/Ir 1/Co 0.8**]$_{10}$/Pt 3	957	500	256	5.00
(ML 4)	//Pt 11/[**Co 0.8/Ir 1/Pt 1**]$_{10}$/Pt 3	637	516	244	6.03
(ML 5)	//Ta 10/[**Al$_2$O$_3$ 1/Co 0.8/Pt 1/**]$_{20}$/Pt 7	1245	228	131	4.33
(ML 6)	//Ta 10/Pt 7/[**Pt 1/Co 0.8/Al$_2$O$_3$ 1**]$_{20}$/Pt 3	1373	358	175	3.72

has been replaced by Al_2O_3 in order to avoid a reduction of the multilayer growth quality with increasing number of repetitions. The dichroism patterns recorded for samples (ML 1)–(ML 6) are displayed in Figs. 4.14. Note a difference between the diffractograms obtained from samples (ML 1)–(ML 4), which exhibit ring-diffraction patterns, and samples (ML 5)–(ML 6), which exhibit two localised spots. It illustrates the difference between diffraction patterns generated by labyrinthine stripe domains (obtained after OOP demagnetization) and by aligned magnetic stripes (obtained after IP demagnetization). However, their analysis remains identical for our purpose. As expected from the large DM interaction present in such multilayers, all dichroism patterns indicate a Néel ordering of the DWs. For the cases of 5 and 10 layers, the sign of the dichroism is found in accordance with the sign of D expected from the position of the Pt layers relative to the Co layers, CW for $D < 0$ in multilayers (ML 1) and (ML 3) [maximum of dichroism at $\psi_X = 90°$], CCW for $D > 0$ in multilayers (ML 2) and (ML 4) [maximum of dichroism at $\psi_X = 270°$]. However, for $L = 20$, a similar dichroism pattern, and hence the same effective chirality, is observed for both stacking orders in multilayers (ML 5) and (ML 6). This observation is in apparent contradiction with the sign of D, which shall not depend on L.

This apparent inconsistency is actually the consequence of the hybrid chiral structures that form in multilayers (ML 5) and (ML 6), but not in multilayers (ML 1)–(ML 4). A micromagnetic modelling with MuMax^3 of the DW profiles can be performed with the input of the magnetic parameters and domain periodicity λ determined from experiments, which are summarised in Table 4.2. For $L = 5$ and $L = 10$, the micromagnetic simulation converges to DWs with a unique chirality in accordance with the sign of the DM interaction, CW Néel for multilayers (ML 1), (ML 3) and CCW Néel for multilayers (ML 2), (ML 4). However, for $L = 20$, the simulations converge to DWs with hybrid chiralities. In order to get a better understanding of this phenomenon beyond the situation expected in multilayers (ML 5), (ML 6) with $|D| \approx 1.0 \, \text{mJ m}^{-2}$, the results of the simulation for varied values of $D = -1.0, 0.0, 1.0, 2.0$ and $2.5 \, \text{mJ m}^{-2}$ are compiled in the different lines of Fig. 4.15. The left column displays cross-sectional views of the DW magnetization profiles, the central column displays the polar angle $\theta(x)$ profiles in layers l_1–l_{20} and the right column displays the azimuthal in-plane angle $\phi(x)$ profiles in layers l_1–l_{20}. Parameters are corresponding to multilayer (ML 6), with $A = 10 \, \text{pJ m}^{-1}$, $M_s = 1.373 \, \text{MA m}^{-1}$, $K_u = 1.43 \, \text{MA m}^{-1}$, in a multilayer geometry given by $t_{FM} = 0.8 \, \text{nm}$ and $p = 2.8 \, \text{nm}$, and cell size of 0.25 nm, 8 nm and 0.2 nm along the x, y and z directions. From these curves, it appears that for a large range of DM interaction values, hybrid chiral structures are indeed formed with strong dependence of the magnetization profile on the vertical position. The individual $\theta(x)$ profiles in the different layers differ significantly from the average DW profile, while the component of **m** in the plane of the layers, described by the $\phi(x)$ profiles, reverses depending on the vertical position. Only for very large values[4] of $|D| \geq$

---

[4]This threshold value only concerns the present set of magnetic parameters; it varies with L, M_s, K_u, *etc.*
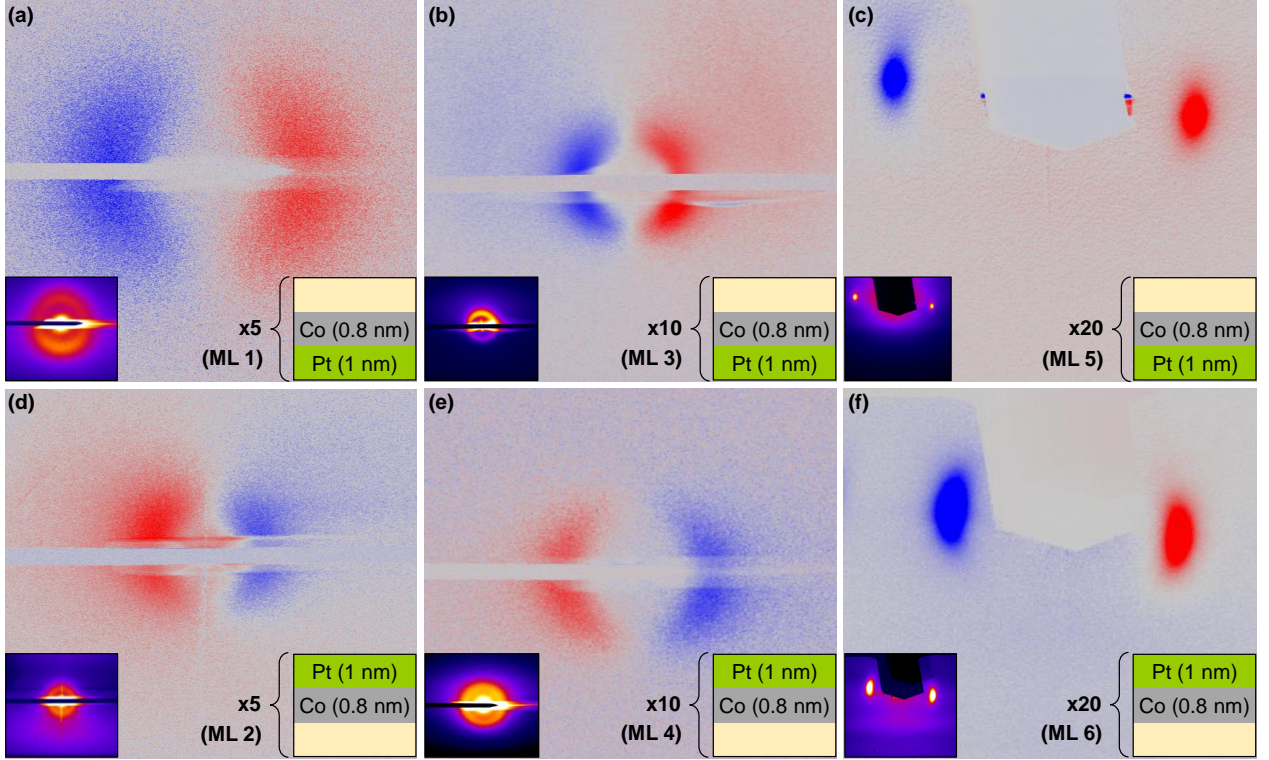
Figure 4.14: (a)–(f) Normalised dichroism patterns recorded for samples (ML 1)–(ML 6), see Table 4.2. In each panel, left inset is the corresponding sum (CL)+(CR) image and right inset is a schematic of the multilayer.

$2.5\,\mathrm{mJ\,m^{-2}}$, which are experimentally excluded for a thickness of Co of $0.8\,\mathrm{nm}$, a uniform chirality can be imposed in all layers. For values of D such as the ones found in multilayers (ML 5) and (ML 6), the magnetic configuration is expected to correspond to Figs. 4.15a,c, respectively. Such hybrid chirality explains the results of the above XRMS experiment: due to the strong interaction between X-rays and the Co at its L_3 edge, the penetration depth of the light is limited to around 4 or 5 magnetic layers from the top. Consequently, the circular dichroism in XRMS performed in the present conditions is mostly sensitive to the top part of the DWs. The presence of hybrid chiral DWs is therefore consistent with the observation that both stacking orders of multilayers (ML 5) and (ML 6) result in an identical CW Néel chirality in XRMS, which is imposed —in surface only— by the dipolar interactions, irrespective of the DM interaction sign. This observation of a unique CW chirality in the top layers of both [Pt/Co/Al$_2$O$_3$] and [Al$_2$O$_3$/Co/Pt] multilayer combinations therefore constitutes an **experimental demonstration** of the formation of hybrid chiral structures in multilayers.

In the discussion and simulations presented above, no electronic interlayer coupling between Co layers is considered, due to the presence of oxide spacers for the multilayers with 20 repeats. However, the situation may be different for the case of metallic spacers, in which case the presence of electronic interlayer coupling affects the vertical structure of the DWs. It contributes to form a larger Bloch part inside the middle layers, which is under present investigation combining micromagnetic simulations using measured values of the coupling and Lorentz transmission electron microscopy observation in a collaboration with the Glasgow team. Note that extensive micromagnetic modelling as demonstrated above also allows to estimate the value of D from the observed domain periodicity, by taking into account the internal reorientation of magnetic chirality caused by dipolar interactions, as detailed in Appendix C. Also, note that as an alternative to the description of hybrid chiral skyrmions within our numerical model, a description based on layer-dependent ansatz profile functions has been simultaneously developed by Lemesh *et al.* [195].
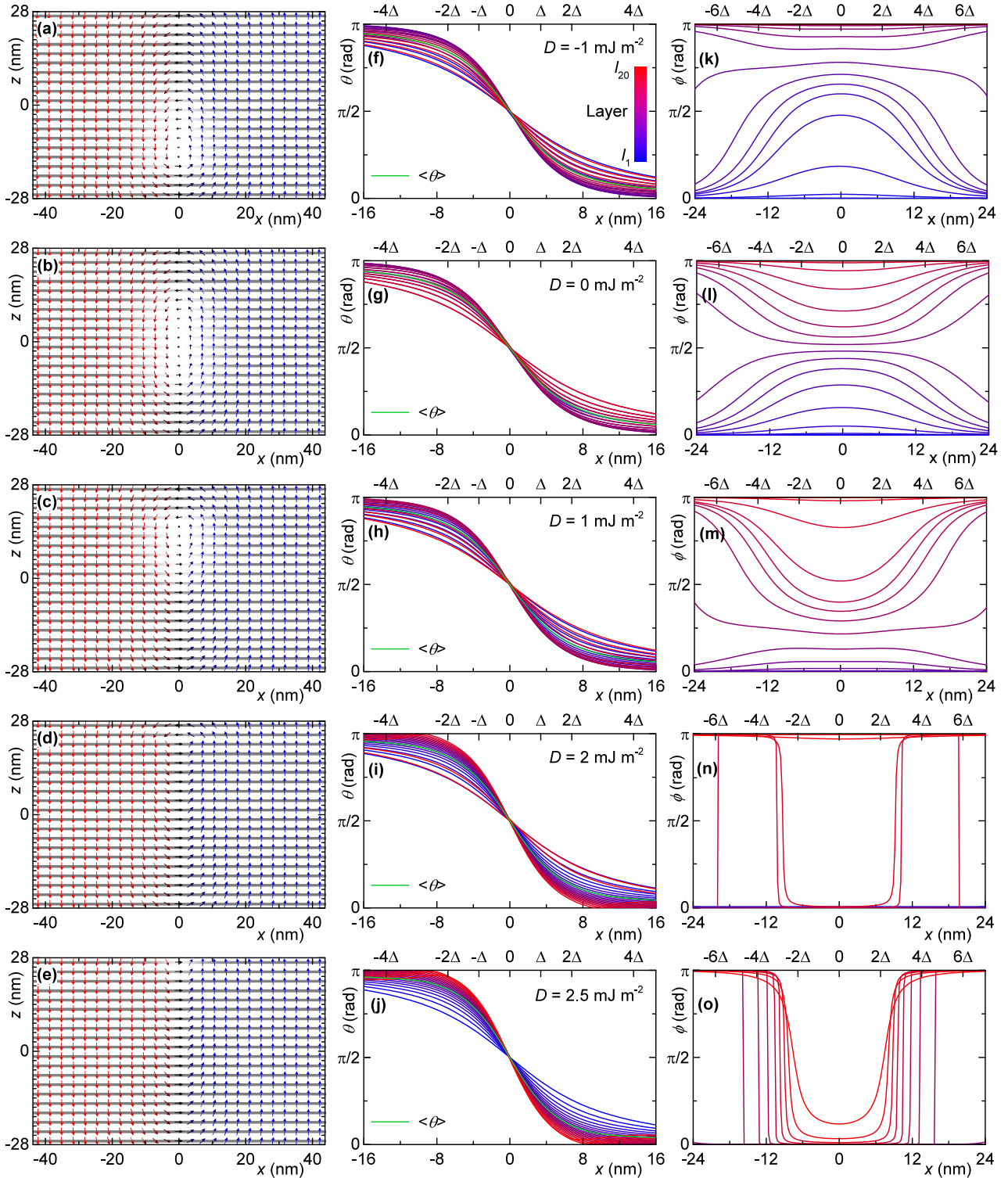
Figure 4.15: (a–e) Cross-section of a half domain period for periodic DW pairs in a multilayer with $L = 20$, $t_{Co} = 0.8$ nm, $p = 2.8$ nm. The DM interaction is varied between $D = -1.0$, 0.0, 1.0, 2.0 and 2.5 mJ m^{-2} (top to bottom), where the grey-tone areas correspond to the Co layers. The direction of the magnetization is indicated by the arrows, its vertical component m_z by the colour of the arrows from red (-1) to blue (+1), its transverse component m_y by the colour of the grid from black (-1) to white (+1). (f–j) Polar angle $\theta(x)$ and (k–o) azimuthal angle $\phi(x)$ in each layer across the DW for $D = -1.0$–2.5 mJ m^{-2}. See Fig. 2b for a definition of θ and ϕ, here used for DWs. The blue to red colour of the curves correspond to layers l_1 to l_{20}. The green curve in each panel of the central column indicates $<\theta>(x)$, the averaged DW profile.
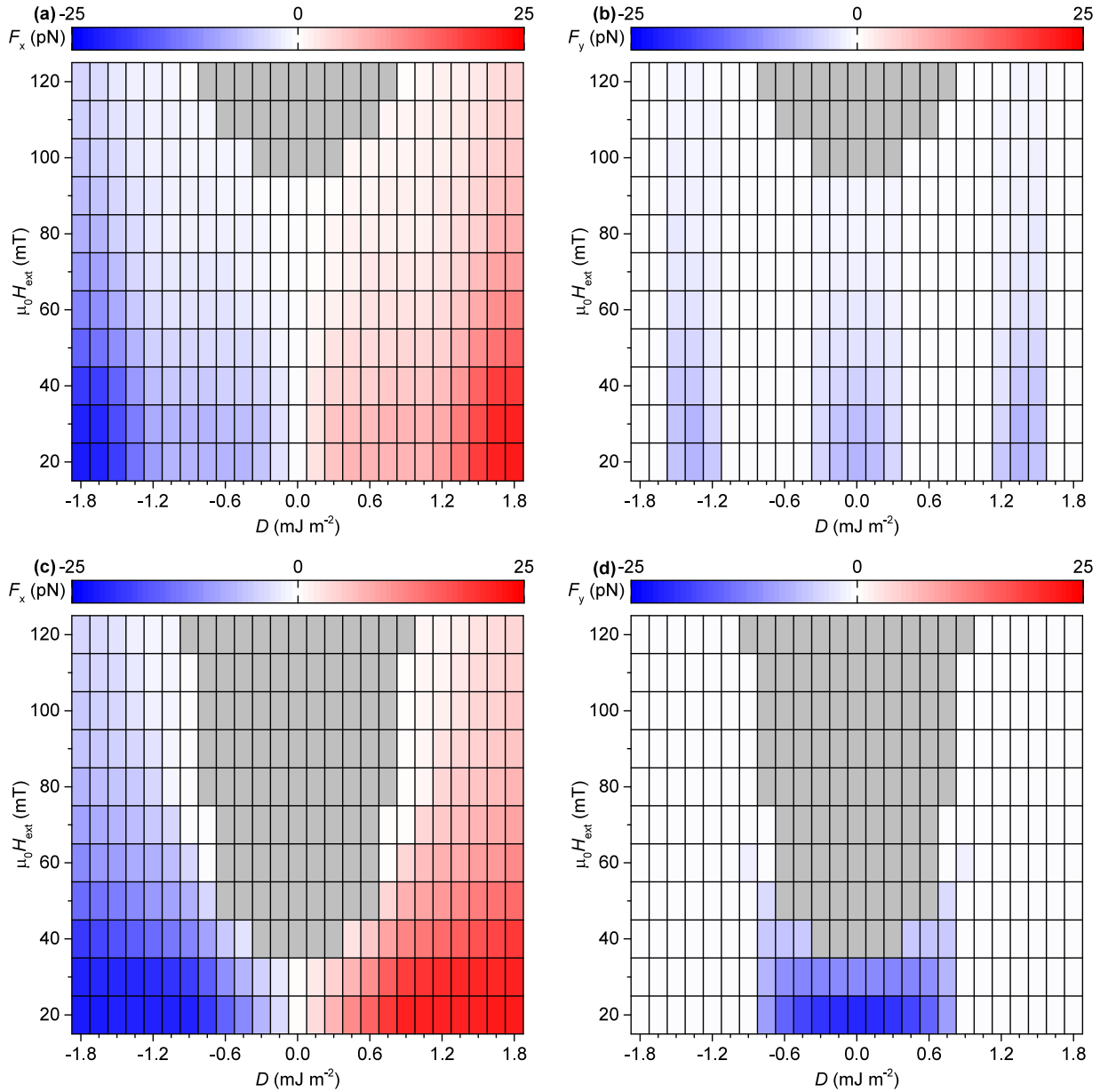
Figure 4.16: (a) Longitudinal $\sum_i F_{\mathrm{x,i}}$ and (b) transverse $\sum_i F_{\mathrm{y,i}}$ current-induced total force as a function of D and $\mu_0 H_{\mathrm{ext}}$ for $L = 3$ layers in the $\mathbf{m}(r, z)$ model, (c) Longitudinal LF_{x} and (d) transverse LF_{y} current-induced total force as a function of D and $\mu_0 H_{\mathrm{ext}}$ for $L = 3$ layers considered with a unique 1D profile. In both cases of independent $L = 3$ layers or 1D model, one colour is present in each cell and indicates the total forces acting on the skyrmion in l_1, l_2 and l_3. Grey colour indicates parameters resulting in unstable skyrmion configurations that collapse.

4.6 Optimisation of spin-injection in multilayers - bis

As it was introduced in Chapter 3, the total driving forces for current-induced motion of magnetic skyrmions rely entirely on their chirality. Therefore, it can be anticipated that the formation of hybrid chiral skyrmions shall profoundly affect their motion. A good illustration of this influence can be drawn from the further analysis, in the framework of the Thiele modelling, of the skyrmion profiles obtained in §4.4 for $L = 3$. We consider, for example, a multilayer geometry in which a Pt layer is located below each FM and thus injects the same amount and same polarisation of spin current in each FM, with $\theta_{\mathrm{eff}} J = 2 \times 10^{10}\,\mathrm{A\,m^{-2}}$ [case (IV) in Fig. 4.7].
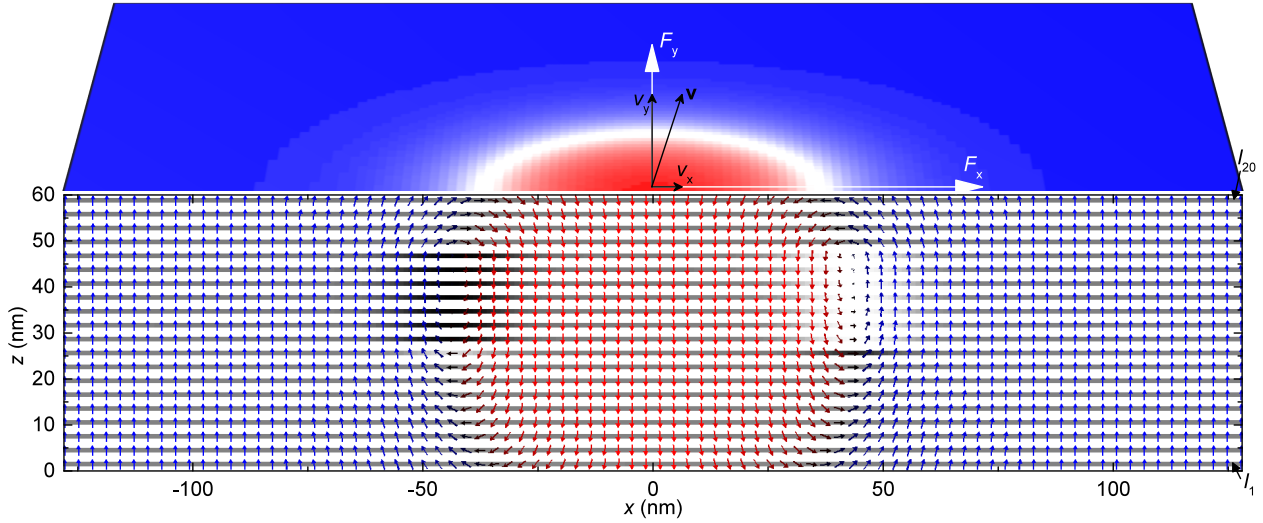
Figure 4.17: Cross-sectional view of layers l_1–l_{20} in a hybrid chiral skyrmion for $L = 20$ and $D = 0.8\,\mathrm{mJ\,m^{-2}}$, stabilised for $\mu_0 H_{\mathrm{ext}} = 200\,\mathrm{mT}$. The grey-tone areas correspond to the Co layers. The direction of the magnetization is indicated by the arrows, its vertical component m_z by the colour of the arrows from red (-1) to blue (+1), its transverse component m_y by the colour of the grid from black (-1) to white (+1). The top perspective view shows m_z in the top layer l_{20}.

The longitudinal (F_x) and transverse (F_y) components of the total driving force created by the SOTs can be directly determined by summing forces in each layer, computed with (3.6) from the (m_r, m_φ, m_z) profiles. Similar to Fig. 4.11, the calculated total F_x and F_y are displayed as a function of D and $\mu_0 H_{\mathrm{ext}}$ in Fig. 4.16. Again, a comparison is shown between a layer-resolved model (Figs. 4.16a,b) and a simplified 1D model excluding vertical variations of **m** (Figs. 4.16c,d). Let us focus our analysis on the crucial F_x term (Figs. 4.16a,c), while F_y (Figs. 4.16b,d) is not a reliable force as its sign changes with the chirality of the Bloch profile, which is not fixed[5]. Still, F_y gives indications about the presence of a Bloch component in the profile. For $|D| \geq 1.65\ \mathrm{mJ\,m^{-2}}$, skyrmions present a uniform chirality and identical forces are provided by the two models. However for $|D| < 1.65$ mJ m^{-2}, a significantly reduced value of F_x is found by the layer-resolved model as compared to the 1D model, because of the formation of hybrid chiral skyrmions. Due to opposite chiralities that can form, $e.g.$, in l_1 and l_3, the driving forces in these two layers are of opposite sign and cancel each other. It results that in hybrid chiral skyrmions, only the central layer contributes to the total driving force, which is thus significantly reduced. In the presence of hybrid chiral skyrmions, it thus appears important to **match the spin injection geometry** with the details of the chiral magnetic textures, in order to obtain their efficient motion.

To further illustrate the link between hybrid chirality and motion efficiency, we can investigate the skyrmion motion in multilayers with $L = 20$, similar to multilayer (ML 6) of Table 4.2, which can be expected to host hybrid chiral skyrmions as D cannot be large enough to impose a unique chirality. A typical example of hybrid skyrmion configuration, obtained for $D = 0.8\,\mathrm{mJ\,m^{-2}}$, is shown in Fig. 4.17. The dynamic micromagnetic simulations[6] are performed with MuMax[3]. Three types of spin injection geometries have been considered among the ones introduced in Fig. 4.7: (i) a geometry for which spins of opposite polarizations are injected into bottom (l_1) and top (l_{20}) FM layers, case (II), referred to as "Opposite" injection; (ii) a geometry for which spins of identical polarization are injected into bottom (l_1) and top (l_{20}) FM layers, case (III), referred to

---

[5]A random ensemble of skyrmions will have half skyrmions with CCW Bloch profiles and half skyrmions with CW Bloch profiles.

[6]The geometry is changed to [Pt (1.0 nm)/Co (1.0 nm)/Al$_2$O$_3$ (1.0 nm)]$_{20}$ instead of Co(0.8 nm) for accelerating the computations.
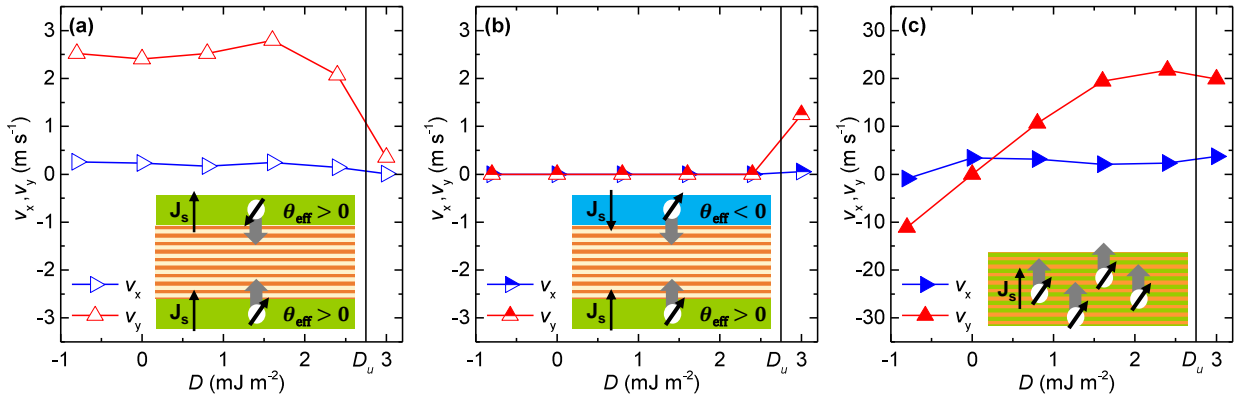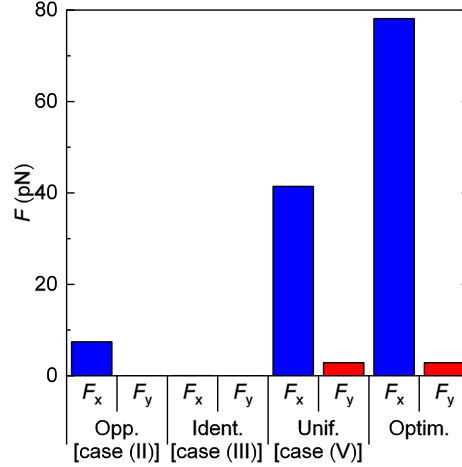
Figure 4.18: Longitudinal (v_x) and transverse (v_y) velocities as a function of D for (a) "Opposite" [case (II)], (b) "Identical" [case (III)] and (c) "Uniform" [case (V)] spin-injection configurations. In each panel the schematic in inset represents the spin injection geometry. The vertical line at $D = D_\text{u}$ separates hybrid chiral skyrmions for $|D| < D_\text{u}$ and skyrmion with uniform chirality for $|D| > D_\text{u}$. For $D < D_\text{u}$, the field is set at $\mu_0 H_\text{ext} = 200\,\text{mT}$, while for $D > D_\text{u}$, the field is set at $\mu_0 H_\text{ext} = 300\,\text{mT}$, to prevent its instability against transition to stripe domain states.

as "Identical" injection; and (iii) a geometry for which an equivalent spin current is injected into each layer, cases (IV) and (V), referred to as "Uniform" injection. The evolution of the resulting expected velocities as a function of D is displayed in Figs. 4.18a–c for these three geometries, considering an isolated skyrmion inside a simulation space with periodic boundary conditions. The external field is varied between $\mu_0 H_\text{ext} = 200\,\text{mT}$ and $\mu_0 H_\text{ext} = 300\,\text{mT}$ when D is increased, in order to retain confined skyrmion configurations[7]. Damping is set as $\alpha = 0.1$ and the spin current as $\theta_\text{eff} J = 2 \times 10^{10}\,\text{A m}^{-2}$.

As already explained above, the skyrmion chiralities in all layers evolve with the value of D. As the DM interaction progressively overcomes the dipolar interactions, less and less layers adopt a reversed chirality with respect to the one favoured by the DM interaction. The profile then evolves towards adopting a uniform chirality above a threshold DM interaction value, which is here referred to as D_u. With the present parameters, $D_\text{u} = 2.8\,\text{mJ m}^{-2}$, beyond any value that has been achieved experimentally so far. The resulting velocities reflect this evolution of chirality with D. In the "Opposite" geometry (Fig. 4.18a), the velocity is found nearly constant for hybrid chiral skyrmions ($|D| < D_\text{u}$), before it falls close to zero for a uniform chirality ($|D| > D_\text{u}$). The reason for this behaviour is that in a hybrid chiral configuration, l_1 and l_{20} show opposite chiralities. Combined with opposite spin injections, the driving forces add up. On the contrary, for a uniform chirality, the opposite spin injections in l_1 and l_{20} generate cancelling forces. Conversely, in the "Identical" geometry, the opposite situation is found, resulting in zero velocity up to D_u, which then rises for $|D| > D_\text{u}$, again due to the matching between local chiralities and spin injection. In the "Uniform" geometry, the transverse velocity is found to be roughly proportional to D, before it saturates around D_u. This is because the value of D controls the overall chirality of the skyrmion, that is, the balance between layers with CCW and CW chiralities, and thus the extent to which the total force resulting from all profiles in the 20 layers is compensated or not. The most efficient motion in this geometry is achieved for a uniform chirality, when $|D| > D_\text{u}$. Note that a factor of ten appears between the maximal velocities obtained in the "Uniform" geometry and in the two other geometries, because the injection occurs there in all 20 layers instead of being restrained to two external layers only. Note that velocity is mainly transverse here because of the skyrmion Hall effect. With $\mathbf{G}$ along $+\hat{\mathbf{z}}$ in the present example, the mainly longitudinal force F_x along $+\hat{\mathbf{x}}$ is converted into a mainly transverse v_y velocity along $+\hat{\mathbf{y}}$.

---

[7]In turn, this affects moderately the values obtained for the velocity, due to slightly different skyrmion sizes.

Figure 4.19: Longitudinal (F_{x}) and transverse (F_{y}) total forces acting on a hybrid chiral skyrmion hosted in a multilayer with $L = 20$ and $D = 0.8\,\mathrm{mJ\,m^{-2}}$, considering different spin injection geometries: "Opposite" [case (II)], "Identical" [case (III)], "Uniform" [case (V)] and "Optimised".

These results are consistent with the velocities that can be calculated within the model of Chapter 2 combined with the Thiele approach. For a skyrmion stabilised in $N = 20$ layers, for $D = 0.8\,\mathrm{mJ\,m^{-2}}$, $\mu_0 H_{\mathrm{ext}} = 200\,\mathrm{mT}$, $M_{\mathrm{s}} = 1.3\,\mathrm{MA\,m^{-1}}$, $t_{\mathrm{FM}} = 1\,\mathrm{nm}$, $p = 3\,\mathrm{nm}$, $\theta_{\mathrm{eff}} J = 2 \times 10^{10}\,\mathrm{A\,m^{-2}}$, a hybrid profile similar to the one shown in Fig. 4.17 is obtained. The total force acting on the skyrmion, summed over the 20 layers, is calculated according to (3.5) and (3.6) in different spin injection geometries. Another geometry is analysed in addition to the geometries already introduced above, referred to here as "Optimised", in which a HM layer is present under each FM, for each of which the sign of θ_{eff} is chosen to match the local chirality of the FM layer. This corresponds to an ideal situation in the presence of hybrid chiral skyrmions, for which all layers contribute to the total force, by matching the chirality and the torque in each layer. The absolute values of both force components in each geometry are summarised in Fig. 4.19. As in Fig. 4.18a,b for $D < D_{\mathrm{u}}$, while the forces from top and bottom layers cancel each other for the geometry "Identical" due to the hybrid chirality, they add up in the geometry "Opposite". Larger velocities are obtained in geometries "Uniform" and "Optimised" mainly because the SOTs are acting in all 20 layers. The largest velocity is obtained when the sign of the injected spins matches the local chirality in all layers as in the "Optimised" geometry, while it is reduced by nearly half in the "Uniform" injection case, because the torques in the 4 top layers (l_{17}–l_{20}) with Néel CW chirality compensate the torques acting in 4 of the Néel CCW chirality layers. These results confirm the mechanisms appearing in the previous micromagnetic simulations of skyrmion dynamics.

4.7 How many repetitions in a multilayer?

Among the geometries described above, uniform injection allows to simply rely on identical repetitions of a unique trilayer base unit, whose engineering appears much simpler than using different HM layers. In this case, ensuring a uniform chirality for the skyrmions is desirable in order to optimise the efficiency of the motion, as θ_{eff} is identical in all layers. It appears now that in the usual situation of uniform injection, increasing L is not always beneficial to the skyrmion mobility and that a limit needs to be observed. In the following, the model established in Chapter 2 is utilised to find the dependences on M_{s} and L of the threshold DM interaction value D_{u} that ensures a uniform chirality.

With this aim in mind, the DM interaction can be varied in the model in order to find the minimum value of D that results in a fully Néel skyrmion profile in all layers, for each number of repetitions and set of magnetic parameters. To allow a quantitative comparison between similar
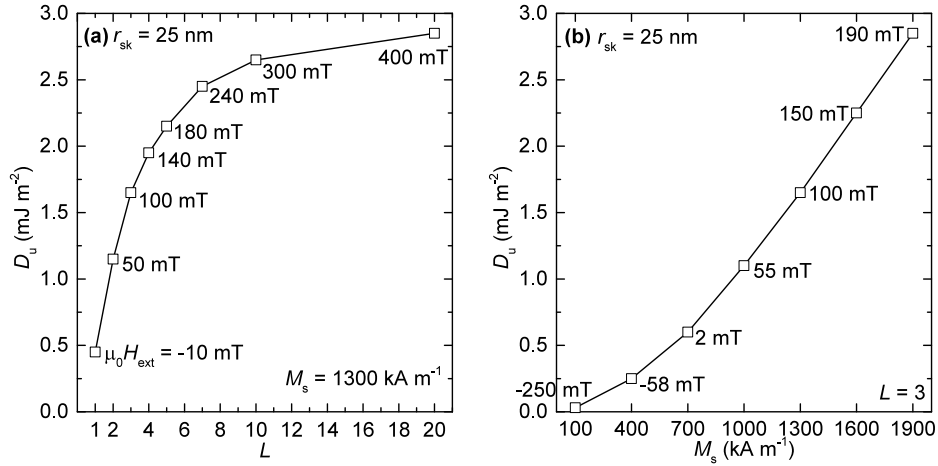
Figure 4.20: Threshold DMI value D_u imposing uniform skyrmion chirality (a) as a function of L for a fixed magnetization $M_s = 1.3 \, \text{MA} \, \text{m}^{-1}$, and (b) as a function of M_s for fixed number of layers $L = 3$. The external field value $\mu_0 H_{\text{ext}}$ is varied in each simulation (as displayed next to each point of the curves) in order to allow comparison between skyrmions of constant size $r_{\text{sk}} = 25 \, \text{nm}$.

skyrmions, $\mu_0 H_{\text{ext}}$ is varied in concert with D in order to keep r_{sk} as close as possible from a fixed value, for example chosen here as 25 nm. The values of D_u are displayed in Figs. 4.20a,b, for $L = 1$–20 at a fixed $M_s = 1.3 \, \text{MA} \, \text{m}^{-1}$, and for $M_s = 0.1$–$1.9 \, \text{MA} \, \text{m}^{-1}$ at a fixed $L = 3$, respectively. In further details, when varying M_s, K_u is also rescaled by the same factor in order to keep a constant uniaxial anisotropy field (that is, K_{eff} remains proportional to M_s), which is necessary to obtain realistically stable skyrmion solutions.

Consistent with intuition, it appears that D_u increases with both M_s and L, albeit each in a different way. As the dipolar field created in a given layer decreases rapidly with distance, the value of D_u tends to saturate when L becomes large enough for the skyrmion to get a narrow cylinder shape. In this case, the multilayer can be seen as a diluted medium with all parameters rescaled by t_{FM}/p, and then D_u is the DM interaction required to compensate the magnetic charges in a semi-infinite geometry. In contrast, as the magnitude of the dipolar field is proportional to M_s, D_u does not saturate when M_s reaches large values. These two graphs **provide guidelines for stabilising skyrmions with uniform chirality in multilayers**.

In experiments, Pt-based multilayers reach a DM interaction magnitude limited to 1.0–2.0 mJ m^{-2} at most. The limit L to retain uniform chirality thus appears very low, $L = 2$–4 for usual values of M_s and $t_{\text{FM}} = 1.4 \, \text{nm}$. Because dipolar interactions are weaker with thinner t_{FM}, for $t_{\text{FM}} \approx 1.0 \, \text{nm}$ a uniform chirality can be obtained for larger values of L, but still, the limit remains below the usual choice of $L = 10$–20 layers [7, 46–49, 179, 196] that has often been made so far. A uniform chirality can be kept when L reaches 10 or more, only for $t_{\text{FM}} \approx 0.8 \, \text{nm}$ or lower, see also experiments in §4.5. Unless M_s is significantly reduced, hybrid chirality is expected to be present in many usual experimental situations, which may then render very challenging the optimisation of the spin-injection scheme to obtain efficient skyrmion motion.

4.8 Achieving faster current-induced motion, now in experiments

In parallel of the different studies about pinning and mobility of skyrmions covered above, different series of multilayers have been deposited and patterned into tracks in order to study current-induced motion in real systems. For conciseness, all experiments are not presented here, but the more illustrative ones are summarised in Table 4.3, which notably reports the maximum velocity achieved in each multilayer, together with the corresponding current densities.

Due to the thin Pt intermediate layers that are not expected to contribute significantly to the

Table 4.3: List of magnetic multilayers investigated in current-induced motion experiments. The composition with thicknesses in nm starting from SiO_2 substrate side on the left, the type of injection geometry according to Fig. 4.7, the measured velocity v, injected current density J, and the possible causes for limitations of velocity are given for each multilayer.

Multilayer stack	Type	v $(m\,s^{-1})$	J $(TA\,m^{-2})$	Observed limitations
Ta 15/Co 0.8/[**Pt 1/Ir 1/Co 0.8**]$_{10}$/Pt 3	(III)	0.5	0.29	strong pinning, skyrmion density
Ta 15/Co 1.0/[**Pt 1/Ir 1/Co 1.0**]$_{10}$/Pt 3	(III)	1	0.33	strong pinning, skyrmion stability
Ta 15/Co 0.8/[**Pt 3/Ir 1/Co 0.8**]$_{5}$/Pt 3	(IV)	2	0.21	skyrmion stability
Ta 10/Pt 8/[**Pt 0.8/Co 0.8/Ta 0.8**]$_{10}$/Ta 10	(III)	–	–	no OOP anisotropy
Ta 20/[**Pt0.8/Co 0.8/Ta 0.8**]$_{10}$/Pt 11	(III)	–	–	no OOP anisotropy
Ta 10/Pt 8/[**Co$_{10}$Fe$_{70}$B$_{20}$ 0.8/Al$_2$O$_3$ 1/Pt 2.4**]$_{20}$	(IV)	6	0.15	skyrmion density (lattice)
Ta 10/Pt 8/[**Co 1.4/Ru 1.4/Pt 0.6**]$_{3}$/Pt 3	(II)	37	0.77	nucleation of stripes (low anisotropy)
Ta 10/[**Pt 8/Co 1.4/Ru 1.4**]$_{3}$/Pt 3	(IV)	38	0.80	skyrmion stability

torques, the multilayer structures investigated in §4.1 correspond to "Identical" injection, or case (III) in Fig. 4.7 deposited in the reverse order, leaving room for improvement. More particularly, according to the experimentally measured parameters, it appears that the multilayer with $t_{Co} = 0.8\,$nm in §4.1 adopts a uniform skyrmion chirality, but probably not the multilayer with $t_{Co} = 1.0\,$nm. The spin-current-injection may thus result in a reduced mobility for $t_{Co} = 1.0\,$nm, which probably explains, at least partially, why a less efficient motion is observed in this multilayer with hybrid chirality.

In principle, Pt/Co/Ta multilayers should allow to reach a better efficiency, due to the optimised spin injection geometry [case (V) in Fig. 4.7]. However, it was not possible to obtain perpendicular magnetization inside this type of multilayers under the present conditions of sputtering deposition, which should nevertheless become possible [46, 190] after more optimisation efforts of the deposition parameters, or with the use of dusting layers. Note that increasing t_{Co} may also mitigate the migration of Ta in the Co layer and thus maybe let it recover perpendicular magnetization.

An interesting result is the lower J_0 found in Pt/Co$_{10}$Fe$_{70}$B$_{20}$/Al$_2$O$_3$ based multilayers, which are expected to adopt an amorphous structure. By increasing L and using oxide spacers, decorrelated inhomogeneities may result in reduced pinning. However, the large L and the low anisotropy resulted in a very large density of densely packed skyrmions, rendering the observation of motion quite difficult. Such structures nevertheless offer good prospects for low-current density motion [46, 47].

A reliable motion has been observed in a multilayer with a limited number of repetitions $L = 3$, in which the material of the NM spacer has been changed from Ir to Ru, as the latter was found to result in more homogeneous stripe domains in MFM images of demagnetized multilayer, maybe indicating reduced material inhomogeneities and pinning. In contrast to previous multilayers, which enabled motion in the creep regime only, the present multilayer exhibits a beginning of transition towards the regime of flow motion. The results of these experiments are now analysed in more details. The multilayer composition is //Ta 10/Pt 8/[Co 1.4/Ru 1.4/Pt 0.6]$_3$/Pt 3, with all thicknesses given in nm. Due to the significantly thicker FM layers allowed by the deposition of Ru instead of Ir, the skyrmion states are found stable, even for $L = 3$, under higher current densities (larger J_n). In the

following motion experiment, the lithographed track width is $2.25\,\mu m$.

In Figs. 4.21a–h, successive MFM images of skyrmions stabilised under a field $\mu_0 H_{\text{ext}} = 20\,\text{mT}$ are recorded, separated each time by the injection of a single pulse of length $12\,\text{ns}$ and $J = 7.7 \times 10^{11}\,\text{A m}^{-2}$. As already demonstrated in Chapter 3, this procedure allows to follow the motion of skyrmions under the effect of current pulses. Even if skyrmions are found sometimes pinned, once they escape the pinning centres they are able to undergo a regular motion induced by the successive pulses. For some skyrmions that are unambiguously distinguishable from their neighbours, their positions in Figs. 4.21a–h are highlighted by different colours (blue, red, green, orange) and trac-ked by the coloured dashed lines. This demonstrates an efficient motion of some skyrmions in the direction of the charge current. Focusing on the red skyrmion, which is depinned after the frame of Fig. 4.21c, it travels $2200\,\text{nm}$ until the frame of Fig. 4.21h, which allows to deduce a skyrmion velocity of $37\,\text{m s}^{-1}$. This large velocity, combined with the observation of a regular motion, are indications of reaching close to the flow regime, $i.e.$, that J is slightly above J_0. Note however that once again J used here is not far from the nucleation current density J_{n}, and some stripe and skyrmion nucleation events occur in the centre of the track.

Another argument supporting a beginning of transition towards flow motion in the present experiment is given by the observation of the skyrmion Hall effect in this multilayer. The positions of all skyrmions are tracked for 30 successive pulses of length $10\,\text{ns}$ and $J = -8.2 \times 10^{11}\,\text{A m}^{-2}$. Here, skyrmions are stabilised under $\mu_0 H_{\text{ext}} = 23\,\text{mT}$, in order to limit the nucleation of stripe domains under current. The traces of the tracked skyrmion positions from the initial frame (black colour) to the frame recorded after the injection of 30 pulses (red colour) are shown in Figs. 4.22. Consistent with the SOT origin of the motion, the longitudinal direction of motion again follows J (the direction of the current is reversed here as compared to Fig. 4.21). Many skyrmion trajectories roughly align parallel together but not along the current direction. A transverse motion appears, as highlighted by the blue segments drawn along the trajectories of the most mobile skyrmions, which is characterised by a skyrmion Hall angle of about $\Theta_{\text{sk}} \approx 15\text{–}25°$. Note that the two longest segments on the right, and only them, are not strictly skyrmions but correspond in the MFM images to domains alternating between skyrmion and stripe configurations, elongating in the direction of motion under the skyrmion Hall effect. All others points track skyrmions that are stable in all images. This value of the skyrmion Hall angle remains nevertheless much lower than its expected value for an ideally uniform medium (around $60°$ for $r_{\text{sk}} = 40\,\text{nm}$ and $\alpha = 0.1$). It suggests that inhomogeneities are still affecting the motion for J slightly above J_0, in agreement with the results of micromagnetic simulations of skyrmion motion in granular media of Figs. 4.4b,d.

A point probably requiring further attention is the actual distribution of the currents in the multilayers. From measurements on thicker $20\,\text{nm}$ films, we have determined the resistivities of Pt and Ta in particular to be $\rho(\text{Pt}) \approx 30\,\mu\Omega\,\text{cm}$ and $\rho(\text{Ta}) \approx 120\,\mu\Omega\,\text{cm}$. The magnitude of the spin currents originating from Ta are thus expected to be largely reduced when compared to the assumption of a uniform current density in the multilayers. Also, the precise thickness of the transition from β-phase to α-phase of Ta is known to be important for the value of ρ and θ_{SHE} [197]. An optimised layer design with respect to current distribution may improve the present results.

In order to summarise the current-induced motion experiments for all the multilayers studied above, it is interesting to compare their results with the observations gathered in other systems, as shown in 4.23. Let us proceed in the order of Table 4.3. The point plotted for [Ir 1/Co 0.8/Pt 1]$_{11}$ is indeed off from the main trend, because of its inefficient current-injection geometry of type (III), when other structures inject current in all layers. The point plotted for [Ir 1/Co 0.8/Pt 3]$_6$ joins the main trend, while the result achieved for [Pt 2.4/Co$_{10}$Fe$_{70}$B$_{20}$ 0.8/Al$_2$O$_3$ 1]$_{20}$ is satisfying and in line other results obtained with CoFeB alloys. An unresolved question at present is whether the Ir or Ru NM layers are able to limit the diffusion of the vertical spin currents. If not, spin currents originating in Pt layers above and below each FM layer may contribute, with competing influences, to the total torque, thus reducing the overall SOT. Indeed, motion is not found more efficient in [Pt 8/Co 1.4/Ru 1.4]$_3$ than in [Pt 0.6/Co 1.4/Ru 1.4]$_3$, suggesting a limited gain obtained by moving
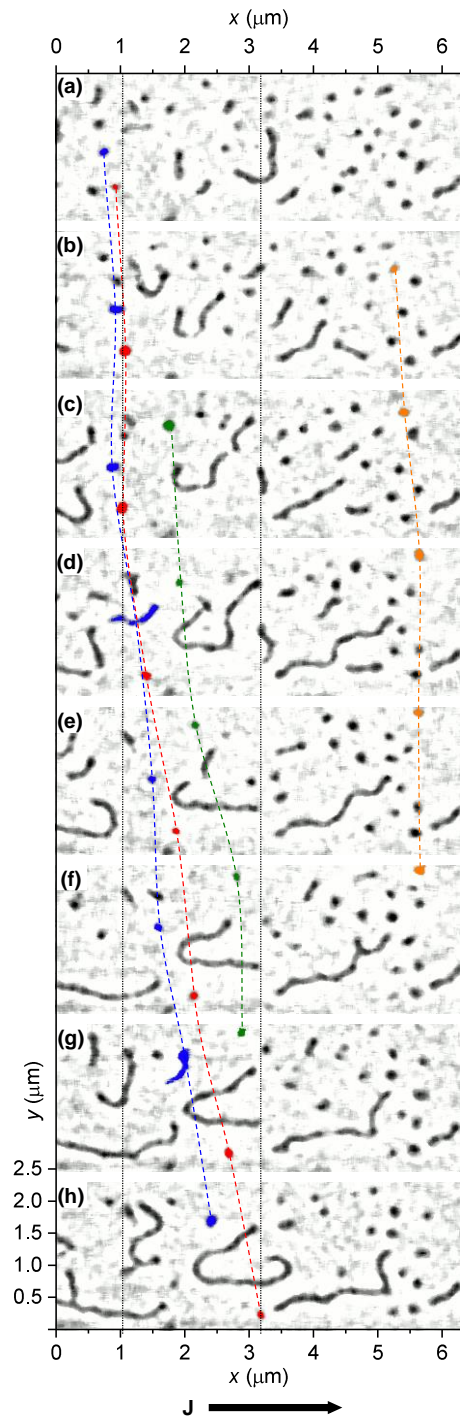
Figure 4.21: MFM images of (a) the initial magnetic configuration in the track, and (b–h) of the magnetic configuration observed after the injection of successive single pulses, for $J > 0$. All pulses are $12\,\text{ns}$ long with $J = 7.7 \times 10^{11}\,\text{A}\,\text{m}^{-2}$. The motion of some skyrmions is highlighted by a coloured filling, linked by the dashed lines. The positions of the red skyrmion at frames c and h are reported by the dotted line.
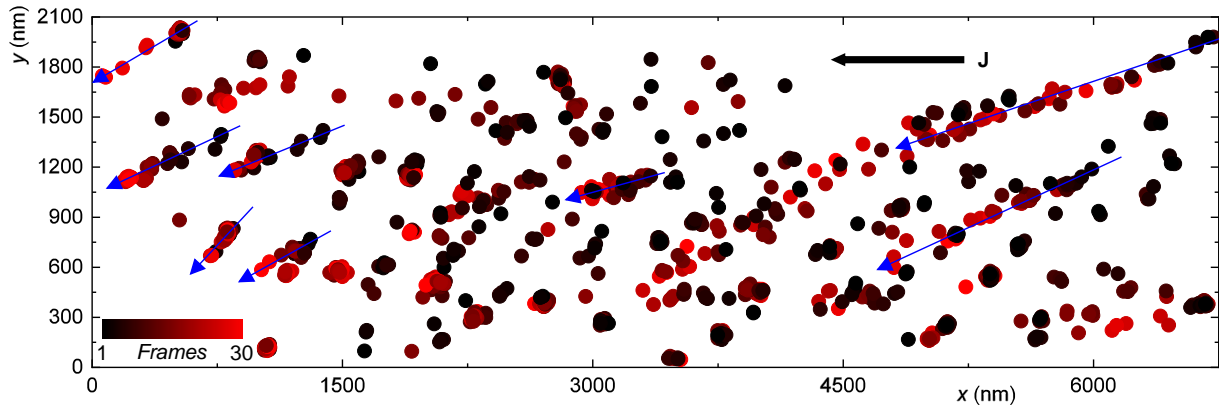
Figure 4.22: Traces of the tracked skyrmion positions, for $J < 0$, with the repetition of pulses encoded by the colour, from black (initial) to red (after 30 single pulses of 10 ns and $J = -8.2 \times 10^{11}\,\mathrm{A\,m^{-2}}$). The sideways motion of the most mobile skyrmions is indicated by the blue lines, revealing longitudinal and transverse velocities components.

towards uniform injection using Pt and Ru spacers, which may explain why the efficiency for this last series of samples appears five times slower than expected (from a linear evolution starting from depinning current $J_0 = 2.5 \times 10^{11}\,\mathrm{A\,m^{-2}}$, represented by the dashed line).

4.9 Cancelling the skyrmion Hall effect

In many situations, the applicability of skyrmion manipulation in nanotrack devices may be limited by the existence of the skyrmion Hall effect. Even if it may lead, in principle, to an acceleration of the longitudinal velocity by a factor $\sqrt{1+\eta^2}/\eta$ (due to the conversion into longitudinal motion of the repulsion force of the confining potential located at edges of the track, see §3.2), in practice this velocity enhancement has not yet been observed in experiments due to the unavoidable presence of defects located at the edges [45]. Moreover, the skyrmion may be expulsed across the edges when the confining potential is overcome [178]; the reduction in size of skyrmions moving along an edge causes their deceleration; and it may even lead to their temperature-activated annihilation. Therefore, conditions in which the skyrmion Hall effect can be compensated are highly desirable to induce an efficient motion of the skyrmions along the direction of the track. In the following, the possibility of compensating the skyrmion Hall effect by exploiting hybrid chirality in multilayers is discussed.

Because Néel skyrmions are driven along x while Bloch skyrmions are driven along y, it appears that the skyrmion Hall effect can be compensated in the presence of hybrid chiral skyrmions, if the resulting force $\mathbf{F} = F_\mathrm{x}\hat{\mathbf{x}} + F_\mathrm{y}\hat{\mathbf{y}}$ makes an angle with x opposite to the deflection angle $\mathrm{atan}\,(1/\eta)$. Different from Chapter 3, the skyrmion Hall angle Θ'_sk considered here designates the angle of the motion with respect to the current direction (and not with the driving force). Let us first analyse how the velocity of a hybrid chiral skyrmion evolves as a function of the damping parameter α, which controls to which extent the motion is affected by gyrotropic forces. To this effect, the hybrid skyrmion profile obtained in §4.4 for $L = 3$ with $D = 1.35\,\mathrm{mJ\,m^{-2}}$ and $\mu_0 H_\mathrm{ext} = 50\,\mathrm{mT}$ is analysed within the Thiele approach, as shown in Fig. 4.24. It can notably be seen that $\Theta'_\mathrm{sk} = \Theta_\mathrm{sk} + \mathrm{atan}\,(F_\mathrm{y}/F_\mathrm{x}) = \mathrm{atan}\,(1/\eta) + \mathrm{atan}\,(F_\mathrm{y}/F_\mathrm{x})$. Two profiles are solutions and are to be considered that have intermediate chirality between Néel and Bloch in the top layer, one with $\phi > 0$ and one with $\phi < 0$, and hence, opposite signs of F_y. The chirality is Néel CCW in the two other layers. In the limit of dissipationless motion ($\eta \to 0$), $v_\mathrm{x} = -F_\mathrm{y}/G$ and $v_\mathrm{y} = F_\mathrm{x}/G$, while in the limit of very large dissipation ($\eta \gg 0$), $v_\mathrm{x} = F_\mathrm{x}/(\eta G)$ and $v_\mathrm{y} = F_\mathrm{y}/(\eta G)$. For finite values of α between these two regimes, the velocity vector continuously evolves from one limit case to the other,
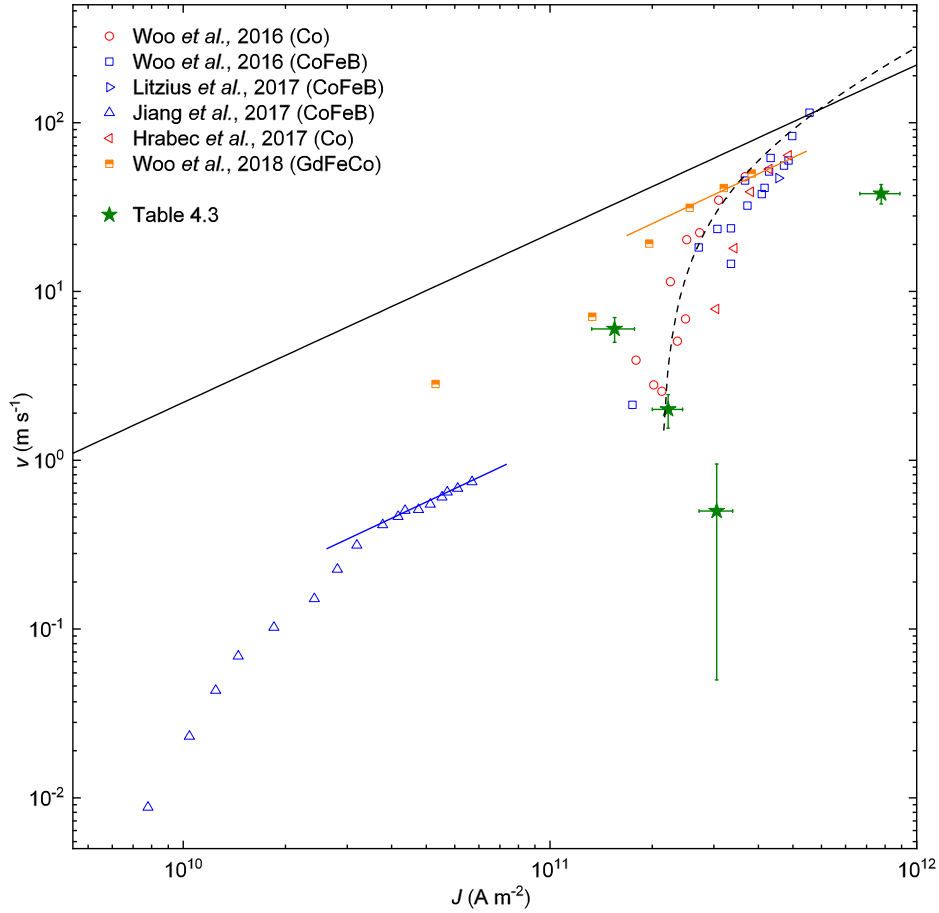
Figure 4.23: Comparison of motion results with other systems, displaying v as a function of J: Red circles: [Pt ($3\,\text{nm}$)/Co ($0.9\,\text{nm}$)/Ta ($4\,\text{nm}$)]$_{15}$ and blue squares: [Pt ($4.5\,\text{nm}$)/CoFeB ($0.7\,\text{nm}$)/MgO ($1.4\,\text{nm}$)]$_{15}$, from Woo *et al.* [46]. Blue right triangles: [Pt ($3.2\,\text{nm}$)/CoFeB ($0.7\,\text{nm}$)/MgO ($1.4\,\text{nm}$)]$_{15}$, from Litzius *et al.* [47]. Up blue triangles: [Ta ($5\,\text{nm}$)/Co$_{20}$Fe$_{60}$B$_{20}$ ($1.1\,\text{nm}$)/TaO$_x$ ($3\,\text{nm}$)]$_1$, from Jiang *et al.* [45]. Left red triangles: Pt ($5\,\text{nm}$)/CoNiCo ($1.5\,\text{nm}$)/Au ($3\,\text{nm}$)/CoNiCo ($1.5\,\text{nm}$)/Pt ($5\,\text{nm}$), from Hrabec *et al.* [188]. Half-filled orange squares: [Pt ($3\,\text{nm}$)/Gd$_{25}$Fe$_{65.6}$Co$_{9.4}$ ($5\,\text{nm}$)/MgO ($1\,\text{nm}$)]$_{20}$, from Woo *et al.* [198]. Green stars: Results from Table 4.3. The black line is aligned with $v \propto J$ and crosses the best result for v. As can be seen from the blue and orange lines, these two series of measurements have reached a regime far from pinning where velocity appears proportional to applied current. The dashed line identifies the expected velocity for a critical depinning current $J_0 = 2.5 \times 10^{11}\,\text{A}\,\text{m}^{-2}$.

as shown in Fig. 4.24. The resulting longitudinal and transverse velocity components are displayed as a function of α in Fig. 4.25a. As a result of dissipation, the global velocity decreases with α, together with a rotation of the direction of motion, as shown in Fig. 4.25b, which displays $|\mathbf{v}|$ and Θ'_{sk} as a function of α. For one of the two signs of the Bloch component, here with $\phi > 0$, the skyrmion Hall effect is compensated, with $v_y = 0$ and $\Theta'_{\text{sk}} = 0$, for one specific value of $\alpha \approx 0.35$ at which $\text{atan}\,(1/\eta) = -\,\text{atan}\,(F_y/F_x)$. This demonstrates the possibility of cancelling the skyrmion Hall angle in hybrid chiral skyrmions.

However, α is not an easily controllable parameter in magnetic multilayers. For this reason, it may be more interesting to achieve cancellation of the skyrmion Hall effect by controlling, for example, the external magnetic field as α is fixed. The evolution of (v_x, v_y) and $(|\mathbf{v}|, \Theta'_{\text{sk}})$ with $\mu_0 H_{\text{ext}}$ for a fixed value of $\alpha = 0.4$ are shown in Figs. 4.25c,d, respectively. Again, $L = 3$ with $D = 1.35\,\text{mJ}\,\text{m}^{-2}$. Upon varying the external field, the skyrmion expands or reduces size, which affects
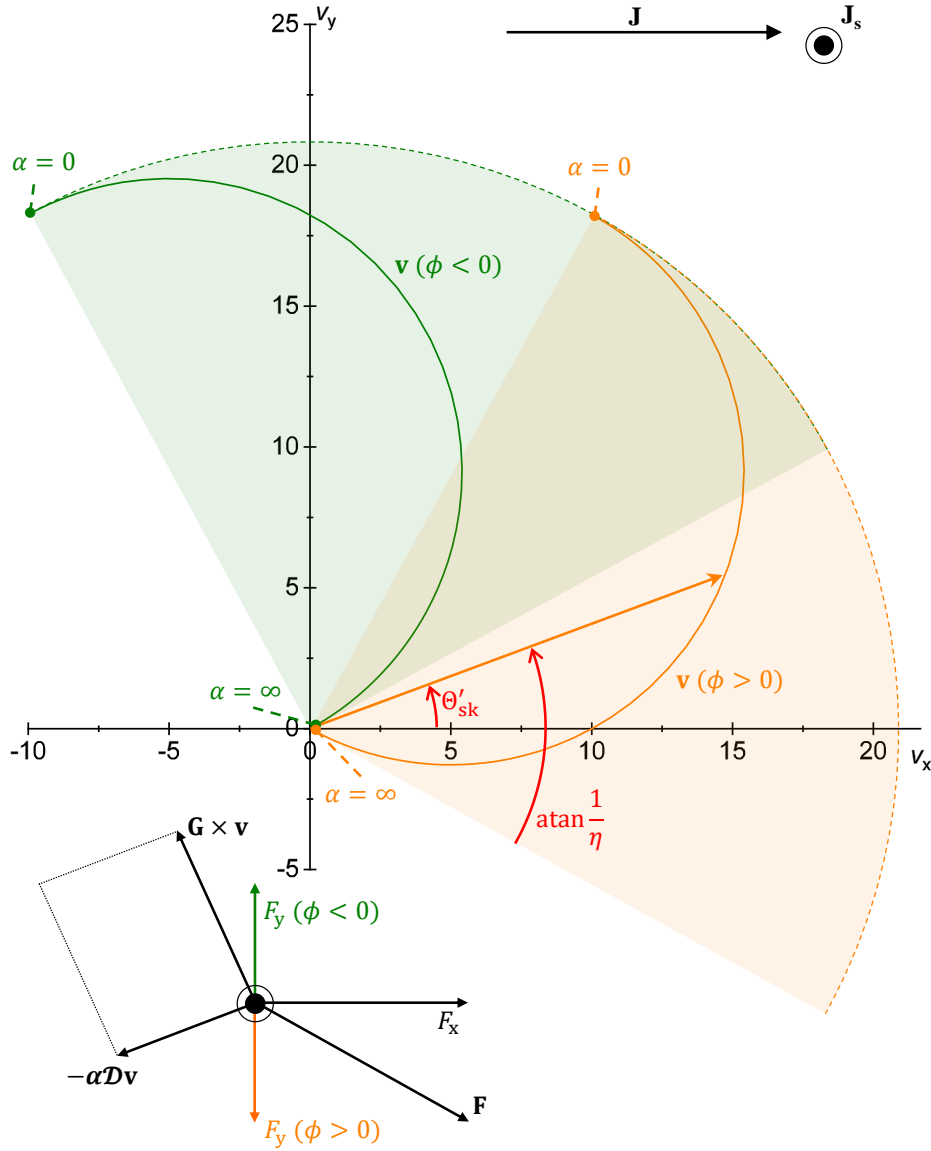
Figure 4.24: Evolution of the Thiele velocity vector $\mathbf{v}$ in the $(v_{\mathrm{x}}, v_{\mathrm{y}})$ plane (green and orange solid lines) depending on damping parameter α. The two situations in which the Bloch component of the top layer verifies $\phi < 0$ (in green) and $\phi > 0$ (in orange) are analysed. For α ranging 0–∞, $\mathrm{atan}\,(1/\eta)$ evolves from 90° to 0° and $\mathbf{v}$ evolves in the green or orange quarter circle depending on the sign of ϕ. The skyrmion Hall angle Θ'_{sk} is now defined as the angle of the motion with respect to the current direction $\mathbf{J}$. The balance of Thiele forces is shown below the velocity graph; for the displayed case, $\alpha = 0.15$ and $\phi > 0$.
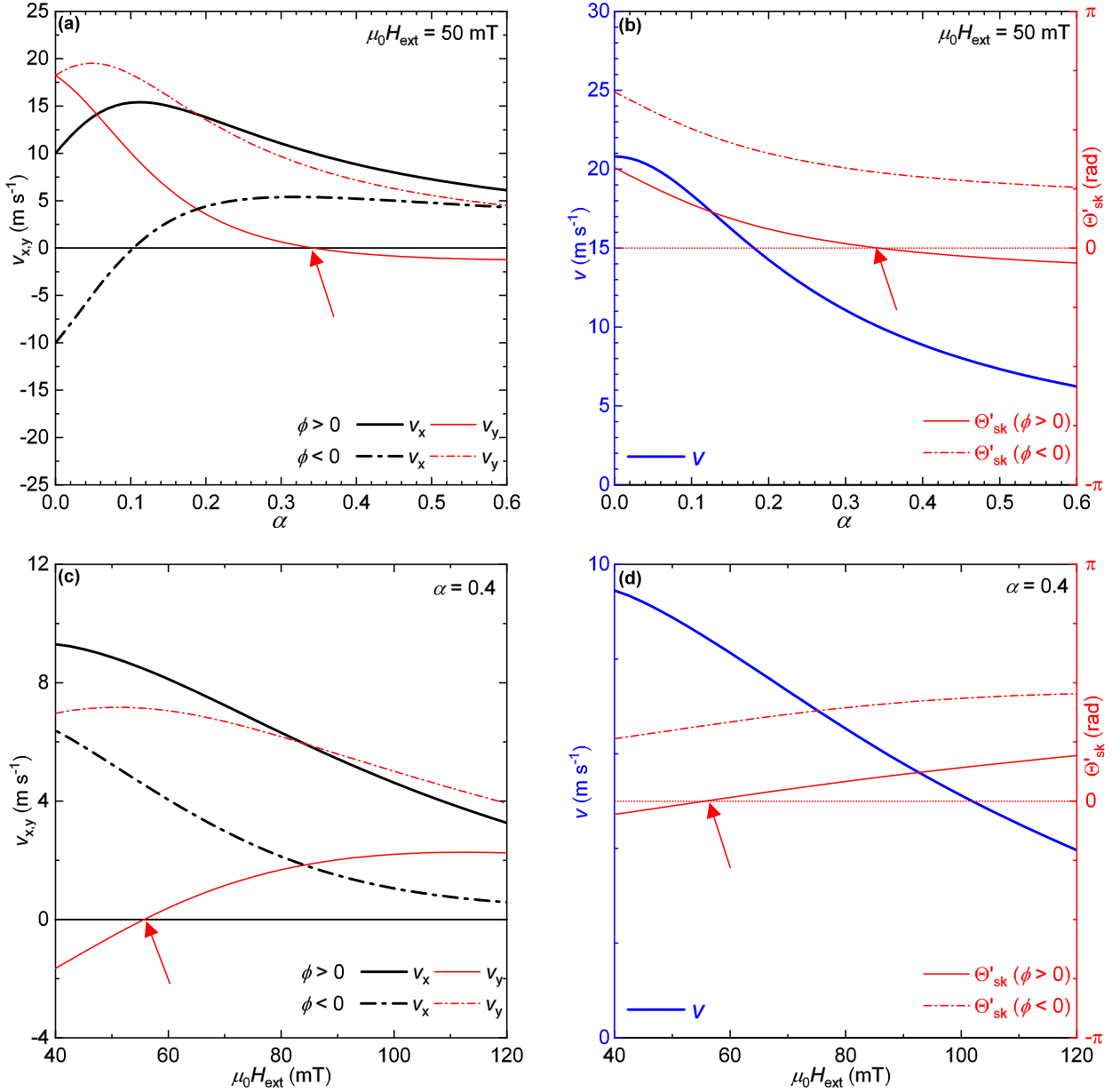
Figure 4.25: (a) Longitudinal (black curves) and transverse (red curves) velocity components; (b) total velocity (blue curve, left scale) and skyrmion Hall angle (red curves, right scale) as found by solving the Thiele equation as a function of damping parameter α, for $\mu_0 H_{\text{ext}} = 50\,\text{mT}$. (c,d) Same, as found by solving the Thiele equation as a function of external field $\mu_0 H_{\text{ext}}$, for $\alpha = 0.4$. Here, $L = 3$ and $D = 1.35\,\text{mJ}\,\text{m}^{-2}$. Solid curves are for a CW Bloch component in the skyrmion profile ($\phi > 0$), while dash-dotted curves are for a CCW Bloch component in the skyrmion profile ($\phi < 0$). Varying either α or $\mu_0 H_{\text{ext}}$, a zero-crossing point exists for the skyrmion Hall angle when $\phi > 0$. Compensation of the skyrmion Hall angle is denoted by the red arrow in each panel.

the value of the dimensionless parameter a determining the Thiele factor $\mathcal{D}$ in (3.6). Because $\eta = \alpha a/4$, η continuously evolves with the field, as it was the case for varying α above, while the ratio between F_{x} and F_{y} is only weakly affected. For this reason, a compensation of the skyrmion Hall effect similar to the one found just above occurs at a particular field, here $\mu_0 H_{\mathrm{ext}} \approx 55\,\mathrm{mT}$. Even if this mechanism relies on dissipation, a significant velocity is still achieved at the compensation point. The distinction between skyrmions with $\phi > 0$ and skyrmions with $\phi < 0$, if they constitute metastable states at RT, also allows envisaging to sort them according to their chirality. In conclusion, this regime of compensation of the skyrmion Hall effect for hybrid chiral skyrmions may be targeted if a straight motion collinear to the current direction is required. The approach described here is similar to the compensation of the skyrmion Hall effect that has been recently proposed in more complex material systems, by exploiting a composite DM interaction of mixed interfacial and bulk origins [199].

How to obtain very small skyrmions?

In this chapter, I describe some new approaches that have been investigated to further reduce the size of RT skyrmions in magnetic multilayers. Not only this issue challenges our fundamental understanding of the mechanisms shaping and stabilising skyrmions, but it is of crucial importance regarding the prospects for applications of skyrmions. It will appear that the question of size is actually a question of stability, that is largely influenced by the dipolar field of FMs. Consequently, two ideas have emerged and have been attempted in the aim of limiting the detrimental effects of the dipolar field: reducing the saturation magnetization M_{s} of the multilayers by FMs combination, which is the topic of §5.3; and stabilising antiferromagnetic skyrmions inside SAF systems, which is the topic of §5.4 and §5.5.

5.1 The minimal stability criterion

In the absence of strong thermal agitation, which corresponds to the case of atomically-thin systems studied at cryogenic temperatures, the important consideration for the stability of skyrmions is whether the applied field remains lower than a critical value for collapse. Its value depends on the parameters of the Hamiltonian, and for a field above it the system gains energy by unwinding the skyrmions through an isotropic collapse [137]. However, at RT the situation is very different from the one at cryogenic temperatures. The (thermal) stability of skyrmions now depends on whether the difference of energy between the stable radius and the collapse radius — the saddle point of the minimum energy path towards annihilation — remains larger than what can be overcome by thermal fluctuations. As a starting point, we can analyse the origins of the thermal stability barrier of skyrmions within the variational approach (see §2.1). Following the observation that at very low radii $(r \to 0)$ $E_{\mathrm{sk}} \approx 8\pi ALt$, as was confirmed in §2.6, we find the energy barrier as the difference between this exchange energy value, being the barrier top, and the energy minimum $E_{\mathrm{sk}}^{(\mathrm{stab})}$ located at $r_{\mathrm{sk}}^{(\mathrm{stab})}$ as given in (2.8), which provides for a single layer

$$E_{\mathrm{B}} = \frac{\pi Lt D^2 I_2^2}{2(K_{\mathrm{eff}} I_3 + B_{\mathrm{z}} M_{\mathrm{s}} I_4)}. \tag{5.1}$$

Combining it with the equilibrium radius found in (2.7) results in

$$E_{\mathrm{B}} = \pi Lt D I_2 r_{\mathrm{sk}} \tag{5.2}$$

which shows that E_{B} is proportional to both D and r_{sk}. Most often, a given thermal stability is targeted, expressed by the thermal stability factor $\Delta = E_{\mathrm{B}}/k_{\mathrm{B}}T$, e.g., $\Delta > 40$ is a target for experimental studies. As the skyrmion size can be controlled by the external magnetic field, the requirement is then simply that

$$D_{\mathrm{s}} r_{\mathrm{sk}} > \frac{\Delta_0 k_{\mathrm{B}} T}{\pi L I_2} \tag{5.3}$$

with $D_{\mathrm{s}} = tD$ (see §1.1), and Δ_0 the required thermal stability factor.

Skyrmions compressed (by field or anisotropy) towards values of r_{sk} that do not satisfy (5.3) become unstable at RT. Equation (5.3) thus suggests that the minimum skyrmion size in a given system evolves as $1/D_s$. Notably, **increasing the thickness of the FM layer is not expected to provide any additional stability**, under the scope of the present simple approach, because D_s, and not D, is here the key parameter.

Next, the study of the link between thermal stability and skyrmion sizes within the numerical model designed in Chapter 2 allows to go beyond the oversimplified analysis provided by the variational approach. At this stage, an infinite coupling between layers is assumed, which seems reasonable for thin spacers and limited L, as in $[Pt(1.0\,nm)/Co(1.0\,nm)/NM(1.0\,nm)]_5$, which we choose for the present example. On the contrary, for oxide spacers mediating no interlayer electronic coupling, but only subject to dipolar couplings, or larger values of L, this approach can be invalid. Note that infinite coupling actually corresponds to the 1D model discussed in Chapter 4. The method of §2.6 allows to determine the barrier height very easily, under the condition that a "compact skyrmion" is formed, with $dE_{sk}/dr_{sk} < 0$ for $r_{sk} \to 0$. Otherwise, the top of the barrier is not located at $r_{sk} \approx 0$ but at a radius that varies with the magnetic parameters —see, *e.g.*, Figs. 2.3a,c—, which prevents from simply determining E_B as $E_A(0) - E_{sk}(r_{sk})$. When $dE_{sk}/dr_{sk} > 0$ for $r_{sk} \to 0$, it is indeed required to study the whole dependence of E_{sk} from the equilibrium r_{sk} down to 0, in order to determine E_B. To avoid this issue, in the following only the values of D large enough so that $dE_{sk}/dr_{sk} < 0$ for $r_{sk} \to 0$ are considered.

By inspection of the radius dependence of all individual energy terms of the skyrmion, presented before in Fig. 2.5, we can see that E_{Keff} increases almost linearly with radius (it is best fitted by a power function $r_{sk}^{1.05}$), which differs from what is obtained within the variational approach. Consequently, the K_{eff} term does not simply shift the required external field values, but it opposes the D term in stabilising the skyrmion against thermal fluctuations by shifting upwards the energy minimum compared to $E_A(0)$. Reducing K_{eff} is thus expected to be directly beneficial to the thermal stability of skyrmions.

For a given K_{eff}, using the barrier heights determined with the method of 2.6, two $(D, \mu_0 H_{ext})$ diagrams can be drawn for the skyrmion radius and its thermal stability, as shown in Fig. 5.1a and Fig. 5.1b respectively, in order to visualise their correlated variations with magnetic parameters. Here $A = 10\,pJ\,m^{-1}$, $M_s = 1.0\,MA\,m^{-1}$, $K_u = 0.65\,MJ\,m^{-3}$, while D and $\mu_0 H_{ext}$ vary in the range 0.2–$2.0\,mJ\,m^{-2}$ and 20–$200\,mT$, respectively. As was found within the variational approach, smaller stable skyrmions can be stabilised for larger values of D.

It is necessary to keep in mind however that these values of E_B are to be significantly reduced for a more realistic modelling of the interlayer coupling: in practice, the coupling between distant FM layers is finite, sometimes small (smaller than all other interactions) or even negligible (as with oxide spacer layers), which is expected to reduce the thermal stability reached in multilayers. Notably, one can imagine that the annihilation of skyrmions could occur layer by layer successively, which may divide the energy barrier in smaller successive steps. This might affect the benefit of magnetic multilayers for increasing the thermal stability of skyrmions, which requires further investigation. Also, complex consequences of hybrid chirality on the thermal stability of multilayered skyrmions can be anticipated, but they have not been studied so far.

To summarise, **reducing K_{eff} towards smaller values** is the most accessible optimisation level that is expected to benefit the thermal stability of smaller skyrmions. Increasing D_s would also directly allow to reduce the minimal size of skyrmions, which suggests that finding systems in which **larger DM interaction magnitudes** are at play remains a very pertinent research direction for the future. However, there are no established solutions known at present to enlarge D_s further than in Pt/Co based systems. An easier strategy expected to enhance the thermal stability of skyrmions (and therefore to allow reducing their size at RT) then remains to **increase the number of interfaces** by employing multilayers [7]. In the limit of infinite coupling between layers, the total skyrmion energy is multiplied by L, potentially reducing the minimal skyrmion size by a same factor of L. Even if the impact of finite or even negligible interlayer coupling is
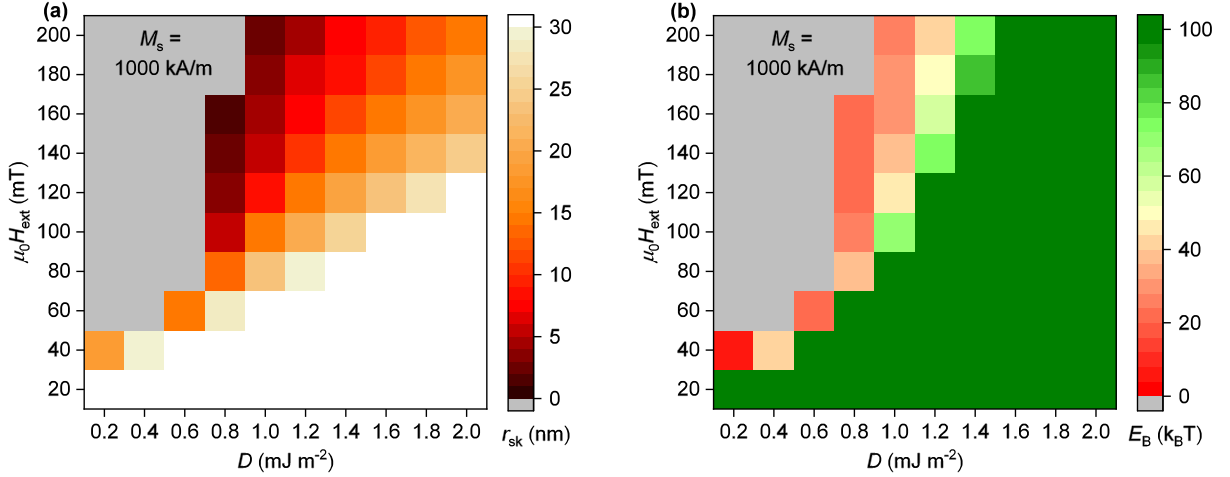
Figure 5.1: $(D, \mu_0 H_{\text{ext}})$ diagrams for (a) r_{sk} and (b) E_{B}, as indicated by the colour scales, for $M_{\text{s}} = 1.0\,\text{MA}\,\text{m}^{-1}$. Grey indicates parameters for which the skyrmion collapses towards zero radius.

still unknown, it can be anticipated that it would limit, but not cancel, the effectiveness of the multilayer approach.

5.2 The role of the dipolar field in skyrmion stability

The impact of dipolar interactions on size and thermal stability of skyrmions has not yet been addressed in this thesis. The distant component of the dipolar interactions contributes to stabilise skyrmion configurations by decreasing their energies, which in turn require larger external field values to avoid expansion into stripes and to remain confined below a given radius. In order to first observe this effect of dipolar interactions on skyrmion profiles, their sizes are compared for two different values of M_{s} (and hence of the dipolar interactions strength) in Figs. 5.2a,b. For each value of M_{s}, $1.0\,\text{MA}\,\text{m}^{-1}$ (with $K_{\text{u}} = 0.8\,\text{MJ}\,\text{m}^{-3}$) and $1.3\,\text{MA}\,\text{m}^{-1}$ (with $K_{\text{u}} = 1.2\,\text{MJ}\,\text{m}^{-3}$), the evolution of skyrmion size with the external field applied to multilayers is displayed. Again $t = 1.0\,\text{nm}$ and $p = 3.0\,\text{nm}$, $A = 10\,\text{pJ}\,\text{m}^{-1}$, $D = 1.35\,\text{mJ}\,\text{m}^{-2}$, and the number of magnetic layers varies in the range $L = 3$–20. By comparing these two graphs, it is confirmed that the dipolar interactions, increasing with M_{s} and L, enlarge the equilibrium size of the skyrmions. They also reduce the susceptibility of skyrmion size with external field.

The aim is now to determine whether the distant dipolar interaction energy term $E_{\text{lr}}(r_{\text{sk}})$ (defined in Chapter 1 as $E_{\text{dem}} + E_{\text{Ku}} - E_{\text{Keff}}$) results into a stronger or a weaker thermal stability barrier. To this effect, the previous $(D, \mu_0 H_{\text{ext}})$ diagrams are computed again for a much reduced value of $M_{\text{s}} = 0.2\,\text{MA}\,\text{m}^{-1}$, K_{eff} as above, while D and $\mu_0 H_{\text{ext}}$ vary in the range 0.2–$2.0\,\text{mJ}\,\text{m}^{-2}$ and 0.1–$1.0\,\text{T}$, respectively. The diagrams for r_{sk} and E_{B} are given in Figs. 5.3a,b, respectively. The Zeeman energy E_{ext} takes identical values for $\mu_0 H_{\text{ext}} = 0.1$–$1\,\text{T}$ with $M_{\text{s}} = 0.2\,\text{MA}\,\text{m}^{-1}$, and for $\mu_0 H_{\text{ext}} = 20$–$200\,\text{mT}$ with $M_{\text{s}} = 1.0\,\text{MA}\,\text{m}^{-1}$, explaining the similar aspects of the diagrams of Figs. 5.1 and 5.3. The main difference between the two systems thus resides in the difference with respect to the E_{lr} term.

A good figure of merit to evaluate the potential for RT stability of small skyrmions is given by the thermal stability to radius ratio $E_{\text{B}}/r_{\text{sk}}$. By comparison of Figs. 5.4a and 5.4b, which display $E_{\text{B}}/r_{\text{sk}}$ for both values of M_{s}, it appears that the ratio $E_{\text{B}}/r_{\text{sk}}$ is enhanced for all the smaller skyrmions that appear in the part of the diagram labelled (I). The ratio between the values of $E_{\text{B}}/r_{\text{sk}}$ achieved for $M_{\text{s}} = 0.2\,\text{MA}\,\text{m}^{-1}$ and for $M_{\text{s}} = 1.0\,\text{MA}\,\text{m}^{-1}$ is displayed in Fig. 5.4c, where the green colour corresponds to an enhanced stability at lower M_{s}. We can thus expect that **reducing M_{s} be beneficial to the thermal stability** of small skyrmions, which would allow
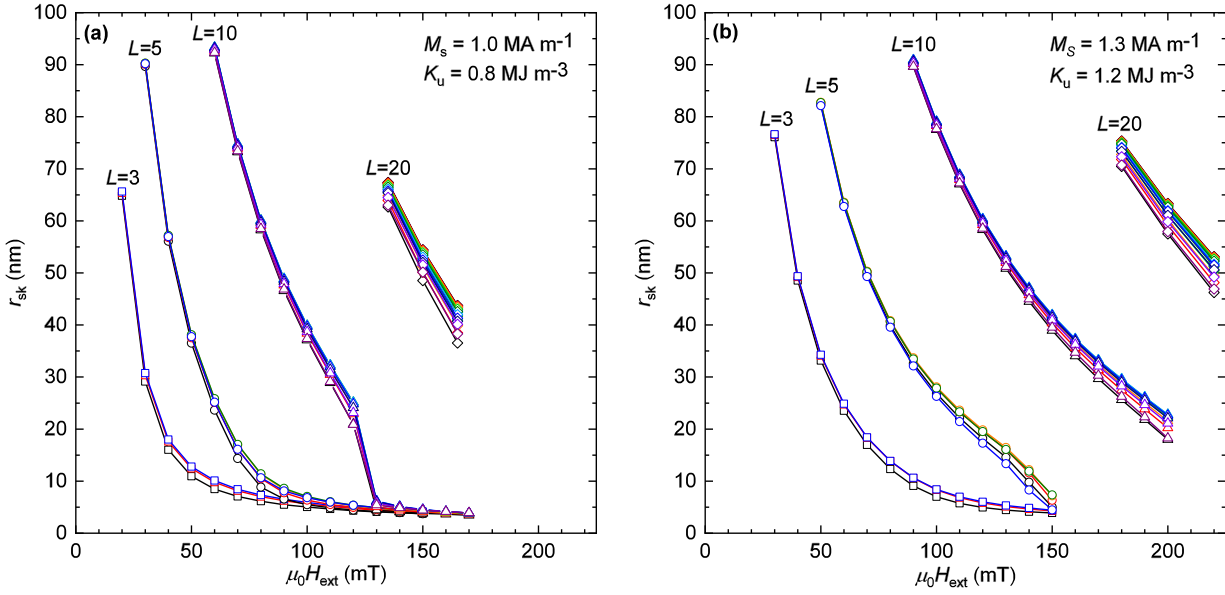
Figure 5.2: Skyrmion radii r_{sk} in the different layers as a function of $\mu_0 H_{ext}$ for $L = 3$ (squares), $L = 5$ (circles), $L = 10$ (triangles) and $L = 20$ (diamonds), for (a) $M_s = 1.0\,\mathrm{MA\,m^{-1}}$ and (b) $M_s = 1.3\,\mathrm{MA\,m^{-1}}$. The different colour lines indicate r_{sk} in different layers.

to further decrease the size of RT stable skyrmions in multilayers. Another advantage of reducing M_s is that a better control on skyrmion size, independent of the influence of dipolar interactions, is expected. Finally, the occurrence of hybrid chirality, arising when dipolar interactions compete with the DM interaction as described in Chapter 4, would also be mitigated.

5.3 Light magnetization elements insertion

To achieve the goal of reducing M_s, different possibilities for inserting FM elements with a lighter magnetization have been investigated experimentally in this thesis. A first approach that has been attempted in order to reduce M_s in Pt/Co/Ru-based multilayers is the insertion a Ni layer in the middle of the Co layer. This method unfortunately turns out not to allow enhanced stability,
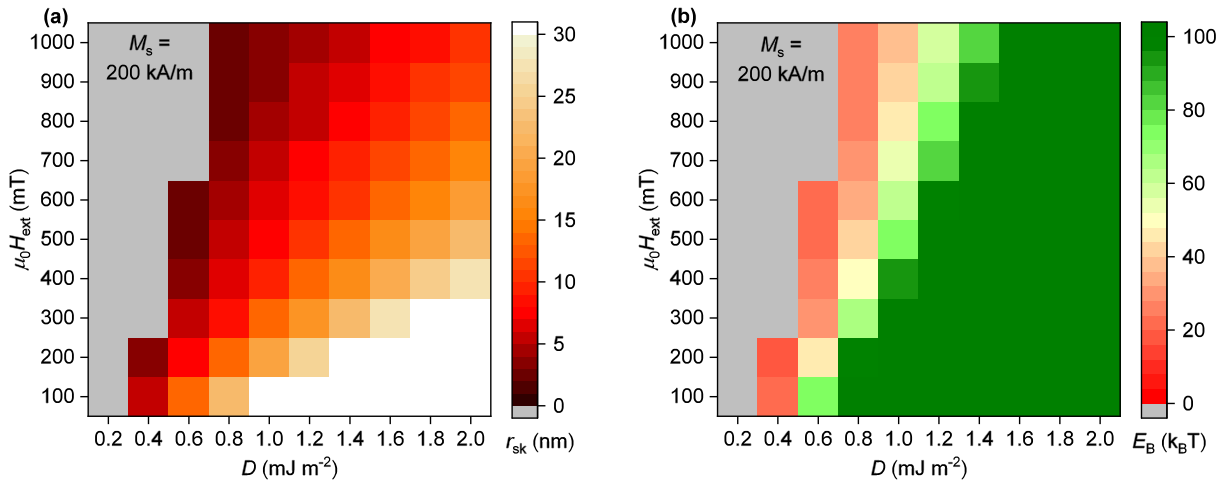
Figure 5.3: $(D, \mu_0 H_{ext})$ diagrams for (a) r_{sk} and (b) E_B, as indicated by the colour scales, for $M_s = 0.2\,\mathrm{MA\,m^{-1}}$. Grey indicates parameters for which the skyrmion collapses towards zero radius.
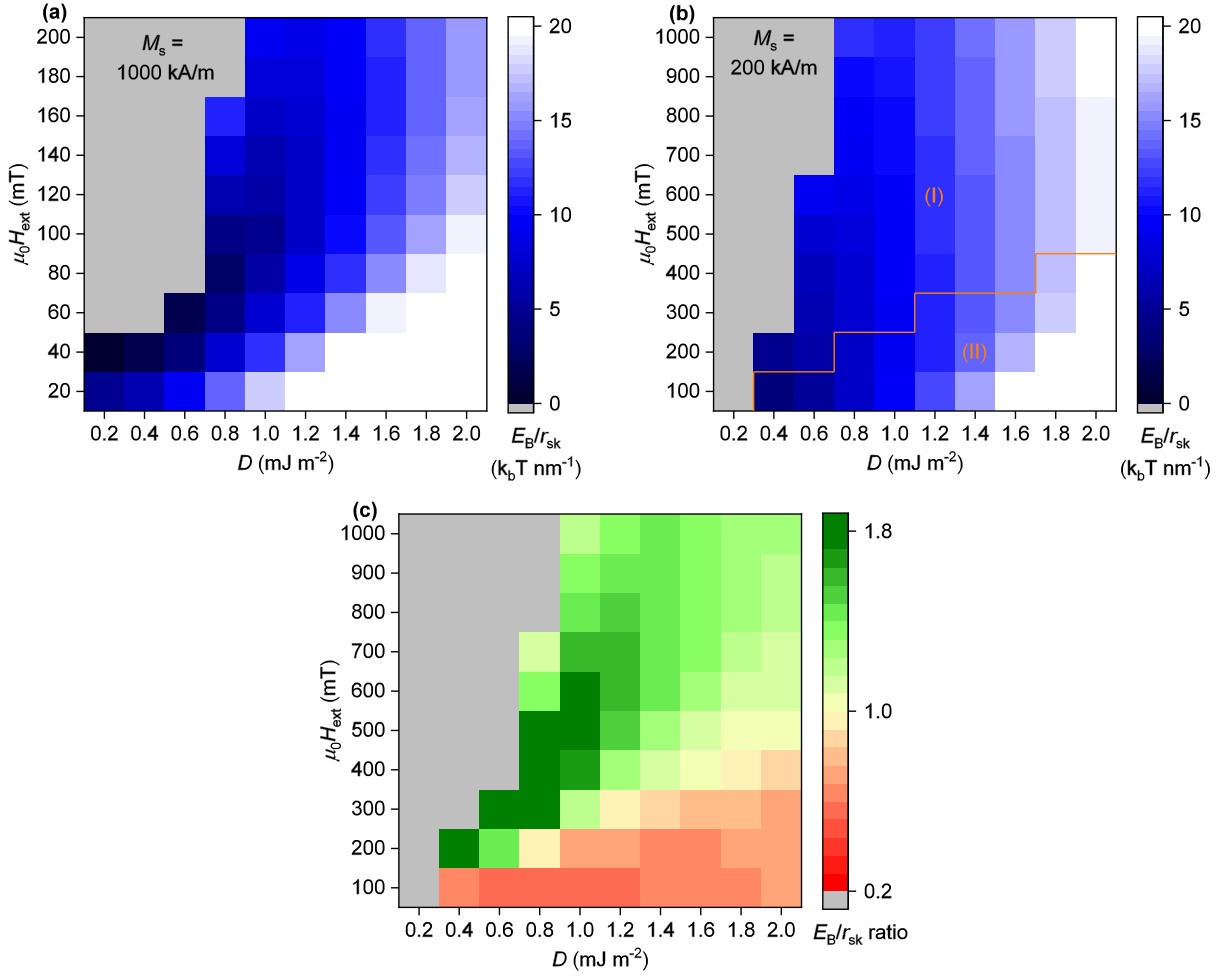
Figure 5.4: $(D, \mu_0 H_{\text{ext}})$ diagrams for $E_{\text{sk}}/r_{\text{sk}}$, with (a) $M_{\text{s}} = 1.0\,\text{MA m}^{-1}$, (b) $M_{\text{s}} = 0.2\,\text{MA m}^{-1}$, and (c) ratio between both, as indicated by the colour scales. In panel b, the orange line separates part (I), for which ratio $E_{\text{B}}/r_{\text{sk}}$ is enhanced due to reduced M_{s} and part (II), for which $E_{\text{B}}/r_{\text{sk}}$ is reduced due to reduced M_{s}. Grey indicates parameters for which the skyrmion collapses towards zero radius.

as it is detailed below.

Given that Ni possesses a saturation magnetization about three times smaller than Co, the average magnetization reduces due to the insertion of Ni in the FM. Moreover, being directly in contact, Co and Ni layers are very strongly exchange coupled, thus forming a single FM layer of coherent magnetization direction. In the resulting Pt/Co/Ni/Co/Ru multilayer, a strong magnetic anisotropy is expected from the conserved Pt/Co interface [200, 201]. Note that some smaller yet significant perpendicular magnetic anisotropy is expected at the Co/Ru interface as well [202]. In contrast, magnetic anisotropy would be smaller at Pt/Ni interfaces [128], potentially preventing from obtaining perpendicular magnetic anisotropy in Pt/Ni/Ru-based multilayers. These different considerations have motivated the choice of the Pt/Co/Ni/Co/Ru multilayer structure. Magneto-metry measurements of such $[\text{Pt/Co/Ni/Co/Ru}]_{10}$ multilayers are shown in Figs. 5.5a (IP field) and 5.5b (OOP field), for a constant $t_{\text{Co}} = 0.4\,\text{nm}$, with a t_{Ni} varying between 0 and 6.0 nm. A large perpendicular anisotropy is found up to $t_{\text{Ni}} = 4.0$–5.0 nm, consistent with a largely reduced M_{s}.

Within the assumption of a simple addition of the Co and Ni layers, without further modification of their properties, by summing moments over the two Co layers and the Ni layer the average
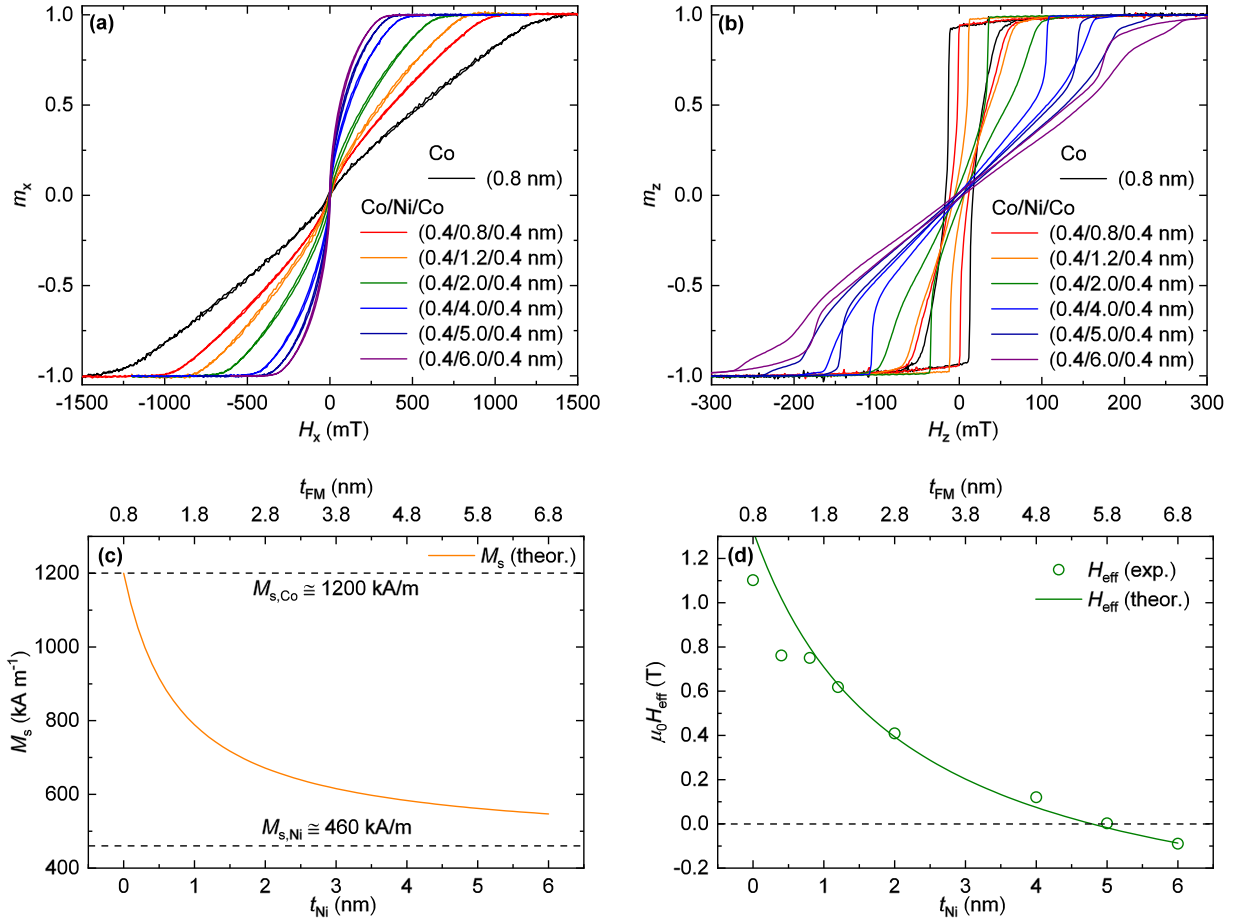
Figure 5.5: (a) IP and (b) OOP magnetometry measurements in $[\mathrm{Pt}/\mathrm{Co}\,(0.8\,\mathrm{nm})/\mathrm{Ru}]_{10}$ and $[\mathrm{Pt}/\mathrm{Co}\,(0.4\,\mathrm{nm})/\mathrm{Ni}\,(t_{\mathrm{Ni}})/\mathrm{Co}\,(0.4\,\mathrm{nm})/\mathrm{Ru}]_{10}$ multilayers with $t_{\mathrm{Ni}} = 0.8,\ 1.2,\ 2.0,\ 4.0,\ 5.0$ and $6.0\,\mathrm{nm}$. (c) Theoretically expected evolution of M_{s} with t_{Ni}. (d) Measured anisotropy field H_{eff} as a function of t_{Ni} (circles), and theoretically expected evolution of H_{eff} with t_{Ni} (line).

magnetization of the FM layer is expected to follow

$$M_{\mathrm{s}} = \frac{t_{\mathrm{Co}} M_{\mathrm{s,Co}} + t_{\mathrm{Ni}} M_{\mathrm{s,Ni}}}{t_{\mathrm{Co}} + t_{\mathrm{Ni}}} \tag{5.4}$$

with $M_{\mathrm{s,Co}} \approx 1200\,\mathrm{kA\,m^{-1}}$ and $M_{\mathrm{s,Ni}} \approx 460\,\mathrm{kA\,m^{-1}}$ (estimated from magnetometry measurements), as displayed in Fig. 5.5c. The demagnetizing energy density can be written as $\varepsilon_{\mathrm{dem}} = K_{\mathrm{dem}}(m_{\mathrm{z}}^2 - 1)$, with

$$K_{\mathrm{dem}} = \frac{1}{t_{\mathrm{Co}} + t_{\mathrm{Ni}}} \left(t_{\mathrm{Co}} \frac{\mu_0 M_{\mathrm{s,Co}}^2}{2} + t_{\mathrm{Ni}} \frac{\mu_0 M_{\mathrm{s,Ni}}^2}{2} \right) \tag{5.5}$$

that is to be compared with the perpendicular magnetic anisotropy originating from the different interfaces $\varepsilon_{\mathrm{K}} = -K_{\mathrm{u}} m_{\mathrm{z}}^2$, with

$$K_{\mathrm{u}} = \frac{K_{\mathrm{s}}}{t_{\mathrm{Co}} + t_{\mathrm{Ni}}} \tag{5.6}$$

which finally provides

$$K_{\mathrm{eff}} = K_{\mathrm{u}} - K_{\mathrm{dem}} = \frac{1}{t_{\mathrm{Co}} + t_{\mathrm{Ni}}} \left(K_{\mathrm{s}} - t_{\mathrm{Co}} \frac{\mu_0 M_{\mathrm{s,Co}}^2}{2} - t_{\mathrm{Ni}} \frac{\mu_0 M_{\mathrm{s,Ni}}^2}{2} \right). \tag{5.7}$$
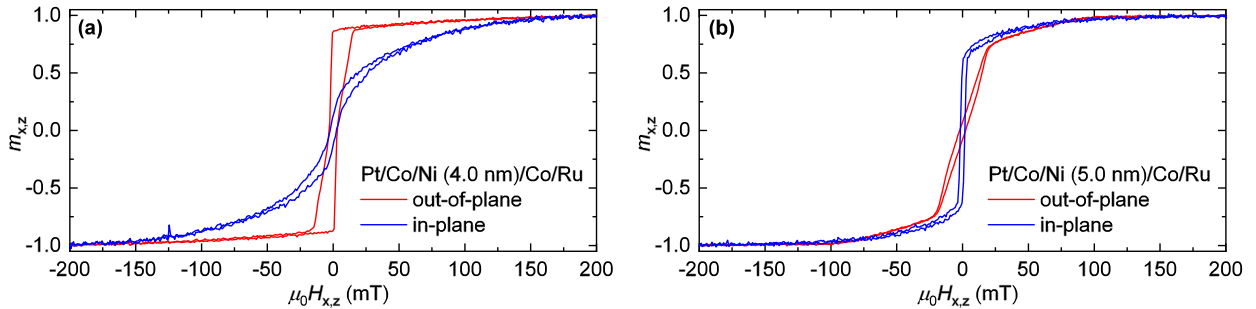
Figure 5.6: IP and OOP magnetometry measurements in Pt/Co (0.4 nm)/Ni (t_{Ni})/Co (0.4 nm)/Ru, for a single composite magnetic layer with (a) $t_{Ni} = 4.0$ nm and (b) $t_{Ni} = 5.0$ nm.

Consequently, the spin reorientation Ni thickness is predicted to be

$$t_{Ni,SRT} = \frac{2K_s - t_{Co}\mu_0 M_{s,Co}^2}{\mu_0 M_{s,Ni}^2}. \tag{5.8}$$

To verify whether there is indeed such layers separation, the dependence of $\mu_0 H_{eff} = 2K_{eff}/M_s$ with t_{Ni} is extracted from the magnetometry measurements. Because of their large total thickness, the present multilayers are subject to form dense stripe domains, making that $\mu_0 H_{eff}$ is not simply the saturation field from the IP magnetometry measurement, but needs to be found as the difference between areas above curves for IP and OOP measurements [124]. Using this technique for finding H_{eff}, the experimentally determined values (circles) are compared to the predictions (line) of (5.7) in Fig. 5.5d, showing an excellent agreement, except for the points at $t_{Ni} = 0$ and 0.4 nm, which are found slightly off the curve. A small additional contribution to the perpendicular magnetic anisotropy is expected from the added Co/Ni and Ni/Co interfaces [130]; because these Co/Ni and Ni/Co interfaces are not yet completely formed for $t_{Ni} \leq 0.8$ nm, K_s increases slightly until $t_{Ni} = 0.8$ nm, explaining this deviation. These measurements therefore suggest that the different FM layers do not intermix or change properties when in contact, but rather remain segregated and accumulate their different magnetizations. From the present modelling, a spin-reorientation thickness $t_{Ni,SRT} \approx 4.8$ nm is found.

This result for $t_{Ni,SRT}$ is further confirmed by the measurement of Pt/Co (0.4 nm)/Ni (t_{Ni})/Co (0.4 nm)/Ru structures composed of a single magnetic layer, for both $t_{Ni} = 4.0$ and 5.0 nm, as displayed in Figs. 5.6a,b, respectively. The relative positions of the OOP and IP curves are swapped when increasing t_{Ni} from 4.0 to 5.0 nm, indicating the reorientation from OOP anisotropy ($K_{eff} > 0$) to IP anisotropy ($K_{eff} < 0$) at 4.0 nm $< t_{Ni,SRT} <$ 5.0 nm.

It appears from these measurements that the properties of Pt/Co and Co/Ru interfaces are only weakly affected by the insertion of a different FM element, such as Ni, away from the interfaces. Neglecting any variation of interfacial properties in a simple reasoning (additional Co/Ni and Ni/Co interfaces only slightly modify K_s), we can consider surface anisotropy value K_s and surface DM interaction parameter D_s fixed. We have seen before (in §5.1) that it is important to limit the effective anisotropy K_{eff} of the multilayers in order to obtain more stable skyrmions. In consequence, a thickness close to the spin reorientation transition needs to be chosen, *e.g.*, around Co(0.4 nm)/Ni(4.8 nm)/Co(0.4 nm) for the present case. Let us analyse how the skyrmion energy functional (2.1) for $E_{sk}(r_{sk})$ is affected by the present increase of t and reduction of M_s, after insertion of t inside the integrand, by comparing Pt/Co/Ru and Pt/Co/Ni/Co/Ru structures with a similar low K_{eff}. The exchange term has a weak influence on skyrmion size and stability. Both DM interaction term ($\propto D_s$) and anisotropy term ($\propto K_s$) are unchanged. Variations of the external field term are irrelevant because they simply rescale the field dependence, which can be compensated by varying the applied field. In an approximation obtained by averaging over both Co layers and the Ni layer, the dipolar field H_{dip} scales with the average M_s determined by (5.4). The dipolar energy

per unit surface is thus expected to evolve as tM_s^2, which remains unchanged because tM_s^2 follows the constant K_s in order to be close from the spin reorientation thickness in both cases. Therefore, all the prefactors of the density terms present in the functional (2.1) shall remain unchanged in a simple approximation. Most effects are then expected to originate in a difference of distant interactions, detailed in the forms of H_{dip} and $E_{lr}(r_{sk})$, due to the increase of the ratio between layer thickness t and skyrmion size. Unfortunately, this is expected not to reduce, but on the contrary, to reinforce the impact of the dipolar field. Due to the independence of D_s and K_s on insertion, we can thus postulate in view of this simple analysis that **no obvious benefit from Ni insertion is expected**. Further studies are nevertheless required in order to definitely confirm this hypothesis.

An alternative multilayer combination that has been developed is Pt/Co/Ni, which can also provide a reduced M_s. In order to overcome the issue described just above of having all energy term prefactors conserved upon insertion of additional FM layers, the regime in which both Co and Ni layers are thin has been explored. For such thin layers, below 0.4 nm, interfaces quality and properties are expected to be highly dependent on the individual layer thicknesses. For this reason, a modelling similar as above cannot be performed, and M_s, H_{eff} and D need to be directly measured. M_s is determined by RT-Superconducting Quantum Interference Device (SQUID) measurements, H_{eff} by other magnetometry measurements, while D and D_s are deduced from MFM measurements of the stripe domains periodicity of demagnetized multilayers, combined with modelling of the stripe domains periodicity dependence on D (see Appendix C). For [Pt/Co (t_{Co})/Ni $(0.4\,\text{nm})]_6$ multilayers, IP magnetometry measurements are displayed in Fig. 5.7a, and the results of the SQUID measurements in 5.7b. The anisotropy field can be extracted as done above, which is shown in Fig. 5.7c. This also provides us with K_{eff}, as the evolution of M_s is known. Using one of the models presented in Appendix C, the value of D can be determined and is displayed in Fig. 5.7d. As expected, D (blue curve) decreases with t_{Co}, with almost an inverse thickness dependence once the interfaces are formed. This can be seen by looking at the surface DM interaction $D_s = Dt_{Co}$, which increases until $t_{Co} \approx 0.4\,\text{nm}$, before stabilising at around $0.5\,\text{pJ m}^{-1}$, around twice less than the value obtained in Pt/Co/Ru (see Appendix A). Note that D_s reaches a constant value when calculated with t_{Co} but not with $t_{Co} + t_{Ni}$, which indicates that here the Ni layer plays a minor role in the magnetization behaviour.

It appears from this series of multilayers that for thin FM layers, such as Co $(0.4\,\text{nm})$/Ni $(0.4\,\text{nm})$ for example, a large perpendicular anisotropy is found, which limits their prospects for skyrmion stabilisation. However, this anisotropy reduces significantly for lower Pt layer thicknesses of 0.4 nm and below, and it can be further controlled by varying the degree of texture of the interfaces through reducing the buffer layer thickness. In this case, the question of whether the DM interaction remains significant arises, as well as the question of whether the quality of the interfaces remains sufficiently high to allow skyrmion motion free of pinning, which are under present investigation. Nevertheless, under the condition that a significant D_s is conserved, we can anticipate that such Pt/Co/Ni structures, with reduced individual layer thicknesses in the 1–2 atomic layer regime, should be very suitable for optimising the thermal stability of small skyrmions, by (i) **maximising the direct interlayer electronic coupling between layers**, and (ii) **increasing the number of interfaces in order to maximise the total DM interaction energy** (D_s term) in a system of fixed total thickness.

5.4 Stabilisation of antiferromagnetic skyrmions in SAF systems

As an alternative to reducing M_s by insertion of Ni, which turns out to raise difficulties, another strategy aiming at avoiding the effects of distant dipolar interactions has been investigated, based on the compensation of the magnetization. Inside antiferromagnetic materials for example, the generated dipolar field is vanishing due to the alternating directions of neighbouring magnetic moments, which counteract each other. Ideally, employing antiferromagnet (AF) layers could therefore allow to host magnetization structures, including AF-based skyrmions, free of any influence
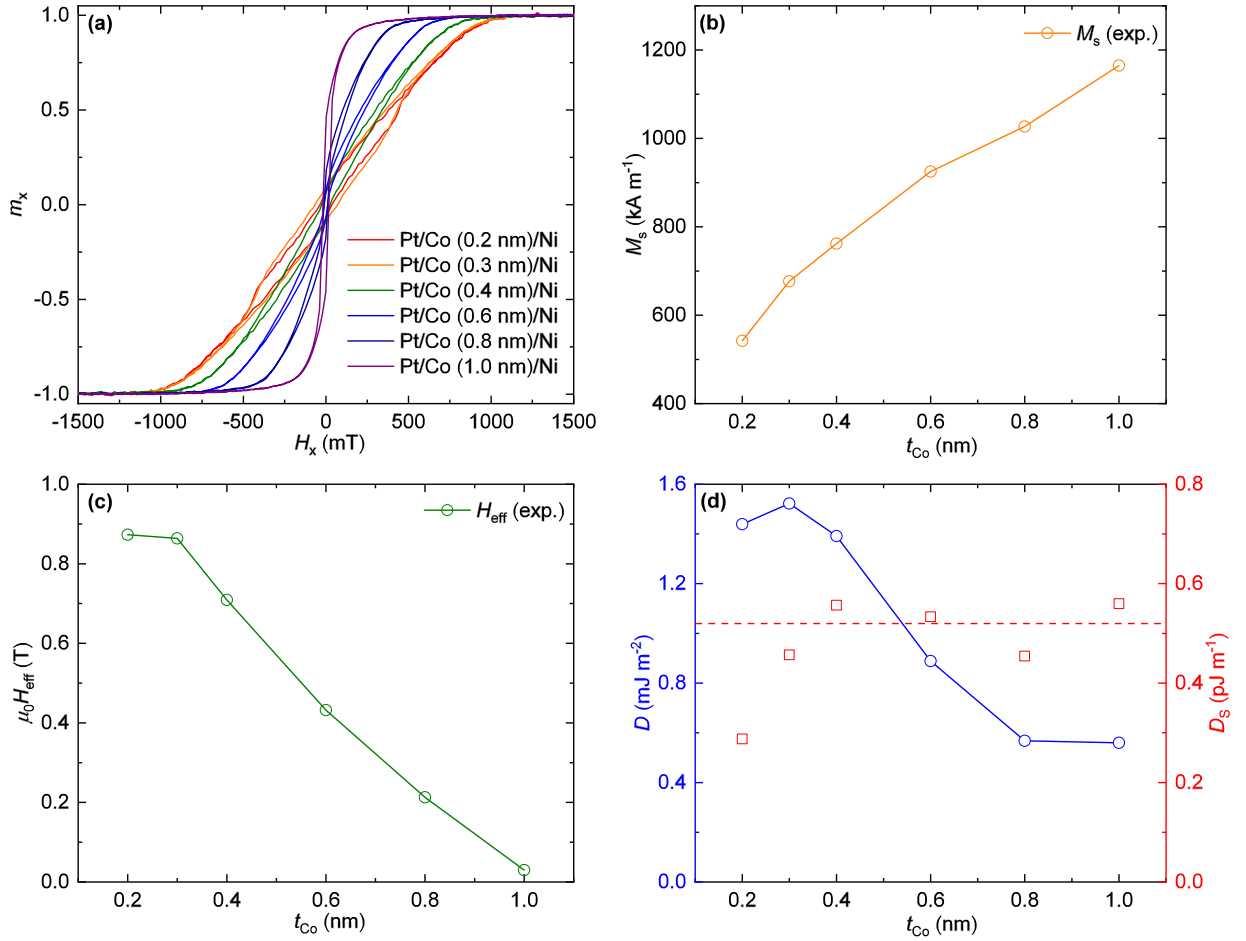
Figure 5.7: (a) IP magnetometry measurements in $[\text{Pt/Co}\ (t_{\text{Co}})/\text{Ni}\ (0.4\,\text{nm})]_6$ multilayers with $t_{\text{Co}} = 0.2, 0.3, 0.4, 0.6, 0.8$ and $1.0\,\text{nm}$. (b) Measured anisotropy field H_{eff} as a function of t_{Co}. (c) Measured M_{s} as a function of t_{Co} (circles). (d) Evolution of D and D_{s} as a function of t_{Co} (circles), measured with a stripe domain period measurement technique.

of the dipolar field [203]. However, controlling the magnetic properties of AF layers and easily detecting the nanoscale magnetic order inside fully compensated AF materials still constitute two considerable challenges facing AF-based skyrmions. In particular, the DM interaction has not been observed in AF thin layers so far.

A more accessible direction is to employ ferrimagnetic materials, in which two sublattices are aligned along opposite directions but are not fully compensating each other, resulting in a reduced total magnetization. The successful stabilisation of magnetic skyrmions in ferrimagnetic-material-based multilayers has been very recently reported [198, 204]. In ferrimagnetic materials, skyrmions largely behave as in ferromagnetic materials with reduced M_{s}, thus showing a reduction of the skyrmion Hall effect [198] and potentially of the skyrmion sizes at RT [204].

In this thesis a different approach has been chosen, in which antiferromagnetic skyrmions can be stabilised in antiferromagnetically coupled FM layers, also called a synthetic antiferromagnet (SAF) system. Hereafter, the term *antiferromagnetic skyrmion* designates a skyrmion structure whose total magnetization compensates across the thickness of the multilayer, irrespective of whether it is hosted in an AF layer or in a SAF system. The present approach is grounded on the fact that most of the dipolar field vanishes inside a SAF structure, because the magnetization compensates in average along the vertical dimension, but it does not vanish completely, which still allows the detection of the magnetization configurations. The antiferromagnetic coupling between the FM layers constituting a SAF system can be obtained from an interlayer indirect electronic exchange coupling, the so-
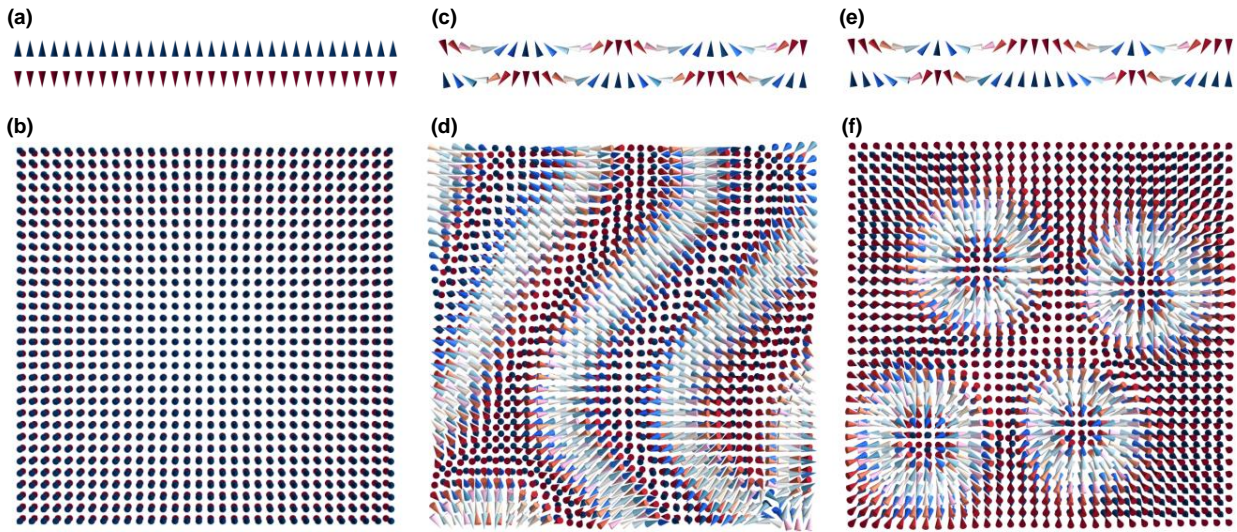
Figure 5.8: (a) Cut view facing $-\hat{\mathbf{y}}$ and (b) top view facing $\hat{\mathbf{z}}$ of a SAF system with large anisotropy. (c) Cut view facing $-\hat{\mathbf{y}}$ and (d) top view facing $\hat{\mathbf{z}}$ of a SAF system with vanishing anisotropy. (e) Cut view facing $-\hat{\mathbf{y}}$ and (f) top view facing $\hat{\mathbf{z}}$ of a SAF system with vanishing anisotropy and subject to a biasing interaction. Arrows indicate the direction of the magnetization, coloured according to m_z from red (-1) to blue (+1).

called Ruderman-Kittel-Kasuya-Yoshida (RKKY) coupling, mediated by an NM [205, 206]. The RKKY coupling between two layers is expressed by the energy density per unit surface $E_{\mathrm{RKKY}} = J_{\mathrm{RKKY}}(\mathbf{m_1} \cdot \mathbf{m_2})$, where J_{RKKY} is the coupling energy (density) — antiferromagnetic for $J > 0$ — and $\mathbf{m_1}$, $\mathbf{m_2}$ are the magnetization directions in the bottom and top FM of the pair of layers, respectively. For the simplest case of a SAF system formed by two FM layers, potential magnetic configurations are described hereafter, and are illustrated in Fig. 5.8.

For many years, perpendicular SAF systems have been utilised to bias magnetic layers in perpendicular spin-valve structures [207–209]. For this usage, it is ensured that each layer of the SAF system possesses a large perpendicular magnetic anisotropy, so that the ground state magnetic configuration is to have both subsystems saturated and antiparallel to each other, with $\mathbf{m_1}$ and $\mathbf{m_2}$ either pointing up (towards $+\hat{\mathbf{z}}$) or down (towards $-\hat{\mathbf{z}}$), as shown in Figs. 5.8a,b.

When the effective perpendicular magnetic anisotropy K_{eff} is reduced down to zero, the magnetization is no longer restrained to $+\hat{\mathbf{z}}$ and $-\hat{\mathbf{z}}$ directions, but becomes on the contrary free to rotate through the layer plane. In the case for which a significant DM interaction is present, the formation of non-collinear, cycloidal arrangements for the magnetic texture is favoured, which are called *spin-spirals*[1], as displayed in Figs. 5.8c,d. Usually, in ferromagnetic systems, spin-spirals are forbidden because distant dipolar interactions promote instead the formation of magnetic stripe domains separated by DWs. On the contrary here, due to the compensation of distant dipolar interactions in SAF systems, such spin-spirals are expected. Spin-spirals in SAF systems have not been studied so far, due to the lack of suitable experimental systems.

A quality of SAF systems is that they are insensitive to moderate external magnetic fields. Because such external fields act on equivalent, antiferromagnetically coupled magnetic moments, it results indeed that their actions compensate over the whole structure. Nevertheless, it is possible to obtain a biasing interaction for SAF systems by leveraging on interlayer electronic coupling with an additional magnetic layer, referred to here as a bias layer (BL). Notably, a uniform magnetization $\mathbf{m_b} = +\hat{\mathbf{z}}$ can be obtained in a BL with strong perpendicular magnetic anisotropy, and coupled ferromagnetically to the bottom layer of the SAF if the BL is located underneath the SAF. Due

---

[1]As they show a continuous rotation of $\mathbf{m}$, they are different from stripe domains.
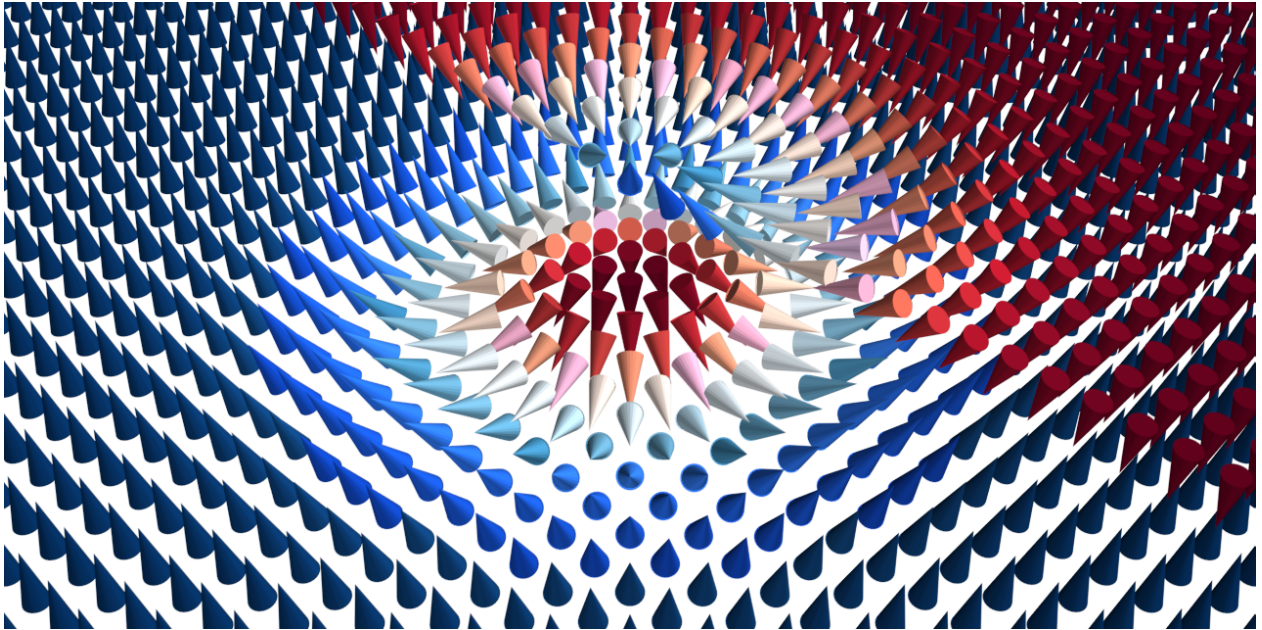
Figure 5.9: Perspective view of an antiferromagnetic skyrmion in a SAF system as obtained in simulations. The view of the top layer is cut at the centre of the skyrmion. Arrows indicate the direction of the magnetization, coloured according to m_z from red (-1) to blue (+1).

to this coupling, the parts of the spin-spiral with $\mathbf{m}_1 = +\hat{\mathbf{z}}$ are expected to expand, while the parts of the spin-spiral with $\mathbf{m}_1 = -\hat{\mathbf{z}}$ are expected to reduce. For a large enough coupling with the BL, some isolated and localised circular magnetization structures can be stabilised, which are actually antiferromagnetic skyrmions, as displayed in Figs. 5.8e,f. They are constituted of two vertically-aligned, individual skyrmions with opposite polarities and identical chirality, as shown by the perspective view displayed in Fig. 5.9.

Note that the configurations shown in Fig. 5.8 and Fig. 5.9 are not only examples representing the uniform, spin-spiral and antiferromagnetic skyrmion configurations, but are the result of micromagnetic simulations performed with MuMax^3, thus demonstrating numerically the viability of obtaining such structures, at least at $0\,\mathrm{K}$. Parameters are $A = 10\,\mathrm{pJ\,m^{-1}}$, $D = 0.6\,\mathrm{mJ\,m^{-2}}$, $M_\mathrm{s} = 1.2\,\mathrm{MA\,m^{-1}}$. For Figs. 5.8a,b, $K_\mathrm{u} = 1.025\,\mathrm{MJ\,m^{-3}}$, for Figs. 5.8c–f, $K_\mathrm{u} = 0.905\,\mathrm{MJ\,m^{-3}}$ (which corresponds to $K_\mathrm{eff} = 0\,\mathrm{MJ\,m^{-3}}$). For Figs. 5.8e,f, the strength of the bias layer coupling acting on the bottom layer of the SAF is $\mu_0 H_\mathrm{bias} = 20\,\mathrm{mT}$.

Let us summarise the requirements in order to stabilise antiferromagnetic skyrmions in a SAF system: (i) a strong antiferromagnetic RKKY coupling between the layers of the SAF; (ii) a significant DM interaction in the layers of the SAF; (iii) a vanishing effective perpendicular magnetic anisotropy K_eff in each layer of the SAF; (iv) a BL with strong perpendicular magnetic anisotropy; and (v) an electronic coupling between the BL and the SAF, adjusted to the suitable strength.

A specific type of Pt/Co/Ru-based multilayers has been developed for this purpose, whose detailed study is reported in Appendix A. A key for the optimisation of the multilayer structure is their sputter deposition, which allows a very good control over the deposition rates and durations, enabling a tuning of the thickness of each layer with a precision of around $0.3\,\text{Å}$. First, it is known that in Co/Ru/Co structures, an electronic antiferromagnetic interlayer coupling is present between the Co layers for the range of Ru layer thicknesses (0.7–0.9 nm) used here [202]. It has been shown that this RKKY coupling remains significant despite the insertion of Pt layers, which still transmit an attenuated RKKY coupling, across Pt/Co/Ru multilayer structures [209–211]. For $t_\mathrm{Pt} = 0.6\,\mathrm{nm}$, the RKKY coupling energy density term is determined as $J_\mathrm{RKKY} = 0.115\,\mathrm{mJ\,m^{-2}}$ (see §A.2). Second, the choice of the asymmetrical Pt/Co/Ru trilayer repetition unit enables symmetry-breaking along the stacking direction, which is required in order to obtain DM interaction. The
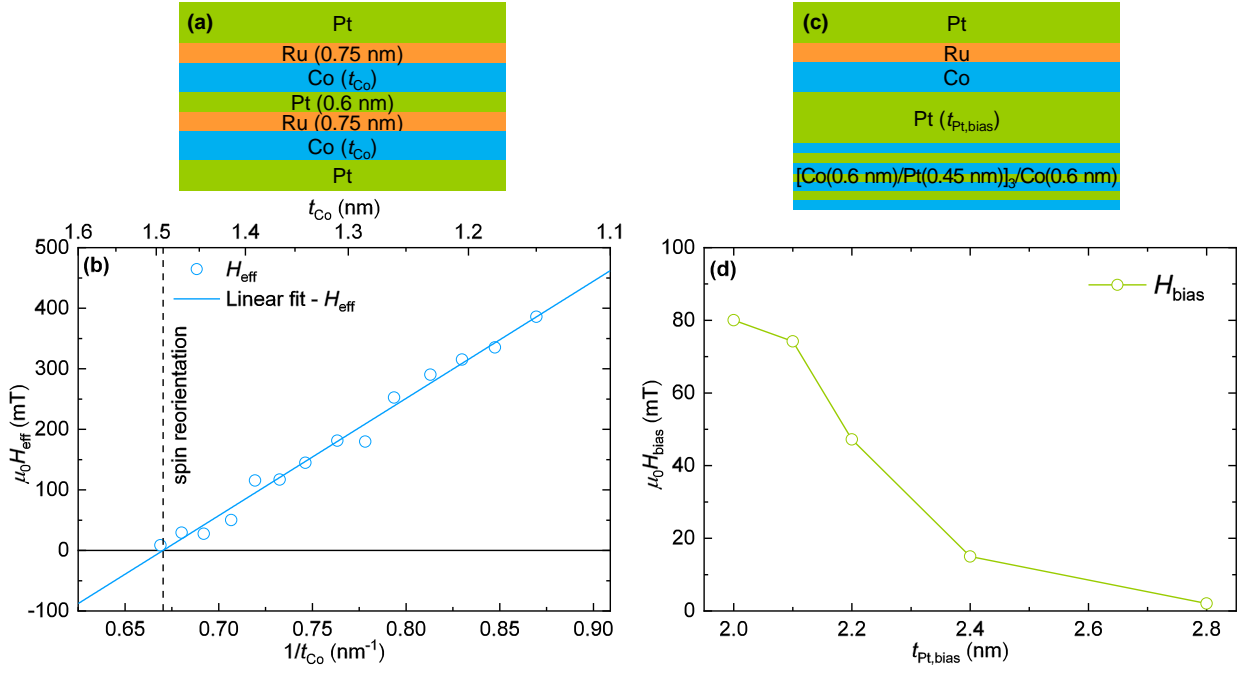
Figure 5.10: (a) Multilayer composition for the determination of the spin reorientation transition thickness of the SAF block. (b) Effective anisotropy field $\mu_0 H_{\text{eff}}$ (cyan circles) as a function of $1/t_{\text{Co}}$. Corresponding cyan line is a linear fit to the data points. It crosses zero at the spin-reorientation thickness $t_{\text{Co}} = 1.49\,\text{nm}$ (dashed line), at which $K_{\text{eff}} = 0$. (c) Multilayer composition for the determination of interlayer bias interaction of the BL block. (d) Evolution of $\mu_0 H_{\text{bias}}$ as a function of $t_{\text{Pt,bias}}$.

Pt/Co interfaces allow a large DM interaction, with an estimated $D_{\text{s}} = 1.12\,\text{pJ m}^{-1}$ (see §A.5), which remains unaffected by the insertion of Co/Ru interfaces [212]. Third, in such multilayer systems, a large interfacial perpendicular magnetic anisotropy K_{s} is obtained. As both DM interaction and perpendicular magnetic anisotropy share this interfacial origin, both K_{u} and D decrease with FM layer thickness, following a $1/t_{\text{Co}}$ dependence. As the effective anisotropy evolves as $K_{\text{eff}} = K_{\text{s}}/t_{\text{Co}} - \mu_0 M_{\text{s}}^2/2$, but the DM interaction as $D = D_{\text{s}}/t_{\text{Co}}$, a vanishing effective anisotropy together with a significant DM interaction can be achieved at the spin reorientation transition thickness of the SAF system represented in Fig. 5.10a. This thickness tuning approach is summarised in Fig. 5.10b, which displays the effective anisotropy field H_{eff} as a function of $1/t_{\text{Co}}$, showing that H_{eff} crosses zero at a spin reorientation transition thickness $t_{\text{SRT}} = 1.49\,\text{nm}$. The complete measurement procedure is described in details in §A.1 and §A.2. Finally, a Pt/Co-based multilayer is chosen for the BL, as it possesses a strong perpendicular anisotropy, see composition of the BL block in Fig. 5.10c and details about this choice in §A.6. As shown in Fig. 5.10d, the strength of the coupling between this Pt/Co-based BL and the SAF system (determined by measurements on specific structures, as described in §A.7) can be controlled by tuning the thickness of the intermediate Pt layer, in the range of $t_{\text{Pt,bias}} = 2.0\text{--}2.8\,\text{nm}$. This tunability of the biasing interaction is essential to be able to stabilise antiferromagnetic skyrmions. From the point of view of magnetic properties of the layers and their materials, **a Pt/Co/Ru-based SAF system biased by a Pt/Co-based multilayer appear to be perfectly suitable** to attempt the stabilisation and observation of antiferromagnetic skyrmions at RT.

In order to demonstrate it, three SAF-system-based multilayers have been selected: (i) a SAF system with a significant perpendicular anisotropy (Fig. 5.11a); (ii) a SAF system with vanishing perpendicular anisotropy (Fig. 5.11b); and (iii) a SAF system with vanishing perpendicular aniso- tropy deposited above a BL, which are separated from each other by a spacer Pt layer of thickness $t_{\text{Pt,bias}} = 2.2\,\text{nm}$ (Fig. 5.11c). Each of these three multilayers constitute the experimental reali-
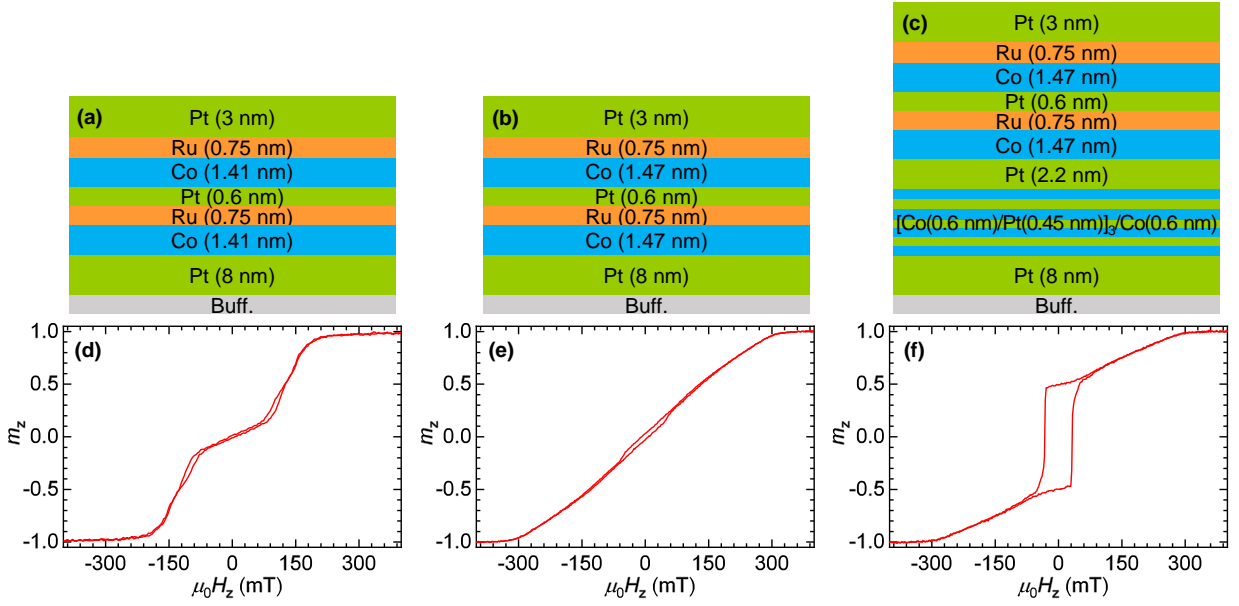
Figure 5.11: Multilayer composition for the SAF system (a) with significant perpendicular magnetic anisotropy, (b) with vanishing perpendicular magnetic anisotropy and (c) with vanishing perpendicular magnetic anisotropy on top of a BL with a Pt (2.2 nm) spacer. OOP magnetometry loops for the SAF system (d) with perpendicular magnetic anisotropy, (e) with vanishing perpendicular magnetic anisotropy and (f) with vanishing perpendicular magnetic anisotropy on top of a BL with a Pt (2.2 nm) spacer.

sation of one of the systems of the predictive simulations displayed above, corresponding to Figs. 5.8a,c,e, respectively. Their OOP magnetometry characterisations are provided in Figs. 5.11d–f, respectively. The loop for system (i) indeed exhibits two switching steps[2], characteristic of antiferromagnetic RKKY coupling of perpendicularly magnetized layers, while the loop of system (ii) exhibits a linear field susceptibility followed by magnetic saturation at $2\mu_0 H_{\mathrm{RKKY}}$, characteristic of antiferromagnetic RKKY coupling of layers without anisotropy [213]. The loop of system (iii) is similar to the one of system (ii), but the loop of the SAF is superimposed with the loop of the BL layer.

The magnetic configurations in these three systems have been then observed by MFM (see details in Appendix B). Each system has been first demagnetized by the application of a decaying, alternating IP magnetic field. For system (iii) only, the demagnetization has been followed by the saturation of the BL through the application of an OOP magnetic field of magnitude $\mu_0 H_{\mathrm{z}} = 60\,\mathrm{mT}$. The image recorded for system (i) is displayed in Fig. 5.12a. It features a few bended lines of mixed but mostly dark contrast, separating uniform domains showing no contrast. This corresponds to the magnetic configuration sketched in Fig. 5.8a, hosting uniform, antiferromagnetic domains with perpendicular magnetic order, separated by DWs. The DWs are appearing because of the small vertical separation between both Co layers, which generates in total a small but non-cancelling dipolar field. The image recorded for system (ii) is displayed in Fig. 5.12b, in which intertwined contrast variations appear. As detailed below, such magnetic signal can be assigned to the residual stray field generated by a spin-spiral order. Cuts through the spin-spiral image are displayed in Fig. 5.12d, which indeed correspond to sinusoidal profiles, according to the fitted curves. Cuts b2 and b3 exhibit a periodicity of around 300 nm, slightly more for b1. In order to get the profile of the spirals more accurately, avoiding any perturbations or deformations originating from the presence of a magnetic tip, the same multilayer has been imaged by nitrogen-vacancy

---

[2]These steps are not very sharp, maybe indicating a reversal through domain formation.

(NV)-centre microscopy by the team of V. Jacques, based in Montpellier. In this experiment, the local magnetic field is imaged by monitoring the photoluminescence of an NV defect located at the extremity a scanning diamond tip. It can thus provide maps of the dipolar field generated by a magnetic configuration with nm-scale resolution and very good sensitivity, without causing any perturbations. The characteristic periodicity of the spirals observed with NV-centre microscopy is $\lambda \approx 260\,\text{nm}$. Finally, the image recorded for system (iii) is displayed in Fig. 5.12c. In this image, several isolated dots with dark contrast are observed, which is interpreted as the stray field signature of antiferromagnetic skyrmions. An analysis of the signal expected from isolated antiferromagnetic skyrmions is provided in Appendix B. Cuts through the isolated dots are displayed in Fig. 5.12e, and fitted to Gaussian peak functions in order to extract a characteristic width. In the very simple assumption that the width at half maximum is directly linked to the skyrmion diameter, values for the radius $r_{\text{MFM}} \approx 65\,\text{nm}$, $50\,\text{nm}$, $58\,\text{nm}$ and $55\,\text{nm}$ are obtained for cuts c1, c2, c3 and c4, respectively. The real size of the antiferromagnetic skyrmions is definitely smaller than these measures, due to probe tip size effects and spreading of the dipolar fields with lift height in MFM. Further imaging of this multilayer with NV-centre microscopy is on-going, in order to characterise more precisely and hopefully, even quantitatively, the observed profiles.

The measurements of the magnetic configuration in these three SAF systems have actually been performed under low pressure, in order to increase the sensitivity of the measurement by enhancing the resonance quality factor Q of the probe cantilever. Otherwise, no magnetic signal above the noise level is measured for MFM imaging performed under usual atmospheric conditions. This constitutes a first indication that the magnetization in the system is compensated, as ferromagnetic skyrmions can be routinely observed in ambient conditions and would result in much larger signal amplitudes than what is observed here.

In order to provide a more quantitative comparison of signal levels, the magnetic contrast observed for the demagnetized BL is shown in Fig. 5.13a. The signal obtained from this ferromagnetic [Pt $(0.45\,\text{nm})$/Co $(0.6\,\text{nm})]_4$ structure (which contains in total around the same amount of magnetic moments than the SAF system) is more than one order of magnitude larger than the signal obtained from the SAF structures in Figs. 5.12a–c (note the different scales for the phase shift in lift mode). Notably, the height of a cut profile through the small circular domain near the centre of the image is larger than $10°$, to be compared to the $1°$ scale in other images. This comparison strongly supports that the features observed in the present SAF images are generated by compensated magnetic moments.

Some background signal, weak compared to the main features of the images, appears everywhere, as can be better seen in the uniform domains of Fig. 5.12a, for example. It may originate from small thickness or magnetization variations in the BL and SAF parts of the structure, due to the polycrystalline nature of the materials used in these multilayers. This background signal has been separately measured from a saturated BL alone and from a uniform SAF with anisotropy alone, as displayed in Figs. 5.13b,c respectively. Again, the fact that the magnetic features that we are imaging have a contrast level only slightly larger than this fluctuation background supports that they are generated by compensated magnetic moments.

Further information can be obtained from analysing the periodicity of the spin-spirals observed in Fig. 5.12b. Let us first consider the case of an isotropic, single layer system. For a spin-spiral propagating along x and uniform along the transverse direction y, the energy per unit surface of the magnetization texture is obtained as

$$\varepsilon = t\left[A \sum_{i=x,y,z} \left(\frac{dm_i}{dx}\right)^2 + D\left(m_z \frac{dm_x}{dx} - m_x \frac{dm_z}{dx}\right) + K_{\text{eff}}\left(1 - m_z^2\right) + \varepsilon_{\text{lr}} \right] \tag{5.9}$$

where the effective anisotropy is introduced together with ε_{lr}, the correction related to distant dipolar interactions. This correction is equal to $-\mu_0 M_s\left(\mathbf{m}\mathbf{H}_{\text{dem}} + M_s m_z^2\right)/2$, the difference between dipolar energies obtained considering the explicit solution for the dipolar field $\mathbf{H}_{\text{dem}}$ and
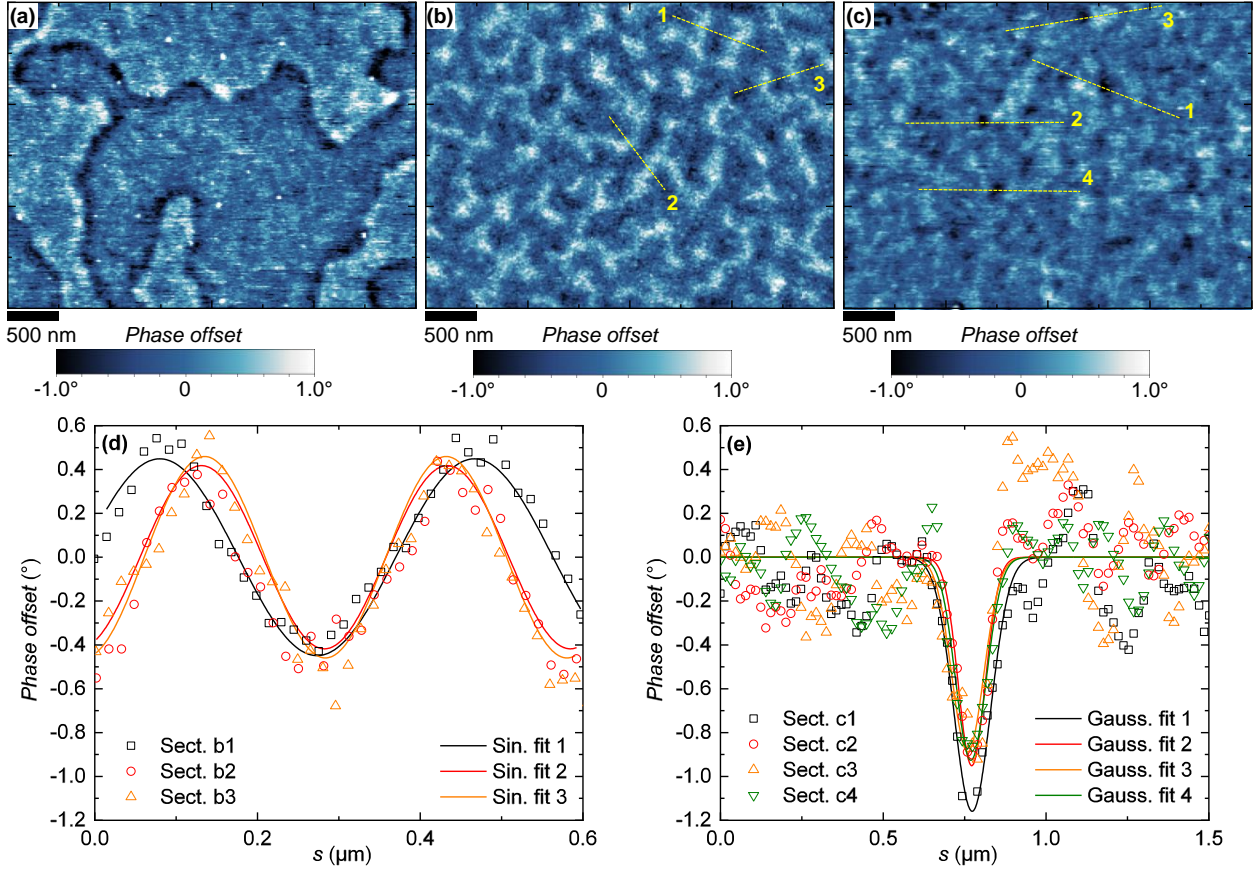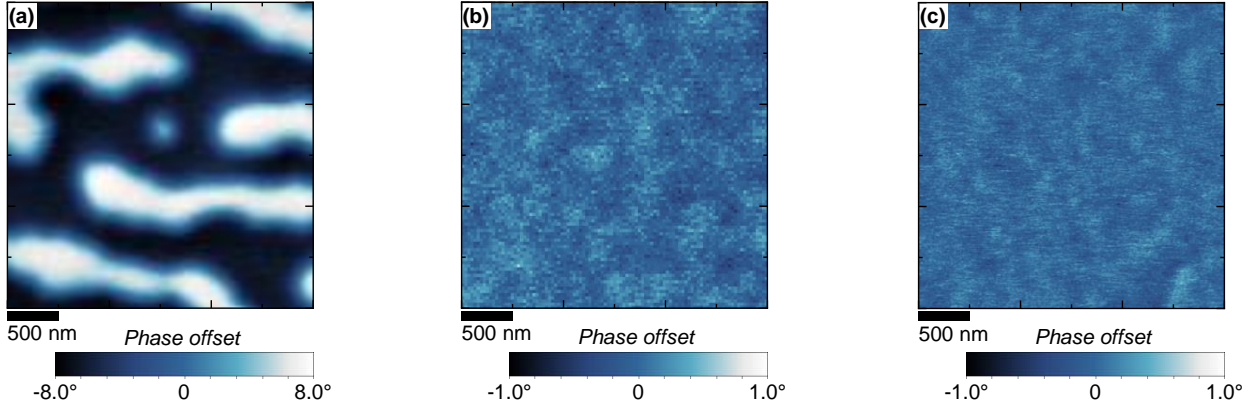
Figure 5.12: MFM images recorded at zero external field for the SAF system (a) with perpendicular magnetic anisotropy, (b) with vanishing perpendicular magnetic anisotropy and (c) with vanishing perpendicular magnetic anisotropy on top of a BL with a Pt (2.2 nm) spacer. Images size is 4 μm × 3 μm. The phase shift in lift mode is given by the colour scale below each image. Numbered yellow lines indicate the location of the cuts performed in the analysis of images b and c. (d) Cut sections b1, b2 and b3 of the MFM signal (phase offset in lift mode) acquired in the SAF system with vanishing perpendicular magnetic anisotropy. Solid curves are fits of the measurement points to sinusoids. (e) Cut sections c1, c2, c3 and c4 of the MFM signal (phase offset in lift mode) acquired in the BL-SAF system. Solid curves are fits of the measurement points to Gaussian peaks. The horizontal axis for cut sections is the distance along each corresponding line in panels b and c.

considering the effective anisotropy approximation. For the system to form spontaneously spin-spirals, it is necessary that the DMI parameter D be larger than the DM interaction critical value $D_{c} = 4\sqrt{A|K_{eff}|}/\pi$ [61]. In general, the spin-spiral shows a non-regular rotation of the magnetization, due to the influence of the anisotropy combined with distant dipolar interactions [61, 214]. For a vanishing anisotropy and negligible dipolar interactions however, as is expected for the present compensated SAF structure, the minimal energy state is a regular magnetic cycloid with Néel ordering, which is indeed confirmed by the simulation displayed in Fig. 5.8c. As the magnetization is only slowly varying along the cycloidal order (on a scale much longer than the magnetic layer spacing $p = 2.82$ nm), indeed $\varepsilon_{lr} \approx 0$ due to the compensation of the magnetization. In our SAF system (ii), Néel cycloids are thus expected in both layers, for which we can simplify (5.9) into

$$\varepsilon = 2t_{Co}\left[A\left(\frac{dm_{x}}{dx}\right)^{2} + A\left(\frac{dm_{z}}{dx}\right)^{2} + D\left(m_{z}\frac{dm_{x}}{dx} - m_{x}\frac{dm_{z}}{dx}\right)\right] \quad (5.10)$$

where the prefactor $2t_{Co}$ stands for the summation over the two antiferromagnetically coupled

Figure 5.13: MFM images recorded at RT and zero external field for (a) the demagnetized BL with alternate up and down domains, (b) the saturated BL inside a single domain and (c) the saturated SAF system with perpendicular magnetic anisotropy and no BL inside a single domain. Images size is $3\,\mu\text{m} \times 3\,\mu\text{m}$. The phase shift in lift mode is given by the colour scale below each image.

layers, which have identical energies, as one spin-spiral is simply shifted by half a period compared to the other. Its solution is found from variational approach and is a cycloid of the form $[m_x, m_y, m_z] = [\cos(kx), 0, \pm\sin(kx)]$, depending on the sign of D [61]. The RKKY coupling energy is zero compared to the ground state in this simple model, as all moments are perfectly antialigned. Using this solution, we can express the average energy density of the cycloid state

$$\varepsilon_k = \frac{k}{2\pi}\int_0^{2\pi/k} \varepsilon\, dx = \frac{2kt_{\text{Co}}}{2\pi}\int_0^{2\pi/k}\left(k^2 A - kD\right)dx = 2t_{\text{Co}}\left(k^2 A - kD\right) \tag{5.11}$$

as a function of the characteristic propagation wavenumber k. Minimising this energy with respect to k yields $k = D/2A$, that is, a periodicity of $4\pi A/D$. Using $A = 10\text{–}14\,\text{pJ}\,\text{m}^{-1}$ [7], we can estimate from the experimental periodicity in Fig. 5.12b and obtained by NV-centre microscopy that $D = 0.5\text{–}0.7\,\text{mJ}\,\text{m}^{-2}$. This value falls close compared to $D = 0.76\,\text{mJ}\,\text{m}^{-2}$ found from domain spacing measurements performed on similar, ferromagnetically coupled multilayers (see §A.5). The difference could originate in a weak anisotropy remaining in the SAF, as 1.47 nm may differ from the precise value of the spin reorientation thickness by a few percent, or in higher-order anisotropy terms. Note that determining the spin-spiral periodicity constitutes an independent measurement of the DM interaction amplitude for the present type of system, which could be used in future studies if a way to improve the precision of such measurements is found. Finally, the observed periodicity is therefore found compatible with the formation of spin-spirals inside the SAF system.

A conclusive experimental result is given by the observation of the antiferromagnetic skyrmions present in system (iii) under applying an external OOP field, in order to better understand the origins of their magnetic contrast. Images recorded for increasing values of $\mu_0 H_z = 20\,\text{mT}$, $60\,\text{mT}$ and $100\,\text{mT}$ are shown in Figs. 5.14a–c, respectively. By applying moderate fields, the magnetic contrast of the dark spots gradually increase, see Figs. 5.14a,b. This behaviour is consistent with the expected modulation of skyrmion size in the bottom and top layers, which should degrade the magnetic compensation and result in larger contrasts inside the antiferromagnetic skyrmion. In Fig. 5.14b, interaction with the magnetic tip can be noticed from the dark horizontal scars around the top skyrmion, probably due to the lower degree of compensation of the total magnetic moment of the antiferromagnetic skyrmion. At 100 mT and beyond, the dark spots even disappear, consistent with the annihilation of the antiferromagnetic skyrmions when the RKKY coupling between the two layers of the SAF is overcome.

Note that such isolated antiferromagnetic skyrmions were not observed for Co layer thicknesses
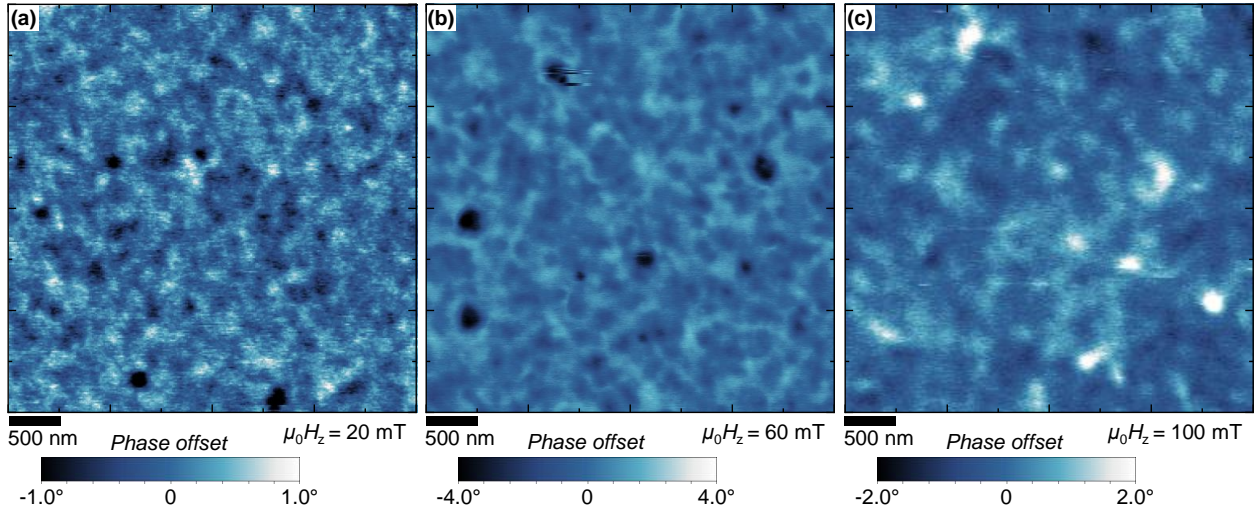
Figure 5.14: MFM observations of the BL-SAF with a Pt (2.2 nm) spacer, recorded under an external field of (a) $\mu_0 H_z = 20$ mT, (b) $\mu_0 H_z = 60$ mT and (c) $\mu_0 H_z = 100$ mT. Images size is 4 μm × 4 μm. The phase shift in lift mode is given by the colour scale below each image.

too distant from the spin reorientation transition, nor for much weaker or much stronger biasing interaction with the BL. This is consistent with the interpretation of having antiferromagnetic skyrmions at $t_{\mathrm{Pt,bias}} = 2.2$ nm, as for a weaker $\mu_0 H_{\mathrm{bias}}$ (larger $t_{\mathrm{Pt,bias}}$), the spin-spiral remains unaffected, while for a stronger $\mu_0 H_{\mathrm{bias}}$ (smaller $t_{\mathrm{Pt,bias}}$), the antiferromagnetic skyrmions are expected to be unstable. In conclusion, it is found that for tailored magnetic properties, biased Pt/Co/Ru-based SAF multilayer systems **can host antiferromagnetic skyrmions**.

5.5 Expectations for antiferromagnetic skyrmions in SAF systems

The MFM images recorded in the previous section provide an experimental demonstration and a qualitative understanding of the stabilisation of antiferromagnetic skyrmions in SAF systems. However, the resolution of the MFM imaging technique does not allow for a quantitative analysis of the skyrmion size or profiles. In the aim of obtaining a more quantitative understanding of the properties of antiferromagnetic skyrmions in SAF systems, the interlayer RKKY interaction as well as the biasing interaction have been incorporated in the numerical model of Chapter 2, in order to predict their expected radial profiles. The m_z profiles are obtained for $\mu_0 H_{\mathrm{bias}} = 20$–80 mT, $D = 0.3$–0.8 mJ m^{-2}, and displayed in Figs. 5.15a–d. The results have been compared to the profiles provided by MuMax[3] (circles in Figs. 5.15a,b), which shows an excellent agreement. Due to the strong antiferromagnetic coupling inside the SAF system, a rather small deviation from $\mathbf{m}_1(r) = -\mathbf{m}_2(r)$ is found, but it still explains the detectable MFM signal (as shown in Appendix B, the dipolar field resulting from these antiferromagnetic skyrmion configurations can be predicted, which suggests measurable field gradients). The skyrmion size increases with D, the DM interaction being a stabilising interaction, and reduces with $\mu_0 H_{\mathrm{bias}}$, the biasing interaction being a destabilising interaction. Therefore, the antiferromagnetic skyrmion state results from the equilibrium between these two interactions.

In order to investigate the benefits of antiferromagnetic skyrmions hosted in SAF systems for RT stability of small skyrmions, the energy barrier of the minimum energy path towards skyrmion annihilation is evaluated following the method established in §2.6. As shown in Fig. 5.16a, all energy terms decrease towards zero for $r_{\mathrm{sk}} \to 0$ except the exchange interaction term E_{A}, which validates the approach for determining the energy barrier. An example of energy barrier determination is
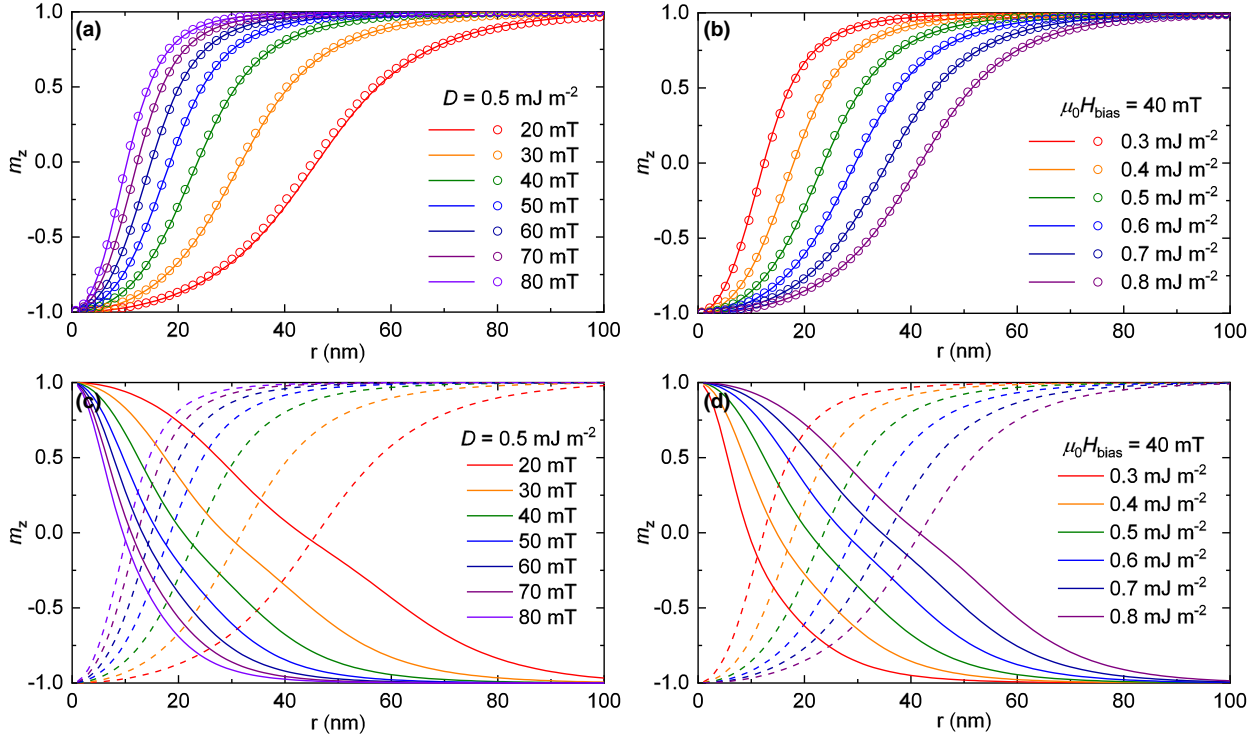
Figure 5.15: (a) Magnetization profiles $m_z(r)$ in the bottom layer of the SAF for $D = 0.5\,\mathrm{mJ\,m^{-2}}$ and $\mu_0 H_{\mathrm{bias}} = 20\text{–}80\,\mathrm{mT}$. (b) Magnetization profiles $m_z(r)$ in the bottom layer of the SAF for $\mu_0 H_{\mathrm{bias}} = 40\,\mathrm{mT}$ and $D = 0.3\text{–}0.8\,\mathrm{mJ\,m^{-2}}$. Coloured lines display the results of the numerical model for axisymmetric profiles, while circles display the results obtained with MuMax^3. (c) Same than (a) for the top layer of the SAF (solid lines). (d) Same than (b) for the top layer of the SAF (solid lines). Dashed lines remind the profiles in the bottom layer of the SAF.

displayed in Fig. 5.16b, for $D = 0.5\,\mathrm{mJ\,m^{-2}}$ and $\mu_0 H_{\mathrm{bias}} = 80\,\mathrm{mT}$, and the $(D, \mu_0 H_{\mathrm{bias}})$ diagrams for the skyrmion radius r_{sk} and energy barrier E_{B} are shown in Figs. 5.16c,d, respectively. Similar as before, the thermal stability is proportional to D, which could **enable sub-10 nm skyrmions stable at RT**, for $D \geq 0.7\,\mathrm{mJ\,m^{-2}}$. Note that as expected in the present SAF system, anisotropy term E_{Ku} and dipolar interactions term E_{dem} almost completely compensate (see curves in Fig. 5.16c), as a result of the compensation of the magnetization.

Beyond the present system, the thermal stability of skyrmions can be expected to be enhanced in SAF systems formed by more layers (4 layers, 6 layers, *etc.*, see principle in Fig. 5.17a). Note that a limit to enhancing the thermal stability of antiferromagnetic skyrmions by coupling more layers inside SAF systems exists, which lies in the transition towards ferromagnetic stripe domains occurring when dipolar interactions between layers overcome the RKKY coupling [215–218]. Stronger RKKY coupling fields between the FM layers are then required to couple antiferromagnetically 6 layers or more, but it has been verified that at least 4 layers could be used while keeping the present SAF system properties. Similar as above, $(D, \mu_0 H_{\mathrm{bias}})$ diagrams for the skyrmion radius r_{sk} and energy barrier E_{B} are shown in Figs. 5.17b,c, respectively, now for $L = 4$ antiferromagnetically coupled FM layers. Sub-10 nm skyrmions stable at RT can be achieved for $D \geq 0.4\,\mathrm{mJ\,m^{-2}}$.
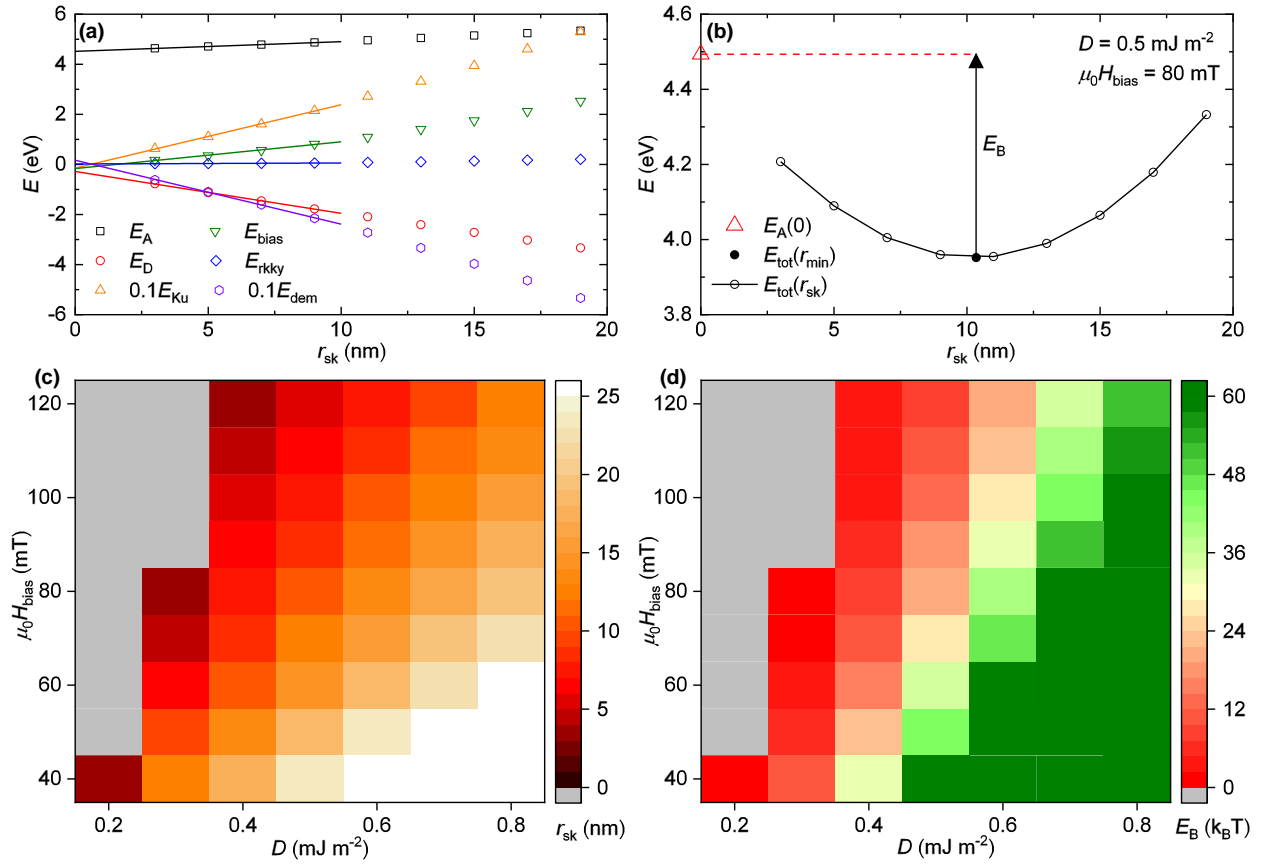
Figure 5.16: (a) Different terms of the skyrmion energy E_{tot} as a function of r_{sk}. (b) E_{tot} as a function of r_{sk}, and calculation of the energy barrier E_{B}, the energy difference between the energy minimum (filled triangle) and the collapse radius ($r_{\text{sk}} \to 0$) (red triangle), for $D = 0.5\,\text{mJ}\,\text{m}^{-2}$ and $\mu_0 H_{\text{bias}} = 80\,\text{mT}$. ($D$, $\mu_0 H_{\text{bias}}$) diagrams for (c) r_{sk} and (d) E_{B}. Grey indicates that the skyrmion configuration collapses towards zero radius.
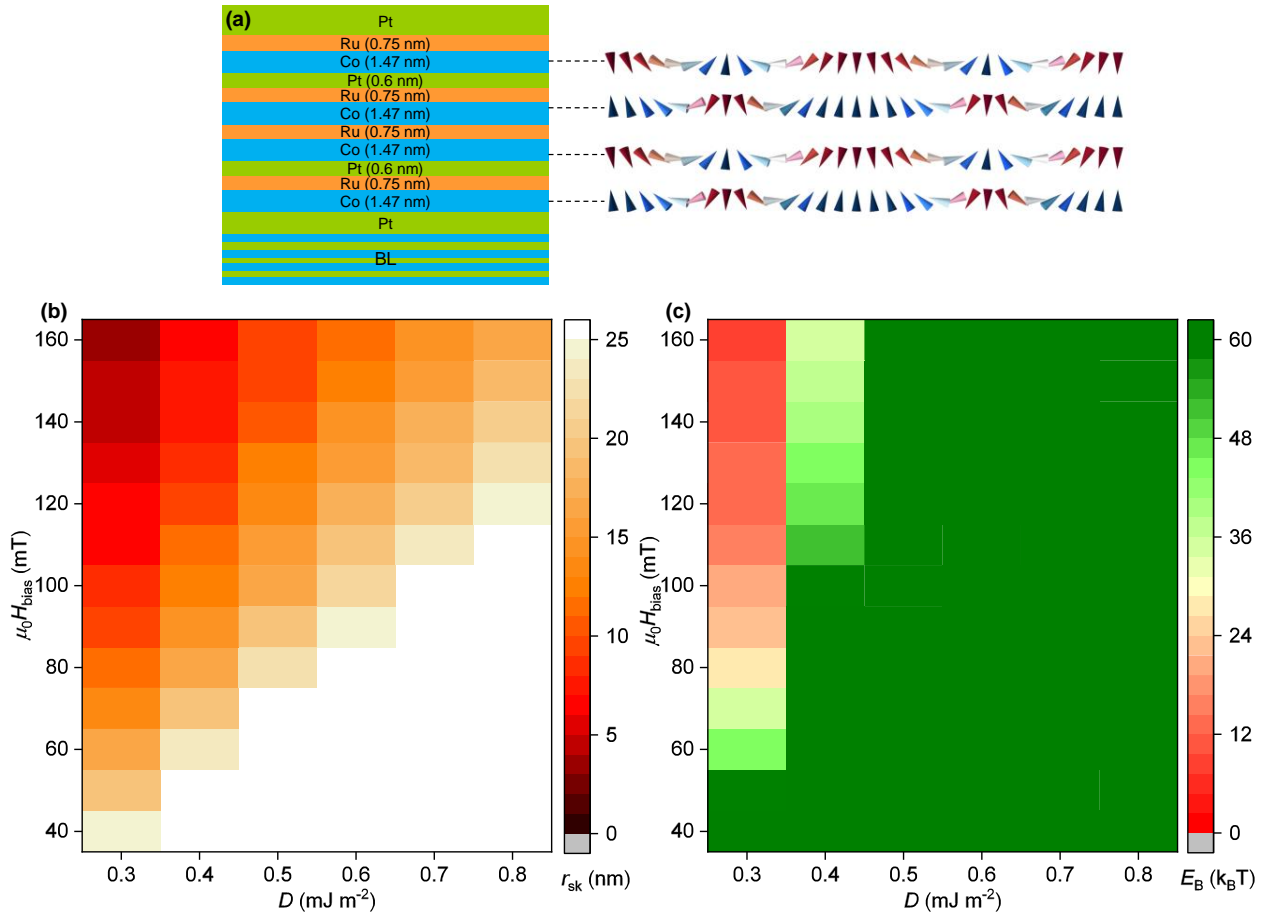
Figure 5.17: (a) Schematic of the proposed SAF system with $L = 4$, and possibly resulting configuration with the direction of **m** alternating every two layers. For a SAF system with $L = 4$, $(D, \mu_0 H_{\text{bias}})$ diagrams for (b) r_{sk} and (c) E_{B}.

<div align="right">

Chapter 6

</div>

Perspective: what is next?

6.1 Summary

Before the beginning of this work, specific magnetic multilayers were just conceived, which allow the stabilisation of magnetic skyrmions at room temperature. At this time, many questions were remaining with regard to their shape, and to the mechanisms ensuring their stability in multilayers. An objective was to be able to reduce the size of the skyrmions while preserving their mobility and the possibilities for their manipulation. This thesis tackled these issues by attempting to find how to balance properly the different magnetic interactions determining the skyrmion properties in multilayers, in order to achieve fast, and small skyrmions.

In **Chapter 2**, a numerical model of isolated magnetic skyrmions stabilised in multilayers is designed. It allows to obtain a more precise description of the skyrmion profiles than previous analytical models. By using the cylindrical symmetry of skyrmions, the calculation of the dipolar interaction fields and energies is greatly simplified. This model has been verified by comparing its results against a standard micromagnetic simulation tool. It allows to distinguish properly skyrmions and bubbles according to their energy dependence with size. An equivalent of this model in the linear geometry allows to assess the stability of skyrmions against elongation into stripe domains. Finally, the energy dependence with size of skyrmions that can be provided allows to approximate the thermal stability of isolated skyrmions. This model has proven useful in the analysis of skyrmion properties for many occasions during this thesis.

In **Chapter 3**, three different essential functionalities for electrical skyrmion control and manipulation are demonstrated in magnetic multilayers. The first is skyrmion nucleation, which is achieved with pulse current injection either in uniform geometries or in geometric constrictions. The mechanism is analysed as being mainly of thermal origin. The second is skyrmion displacement, which is demonstrated under spin-orbit torques obtained from adjacent heavy-metal layers. The third is the individual skyrmion detection, which can be realised by transverse conductivity measurements in Hall configuration devices, through the anomalous Hall effect resulting from the skyrmions. No evidence of topological Hall effect could be obtained in the present multilayer system. These three skyrmion manipulation schemes are compatible with each other, and promising for the future conception of skyrmion-based devices.

In **Chapter 4**, the question of how to enhance the efficiency of skyrmion motion is addressed. On the one side, the pinning behaviour of skyrmions under current-induced motion is evidenced. A model for the granular aspect of magnetic multilayers allows to quantify the impact of materials inhomogeneities in causing pinning. The effect of grains size and type is analysed, which provides two directions for recovering a lower pinning in multilayers: either to obtain epitaxial films with very extended grains, or on the contrary to target amorphous structures free of grains. On the other side, the role of spin-current injection is analysed. It is demonstrated that in magnetic multilayers, hybrid chiral skyrmions can form due to the competition between the Dzyaloshinskii-Moriya and dipolar interactions. The formation of such hybrid chiral textures is evidenced experimentally in domain-walls using an X-ray diffraction technique. The presence of hybrid chirality requires to reconsider

the spin-injection geometry in order to drive magnetic skyrmions efficiently and increase their mobility. Under the guidance of these considerations, experimental studies of skyrmion motion are realised, which demonstrate velocities of the order of $40 \, \mathrm{m \, s^{-1}}$ close from flow motion, for skyrmions of around 40 nm in radius, exhibiting a skyrmion Hall angle of around 15–25°. A perspective for this part is the possibility of cancelling the skyrmion Hall effect relying on hybrid chiral skyrmions, which is theoretically proposed.

In **Chapter 5**, the objective of reducing the size of skyrmions is pursued. It is shown that the question of their size is intimately related to the question of their thermal stability, which is enhanced for lower effective anisotropy, stronger Dzyaloshinskii-Moriya interactions, larger number of interfaces, and weaker dipolar interactions. In the aim of weakening the dipolar interactions, two directions are investigated experimentally. The first is the reduction of the magnetization by combination of different ferromagnetic materials in Co/Ni/Co layers. It is found that due to the absence of alloying effects at the usual layer thicknesses, in a simple view no enhancement of the thermal stability of skyrmions in Co/Ni/Co layers is expected. However, it is proposed that the realisation of Pt/Co/Ni multilayers with atomically thin layers may allow to stabilise smaller skyrmions after further optimisation. The second direction that is investigated to avoid dipolar interactions is the design of synthetic antiferromagnet multilayered systems. It is shown that the stabilisation of antiferromagnetic skyrmions can be anticipated in biased synthetic antiferromagnets. Suitable Pt/Co/Ru multilayers are designed, and optimised in **Appendix A**, which possess all the properties required to stabilise antiferromagnetic skyrmions. Subsequently, spin-spirals (stabilised in synthetic antiferromagnets) and antiferromagnetic skyrmions (stabilised in biased synthetic antiferromagnets) are directly observed at room temperature using magnetic force microscopy. The modelling of antiferromagnetic skyrmions predicts the possibility of stabilising room-temperature sub-10 nm skyrmions.

In the discussions of Chapters 4 and 5, either we have attempted to enhance the current-induced velocity or we have sought to reduce the size of room-temperature skyrmions, but so far we have never addressed these two objectives together. Such fast and small skyrmions would nevertheless be very beneficial for applications. As an outlook, we can try to answer the following question: can we realise room-temperature stable skyrmions that tend to be simultaneously mobile and compact?

6.2 Outlook: small and mobile

Relation between size and velocity — To tackle this question a first answer can be drawn, from the theoretical side, by use of the Thiele modelling. We can study for a typical multilayer how the different quantities, namely, SOT forces $F_{\mathrm{x,y}}$ and dissipation factor $\mathcal{D}$, evolve with the size of the skyrmions. We consider skyrmion motion in the absence of boundaries (case of an infinite film, Fig. 3.6a) and directed along boundaries (along track edges, Fig. 3.6b). The total F and $\mathcal{D}$ are obtained, for $L = 3$, from the micromagnetic skyrmion profiles found with the model of Chapter 2 and are plotted as a function of r_{sk} in Fig. 6.1c. The size of the skyrmion is tuned by the external field ranging $\mu_0 H_{\mathrm{ext}} = 10$–70 mT. Parameters are here $A = 10 \, \mathrm{pJ \, m^{-1}}$, $D = 1.35 \, \mathrm{mJ \, m^{-2}}$, $M_{\mathrm{s}} = 0.956 \, \mathrm{MA \, m^{-1}}$, $K_{\mathrm{u}} = 0.717 \, \mathrm{MJ \, m^{-3}}$, $\theta_{\mathrm{eff}} J = 1 \times 10^{10} \, \mathrm{A \, m^{-2}}$ and $\alpha = 0.2$, in a multilayer geometry given by $t_{\mathrm{FM}} = 0.6$ nm and $p = 2.4$ nm. The total force F appears close from being proportional to r_{sk}, while $\mathcal{D}$ also increases with r_{sk} but shows a positive offset preventing it from crossing zero for $r_{\mathrm{sk}} \to 0$, consistent with the expressions displayed in (3.6). As G is constant, the variations of $\mathcal{D}$ determine the ones of the dissipation to deflection ratio $\eta = \alpha \mathcal{D}/G$. The resulting velocities are displayed in Fig. 6.1b for the two boundary conditions, infinite plane (v_{inf}, dashed line) and track (v_{edge}, solid line). In the infinite plane case, according to (3.7) v_{inf} is proportional to $F/\sqrt{1 + \eta^2}$, which explains the particular aspect of the velocity curve with radius, and why $v_{\mathrm{inf}} \to 0$ when $r_{\mathrm{sk}} \to 0$. In the track case, v_{edge} is proportional to F/η according to (3.10). As the variations of F and η partially compensate each other at large radii, v only slightly reduces when r_{sk} decreases down to 40 nm. However, as $\mathcal{D}$ and hence η converge to a non-zero value when $r_{\mathrm{sk}} \to 0$, v drops at
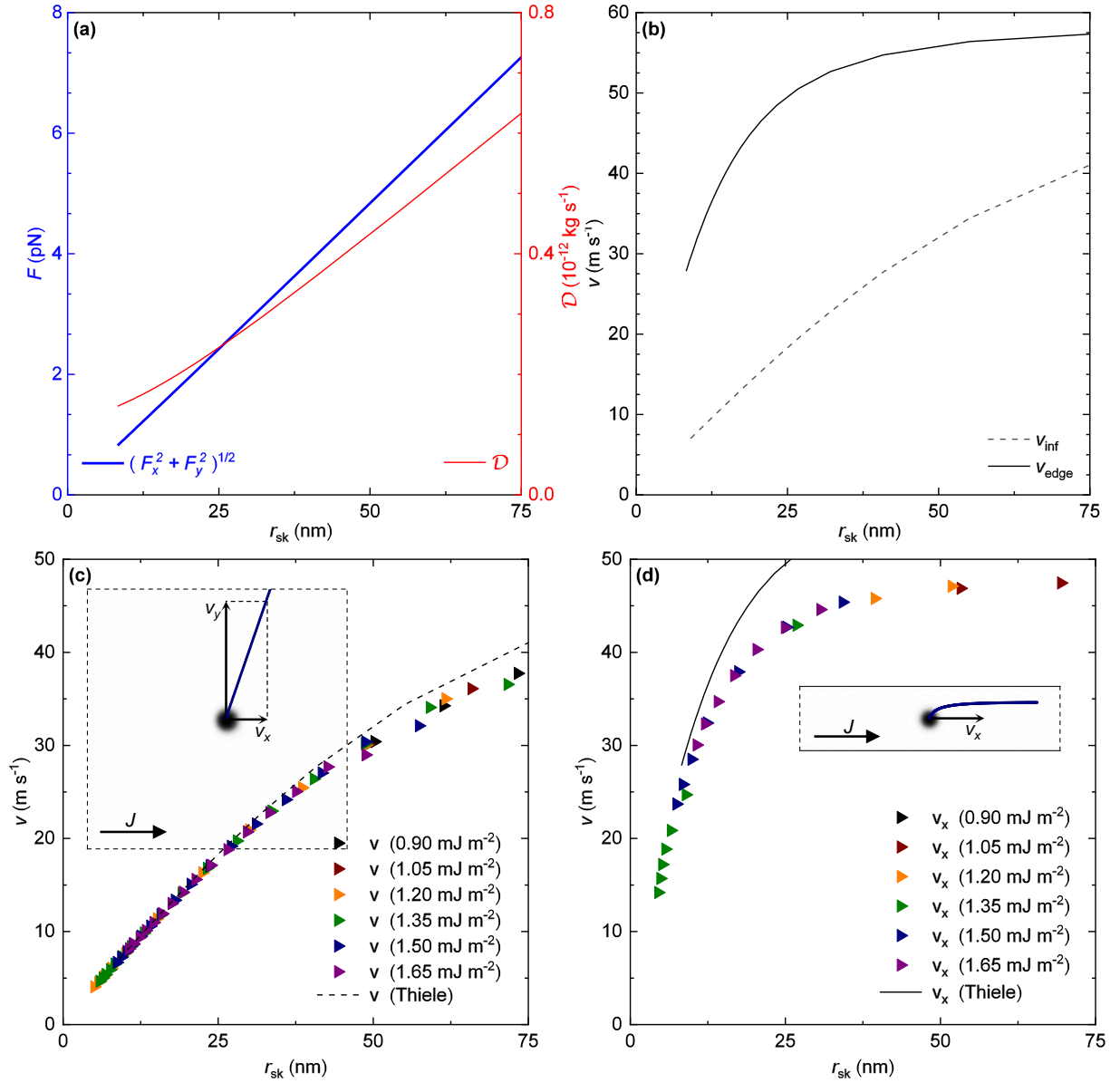
Figure 6.1: (a) Total force and dissipation factor predicted by Thiele modelling of the micromagnetic profiles. (b) Resulting velocities predicted by Thiele modelling of the micromagnetic profiles, in the infinite plane (dashed line) and in a track (solid line). Steady-regime velocities (c) v in the infinite plane and (d) v_x in a track, with lines reporting the velocities predicted in panels a and b. Insets remind the micromagnetic simulation geometry in each case.

smaller radii and $v \to 0$ when $r_{sk} \to 0$. In the framework of the Thiele equation, a diminution of the velocity of smaller skyrmions is therefore predicted, which can be understood as the consequence of the diminution of the geometric factors $b_{x,y}$ appearing in the expressions of $F_{x,y}$ in (3.5) and (3.6). These results are consistent with what can be deduced using Ansatz profiles only considering two parameters for the skyrmion profiles [89].

In order to confirm these results, the velocity of small skyrmions has been studied more extensively with the help of dynamical micromagnetic simulations, thus modelling the spin-torque dynamics occurring inside skyrmions without relying on the rigidity assumption of the Thiele equation. The values of D and $\mu_0 H_{ext}$ are varied independently, with all other parameters kept identical, which results in various skyrmion profiles covering a wide range of values for r_{sk}. The velocity achie-

ved in the infinite plane case is displayed as a function of r_{sk} in Fig. 6.1c, for various values of $D = 0.9$-1.65 mJ m^{-2} and $\mu_0 H_{ext} = 0$–130 mT. An important result is that v is determined by r_{sk} only, and not by the precise values of the different magnetic parameters leading to a given skyrmion radius, confirming the results of the simpler Thiele model. Moreover, the velocity follows closely the predictions of the Thiele equation for $r_{sk} < 50$ nm (dashed line in Fig. 6.1c) but then deviates for $r_{sk} > 50$ nm. This shows that deformations do not play a role at the present current densities for the smaller skyrmions, but becomes more and more important as the skyrmion radius increases above 50 nm because their dynamics no longer correspond to rigid objects. The velocity achieved inside tracks with confinement is displayed as a function of r_{sk} in Fig. 6.1d, for various values of $D = 0.9$-1.65 mJ m^{-2} and $\mu_0 H_{ext} = 0$–130 mT. Again, v is determined by r_{sk} only. However, a large difference with the predictions of Thiele modelling (solid line in Fig. 6.1d) is observed in the track case for all skyrmions with $r_{sk} > 10$ nm, due to the important role played by the deformations of the skyrmions when they interact with edges[1]. Still, the skyrmion velocity rapidly decreases for small values of r_{sk}, as expected because $F \to 0$ when $r_{sk} \to 0$. Therefore, it is confirmed that **smaller skyrmions intrinsically move slower** at a given current density in the case of spin-orbit torque motion. However, note that from the point of view of applications, the separating distance between different storage or functional sites of devices can be reduced accordingly to the reduction of size of the skyrmions. Therefore, as skyrmion velocity and required travel distances are both reducing proportionally to the size of the skyrmions, the operation times in applications are expected to remain unaffected.

We might therefore reconsider the skyrmion velocities gathered in Chapter 4 by taking into account this effect of the size. A better figure of merit for the motion efficiency is given by $v/(4r_{sk})$, which represents the operation time between two functional sites. At the same time, this allows to include the expected linear dependence of v on r_{sk}. The previous comparison graph is amended to display $v/4r_{sk}$ as a function of J, and shown in Fig. 6.2. In light of this new criterion, the efficiency achieved for [Pt 0.6/Co 1.4/Ru 1.4]$_3$ appears only twice less than what can be expected based on the best results (black line), while the efficiency achieved for [Pt 2.4/Co$_{10}$Fe$_{70}$B$_{20}$ 0.8/Al$_2$O$_3$ 1]$_{20}$ appears even more encouraging and shall motivate additional multilayer development efforts, using such materials and a Pt layer located above the FM, in order to allow for a better control of the skyrmion density in this particular structure.

Link between anisotropy and stability under current — We have seen in the previous chapter that ensuring a small anisotropy K_{eff} is beneficial to the stability of skyrmions, which allows to reduce their minimal stable size at RT. However, for low values of K_{eff}, it can be expected that deformations under current of the less rigid skyrmion texture can be amplified. It appears in the micromagnetic study presented above that deformations of skyrmions are detrimental to their motion, and it has been found that skyrmions can even be destabilised or destroyed under current-induced torques in the case of a weak perpendicular anisotropy, due to non-isotropic elongations [219]. Another striking example of what occurs when the anisotropy is too weak is that, when the torque is strong enough to verify $(\hbar/2e)(J/\mu_0 M_s t_{FM})\theta_{eff} > H_{eff}$, the equilibrium configuration of the system is to have all magnetic moments aligned in the plane, overcoming the perpendicular order. As a consequence, some trade-off probably needs to be found, between a too weak anisotropy leading to deformations and a too high anisotropy leading to unstable skyrmions solutions. A quantitative determination of the suitable K_{eff} is left for future studies as it requires further investigation. As the strategy presented above to stabilise antiferromagnetic skyrmions in SAF systems relies on reaching the point of vanishing anisotropy and using additional bias, deformations of skyrmions shall limit the velocities that can be achieved with the present multilayer composition. By obtaining larger values of D, either K_{eff} or $\mu_0 H_{bias}$ could be increased, allowing better stability under current and increasing the potential velocities.

---

[1]Note that the skyrmion size reduces as compared to equilibrium size when it is interacting with edges, which also slows down the motion. Nevertheless this effect is already taken into account here, as the values of r_{sk} used in Fig. 6.1d are the ones in the steady-regime, when the skyrmion are indeed already compressed along the edge.
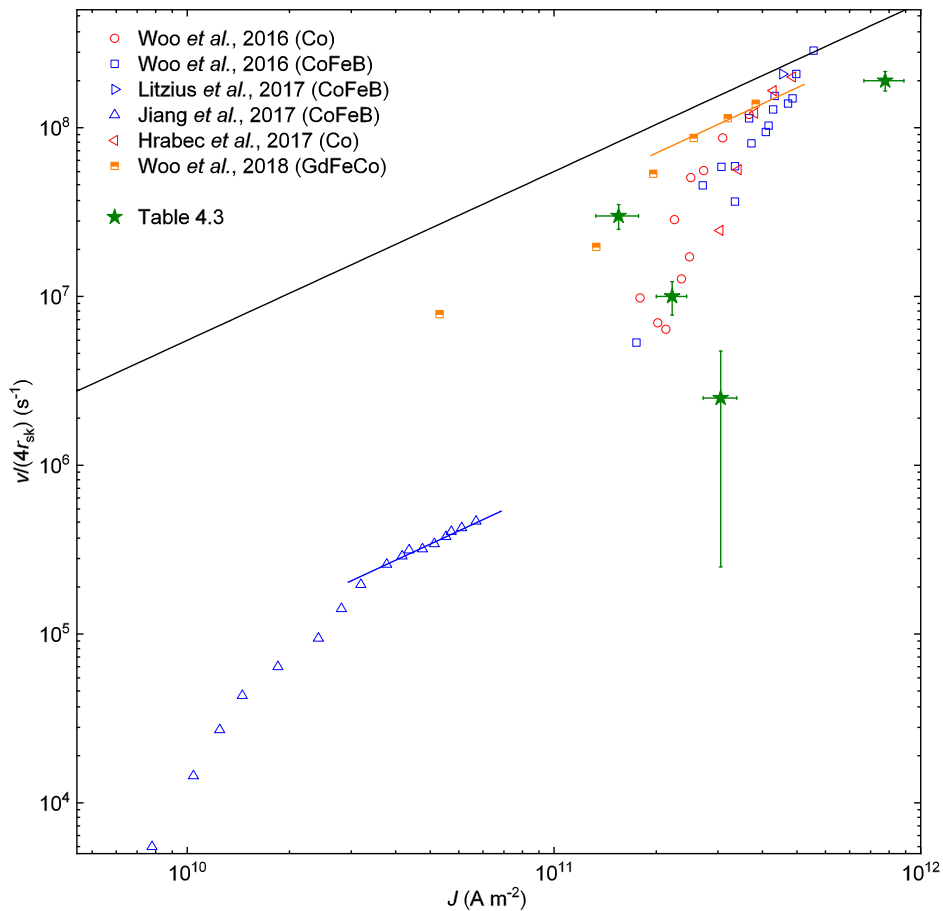
Figure 6.2: Comparison of motion results with other systems, displaying $v/(4r_{\mathrm{sk}})$ as a function of J: Red circles: [Pt (3 nm)/Co (0.9 nm)/Ta (4 nm)]$_{15}$ and blue squares: [Pt (4.5 nm)/CoFeB (0.7 nm)/MgO (1.4 nm)]$_{15}$, from Woo *et al.* [46]. Blue right triangles: [Pt (3.2 nm)/CoFeB (0.7 nm)/MgO (1.4 nm)]$_{15}$, from Litzius *et al.* [47]. Up blue triangles: [Ta (5 nm)/Co$_{20}$Fe$_{60}$B$_{20}$ (1.1 nm)/TaO$_x$ (3 nm)]$_1$, from Jiang *et al.* [45]. Left red triangles: Pt (5 nm)/CoNiCo (1.5 nm)/Au (3 nm)/CoNiCo (1.5 nm)/Pt (5 nm), from Hrabec *et al.* [188]. Half-filled orange squares: [Pt (3 nm)/Gd$_{25}$Fe$_{65.6}$Co$_{9.4}$ (5 nm)/MgO (1 nm)]$_{20}$, from Woo *et al.* [198]. Green stars: Results from Table 4.3. The black line is aligned with $v/(4r_{\mathrm{sk}}) \propto J$ and crosses the best result for $v/(4r_{\mathrm{sk}})$. As can be seen from the blue and orange lines, these two series of measurements have reached a regime far from pinning where velocity appears proportional to applied current.

Velocity in compensated textures — Also, for materials which exhibit a partial or total compensation of the magnetization, such as ferrimagnets or AFs, the resulting M_{s} is reduced, which increases in turn the effects of the torque, according to (3.2) (actually, one needs to consider the coupled equations of both sublattices, as in [204]). Similarly, one might consider the effect of spin-currents on SAF systems. Antiferromagnetic skyrmions in SAF systems could benefit from increased velocities according to very recent studies [139, 204], even if further investigation is required to understand to what extent in practice. Even if this predicted effect relies on the RKKY coupling, it has a different origin than the mechanism allowing largely increased current-induced velocities for chiral DWs in SAF systems [92]. At least, we can anticipate that current-induced motion in Pt/Co/Ru-based SAF multilayers shall be as effective as in its FM equivalent, given that efficient motion could be obtained in very similar multilayers of composition [Pt/Co/Ru]$_3$ (§4.8). In comparison with the prospects for current-induced motion that can be reasonably expected from Pt/Co/Ru-based SAF skyrmion systems, no current-induced motion could be demonstrated so far

for ferrimagnetic-material-based very small skyrmions, due to considerable pinning effects originating in the higher inhomogeneity and intermixing of ferrimagnet films. This is in contrast with velocities of the order of the $\mathrm{km\,s^{-1}}$ reached by ferromagnetic DWs [204]. Hopefully, further work on materials for ferrimagnet-based skyrmions may allow their depinning. This reminds us that whatever strategy is followed for stabilising small skyrmions, taking into account the length scale of magnetic inhomogeneities and seeking higher interfaces quality remains key for the success of future experimental developments towards small and mobile skyrmions.

Avoiding the skyrmion Hall effect — Together with raising the limitations to skyrmion depinning and mobility, finding a mean to mitigate or control the skyrmion Hall effect and its consequences on skyrmion motion remains a very pertinent direction for future research, in order to obtain more reliable motion. Indeed, the presence of the skyrmion Hall effect sets a maximum to the achievable velocities, above which skyrmions are expulsed through track edges [178]. In principle, the skyrmion Hall effect is cancelled for antiferromagnetic skyrmions such as the ones obtained in §5.4. Due to the opposite polarities for the two skyrmions stabilised in each individual layer of the SAF system, with $Q = 1$ for the skyrmion with $m_z(0) = 1$ and $Q = -1$ for the skyrmion with $m_z(0) = -1$, the topological charge cancels out and the gyrotropic term becomes $G = 0$ by summing over the two layers. This shall result in suppressing the skyrmion Hall effect [220, 221]. This research direction is promoted by some recent results showing the partial compensation of the skyrmion Hall effect in ferrimagnetic alloys, based on the same principle [198].

In the future, antiferromagnetic skyrmions such as the ones obtained in §5.4 could thus allow for the desired small sizes, shall be free of the skyrmion Hall effect and might potentially benefit from a very favourable torque engineering in compensated materials to countervail the velocity drop associated to the reduction of skyrmion size. Further experiments on the Pt/Co/Ru-based SAF multilayer system shall allow to determine the most favourable parameters and conditions in order to obtain motion experimentally, which is then expected to be aligned with the direction of the current flow.

6.3   Future directions

The continuation of this thesis implies to work towards achieving experimentally the stabilisation of $10\,\mathrm{nm}$ skyrmions and observe their current-induced motion. Different directions are under present investigation:

- A direct improvement of the last results of this thesis can be anticipated with the realisation of synthetic antiferromagnets including 4, 6 or even more coupled layers.

- Reducing each individual ferromagnetic layer thickness, while controlling the anisotropy to keep it slightly before reorientation, would allow to reinforce the strength of the Dzyaloshinskii-Moriya interactions in the balance with other interactions. Combining between larger number of interfaces, stronger Dzyaloshinskii-Moriya interactions and compensation of magnetization, point together towards achieving smaller skyrmion sizes.

- On the materials engineering aspect, the realisation of skyrmion multilayer structures closer from epitaxial quality, for example by exploring substrate heating or post-deposition annealing, could also solve several issues raised along this thesis, as well as it could unlock the full potential for optimisation of the magnetic properties controlling the stability and mobility of skyrmions.

- Understanding the role of effective anisotropy and RKKY coupling in the current-induced motion of antiferromagnetic skyrmions, in synthetic antiferromagnet systems, should allow to improve the present best results of efficiency of the motion.

Many possibilities for future developments and further use of skyrmions can be foreseen. They range from short-term objectives to longer-term investigations:

- Studying the dynamics of skyrmion lattices shall be very interesting and bring a new understanding of skyrmion dynamics, beyond the descriptions provided in this thesis, which are focused on the dynamics of individual skyrmions.

- The electrical detection of magnetic skyrmions by the anomalous Nernst effect is a possibility that is under present investigation by collaborators at the Physikalisch-technische Bundesanstalt in Germany, using the multilayers presented in this thesis.

- The role of direct interlayer interactions in the stability of skyrmions in magnetic multilayers shall also be studied more rigorously. Extension of the present models need to be developed.

- The localised, quasi-particular nature of skyrmions provides them with various fundamental properties of punctual objects in bidimensional systems, whose physics remain to be explored. Several experiments towards this direction have already been performed [222].

- Beyond the study of Pt/Co/Ru multilayers presented in Appendix A, the fine variations of magnetic properties other than RKKY with Ru layer thickness are still not fully understood. Additional studies, for example combining Brillouin light scattering, harmonic measurements of torques, *etc.*, shall provide more light on the role of Ru, complementary to many other parallel works [223–225].

- The use of rare-earth ferrimagnetic layers inside magnetic multilayers hosting skyrmions shall provide rich spin-injection and dynamics behaviours [226]. Another direction in order to renew spin-injection for skyrmion dynamics would be to combine skyrmions multilayers and topological insulators.

- About material choices, finding new combinations of elements, alloys and oxides inducing stronger Dzyaloshinskii-Moriya interactions definitely remains a direction that requires to be explored. Notably, it may be beneficial to be able to replace the couple Pt/Co, which has been constantly used in this thesis to obtain perpendicular anisotropy and Dzyaloshinskii-Moriya interaction, by other couples in order to obtain more flexibility in the multilayer design and to be able to replace Pt by more common elements.

List of Figures

List of Tables

Material optimisation for multilayered systems: the example of Pt/Co/Ru

In the following, I detail the material optimisation that has been performed during this work on the Pt/Co/Ru multilayer combination. Finding the most suitable relative compositions, by tuning the thicknesses of the different layers, is key for obtaining the desired fine balance of all magnetic properties that is required to stabilise skyrmions, and especially antiferromagnetic skyrmions, as introduced in §5.4. A similar yet less detailed optimisation has been performed on several other combinations, including for example Pt/Co/Ni, Pt/Co/Pd, Pt/Co/Ni/Co. For the sake of conciseness, I only present results for Pt/Co/Ru, but all systems can be studied following the same procedure detailed here, irrespective of the presence or absence of an antiferromagnetic RKKY coupling. We first see how combined IP and OOP magnetometry measurements allow to determine the magnetic anisotropy and the RKKY coupling in multilayers, which constitutes two crucial tunable parameters. I then describe the influence of the thicknesses of the three layers — Co, Pt and Ru — on these properties. I extend this discussion by analysing the fine interplay between the Ru layer thickness and the magnetic anisotropy. I finally detail the optimisation of the properties of the Pt/Co multilayer used as a bias layer adjacent to the Pt/Co/Ru system, when its indirect electronic exchange coupling is mediated by a thicker Pt layer, a type of bias layer that has been employed in the study presented in §5.4.

All layers are deposited on thermally oxidised Si wafers after a Ta(5 nm)/Pt(8 nm) buffer layer. The interest of the Ta underlayer is to promote a good adherence of the layers deposited on SiO_2, while the thick Pt layer results in a textured (111)-oriented atomic structure, thus favouring a strong uniaxial perpendicular anisotropy K_u at Pt/Co interfaces, at the same time as it is able to provide vertical spin currents when an electrical charge current flows in. It has been verified that the precise thicknesses of Ta (in the range 5–10 nm) and Pt (in the range 3–8 nm) in the buffer layer is not significantly affecting the magnetic properties of the deposited multilayers. Likewise, a Pt(3 nm) capping layer is deposited on top of all multilayers in order to prevent oxidation, without any significant role of the precise thickness of this layer. Even if all the systems studied within this thesis are not described in details as part of this appendix (which is focused on Pt/Co/Ru), I nevertheless provide here a list of the sputtering parameters used for Pt/Co/Ru and all the other materials studied in this thesis, see Table A.1. All layers are deposited from 75 mm targets by direct current magnetron sputtering, except Al_2O_3 which is deposited by radio frequency sputtering, in a system with base pressure $\leq 5 \times 10^{-8}$ mbar.

A.1 Determination of magnetic anisotropy and RKKY coupling

For the range of Ru layer thicknesses of interest here (0.6–1.0 nm, around the first antiferromagnetic peak of the RKKY coupling in Ru), the magnetic behaviour of Pt/Co/Ru multilayers is strongly influenced by the presence of the antiferromagnetic coupling between the Co layers. In order to be able to determine both magnetic anisotropy and RKKY coupling strengths from magnetometry measurements, it is necessary to consider the particular field-dependent evolution of

Table A.1: Sputtering parameters used for multilayer depositions: Argon gas pressure, current intensity, power density, target to substrate distance and resulting calibrated deposition rate for each material.

Target	Ar gas pressure (mbar)	Current (mA)	Power density (W cm^{-2})	Target height (mm)	Deposition rate (Å s^{-1})
Ta	$2.5\ 10^{-3}$	150	0.97	130	1.18
Ru	$2.5\ 10^{-3}$	175	1.26	130	1.49
Au	$2.5\ 10^{-3}$	200	1.97	130	7.5
Pt	$2.5\ 10^{-3}$	200	2.06	130	5.5
Co	$2.5\ 10^{-3}$	125	0.93	130	0.88
Ni	$2.5\ 10^{-3}$	200	1.67	130	1.95
$Co_{10}Fe_{70}B_{20}$	$2.5\ 10^{-3}$	125	1.65	130	1.46
Al_2O_3	$4\ 10^{-2}$	-	2.26	130	0.28

the magnetization of the multilayer. Some typical examples of IP and OOP magnetometry measurements performed on $[Pt/Co/Ru]_2$ systems are shown in Figs. A.1(a–d), for increasing Co layer thicknesses. Different behaviours occur depending on the effective perpendicular magnetic anisotropy field $\mu_0 H_{\rm eff} = 2K_{\rm eff}/M_{\rm s}$ of the system relative to the RKKY coupling strength $\mu_0 H_{\rm RKKY}$ [213]. For IP measurements (blue curves) of multilayers with perpendicular magnetic anisotropy, the IP magnetic component increases linearly with the applied field, until it saturates at a field value $\mu_0 H_{\rm sat} = \mu_0 H_{\rm eff} + 2\mu_0 H_{\rm RKKY}$ (Figs. A.1a,b). When no perpendicular magnetic anisotropy is present ($\mu_0 H_{\rm eff} \approx 0$), it saturates at $\mu_0 H_{\rm sat} = 2\mu_0 H_{\rm RKKY}$ (Fig. A.1c). For OOP measurements (red curves) and $\mu_0 H_{\rm eff} \gg \mu_0 H_{\rm RKKY}$ (Fig. A.1a), the magnetization remains zero for increasing fields of both polarities, because the system retains the antiferromagnetic configuration with one FM layer pointing up and one FM layer pointing down. For applied fields of both polarities larger than $\mu_0 H_{\rm RKKY}$, the magnetization suddenly reverses in the layer where it is initially opposing the applied field and the total magnetization saturates to $m_z = \pm 1$. For $\mu_0 H_{\rm eff} \approx \mu_0 H_{\rm RKKY}$ (Fig. A.1b), the reversal does not occur in one sharp step but with a finite susceptibility, due to domains formation. When the perpendicular magnetic anisotropy is further reduced, a gradual rotation of the magnetization in the layers (spin-flip transition) occurs before the reversal of the magnetization, which prevents from extracting precisely $\mu_0 H_{\rm RKKY}$ from the measurement. When no perpendicular magnetic anisotropy is present (Fig. A.1c), the OOP component of the magnetization behaves as the IP component and increases linearly with the applied field, until it saturates at a field value $\mu_0 H_{\rm sat} = 2\mu_0 H_{\rm RKKY}$. When IP magnetic anisotropy is present ($\mu_0 H_{\rm eff} < 0$), then the magnetization saturates at $\mu_0 H_{\rm sat} = -\mu_0 H_{\rm eff} + 2\mu_0 H_{\rm RKKY}$. Therefore, it is possible to extract both magnetic anisotropy and RKKY coupling from these two measurements only as long as the perpendicular magnetic anisotropy is strong enough to ensure the absence of spin-flip transition in the OOP measurements, corresponding here to $t_{\rm Co} \leq 1.36\,{\rm nm}$.

A.2   Determination of the spin reorientation transition

By varying $t_{\rm Co}$ in the multilayer composition, it is thus possible to tune the relative strengths of the effective perpendicular anisotropy and RKKY coupling. This is because $\mu_0 H_{\rm eff} = 2K_{\rm u}/M_{\rm s}$, while $\mu_0 H_{\rm RKKY} = 2J_{\rm RKKY}/(t_{\rm Co}M_{\rm s})$. As $K_{\rm u}$ is a term of interfacial origin, which is thus inversely proportional to the FM layer thickness, both $\mu_0 H_{\rm eff}$ and $\mu_0 H_{\rm RKKY}$ exhibit a $1/t_{\rm Co}$ dependence. However, due to the shift in $\mu_0 H_{\rm eff}$ related to the shape anisotropy factor $-\mu_0 M_{\rm s}$ [see (1.5)], at the spin-reorientation transition $K_{\rm eff} = 0$ (by definition) whereas $\mu_0 H_{\rm RKKY}$ remains significant.

A series of $[Pt/Co/Ru]_2$ multilayers with $t_{\rm Co}$ ranging 1.15–1.52 nm has been deposited in order to find the thickness at which the spin-reorientation transition occurs. The values of $\mu_0 H_{\rm sat}$ and
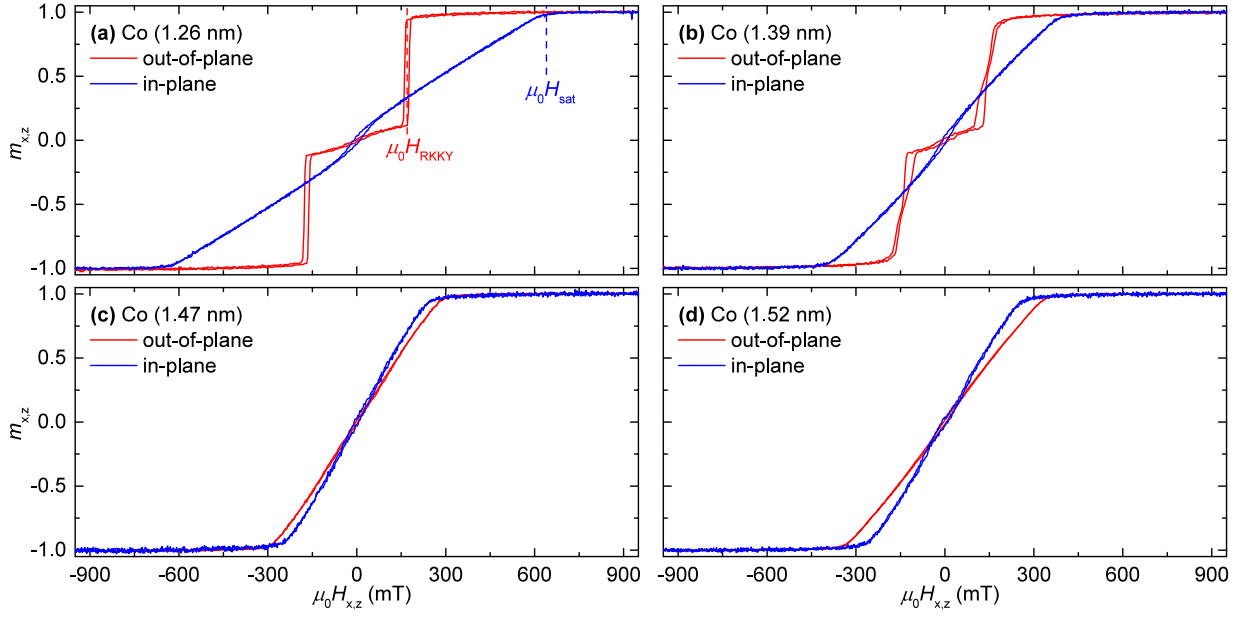
Figure A.1: IP (m_{x}, blue curve) and OOP (m_{z}, red curve) magnetization as a function of an IP (H_{x}) and OOP (H_{z}) applied field, respectively, for $[\mathrm{Pt}(0.6\,\mathrm{nm})/\mathrm{Co}(t_{\mathrm{Co}})/\mathrm{Ru}(0.75\,\mathrm{nm})]_2$ with (a) $t_{\mathrm{Co}} = 1.26\,\mathrm{nm}$, (b) $t_{\mathrm{Co}} = 1.39\,\mathrm{nm}$, (c) $t_{\mathrm{Co}} = 1.47\,\mathrm{nm}$ and (d) $t_{\mathrm{Co}} = 1.52\,\mathrm{nm}$.

$2\mu_0 H_{\mathrm{RKKY}}$ in this series of multilayers, determined as presented above, are shown as a function of t_{Co} in Fig. A.2a. As, $\mu_0 H_{\mathrm{sat}} = \mu_0 H_{\mathrm{eff}} + 2\mu_0 H_{\mathrm{RKKY}}$ for the present thicknesses, the intersection of the linear fits of $\mu_0 H_{\mathrm{sat}}$ and $2\mu_0 H_{\mathrm{RKKY}}$ with respect to $1/t_{\mathrm{Co}}$ allows to find that the spin-reorientation transition occurs at $t_{\mathrm{Co}} = 1.49\,\mathrm{nm}$, as shown also in Fig. 5.10. At this thickness, no effective anisotropy is present in the magnetic multilayer, being consistent with the very similar aspects of the IP and OOP magnetization measurements close to the spin-reorientation transition (Fig. A.1c, with $t_{\mathrm{Co}} = 1.47\,\mathrm{nm}$). Note that the intercept of the fit of $\mu_0 H_{\mathrm{eff}}$ (Fig. A.2b) towards infinite thickness ($1/t_{\mathrm{Co}} \to 0$) indicates that $\mu_0 H_{\mathrm{eff}} \approx -\mu_0 M_{\mathrm{s}}$ at infinite thickness, which corresponds to the anisotropy due to the demagnetizing fields. Therefore, K_{u} tends towards 0 at infinite thickness, meaning that K_{v} is negligible in this system, according to (1.4). From the fit of $2\mu_0 H_{\mathrm{RKKY}}$ as a function of $1/t_{\mathrm{Co}}$, J_{RKKY} is found to be $0.115\,\mathrm{mJ\,m}^{-2}$.

A.3 Optimisation of RKKY coupling with regard to t_{Pt} and t_{Ru}

As the antiferromagnetic RKKY coupling field between FM layers is strongly dependent on the thickness of the NM spacer(s) mediating the coupling, it has been necessary to find the optimal composition, aiming at maximising the antiferromagnetic RKKY coupling field in Pt/Co/Ru. The measurements on $[\mathrm{Pt/Co/Ru}]_2$ systems described in the previous section §A.2 correspond to a structure in which both t_{Pt} and t_{Ru} have been finely optimised to maximise the RKKY coupling field, without sacrificing other properties such as DM interaction and uniaxial anisotropy K_{u}.

The dependence of $\mu_0 H_{\mathrm{RKKY}}$ with t_{Ru} around the first antiferromagnetic peak of Ru is shown in Fig. A.3a, for a fixed $t_{\mathrm{Pt}} = 0.8\,\mathrm{nm}$. In Co/Ru/Co systems, a peak of antiferromagnetic RKKY is expected around $t_{\mathrm{Ru}} = 0.8$–$0.85\,\mathrm{nm}$ [202]. For the Pt/Co/Ru systems under study, it can be seen that the maximum of coupling rather occurs around $t_{\mathrm{Ru}} = 0.7$–$0.75\,\mathrm{nm}$ [210, 227]. The shift in t_{Ru} for this antiferromagnetic peak of coupling is due to the influence of the Pt layer, which also mediates the interlayer electronic coupling in Co/Ru/Pt/Co [209–211]. The peak is shifted to lower values of t_{Ru} for larger values of t_{Pt}, which then requires to adjust t_{Ru} upon varying t_{Pt} when aiming at maximising the RKKY coupling.
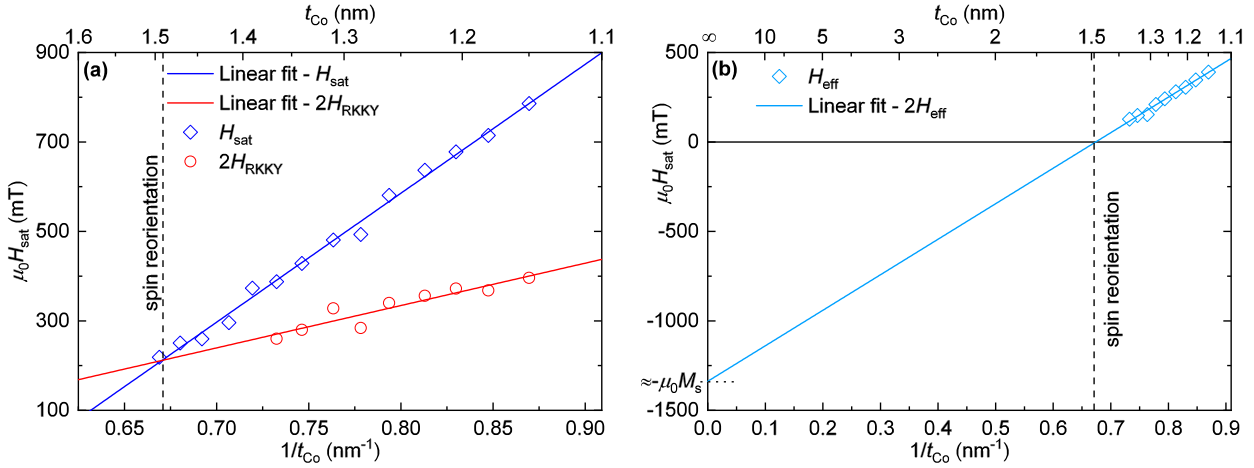
Figure A.2: (a) IP saturation field $\mu_0 H_{sat} = \mu_0 H_{eff} + 2\mu_0 H_{RKKY}$ (blue diamonds) and twice the RKKY coupling field $2\mu_0 H_{RKKY}$ (red circles) as a function of $1/t_{Co}$. Corresponding blue and red lines are linear fits of the experimental measurement points. They intersect at the spin-reorientation thickness $t_{Co} = 1.49\,\text{nm}$ (dashed line), at which $K_{eff} = 0$. (b) $\mu_0 H_{eff}$ measurement points (cyan diamonds) and extension of the fit (blue line) towards infinite thickness, which shows an intercept $\approx -\mu_0 M_s$.

The dependence of $\mu_0 H_{RKKY}$ with t_{Pt} in the range 0.5–1.0 nm is shown in Fig. A.3b, for a fixed $t_{Ru} = 0.8\,\text{nm}$. It confirms the expected exponential decrease of the RKKY coupling with Pt layer thickness owing to the attenuation of the polarized transmitted electrons through Pt [210]. By fitting the experimental values to an exponential decay function of the form $\mu_0 H_{RKKY}(t_{Pt} = 0)\mathrm{e}^{-t_{Pt}/t_d}$, a characteristic attenuation length $t_d = 0.30\,\text{nm}$ is determined.

In order to maximise $\mu_0 H_{RKKY}$, it then appears favourable to reduce t_{Pt} to a lowest acceptable value. However, the Pt layer is also the element that builds up magnetic anisotropy, by favouring a textured atomic structure, and DM interaction in the system, mostly originating in the Pt/Co interface. Given that not only the nearest neighbour Pt and Co atoms, but also more distant atoms are expected to contribute to the DM interaction in the system [123, 228], we decide to keep $t_{Pt} \geq 0.6\,\text{nm}$ in order to maintain significant DM interaction (and interfacial magnetic anisotropy K_u, see §A.4 below). At $t_{Pt} = 0.6\,\text{nm}$, we find that the peak of RKKY coupling is located at $t_{Ru} = 0.75\,\text{nm}$. In conclusion, the optimal composition of the Pt/Co/Ru system for our purpose is determined as $\text{Pt}(0.6\,\text{nm})/\text{Co}(t_{Co})/\text{Ru}(0.75\,\text{nm})$. Notably, the spin reorientation transition is expected around $t_{Co} = 1.49\,\text{nm}$, at which thickness a vanishing perpendicular anisotropy, a significant DM interaction and a strong RKKY coupling are expected to be obtained simultaneously in the system, hence
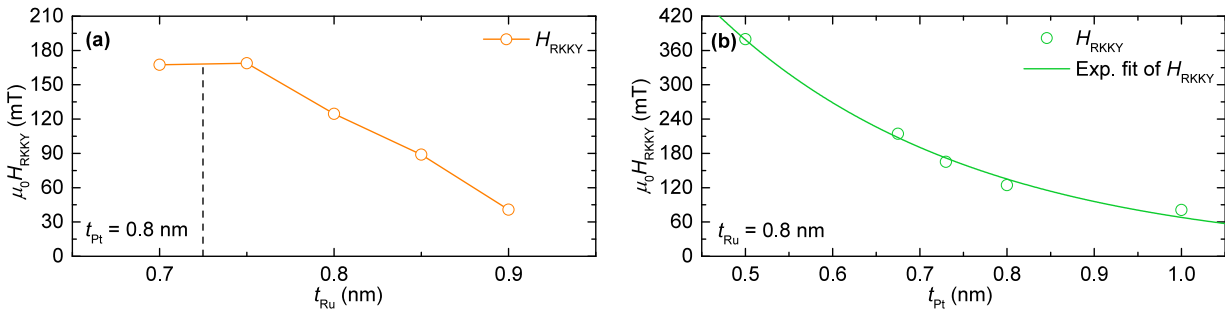
Figure A.3: Antiferromagnetic RKKY coupling in Pt/Co/Ru (a) as a function of t_{Ru} for a fixed $t_{Pt} = 0.8\,\text{nm}$, and (b) as a function of t_{Pt} for a fixed $t_{Ru} = 0.8\,\text{nm}$. The solid line in (b) is a fit of the experimental points to an exponential decay function.
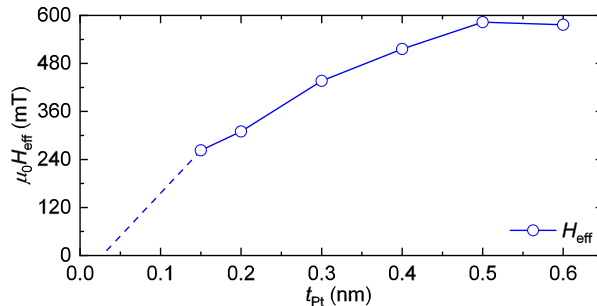
Figure A.4: Effective anisotropy field as a function of t_{Pt}, for a constant $t_{Co} = 1.05\,$nm and $t_{Ru} = 1.4\,$nm.

resulting in conditions that are favourable to the formation of antiferromagnetic spin-spirals (§5.4).

## A.4   Fine variations of anisotropy with t_{Ru} and t_{Pt}

A strong advantage of the present Pt/Co/Ru multilayer system, which has been extensively explored in this work, is its possible utilisation to stabilise different types of skyrmion structures, notably varying between either ferromagnetic or antiferromagnetic skyrmions, depending on the sign of the interlayer RKKY coupling, which can be adjusted by tuning the thickness of the Ru layers. In first approximation, because the magnetic anisotropy of the Co layers has an interfacial origin, it should only depend on t_{Co} and on the nature of the Co interfaces (here Pt/Co and Co/Ru), but not on the individual thicknesses t_{Ru} or t_{Pt} of the other layers.

Refining this analysis however, the change of atomic ordering in the layers upon varying the thickness of Pt (which progressively builds up a (111)-oriented granular surface through its thickness) is expected to affect the quality of the Pt/Co interfaces, as well as the amount of strain in the multilayer stacking. For this reason, a study of the perpendicular anisotropy with respect to the changes of thickness in the intermediate Pt layers has been performed, in the range 0–0.6 nm. To allow the direct measurement of the perpendicular anisotropy, multilayers with structure $[Pt(t_{Pt})/Co(1.05\,nm)/Ru1.4\,nm]_2$ have been deposited, in which the thickness of the Ru layers is chosen on purpose to be ferromagnetic. A small difference may exist between the anisotropy measured in this series of multilayers for $t_{Ru} = 1.4\,$nm and the anisotropy that would be found for $t_{Ru} = 0.75\,$nm, but the latter cannot be measured because it would result in antiferromagnetically coupled layers with strong variations of the RKKY coupling, thus affecting the loops. We can nevertheless anticipate a similar thickness dependence behaviour in both t_{Ru} values.

The evolution of the anisotropy $\mu_0 H_{eff}$ of the multilayer as a function of t_{Pt} is reported in Fig. A.4. It is found that the anisotropy starts to reduce significantly below 0.5 nm of thickness, even if a dusting of Pt in the amount of only a fraction of an atomic monolayer remains sufficient to induce a weak perpendicular magnetic anisotropy. However, perpendicular magnetic anisotropy is not achieved without Pt. Even without performing the measurement of the resulting DM interaction, as it constitutes a much more complex task, we can anticipate, on the basis of experimental reports of texture-induced correlation between anisotropy and DM interaction [120], that the DM interaction must reduce significantly as well for thinner Pt layers, which is the reason for which it seems reasonable to keep $t_{Pt} \geq 0.6\,$nm.

Similarly, a significant variation of the magnetic anisotropy is found experimentally when varying t_{Ru} between the thicknesses of the antiferromagnetic and ferromagnetic peaks, which may impact the thickness requirements if targeting particular magnetic properties. In order to investigate this effect into more details, four series of multilayers have been deposited:

(i) Pt(8 nm)/Co(1.05 nm)/Ru(t_{Ru})/Pt(3 nm),

123
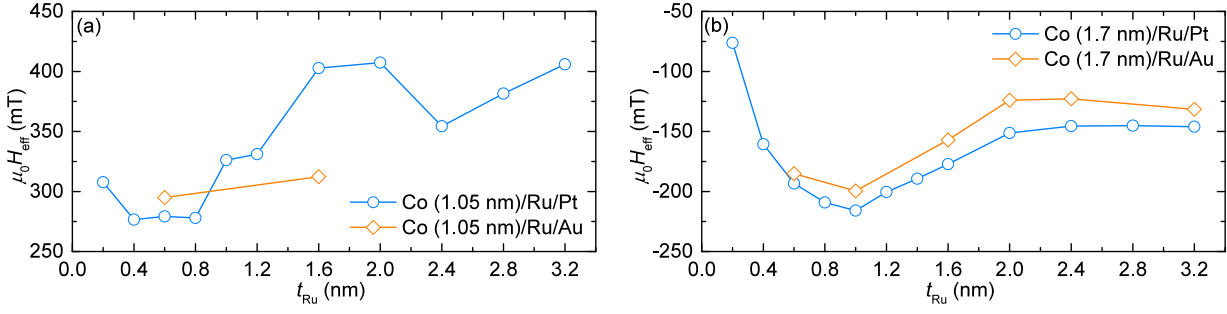
Figure A.5: Effective anisotropy field as a function of t_{Ru}, comparing Pt (cyan circles) and Au (gold diamonds) cappings, for (a) $t_{Co} = 1.05$ nm and (b) $t_{Co} = 1.7$ nm.

(ii) $\mathrm{Pt}(8\,\mathrm{nm})/\mathrm{Co}(1.05\,\mathrm{nm})/\mathrm{Ru}(t_{Ru})/\mathrm{Au}(5\,\mathrm{nm})$,

(iii) $\mathrm{Pt}(8\,\mathrm{nm})/\mathrm{Co}(1.7\,\mathrm{nm})/\mathrm{Ru}(t_{Ru})/\mathrm{Pt}(3\,\mathrm{nm})$,

(iv) $\mathrm{Pt}(8\,\mathrm{nm})/\mathrm{Co}(1.7\,\mathrm{nm})/\mathrm{Ru}(t_{Ru})/\mathrm{Au}(5\,\mathrm{nm})$.

Note that Co layers with $t_{Co} = 1.05$ nm have OOP anisotropy, while they have IP anisotropy when $t_{Co} = 1.7$ nm. The effective perpendicular anisotropy field ($\mu_0 H_{eff}$) as a function of t_{Ru} is shown in Fig. A.5a for series (i) and (ii), and in Fig. A.5b for series (iii) and (iv). It reveals a nonmonotonic modulation of $\mu_0 H_{eff}$ with t_{Ru}. For the case of thicker layers, a minimum of perpendicular anisotropy K_u is observed for $t_{Ru} = 1.0$ nm, while the anisotropy is reinforced for either smaller or larger Ru layer thicknesses. A possible explanation for this particular dependence may be given by the competition between two effects: a strain effect, increasing with the amount of Ru deposited above the Co, which would tend to enhance magnetic anisotropy, and a screening of the top Co/Pt or Co/Au interface, also increasing with the amount of Ru deposited above the Co, which would tend to reduce magnetic anisotropy. As can be seen by the similarity of the curves for Pt and Au capping layers in Fig. A.5b, these effects are mostly independent of the nature of the layers above Ru. For the case of thinner layers, the t_{Ru}-dependence of $\mu_0 H_{eff}$ is even more subtle and suggests oscillating features, which can be due to the quantum effects expected in this small thickness regime. Notably, the magnetic properties of the Co layer can then be influenced by distant layers farther away from the Co interfaces. This appears in Fig. A.5a, where a different evolution of magnetic anisotropy with t_{Ru} is found depending on whether a Pt or a Au capping layer is present. More investigation would be required in order to fully understand these observations.

A.5 Determination of D in Pt/Co/Ru

A series of multilayers with ferromagnetic interlayer coupling and varied repetition number, $[\mathrm{Pt}\,(1.0\,\mathrm{nm})/\mathrm{Co}\,(1.1\,\mathrm{nm})/\mathrm{Ru}\,(1.4\,\mathrm{nm})]_{2,3,4,5,6}$, has been deposited in order to perform domain size measurements and deduce the strength of the DM interaction [7, 46, 229, 230]. The moderate number of layers deposited, combined with the intermediate anisotropy found for $t_{Co} = 1.1$ nm [measured $\mu_0 H_{eff} = 520\,\mathrm{mT}$, corresponding to $K_{eff} = 0.254\,\mathrm{MJ\,m^{-3}}$] allows a convenient measurement of domains spacing around the 100 nm–µm range by MFM. In this series of multilayers, the DM interaction is strong enough compared to dipolar interactions, which ensures a uniform chirality of the DWs through the multilayer thickness. This allows the analysis of the domains spacing within the (λ,δ,ϕ) model ([229, 230], see also Appendix C). Using $A = 10\,\mathrm{pJ\,m^{-1}}$ [7], we can find the DW energies and thus the values of D that correspond to the observed domains spacing, which are listed in Table A.2. For this series of samples, $M_s = 0.975 \pm 0.075\,\mathrm{MA\,m^{-1}}$ is estimated by fitting the experimental domains spacing dependence on L for varied values of M_s. An average DM interaction magnitude $D = 1.02\,\mathrm{mJ\,m^{-2}}$ is estimated. Conversely, the interface DMI parameter is found as

$D_{\mathrm{s}} = 1.12\,\mathrm{pJ\,m^{-1}}$, which gives $D = 0.76\,\mathrm{mJ\,m^{-2}}$ for the SAF systems (ii) and (iii) studied in §5.4 with $t_{\mathrm{Co}} = 1.47\,\mathrm{nm}$, if an inverse dependence on Co layer thickness is strictly observed.

Table A.2: Summary of domain spacing measurements performed in the [Pt (1.0 nm)/Co (1.1 nm)/Ru (1.4 nm)]$_L$ series. The number of repetitions of the magnetic layer L, measured domains periodicity λ and DM interaction amplitude D are given for each multilayer.

Multilayer stack	L	λ (nm)	D (mJ m^{-2})
[Pt(1.0 nm)/Co(1.1 nm)/Ru(1.4 nm)]$_2$	2	2500 ± 312	1.11 ± 0.12
[Pt(1.0 nm)/Co(1.1 nm)/Ru(1.4 nm)]$_3$	3	1130 ± 59	1.00 ± 0.14
[Pt(1.0 nm)/Co(1.1 nm)/Ru(1.4 nm)]$_4$	4	600 ± 37	1.02 ± 0.14
[Pt(1.0 nm)/Co(1.1 nm)/Ru(1.4 nm)]$_5$	5	482 ± 23	0.96 ± 0.14
[Pt(1.0 nm)/Co(1.1 nm)/Ru(1.4 nm)]$_6$	6	365 ± 14	1.02 ± 0.15

A.6 Realisation of a compatible and coercive bias layer

The next required block in the design of multilayers suited to host antiferromagnetic skyrmions is the part that provides a biasing interaction to the system. Note that in a another perspective, such biasing interaction may be used to obtain stable compact skyrmions in usual ferromagnetic multilayers but at zero external field [64]. Different types of structures are known to provide exchange or indirect electronic bias in perpendicularly magnetized systems, among which symmetrical Pt/Co multilayers [208], SAF systems based on such multilayers [209], or AF-based structures employing for example CoO, IrMn or FeMn [231, 232]. Our choice is to rely on symmetrical Pt/Co multilayers, for two main reasons. First, the deposition of the whole multilayer structure is greatly simplified in this case, as the deposition of Pt/Co multilayers is fully compatible and does not affect the magnetic properties of the Pt/Co/Ru multilayer deposited above it. On the contrary, the growth conditions and hence the magnetic properties of the Pt/Co/Ru SAF system are expected to be altered in the case of AF-based structures deposited below it. Depositing an AF-based bias layer over the SAF system allows to avoid such complications, but buries the studied system deep under the top of the multilayer, which is detrimental to its measurement. Second, SAF bias blocks are not desirable in the present case, as they increase the total magnetic moment of the whole system. The related increase in dipolar interactions when accumulating more FM layers in total may lead to the formation of ferromagnetic domains through the entire thickness of the system, ignoring the RKKY coupling elements [215]. As the aim is here to bias a SAF system, a compact FM system is perfectly suitable, thus realising the reversed situation as compared to the more usual configuration in which a FM layer is biased by a SAF block [209].

A requirement is then that the FM bias block needs to be coercive enough to remain saturated for an extended range of applied perpendicular fields, including zero field. In that regard, the very large perpendicular magnetic anisotropy provided by Pt/Co multilayers make them appear especially suitable. Different compositions of the Pt/Co bias multilayer have been tried, by varying the respective thicknesses of Pt and Co. The resulting magnetization curves for OOP applied fields are summarised in Fig. A.6. It appears that a sufficient coercivity is achieved only for $t_{\mathrm{Co}} \geq 0.6\,\mathrm{nm}$. All multilayers of this series with $t_{\mathrm{Co}} \geq 0.6\,\mathrm{nm}$ possess a similar effective anisotropy field ($\mu_0 H_{\mathrm{eff}} \approx 0.3\,\mathrm{T}$), but the reversal of the magnetization in the bias multilayer is less sharp for $t_{\mathrm{Co}} = 0.8\,\mathrm{nm}$ than for $t_{\mathrm{Co}} = 0.6\,\mathrm{nm}$, due to the reinforced role of the dipolar interactions, promoting domains formation during magnetization reversal. Multilayers with $t_{\mathrm{Co}} = 0.6\,\mathrm{nm}$ are thus preferred in order to ensure a uniform magnetization inside the bias block. In order to keep a compact block constituted of strongly coupled magnetic layers, [Pt(0.45 nm)/Co(0.6 nm)]$_4$ is selected to realise the bias multilayer deposited under the SAF system.
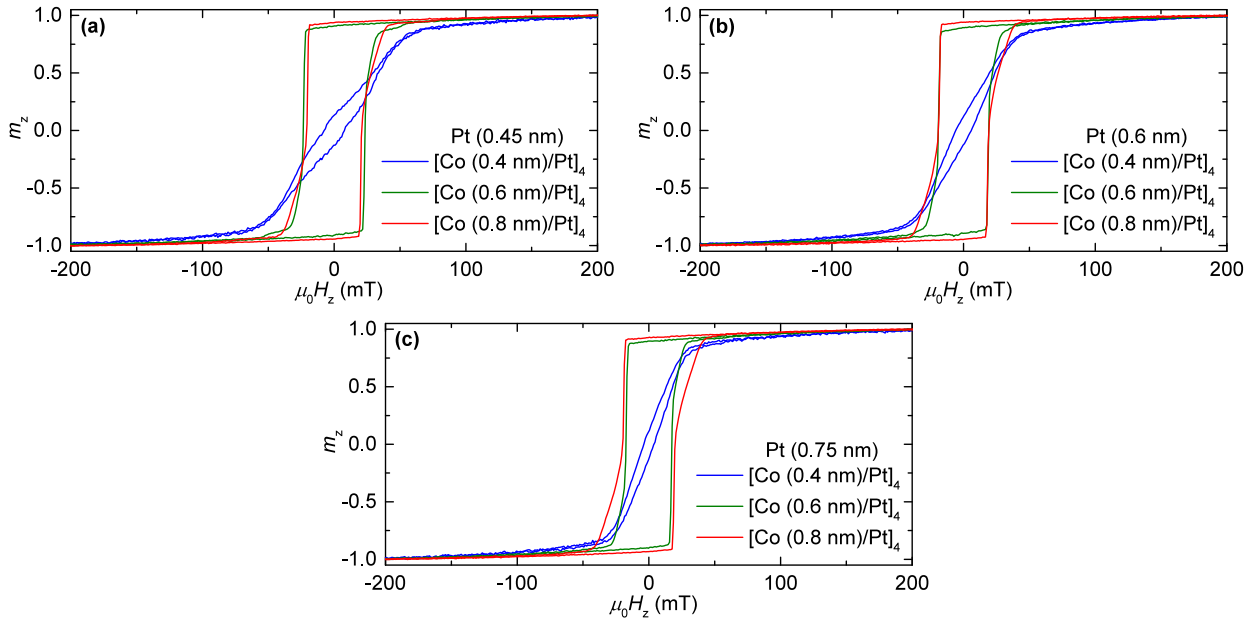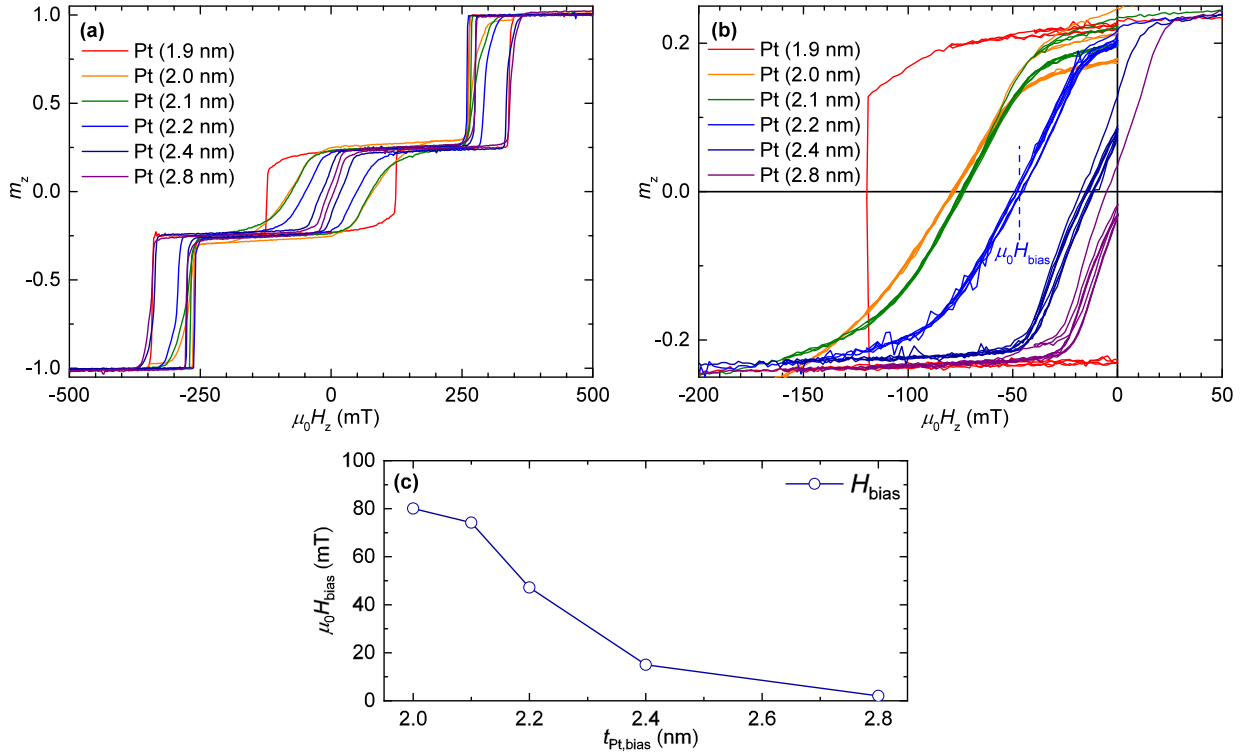
Figure A.6: OOP magnetization curves for bias $[Pt/Co]_4$ multilayers with (a) $t_{Pt} = 0.45\,nm$, (b) $t_{Pt} = 0.6\,nm$, and (c) $t_{Pt} = 0.75\,nm$, for $t_{Co} = 0.4\,nm$ (blue curve), $0.6\,nm$ (green curve) and $0.8\,nm$ (red curve) in each case.

A.7 Adjusting the strength of the biasing interaction

Another advantage of choosing a Pt/Co multilayer for constituting the bias layer of the system is that the coupling strength with the SAF part can be conveniently adjusted, through varying the intermediate Pt layer thickness $t_{Pt,bias}$ in the structure $[Pt/Co]_4/Pt(t_{Pt,bias})/SAF$, which provides an indirect, ferromagnetic electronic coupling in Co/Pt/Co [233]. In order to characterise the ferromagnetic bias coupling strength, a different series of multilayers has been required, as a direct measure of a ferromagnetic coupling between two isolated FM layers only from magnetometry measurements is inaccessible. Contrary to the case of antiferromagnetically coupled layers, for which two switching steps between the antiferromagnetic ordering and the ferromagnetic ordering of the layers occur at a field of $\pm\mu_0 H_{RKKY}$, two ferromagnetically coupled layers reverse simultaneously upon varying an applied field. A series of multilayers with structure $[Pt/Co]_4/Ru(0.8\,nm)/[Co/Pt]_4/Pt(t_{Pt,bias})/Co(\approx 1.5\,nm)$ has been used to measure $\mu_0 H_{bias}$, resulting in the different OOP magnetization curves shown in Figs. A.7a. They present four magnetization levels separated by three switching steps. Describing, *e.g.*, the curves for decreasing values of the applied field (upper branches), the first switching step corresponds to the switching of the $[Pt/Co]_4$ multilayer due to the strong antiferromagnetic coupling mediated by the intermediate Ru layer. It occurs before the switching of the $[Co/Pt]_4$ multilayer because the latter is ferromagnetically coupled to the top FM layer, thus preventing it from switching at this point. The central switching step corresponds to the switching of the top FM layer, and the final switching step corresponds to the reversal of the remaining $[Co/Pt]_4$ multilayer.

The possibility of adjusting the coupling field is demonstrated by the minor OOP magnetization curves shown in Fig. A.7b. After saturating the sample OOP with a strong positive field and reducing the applied field down to zero, the magnetization in the bottom $[Pt/Co]_4$ multilayer is pointing down ($m_z = -1$) while it is pointing up in the central $[Co/Pt]_4$ layer ($m_z = +1$). Because of the SAF structure inside the $[Pt/Co]_4/Ru/[Co/Pt]_4$ block, it constitutes a biasing layer with compensated magnetization and thus increased coercivity up to $120\,mT$. Some Co layers thicker than the spin-reorientation transition thickness are used for the top FM in order to avoid perpendicular anisotropy, which could produce significant coercivity affecting the determination

Figure A.7: (a) OOP magnetization curves of $[Pt/Co]_4/Ru/[Co/Pt]_4/Pt(t_{Pt,bias})/Co$ multilayers with varying $t_{Pt,bias}$ in the range 1.9–2.8 nm. (b) Minor loops of negative magnetization ranging -40–0 mT, -80–0 mT, -120–0 mT, -160–0 mT and -200–0 mT respectively, obtained after positive saturation, for the same multilayers. The zero crossing point of the minor loops allowing to determine $\mu_0 H_{bias}$ from these measurements is shown, as an example, for $t_{Pt,bias} = 2.2$ nm (c) Evolution of $\mu_0 H_{bias}$ as a function of $t_{Pt,bias}$.

of $\mu_0 H_{bias}$. By performing minor magnetization loops down to increasingly negative values of the applied field, it is thus possible to observe the shift of the switching loop of the top FM layer towards negative values by $\mu_0 H_{bias}$. For the particular case of $t_{Pt,bias} = 1.9$ nm (red curve), the magnetization in all layers switches before the reversal of the top FM layer, preventing from measuring $\mu_0 H_{bias}$ (still, it implies that $\mu_0 H_{bias}(t_{Pt,bias} = 1.9$ nm$) > 120$ mT. For all other thicknesses, by performing several loops the non-reversible effects are averaged out, which results in the observation of a clear, central switching curve. It thus allows to determine $\mu_0 H_{bias}$ as the zero-crossing point of the shifted FM layer reversal, as shown in Fig. A.7b, with the value indicated for $t_{Pt,bias} = 2.2$ nm. A thickness of 0.8 nm is used for the intermediate Ru layer of the SAF bias layer, because it is the maximum of antiferromagnetic RKKY coupling for the Co/Ru/Co combination without Pt layers adjacent to the Ru layer.

The evolution of $\mu_0 H_{bias}$ with $t_{Pt,bias}$ is shown in Fig. A.7c. The values of the coupling field are all rescaled to 1.47 nm of thickness of the top Co layer, through a multiplication by their $t_{Co}/1.47$ nm, in order to represent the expected biasing field for the Pt/Co/Ru SAF systems with vanishing anisotropy used in this study. It demonstrates that $\mu_0 H_{bias}$ can be finely adjusted by varying $t_{Pt,bias}$, which thus provide a control on the bias of the bottom layer of the SAF in the targeted $[Pt/Co]_4/Pt(t_{Pt,bias})/SAF$ structure.

<div align="right">

Appendix B

</div>

Imaging the magnetic nanostructures

The imaging of the magnetic configurations hosted by the multilayers of this thesis relies extensively on MFM measurements. In this appendix, we discuss a few important points related to MFM imaging.

B.1 Principle of lift mode

The MFM images shown in this thesis have been recorded with the technique of double pass tapping mode, as sketched in Fig. B.1a. The magnetic tip passes two times over the same location. At the first pass [pass (i) in Fig. B.1a], the topography (height) profile is recorded by direct contact of the tip with the surface. The height profile is deduced because the tip follows closely the surface, as a feedback loop ensures that the cantilever holding the tip always oscillates with the same amplitude. This setpoint amplitude is indeed chosen below the amplitude of the driven oscillations far from the surface, thus requiring the tip to enter in contact interaction with the surface in order to reduce its oscillations amplitude. At the second pass [pass (ii) in Fig. B.1a], the cantilever oscillates at a given lift height from the surface and does not enter into contact with the surface. The oscillations of the tip are perturbed by the action of the dipolar field generated by the magnetic configuration, which acts on the magnetic moment of the tip to produce a detectable phase shift in the cantilever resonance. As the tip is vertically magnetized, this phase shift is proportional to the field gradient $\partial H_{\mathrm{dem,z}}/\partial z$ or $\partial^2 H_{\mathrm{dem,z}}/\partial z^2$ (depending on tip model and relative sizes of tip and characteristic scale for field variations), represented in Fig. B.1b, which allows to produce an image of *phase shift (or offset) in lift mode*, as shown in Fig. B.1c, which resembles the magnetic configuration $m_{\mathrm{z}}(x, y)$. To perform an image, several line scans are realised by shifting the tip along a slow axis, orthogonal to the line scan axis.

Denoting z_{tip} the lift height and Δz the oscillation amplitude of the apex of the tip, due to the oscillations of the cantilever the measured signal is rather

$$\frac{1}{\Delta z} \int_{z=z_{\mathrm{tip}-\Delta z/2}}^{z_{\mathrm{tip}+\Delta z/2}} w(z) \left(\frac{\partial^{(2)} H_{\mathrm{dem,z}}}{\partial z^{(2)}} \right) \Bigg|_z dz \qquad (\mathrm{B.1})$$

where w is a function of the oscillations of the tip, instead of $(\partial^{(2)} H_{\mathrm{dem,z}}/\partial z^{(2)})|_{z_{\mathrm{tip}}}$, as shown in Fig. B.1b. This may reduce strongly the magnetic signal, especially when $\mathbf{H}_{\mathrm{dem}}$ has a strong vertical dependence, as in SAF systems. For this reason, the amplitude in pass (ii) is often much reduced and the lift height reduced to zero or even negative values, in order to increase the sensitivity of the setup. Intrinsically, the resolution of MFM imaging is therefore not only the size of the magnetic volume of the tip, which is estimated around $30\,\mathrm{nm} \times 30\,\mathrm{nm} \times 30\,\mathrm{nm}$, but its oscillating volume.

B.2 Tip and imaging conditions choice

The fact that the MFM tip is magnetic may perturb the imaged magnetic configurations. For this reason, it is required to select a tip magnetization as low as possible (by choosing a thickness
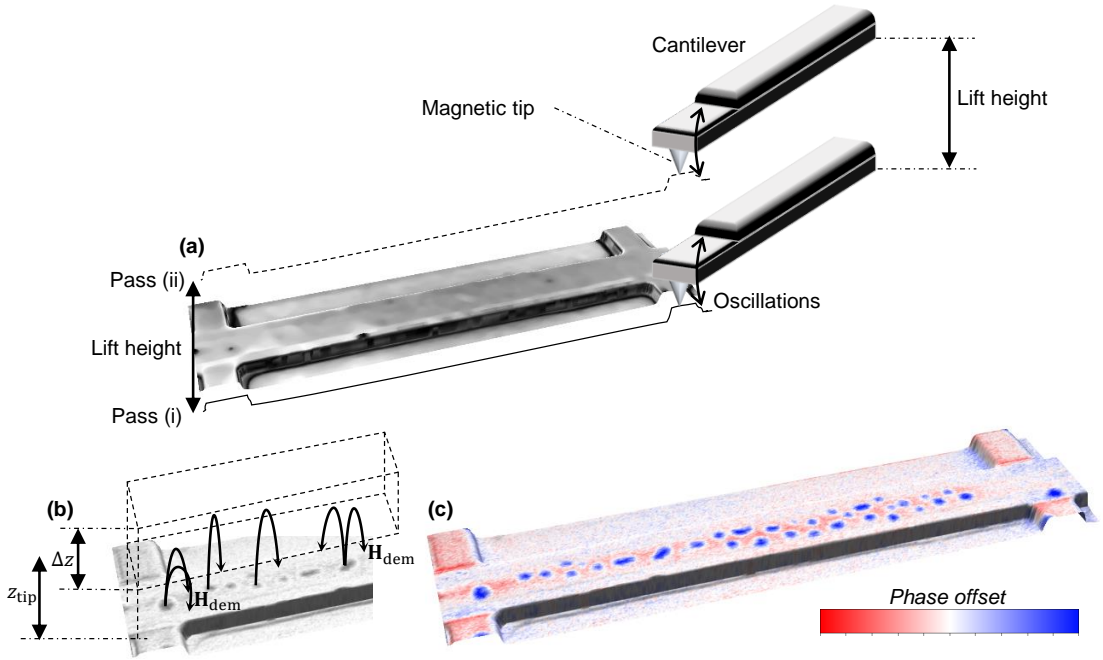
Figure B.1: (a) Perspective view of the topography of a track. The position of the MFM tip during the line scan is represented by the solid trace for pass (i) and by the dashed trace for pass (ii), which is a linescan made above trace (i), being shift by the lift height value. The tip oscillates during both passes. (b) Schematic view of the quantity that is actually measured by MFM, $(\partial H_{\mathrm{dem,z}}/\partial z)|_{z_{\mathrm{tip}}}$ averaged over the oscillation amplitude around the lift height. (c) Resulting phase offset in lift mode image.

of magnetic coating of the tip as thin as possible). Two types of commercial tips have been used in the present work, Asylum Low Moment series tips, and Team Nanotech CFM-ML Pt coated tips with 7 nm of magnetic coating.

For the more challenging imaging of the SAF system, the MFM experiments have been performed under vacuum in order to enhance the signal to noise ratio, by improving the quality factor. Between atmospheric pressure and the reduced pressure $P = 5\,\mathrm{Pa}$ reached in these experiments, the quality factor of the cantilever resonance increases tenfold from $Q = 150$ to $Q = 1500$.

B.3 Prediction of magnetic signal expected from antiferromagnetic skyrmions

In order to allow comparison with the experimental measurements, the field gradients resulting from an antiferromagnetic skyrmion stabilised in a SAF have been determined using the model of Chapter 2. The dipolar field $\mathbf{H}_{\mathrm{dem}}(r, z)$ is computed from the equilibrium skyrmion profiles, determined by energy minimisation for $D = 0.5\,\mathrm{mJ\,m^{-2}}$ and for two values of $\mu_0 H_{\mathrm{bias}} = 40$ and $60\,\mathrm{mT}$. Their equilibrium radii in the bottom layer are 23.6 nm and 14.9 nm, respectively. The dipolar field profiles at arbitrary heights z above the system are shown in Fig. B.2 as radial cuts of the dipolar field above the antiferromagnetic skyrmions, for $\mu_0 H_{\mathrm{bias}} = 40\,\mathrm{mT}$ (Figs. B.2a–c) and 60 mT (Figs. B.2d–f). We analyse separately the radial component H_{r} (Figs. B.2a,d) and the vertical component H_{z} (Figs. B.2b,e) of the dipolar field. Because the antiferromagnetic alignment in the two layers partially cancels the dipolar field, their decay with distance from the skyrmion is expected to be faster than for usual ferromagnetic skyrmions. In each panel, the solid line shows a contour of the outer space where the field is reduced down to 5 mT and below. The first partial derivative
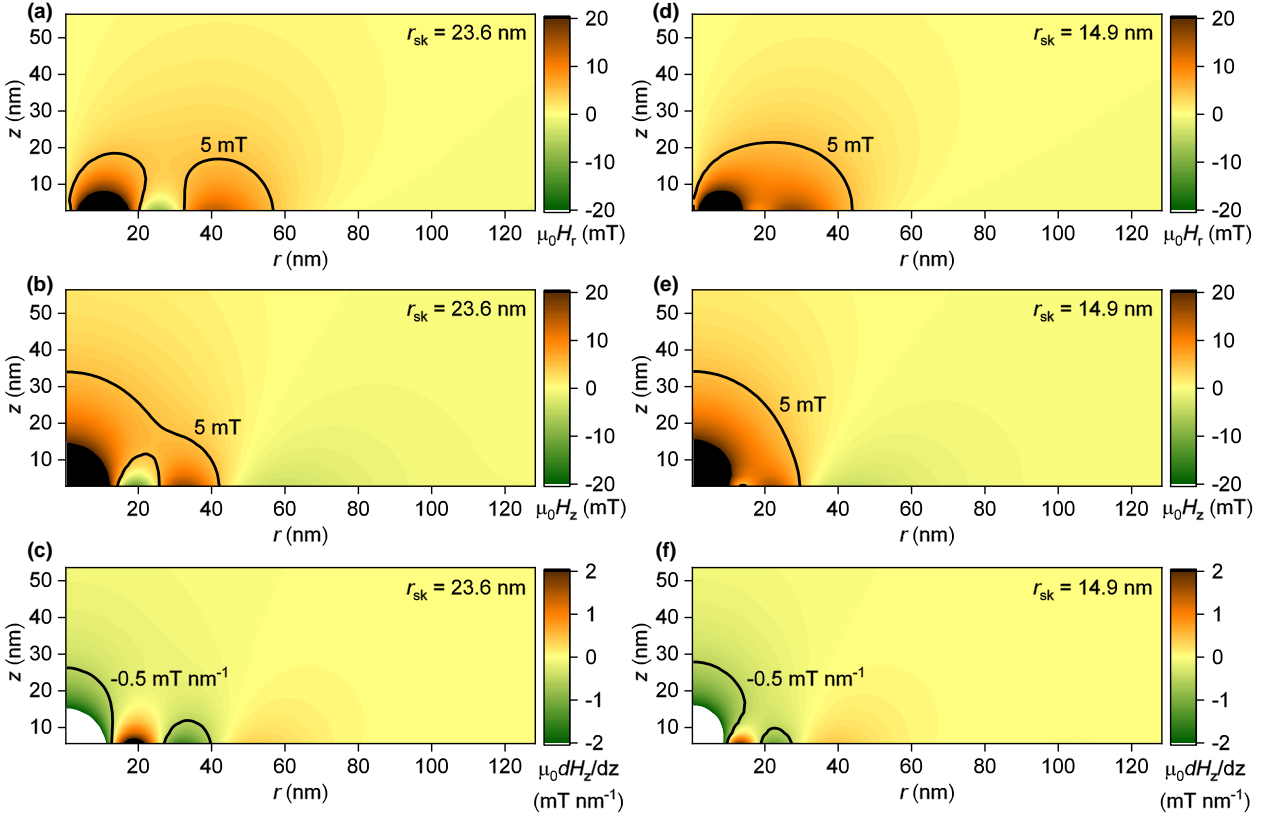
Figure B.2: Colour maps of the dipolar field generated by antiferromagnetic skyrmions in SAF systems. (a) Radial component, (b) vertical component, and (c) first partial z-derivative of the vertical component of the dipolar field generated by an antiferromagnetic skyrmion stabilised under $D = 0.5\,\mathrm{mJ\,m^{-2}}$ and $\mu_0 H_{\mathrm{bias}} = 40\,\mathrm{mT}$. (d–f) Same for the dipolar field generated by an antiferromagnetic skyrmion stabilised under $D = 0.5\,\mathrm{mJ\,m^{-2}}$ and $\mu_0 H_{\mathrm{bias}} = 60\,\mathrm{mT}$. In each panel, a line indicates values reduced to one fourth of the colour scale maximum.

with respect to z of the vertical component of the dipolar field, $\partial H_{\mathrm{dem,z}}/\partial z$, is shown in Figs. B.2c and B.2f. Such derivative of the stray field decays even faster, as it becomes a higher-order term. In each panel, the solid line shows a contour of the outer space where the vertical gradient field is reduced down to $0.5\,\mathrm{mT\,nm^{-1}}$ and below. This highlights the interest of reducing oscillations amplitude and lift height for the second pass. For the present antiferromagnetic skyrmions, the profile hosted in the top layer is actually compressed compared to the bottom one (see Fig. 5.15), and is located closer to the tip, which generates positive fields (negative gradients) on top of the antiferromagnetic skyrmion, thus matching the direction of the saturated biasing layer. This indeed corresponds to dark contrast in our setup, in accordance with the images of §5.4.

Characterising A and D

In this appendix, a micromagnetic model allowing to deduce a value of D from MFM (or any other imaging technique) domains spacing measurements is provided. It may be used when the (λ,δ,ϕ) model from Lemesh *et al.* [229] cannot, because of a non-uniform chirality along the z direction.

In practice, the determination of D from domains periodicity (λ) measurements and magnetostatic considerations appears more accurate and easier to perform with aligned stripe domains. Such magnetic configuration can be obtained after an IP demagnetisation procedure, in contrast to labyrinthine magnetic domains, obtained after an OOP demagnetisation procedure (see Chapter 1). A difference of up to 30 % between the values of λ deduced from IP and OOP demagnetised configurations may occur. However, the modelling of the magnetostatic interactions in the magnetic domains is much easier to perform when considering aligned stripe domains, in which case the deduced values of D can be correct, naturally, only for the IP demagnetised configuration measurement.

Before describing the micromagnetic model, let us briefly review the principle of the (λ,δ,ϕ) model from Lemesh *et al.* [229], which is based on the modelling of the DWs and domains by an ansatz profile with free parameters. Knowing the values of A, D, K_{u} and M_{s}, and exploiting the multilayer geometry characterised by t_{FM}, p and L, the equilibrium value of the three parameters (λ,δ,ϕ) is found as a minimum of energy with respect to each of these parameters. Performing such modelling for a range of values of D is computationally inexpensive as a consequence of the use of an ansatz profile, and this provides $\lambda(D)$ in a few seconds at most. Knowing the experimental value of λ allows to find D under the hypothesis that the system is indeed observed in its ground state of minimal energy.

A more detailed description is required when hybrid chiral DWs are formed. It relies on the micromagnetic description, with the MuMax³ solver [140], of the energies in a DWs-pair, also often referred to as 360°-DW. The modelled space is a tridimensional mesh accounting for the full geometry of the multilayers, made from a slice $\mathbf{m}(x,z)$ that is extended along x and y by almost infinite periodic boundary conditions. Given the experimental value of the domain periodicity λ, and for a given value of D, five different simulations, with x sizes $\lambda-2\,\mathrm{nm}$, $\lambda-1\,\mathrm{nm}$, λ, $\lambda+1\,\mathrm{nm}$ and $\lambda+2\,\mathrm{nm}$ are run successively. Each system is initialised with its DWs having a $\phi = 45°$ in-plane tilt of the magnetization in order to allow it to converge to any kind of hybrid chiral DW texture if stable. Each system is then relaxed in order to find the ground state energy density $\epsilon(\lambda)$. By comparing the five energies, this provides the local value of the variations of energy density, $\partial\epsilon/\partial\lambda$, at λ. Performing this operation for various values of D results in obtaining $(\partial\epsilon/\partial\lambda)|_\lambda(D)$. In the experiment, the measured value of λ shall correspond to the minimum energy configuration of the system, characterised by $(\partial\epsilon/\partial\lambda)|_\lambda = 0$. The value of the DM interaction in the system is then the one such that $(\partial\epsilon/\partial\lambda)|_\lambda = 0$, under the same hypothesis that the system is indeed observed in its ground state of minimal energy. This value of D can be found by interpolation of $(\partial\epsilon/\partial\lambda)|_\lambda(D)$ computed for a few values of D, as this function is locally linear around the result of D.

In figures, the simulation volume is $\lambda \pm d\lambda \times 32\,\mathrm{nm} \times Lp$, respectively, in the x, y and z directions. Two DWs separating up, down and up domains are initialised at $-(\lambda \pm d\lambda)/4$ and

$(\lambda \pm d\lambda)/4$, which corresponds to the $\lambda \pm d\lambda$ periodicity of the stripes. Periodic boundary conditions are calculated for 64×64 identical neighbours in the x and y directions. The cell size is chosen as 0.25 nm, 8 nm and 0.2 nm along x, y and z directions, respectively. It is sufficient to evaluate $(d\epsilon/d\lambda)|_{\lambda}$ for D ranging 0–2 mJ m^{-2}.

References

[1] I. Dzyaloshinsky, "A thermodynamic theory of "weak" ferromagnetism of antiferromagnetics" *J. Phys. Chem. Solids* **4**, 241–255 (1958).

[2] T. Moriya, "Anisotropic Superexchange Interaction and Weak Ferromagnetism" *Phys. Rev.* **120**, 91–98 (1960).

[3] L. Ludgren, O. Beckman, V. Attia, S. P. Bhattacheriee, and M. Richardson, "Helical Spin Arrangement in Cubic FeGe" *Phys. Scr.* **1**, 69–72 (1970).

[4] Y. Ishikawa, K. Tajima, D. Bloch, and M. Roth, "Helical spin structure in manganese silicide MnSi" *Solid State Commun.* **19**, 525–528 (1976).

[5] P. Bak and M. H. Jensen, "Theory of helical magnetic structures and phase transitions in MnSi and FeGe" *J. Phys. C: Solid State Phys.* **13**, L881–L885 (1980).

[6] A. Fert, V. Cros, and J. Sampaio, "Skyrmions on the track" *Nat. Nanotech.* **8**, 152–156 (2013).

[7] C. Moreau-Luchaire, C. Moutafis, N. Reyren, J. Sampaio, C. A. F. Vaz, N. Van Horne, K. Bouzehouane, K. Garcia, C. Deranlot, P. Warnicke, P. Wohlhüter, J.-M. George, M. Weigand, J. Raabe, V. Cros, and A. Fert, "Additive interfacial chiral interaction in multilayers for stabilization of small individual skyrmions at room temperature" *Nat. Nanotech.* **11**, 444–448 (2016).

[8] F. Hellman, A. Hoffmann, Y. Tserkovnyak, G. S. D. Beach, E. E. Fullerton, C. Leighton, A. H. MacDonald, D. C. Ralph, D. A. Arena, H. A. Dürr, P. Fischer, J. Grollier, J. P. Heremans, T. Jungwirth, A. V. Kimel, B. Koopmans, I. N. Krivorotov, S. J. May, A. K. Petford-Long, J. M. Rondinelli, N. Samarth, I. K. Schuller, A. N. Slavin, M. D. Stiles, O. Tchernyshyov, A. Thiaville, and B. L. Zink, "Interface-induced phenomena in magnetism" *Rev. Mod. Phys.* **89**, 025006 (2017).

[9] A. Fert, "Magnetic and Transport Properties of Metallic Multilayers" *Mater. Sci. Forum* **59–60**, 439–480 (1990).

[10] A. Crépieux and C. Lacroix, "Dzyaloshinsky–Moriya interactions induced by symmetry breaking at a surface" *J. Magn. Magn. Mater.* **182**, 341–349 (1998).

[11] L. Landau and E. Lifshitz, "On the theory of the dispersion of magnetic permeability in ferromagnetic bodies" *Phys. Z. Sowjetunion* **8**, 101–114 (1935).

[12] C. Kittel, "Theory of the Structure of Ferromagnetic Domains in Films and Small Particles" *Phys. Rev.* **70**, 965–971 (1946).

[13] C. Kooy and U. Enz, "Domain configuration in thin layers of $BaFe_{12}O_{19}$" *Philips Res. Repts.* **15**, 7–29 (1960).

References

[14] B. Kaplan and G. Gehring, "The domain structure in ultrathin magnetic films" *J. Magn. Magn. Mater.* **128**, 111–116 (1993).

[15] A. N. Bogdanov and U. K. Rößler, "Chiral Symmetry Breaking in Magnetic Thin Films and Multilayers" *Phys. Rev. Lett.* **87**, 037203 (2001).

[16] U. K. Rößler, A. N. Bogdanov, and C. Pfleiderer, "Spontaneous skyrmion ground states in magnetic metals" *Nature* **442**, 797–801 (2006).

[17] M. Bode, M. Heide, K. von Bergmann, P. Ferriani, S. Heinze, G. Bihlmayer, A. Kubetzka, O. Pietzsch, S. Blügel, and R. Wiesendanger, "Chiral magnetic order at surfaces driven by inversion asymmetry" *Nature* **447**, 190–193 (2007).

[18] P. Ferriani, K. von Bergmann, E. Vedmedenko, S. Heinze, M. Bode, M. Heide, G. Bihlmayer, S. Blügel, and R. Wiesendanger, "Atomic-Scale Spin Spiral with a Unique Rotational Sense: Mn Monolayer on W(001)" *Phys. Rev. Lett.* **101**, 027201 (2008).

[19] N. Nagaosa and Y. Tokura, "Topological properties and dynamics of magnetic skyrmions" *Nat. Nanotech.* **8**, 899–911 (2013).

[20] A. N. Bogdanov and D. A. Yalonskii, "Thermodynamically stable vortices in magnetically ordered crystals. The mixed state of magnets" *JETP Lett.* **68**, 101–103 (1989).

[21] A. Bogdanov and A. Hubert, "Thermodynamically stable magnetic vortex states in magnetic crystals" *J. Magn. Magn. Mater.* **138**, 255–269 (1994).

[22] A. Bogdanov and A. Hubert, "The Properties of Isolated Magnetic Vortices" *Phys. Stat. Sol. B* **186**, 527–543 (1994).

[23] S. Mühlbauer, B. Binz, F. Jonietz, C. Pfleiderer, A. Rosch, A. Neubauer, R. Georgii, and P. Böni, "Skyrmion Lattice in a Chiral Magnet" *Science* **323**, 915–919 (2009).

[24] X. Z. Yu, Y. Onose, N. Kanazawa, J. H. Park, J. H. Han, Y. Matsui, N. Nagaosa, and Y. Tokura, "Real-space observation of a two-dimensional skyrmion crystal" *Nature* **465**, 901–904 (2010).

[25] S. Heinze, K. von Bergmann, M. Menzel, J. Brede, A. Kubetzka, R. Wiesendanger, G. Bihlmayer, and S. Blügel, "Spontaneous atomic-scale magnetic skyrmion lattice in two dimensions" *Nat. Phys.* **7**, 713–718 (2011).

[26] N. Romming, C. Hanneken, M. Menzel, J. E. Bickel, B. Wolter, K. von Bergmann, A. Kubetzka, and R. Wiesendanger, "Writing and Deleting Single Magnetic Skyrmions" *Science* **341**, 636–639 (2013).

[27] T. Okubo, S. Chung, and H. Kawamura, "Multiple-q States and the Skyrmion Lattice of the Triangular-Lattice Heisenberg Antiferromagnet under Magnetic Fields" *Phys. Rev. Lett.* **108**, 017206 (2012).

[28] A. O. Leonov and M. Mostovoy, "Multiply periodic states and isolated skyrmions in an anisotropic frustrated magnet" *Nat. Commun.* **6**, 8275 (2015).

[29] S. von Malottki, B. Dupé, P. F. Bessarab, A. Delin, and S. Heinze, "Enhanced skyrmion stability due to exchange frustration" *Sci. Rep.* **7**, 12299 (2017).

[30] K. Karube, J. S. White, D. Morikawa, C. D. Dewhurst, R. Cubitt, A. Kikkawa, X. Yu, Y. Tokunaga, T.-h. Arima, H. M. Rønnow, Y. Tokura, and Y. Taguchi, "Disordered skyrmion phase stabilized by magnetic frustration in a chiral magnet" *Sci. Adv.* **4**, eaar7043 (2018).

[31] A. Belavin and A. Polyakov, "Metastable states of two-dimensional isotropic ferromagnets" *JETP Lett.* **22**, 245–248 (1975).

[32] H.-B. Braun, "Topological effects in nanomagnetism: from superparamagnetism to chiral quantum solitons" *Adv. Phys.* **61**, 1–116 (2012).

[33] M. Hoffmann, B. Zimmermann, G. P. Müller, D. Schrhoff, N. S. Kiselev, C. Melcher, and S. Blügel, "Antiskyrmions stabilized at interfaces by anisotropic Dzyaloshinskii-Moriya interactions" *Nat. Commun.* **8**, 308 (2017).

[34] L. Camosi, S. Rohart, O. Fruchart, S. Pizzini, M. Belmeguenai, Y. Roussigné, A. Stashkevich, S. M. Cherif, L. Ranno, M. de Santis, and J. Vogel, "Anisotropic Dzyaloshinskii-Moriya interaction in ultrathin epitaxial Au/Co/W(110)" *Phys. Rev. B* **95**, 214422 (2017).

[35] L. Camosi, N. Rougemaille, O. Fruchart, J. Vogel, and S. Rohart, "Micromagnetics of antiskyrmions in ultrathin films" *Phys. Rev. B* **97**, 134404 (2018).

[36] A. K. Nayak, V. Kumar, T. Ma, P. Werner, E. Pippel, R. Sahoo, F. Damay, U. K. Rößler, C. Felser, and S. S. P. Parkin, "Magnetic antiskyrmions above room temperature in tetragonal Heusler materials" *Nature* **548**, 561–566 (2017).

[37] F. Zheng, H. Li, S. Wang, D. Song, C. Jin, W. Wei, A. Kovács, J. Zang, M. Tian, Y. Zhang, H. Du, and R. E. Dunin-Borkowski, "Direct Imaging of a Zero-Field Target Skyrmion and Its Polarity Switch in a Chiral Magnetic Nanodisk" *Phys. Rev. Lett.* **119**, 197205 (2017).

[38] I. Kézsmárki, S. Bordács, P. Milde, E. Neuber, L. M. Eng, J. S. White, H. M. Rønnow, C. D. Dewhurst, M. Mochizuki, K. Yanai, H. Nakamura, D. Ehlers, V. Tsurkan, and A. Loidl, "Néel-type skyrmion lattice with confined orientation in the polar magnetic semiconductor GaV_4S_8" *Nat. Mater.* **14**, 1116–1122 (2015).

[39] Y.-O. Tu, "Determination of Magnetization of Micromagnetic Wall in Bubble Domains by Direct Minimization" *J. Appl. Phys.* **42**, 5704–5709 (1971).

[40] W. J. DeBonte, "Properties of thick-walled cylindrical magnetic domains in uniaxial platelets" *J. Appl. Phys.* **44**, 1793–1797 (1973).

[41] E. Schlömann, "Domain walls in bubble films. I. General theory of static properties" *J. Appl. Phys.* **44**, 1837–1849 (1973).

[42] E. Schlömann, "Domain walls in bubble films. II. Static properties of thick films" *J. Appl. Phys.* **44**, 1850–1854 (1973).

[43] E. Schlömann, "Domain walls in bubble films. III. Wall structure of stripe domains" *J. Appl. Phys.* **45**, 369–373 (1974).

[44] W. Jiang, P. Upadhyaya, W. Zhang, G. Yu, M. B. Jungfleisch, F. Y. Fradin, J. E. Pearson, Y. Tserkovnyak, K. L. Wang, O. Heinonen, S. G. E. te Velthuis, and A. Hoffmann, "Blowing magnetic skyrmion bubbles" *Science* **349**, 283–286 (2015).

[45] W. Jiang, X. Zhang, G. Yu, W. Zhang, X. Wang, M. Benjamin Jungfleisch, J. E. Pearson, X. Cheng, O. Heinonen, K. L. Wang, Y. Zhou, A. Hoffmann, and S. G. E. te Velthuis, "Direct observation of the skyrmion Hall effect" *Nat. Phys.* **13**, 162–169 (2017).

[46] S. Woo, K. Litzius, B. Krüger, M.-Y. Im, L. Caretta, K. Richter, M. Mann, A. Krone, R. M. Reeve, M. Weigand, P. Agrawal, I. Lemesh, M.-A. Mawass, P. Fischer, M. Kläui, and G. S. D. Beach, "Observation of room-temperature magnetic skyrmions and their current-driven dynamics in ultrathin metallic ferromagnets" *Nat. Mater.* **15**, 501–506 (2016).

References

[47] K. Litzius, I. Lemesh, B. Krüger, P. Bassirian, L. Caretta, K. Richter, F. Büttner, K. Sato, O. A. Tretiakov, J. Förster, R. M. Reeve, M. Weigand, I. Bykova, H. Stoll, G. Schütz, G. S. D. Beach, and M. Kläui, "Skyrmion Hall effect revealed by direct time-resolved X-ray microscopy" *Nat. Phys.* **13**, 170–175 (2017).

[48] A. Soumyanarayanan, M. Raju, A. L. G. Oyarce, A. K. C. Tan, M.-Y. Im, A. P. Petrović, P. Ho, K. H. Khoo, M. Tran, C. K. Gan, F. Ernult, and C. Panagopoulos, "Tunable room-temperature magnetic skyrmions in Ir/Fe/Co/Pt multilayers" *Nat. Mater.* **16**, 898–904 (2017).

[49] S. D. Pollard, J. A. Garlow, J. Yu, Z. Wang, Y. Zhu, and H. Yang, "Observation of stable Néel skyrmions in cobalt/palladium multilayers with Lorentz transmission electron microscopy" *Nat. Commun.* **8**, 14761 (2017).

[50] X. Z. Yu, N. Kanazawa, Y. Onose, K. Kimoto, W. Z. Zhang, S. Ishiwata, Y. Matsui, and Y. Tokura, "Near room-temperature formation of a skyrmion crystal in thin-films of the helimagnet FeGe" *Nat. Mater.* **10**, 106–109 (2011).

[51] K. Karube, J. S. White, N. Reynolds, J. L. Gavilano, H. Oike, A. Kikkawa, F. Kagawa, Y. Tokunaga, H. M. Rønnow, Y. Tokura, and Y. Taguchi, "Robust metastable skyrmions and their triangular–square lattice structural transition in a high-temperature chiral magnet" *Nat. Mater.* **15**, 1237–1242 (2016).

[52] Y. Tokunaga, X. Z. Yu, J. S. White, H. M. Rønnow, D. Morikawa, Y. Taguchi, and Y. Tokura, "A new class of chiral materials hosting magnetic skyrmions beyond room temperature" *Nat. Commun.* **6**, 7638 (2015).

[53] K. Karube, J. S. White, D. Morikawa, M. Bartkowiak, A. Kikkawa, Y. Tokunaga, T. Arima, H. M. Rønnow, Y. Tokura, and Y. Taguchi, "Skyrmion formation in a bulk chiral magnet at zero magnetic field and above room temperature" *Phys. Rev. Mater.* **1**, 074405 (2017).

[54] S. L. Zhang, G. van der Laan, and T. Hesjedal, "Direct experimental determination of the topological winding number of skyrmions in Cu_2OSeO_3" *Nat. Commun.* **8**, 14619 (2017).

[55] S. L. Zhang, G. van der Laan, and T. Hesjedal, "Direct experimental determination of spiral spin structures via the dichroism extinction effect in resonant elastic soft x-ray scattering" *Phys. Rev. B* **96**, 094401 (2017).

[56] S. A. Montoya, S. Couture, J. J. Chess, J. C. T. Lee, N. Kent, D. Henze, S. K. Sinha, M.-Y. Im, S. D. Kevan, P. Fischer, B. J. McMorran, V. Lomakin, S. Roy, and E. E. Fullerton, "Tailoring magnetic energies to form dipole skyrmions and skyrmion lattices" *Phys. Rev. B* **95**, 024415 (2017).

[57] S. McVitie, S. Hughes, K. Fallon, S. McFadzean, D. McGrouther, M. Krajnak, W. Legrand, D. Maccariello, S. Collin, K. Garcia, N. Reyren, V. Cros, A. Fert, K. Zeissler, and C. H. Marrows, "A transmission electron microscope study of Néel skyrmion magnetic textures in multilayer thin film systems with large interfacial chiral interaction" *Sci. Rep.* **8**, 5703 (2018).

[58] R. Wiesendanger, "Nanoscale magnetic skyrmions in metallic films and multilayers: a new twist for spintronics" *Nat. Rev. Mat.* **1**, 16044 (2016).

[59] P. Milde, D. Kohler, J. Seidel, L. M. Eng, A. Bauer, A. Chacon, J. Kindervater, S. Mühlbauer, C. Pfleiderer, S. Buhrandt, C. Schutte, and A. Rosch, "Unwinding of a Skyrmion Lattice by Magnetic Monopoles" *Science* **340**, 1076–1080 (2013).

[60] N. Romming, A. Kubetzka, C. Hanneken, K. von Bergmann, and R. Wiesendanger, "Field-Dependent Size and Shape of Single Magnetic Skyrmions" *Phys. Rev. Lett.* **114**, 177203 (2015).

[61] S. Rohart and A. Thiaville, "Skyrmion confinement in ultrathin film nanostructures in the presence of Dzyaloshinskii-Moriya interaction" *Phys. Rev. B* **88**, 184422 (2013).

[62] G. Chen, T. Ma, A. T. N'Diaye, H. Kwon, C. Won, Y. Wu, and A. K. Schmid, "Tailoring the chirality of magnetic domain walls by interface engineering" *Nat. Commun.* **4**, 2671 (2013).

[63] G. Chen, J. Zhu, A. Quesada, J. Li, A. T. N'Diaye, Y. Huo, T. P. Ma, Y. Chen, H. Y. Kwon, C. Won, Z. Q. Qiu, A. K. Schmid, and Y. Z. Wu, "Novel Chiral Magnetic Domain Wall Structure in Fe/Ni/Cu(001) Films" *Phys. Rev. Lett.* **110**, 177204 (2013).

[64] G. Chen, A. Mascaraque, A. T. N'Diaye, and A. K. Schmid, "Room temperature skyrmion ground state stabilized through interlayer exchange coupling" *Appl. Phys. Lett.* **106**, 242404 (2015).

[65] O. Boulle, J. Vogel, H. Yang, S. Pizzini, D. de Souza Chaves, A. Locatelli, T. O. Mentes, A. Sala, L. D. Buda-Prejbeanu, O. Klein, M. Belmeguenai, Y. Roussigné, A. Stashkevich, S.-M. Chérif, L. Aballe, M. Foerster, M. Chshiev, S. Auffret, I. M. Miron, and G. Gaudin, "Room-temperature chiral magnetic skyrmions in ultrathin magnetic nanostructures" *Nat. Nanotech.* **11**, 449–454 (2016).

[66] F. Jonietz, S. Mühlbauer, C. Pfleiderer, A. Neubauer, W. Münzer, A. Bauer, T. Adams, R. Georgii, P. Böni, R. A. Duine, K. Everschor, M. Garst, and A. Rosch, "Spin Transfer Torques in MnSi at Ultralow Current Densities" *Science* **330**, 1648–1651 (2010).

[67] X. Yu, N. Kanazawa, W. Zhang, T. Nagai, T. Hara, K. Kimoto, Y. Matsui, Y. Onose, and Y. Tokura, "Skyrmion flow near room temperature in an ultralow current density" *Nat. Commun.* **3**, 988 (2012).

[68] N. S. Kiselev, A. N. Bogdanov, R. Schäfer, and U. K. Rößler, "Chiral skyrmions in thin magnetic films: new objects for magnetic storage technologies?" *J. Phys. D: Appl. Phys.* **44**, 392001 (2011).

[69] B. Dupé, M. Hoffmann, C. Paillard, and S. Heinze, "Tailoring magnetic skyrmions in ultra-thin transition metal films" *Nat. Commun.* **5**, 4030 (2014).

[70] B. Dupé, G. Bihlmayer, M. Böttcher, S. Blügel, and S. Heinze, "Engineering skyrmions in transition-metal multilayers for spintronics" *Nat. Commun.* **7**, 11779 (2016).

[71] J. Sampaio, V. Cros, S. Rohart, A. Thiaville, and A. Fert, "Nucleation, stability and current-induced motion of isolated magnetic skyrmions in nanostructures" *Nat. Nanotech.* **8**, 839–844 (2013).

[72] J. Iwasaki, M. Mochizuki, and N. Nagaosa, "Current-induced skyrmion dynamics in constricted geometries" *Nat. Nanotech.* **8**, 742–747 (2013).

[73] O. Heinonen, W. Jiang, H. Somaily, S. G. E. te Velthuis, and A. Hoffmann, "Generation of magnetic skyrmion bubbles by inhomogeneous spin Hall currents" *Phys. Rev. B* **93**, 094407 (2016).

[74] D. M. Crum, M. Bouhassoune, J. Bouaziz, B. Schweflinghaus, S. Blügel, and S. Lounis, "Perpendicular reading of single confined magnetic skyrmions" *Nat. Commun.* **6**, 8541 (2015).

[75] C. Hanneken, F. Otte, A. Kubetzka, B. Dupé, N. Romming, K. von Bergmann, R. Wiesendanger, and S. Heinze, "Electrical detection of magnetic skyrmions by tunnelling non-collinear magnetoresistance" *Nat. Nanotech.* **10**, 1039–1042 (2015).

References

[76] S. S. P. Parkin, M. Hayashi, and L. Thomas, "Magnetic Domain-Wall Racetrack Memory" *Science* **320**, 190–194 (2008).

[77] M. Hayashi, L. Thomas, R. Moriya, C. Rettner, and S. S. P. Parkin, "Current-Controlled Magnetic Domain-Wall Nanowire Shift Register" *Science* **320**, 209–211 (2008).

[78] I. M. Miron, T. Moore, H. Szambolics, L. D. Buda-Prejbeanu, S. Auffret, B. Rodmacq, S. Pizzini, J. Vogel, M. Bonfim, A. Schuhl, and G. Gaudin, "Fast current-induced domain-wall motion controlled by the Rashba effect" *Nat. Mater.* **10**, 419–423 (2011).

[79] P. P. J. Haazen, E. Murè, J. H. Franken, R. Lavrijsen, H. J. M. Swagten, and B. Koopmans, "Domain wall depinning governed by the spin Hall effect" *Nat. Mater.* **12**, 299–303 (2013).

[80] K.-S. Ryu, L. Thomas, S.-H. Yang, and S. Parkin, "Chiral spin torque at magnetic domain walls" *Nat. Nanotech.* **8**, 527–533 (2013).

[81] S. Emori, U. Bauer, S.-M. Ahn, E. Martinez, and G. S. D. Beach, "Current-driven dynamics of chiral ferromagnetic domain walls" *Nat. Mater.* **12**, 611–616 (2013).

[82] S. Emori, E. Martinez, K.-J. Lee, H.-W. Lee, U. Bauer, S.-M. Ahn, P. Agrawal, D. C. Bono, and G. S. D. Beach, "Spin Hall torque magnetometry of Dzyaloshinskii domain walls" *Phys. Rev. B* **90**, 184427 (2014).

[83] A. Thiaville, S. Rohart, E. Jué, V. Cros, and A. Fert, "Dynamics of Dzyaloshinskii domain walls in ultrathin magnetic films" *Europhys. Lett.* **100**, 57002 (2012).

[84] A. V. Khvalkovskiy, V. Cros, D. Apalkov, V. Nikitin, M. Krounbi, K. A. Zvezdin, A. Anane, J. Grollier, and A. Fert, "Matching domain-wall configuration and spin-orbit torques for efficient domain-wall motion" *Phys. Rev. B* **87**, 020402 (2013).

[85] A. Neubauer, C. Pfleiderer, B. Binz, A. Rosch, R. Ritz, P. G. Niklowitz, and P. Böni, "Topological Hall Effect in the A Phase of MnSi" *Phys. Rev. Lett.* **102**, 186602 (2009).

[86] N. Kanazawa, Y. Onose, T. Arima, D. Okuyama, K. Ohoyama, S. Wakimoto, K. Kakurai, S. Ishiwata, and Y. Tokura, "Large Topological Hall Effect in a Short-Period Helimagnet MnGe" *Phys. Rev. Lett.* **106**, 156603 (2011).

[87] N. Kanazawa, M. Kubota, A. Tsukazaki, Y. Kozuka, K. S. Takahashi, M. Kawasaki, M. Ichikawa, F. Kagawa, and Y. Tokura, "Discretized topological Hall effect emerging from skyrmions in constricted geometry" *Phys. Rev. B* **91**, 041122 (2015).

[88] W. Kang, Y. Huang, X. Zhang, Y. Zhou, and W. Zhao, "Skyrmion-Electronics: An Overview and Outlook" *Proc. IEEE* **104**, 2040–2061 (2016).

[89] A. Fert, N. Reyren, and V. Cros, "Magnetic skyrmions: advances in physics and potential applications" *Nat. Rev. Mat.* **2**, 17031 (2017).

[90] W. Jiang, G. Chen, K. Liu, J. Zang, S. G. te Velthuis, and A. Hoffmann, "Skyrmions in magnetic multilayers" *Phys. Rep.* **704**, 1–49 (2017).

[91] K. Everschor-Sitte, J. Masell, R. M. Reeve, and M. Kläui, "Perspective: Magnetic skyrmions—overview of recent progress in an active research field" *J. Appl. Phys.* **124**, 240901 (2018).

[92] S.-H. Yang, K.-S. Ryu, and S. Parkin, "Domain-wall velocities of up to 750 m s^{-1} driven by exchange-coupling torque in synthetic antiferromagnets" *Nat. Nanotech.* **10**, 221–226 (2015).

[93] T. H. Pham, J. Vogel, J. Sampaio, M. Vaňatka, J.-C. Rojas-Sánchez, M. Bonfim, D. S. Chaves, F. Choueikani, P. Ohresser, E. Otero, A. Thiaville, and S. Pizzini, "Very large domain wall velocities in Pt/Co/GdOx and Pt/Co/Gd trilayers with Dzyaloshinskii-Moriya interaction" *Europhys. Lett.* **113**, 67001 (2016).

[94] K.-J. Kim, S. K. Kim, Y. Hirata, S.-H. Oh, T. Tono, D.-H. Kim, T. Okuno, W. S. Ham, S. Kim, G. Go, Y. Tserkovnyak, A. Tsukamoto, T. Moriyama, K.-J. Lee, and T. Ono, "Fast domain wall motion in the vicinity of the angular momentum compensation temperature of ferrimagnets" *Nat. Mater.* **16**, 1187–1192 (2017).

[95] T. Srivastava, M. Schott, R. Juge, V. Křižáková, M. Belmeguenai, Y. Roussigné, A. Bernand-Mantel, L. Ranno, S. Pizzini, S.-M. Chérif, A. Stashkevich, S. Auffret, O. Boulle, G. Gaudin, M. Chshiev, C. Baraduc, and H. Béa, "Large-Voltage Tuning of Dzyaloshinskii–Moriya Interactions: A Route toward Dynamic Control of Skyrmion Chirality" *Nano Lett.* **18**, 4871–4877 (2018).

[96] A. L. Balk, K.-W. Kim, D. T. Pierce, M. D. Stiles, J. Unguris, and S. M. Stavis, "Simultaneous control of the Dzyaloshinskii-Moriya interaction and magnetic anisotropy in nanomagnetic trilayers" *Phys. Rev. Lett.* **119**, 077205 (2017).

[97] S. Rohart, J. Miltat, and A. Thiaville, "Path to collapse for an isolated Néel skyrmion" *Phys. Rev. B* **93**, 214412 (2016).

[98] P. F. Bessarab, G. P. Müller, I. S. Lobanov, F. N. Rybakov, N. S. Kiselev, H. Jónsson, V. M. Uzdin, S. Blügel, L. Bergqvist, and A. Delin, "Lifetime of racetrack skyrmions" *Sci. Rep.* **8**, 3433 (2018).

[99] P. J. Metaxas, J. P. Jamet, A. Mougin, M. Cormier, J. Ferré, V. Baltz, B. Rodmacq, B. Dieny, and R. L. Stamps, " Creep and Flow Regimes of Magnetic Domain-Wall Motion in Ultrathin Pt/Co/Pt Films with Perpendicular Anisotropy" *Phys. Rev. Lett.* **99**, 217208 (2007).

[100] P. Grünberg, C. Mayr, W. Vach, and M. Grimsditch, "Determination of magnetic parameters by means of Brillouin scattering. Examples: Fe, Ni, $Ni_{0.8}Fe_{0.2}$" *J. Magn. Magn. Mater.* **28**, 319–325 (1982).

[101] X. Liu, M. M. Steiner, R. Sooryakumar, G. A. Prinz, R. F. C. Farrow, and G. Harp, "Exchange stiffness, magnetization, and spin waves in cubic and hexagonal phases of cobalt" *Phys. Rev. B* **53**, 12166–12172 (1996).

[102] T. Devolder, J.-V. Kim, L. Nistor, R. Sousa, B. Rodmacq, and B. Diény, "Exchange stiffness in ultrathin perpendicularly magnetized CoFeB layers determined using the spectroscopy of electrically excited spin waves" *J. Appl. Phys.* **120**, 183902 (2016).

[103] M. Belmeguenai, D. Apalkov, Y. Roussigné, M. Chérif, A. Stashkevich, G. Feng, and X. Tang, "Exchange stiffness and damping constants in diluted $Co_xFe_yB_{1-x-y}$ thin films" *J. Phys. D: Appl. Phys.* **50**, 415003 (2017).

[104] C. Eyrich, W. Huttema, M. Arora, E. Montoya, F. Rashidi, C. Burrowes, B. Kardasz, E. Girt, B. Heinrich, O. N. Mryasov, M. From, and O. Karis, "Exchange stiffness in thin film Co alloys" *J. Appl. Phys.* **111**, 07C919 (2012).

[105] C. Eyrich, A. Zamani, W. Huttema, M. Arora, D. Harrison, F. Rashidi, D. Broun, B. Heinrich, O. Mryasov, M. Ahlberg, O. Karis, P. E. Jnsson, M. From, X. Zhu, and E. Girt, "Effects of substitution on the exchange stiffness and magnetization of Co films" *Phys. Rev. B* **90**, 235408 (2014).

References

[106] M. Heide, G. Bihlmayer, and S. Blügel, "Dzyaloshinskii-Moriya interaction accounting for the orientation of magnetic domains in ultrathin films: Fe/W(110)" *Phys. Rev. B* **78**, 140403 (2008).

[107] A. S. Ahmed, B. D. Esser, J. Rowland, D. W. McComb, and R. K. Kawakami, "Molecular beam epitaxy growth of [CrGe/MnGe/FeGe] superlattices: Toward artificial B20 skyrmion materials with tunable interactions" *J. Cryst. Growth* **467**, 38–46 (2017).

[108] A. Fert and P. M. Levy, "Role of Anisotropic Exchange Interactions in Determining the Properties of Spin-Glasses" *Phys. Rev. Lett.* **44**, 1538–1541 (1980).

[109] M. Heide, G. Bihlmayer, and S. Blügel, "Describing Dzyaloshinskii–Moriya spirals from first principles" *Physica B* **404**, 2678–2683 (2009).

[110] A. Hrabec, N. A. Porter, A. Wells, M. J. Benitez, G. Burnell, S. McVitie, D. McGrouther, T. A. Moore, and C. H. Marrows, "Measuring and tailoring the Dzyaloshinskii-Moriya interaction in perpendicularly magnetized thin films" *Phys. Rev. B* **90**, 020402 (2014).

[111] H. Yang, A. Thiaville, S. Rohart, A. Fert, and M. Chshiev, "Anatomy of Dzyaloshinskii-Moriya Interaction at Co/Pt Interfaces" *Phys. Rev. Lett.* **115**, 267210 (2015).

[112] M. Belmeguenai, J.-P. Adam, Y. Roussigné, S. Eimer, T. Devolder, J.-V. Kim, S. M. Cherif, A. Stashkevich, and A. Thiaville, "Interfacial Dzyaloshinskii-Moriya interaction in perpendicularly magnetized Pt/Co/AlO$_x$ ultrathin films measured by Brillouin light spectroscopy" *Phys. Rev. B* **91**, 180405 (2015).

[113] F. Ajejas, A. Gudín, R. Guerrero, A. A. Barcelona, J. M. Diez, L. de Melo Costa, P. Olleros, M. A. Niño, S. Pizzini, J. Vogel, M. Valvidares, P. Gargiani, M. Cabero, M. Varela, J. Camarero, R. Miranda, and P. Perna, "Unraveling Dzyaloshinskii–Moriya Interaction and Chiral Nature of Graphene/Cobalt Interface" *Nano Lett.* **18**, 5364–5372 (2018).

[114] A. Belabbes, G. Bihlmayer, S. Blügel, and A. Manchon, "Oxygen-enabled control of Dzyaloshinskii-Moriya Interaction in ultra-thin magnetic films" *Sci. Rep.* **6**, 24634 (2016).

[115] H. Yang, O. Boulle, V. Cros, A. Fert, and M. Chshiev, "Controlling Dzyaloshinskii-Moriya Interaction via Chirality Dependent Atomic-Layer Stacking, Insulator Capping and Electric Field" *Sci. Rep.* **8**, 12356 (2018).

[116] H. Yang, G. Chen, A. A. C. Cotta, A. T. N'Diaye, S. A. Nikolaev, E. A. Soares, W. A. A. Macedo, K. Liu, A. K. Schmid, A. Fert, and M. Chshiev, "Significant Dzyaloshinskii–Moriya interaction at graphene–ferromagnet interfaces due to the Rashba effect" *Nat. Mater.* **17**, 605–609 (2018).

[117] J. Cho, N.-H. Kim, S. Lee, J.-S. Kim, R. Lavrijsen, A. Solignac, Y. Yin, D.-S. Han, N. J. J. van Hoof, H. J. M. Swagten, B. Koopmans, and C.-Y. You, "Thickness dependence of the interfacial Dzyaloshinskii–Moriya interaction in inversion symmetry broken systems" *Nat. Commun.* **6**, 7635 (2015).

[118] J. Torrejon, J. Kim, J. Sinha, S. Mitani, M. Hayashi, M. Yamanouchi, and H. Ohno, "Interface control of the magnetic chirality in CoFeB/MgO heterostructures with heavy-metal underlayers" *Nat. Commun.* **5**, 4655 (2014).

[119] B. Zimmermann, W. Legrand, D. Maccariello, N. Reyren, V. Cros, S. Blügel, and A. Fert, "Dzyaloshinskii-Moriya interaction at disordered interfaces from ab initio theory: Robustness against intermixing and tunability through dusting" *Appl. Phys. Lett.* **113**, 232403 (2018).

[120] G. W. Kim, A. S. Samardak, Y. J. Kim, I. H. Cha, A. V. Ognev, A. V. Sadovnikov, S. A. Nikitov, and Y. K. Kim, "Role of the Heavy Metal's Crystal Phase in Oscillations of Perpendicular Magnetic Anisotropy and the Interfacial Dzyaloshinskii-Moriya Interaction in W/Co-Fe-B/MgO Films" *Phys. Rev. Appl.* **9**, 064005 (2018).

[121] N.-H. Kim, D.-S. Han, J. Jung, K. Park, H. J. M. Swagten, J.-S. Kim, and C.-Y. You, "Dependence of interfacial Dzyaloshinskii-Moriya interaction and perpendicular magnetic anisotropy on the thickness of the heavy-metal layer" *Appl. Phys. Express* **10**, 103003 (2017).

[122] A. W. J. Wells, P. M. Shepley, C. H. Marrows, and T. A. Moore, "Effect of interfacial intermixing on the Dzyaloshinskii-Moriya interaction in Pt/Co/Pt" *Phys. Rev. B* **95**, 054428 (2017).

[123] S. Tacchi, R. E. Troncoso, M. Ahlberg, G. Gubbiotti, M. Madami, J. Åkerman, and P. Landeros, "Interfacial Dzyaloshinskii-Moriya Interaction in Pt/CoFeB Films: Effect of the Heavy-Metal Thickness" *Phys. Rev. Lett.* **118**, 147201 (2017).

[124] M. T. Johnson, P. J. H. Bloemen, F. J. A. den Broeder, and J. J. de Vries, "Magnetic anisotropy in metallic multilayers" *Rep. Prog. Phys.* **59**, 1409–1458 (1996).

[125] M. Farle, "Ferromagnetic resonance of ultrathin metallic layers" *Rep. Prog. Phys.* **61**, 755–826 (1998).

[126] P. F. Carcia, "Perpendicular magnetic anisotropy in Pd/Co and Pt/Co thin-film layered structures" *J. Appl. Phys.* **63**, 5066–5073 (1988).

[127] H. Draaisma, W. de Jonge, and F. den Broeder, "Magnetic interface anisotropy in Pd/Co and Pd/Fe multilayers" *J. Magn. Magn. Mater.* **66**, 351–355 (1987).

[128] R. Krishnan, H. Lassri, S. Prasad, M. Porte, and M. Tessier, "Magnetic properties of Ni/Pt multilayers" *J. Appl. Phys.* **73**, 6433–6435 (1993).

[129] R. Cabanel, P. Etienne, S. Lequien, G. Creuzet, A. Barthélémy, and A. Fert, "Magnetic properties of (001)bcc Fe / (001)fcc Ag superlattices" *J. Appl. Phys.* **67**, 5409–5411 (1990).

[130] G. H. O. Daalderop, P. J. Kelly, and F. J. A. den Broeder, "Prediction and confirmation of perpendicular magnetic anisotropy in Co/Ni multilayers" *Phys. Rev. Lett.* **68**, 682–685 (1992).

[131] M. Bersweiler, K. Dumesnil, D. Lacour, and M. Hehn, "Impact of buffer layer and Pt thickness on the interface structure and magnetic properties in (Co/Pt) multilayers" *J. Phys.: Condens. Matter* **28**, 336005 (2016).

[132] W. F. Brown and A. E. LaBonte, "Structure and Energy of One-Dimensional Domain Walls in Ferromagnetic Thin Films" *J. Appl. Phys.* **36**, 1380–1386 (1965).

[133] H. J. G. Draaisma and W. J. M. de Jonge, "Magnetization curves of Pd/Co multilayers with perpendicular anisotropy" *J. Appl. Phys.* **62**, 3318–3322 (1987).

[134] N. Saratz, A. Lichtenberger, O. Portmann, U. Ramsperger, A. Vindigni, and D. Pescia, "Experimental Phase Diagram of Perpendicularly Magnetized Ultrathin Ferromagnetic Films" *Phys. Rev. Lett.* **104**, 077203 (2010).

[135] H. T. Nembach, J. M. Shaw, M. Weiler, E. Jué, and T. J. Silva, "Linear relation between heisenberg exchange and interfacial dzyaloshinskii–moriya interaction in metal films" *Nat. Phys.* **11**, 825–829 (2015).

[136] S. Kim, K. Ueda, G. Go, P.-H. Jang, K.-J. Lee, A. Belabbes, A. Manchon, M. Suzuki, Y. Kotani, T. Nakamura, K. Nakamura, T. Koyama, D. Chiba, K. T. Yamada, D.-H. Kim, T. Moriyama, K.-J. Kim, and T. Ono, "Correlation of the Dzyaloshinskii–Moriya interaction with Heisenberg exchange and orbital asphericity" *Nat. Commun.* **9**, 1648 (2018).

[137] A. O. Leonov, T. L. Monchesky, N. Romming, A. Kubetzka, A. N. Bogdanov, and R. Wiesendanger, "The properties of isolated chiral skyrmions in thin magnetic films" *New J. Phys.* **18**, 065003 (2016).

[138] A. Bernand-Mantel, L. Camosi, A. Wartelle, N. Rougemaille, M. Darques, and L. Ranno, "The skyrmion-bubble transition in a ferromagnetic thin film" *SciPost Phys.* **4**, 027 (2018).

[139] F. Büttner, I. Lemesh, and G. S. D. Beach, "Theory of isolated magnetic skyrmions: From fundamentals to room temperature applications" *Sci. Rep.* **8**, 4464 (2018).

[140] A. Vansteenkiste, J. Leliaert, M. Dvornik, M. Helsen, F. Garcia-Sanchez, and B. Van Waeyenberge, "The design and verification of MuMax3" *AIP Adv.* **4**, 107133 (2014).

[141] J. H. Han, J. Zang, Z. Yang, J.-H. Park, and N. Nagaosa, "Skyrmion lattice in a two-dimensional chiral magnet" *Phys. Rev. B* **82**, 094429 (2010).

[142] M. Vousden, M. Albert, M. Beg, M.-A. Bisotti, R. Carey, D. Chernyshenko, D. Cortés-Ortuño, W. Wang, O. Hovorka, C. H. Marrows, and H. Fangohr, "Skyrmions in thin films with easy-plane magnetocrystalline anisotropy" *Appl. Phys. Lett.* **108**, 132406 (2016).

[143] J. Hagemeister, N. Romming, K. von Bergmann, E. Y. Vedmedenko, and R. Wiesendanger, "Stability of single skyrmionic bits" *Nat. Commun.* **6**, 8455 (2015).

[144] M. Böttcher, S. Heinze, S. Egorov, J. Sinova, and B. Dupé, "B–T phase diagram of Pd/Fe/Ir(111) computed with parallel tempering Monte Carlo" *New J. Phys.* **20**, 103014 (2018).

[145] T. N. G. Meier, M. Kronseder, and C. H. Back, "Domain-width model for perpendicularly magnetized systems with Dzyaloshinskii-Moriya interaction" *Phys. Rev. B* **96**, 144408 (2017).

[146] T. Matsumoto, Y.-G. So, Y. Kohno, Y. Ikuhara, and N. Shibata, "Stable Magnetic Skyrmion States at Room Temperature Confined to Corrals of Artificial Surface Pits Fabricated by a Focused Electron Beam" *Nano Lett.* **18**, 754–762 (2018).

[147] M. E. Knoester, J. Sinova, and R. A. Duine, "Phenomenology of current-skyrmion interactions in thin films with perpendicular magnetic anisotropy" *Phys. Rev. B* **89**, 064425 (2014).

[148] M. Schott, A. Bernand-Mantel, L. Ranno, S. Pizzini, J. Vogel, H. Béa, C. Baraduc, S. Auffret, G. Gaudin, and D. Givord, "The Skyrmion Switch: Turning Magnetic Skyrmion Bubbles on and off with an Electric Field" *Nano Lett.* **17**, 3006–3012 (2017).

[149] I. S. Lobanov, H. Jónsson, and V. M. Uzdin, "Mechanism and activation energy of magnetic skyrmion annihilation obtained from minimum energy path calculations" *Phys. Rev. B* **94**, 174418 (2016).

[150] L. Desplat, D. Suess, J.-V. Kim, and R. L. Stamps, "Thermal stability of metastable magnetic skyrmions: Entropic narrowing and significance of internal eigenmodes" *Phys. Rev. B* **98**, 134407 (2018).

[151] S. Haldar, S. von Malottki, S. Meyer, P. F. Bessarab, and S. Heinze, "First-principles prediction of sub-10-nm skyrmions in Pd/Fe bilayers on Rh(111)" *Phys. Rev. B* **98**, 060413 (2018).

[152] P. F. Bessarab, D. Yudin, D. R. Gulevich, P. Wadley, M. Titov, and O. A. Tretiakov, "Stability and lifetime of antiferromagnetic skyrmions" *Phys. Rev. B* **99**, 140411 (2019).

[153] D. Stosic, J. Mulkers, B. V. Waeyenberge, T. B. Ludermir, and M. V. Milošević, "Paths to collapse for isolated skyrmions in few-monolayer ferromagnetic films" *Phys. Rev. B* **95**, 214418 (2017).

[154] J. Wild, T. N. G. Meier, S. Pöllath, M. Kronseder, A. Bauer, A. Chacon, M. Halder, M. Schowalter, A. Rosenauer, J. Zweck, J. Müller, A. Rosch, C. Pfleiderer, and C. H. Back, "Entropy-limited topological protection of skyrmions" *Sci. Adv.* **3**, e1701704 (2017).

[155] L. Thomas, G. Jan, J. Zhu, H. Liu, Y.-J. Lee, S. Le, R.-Y. Tong, K. Pi, Y.-J. Wang, D. Shen, R. He, J. Haq, J. Teng, V. Lam, K. Huang, T. Zhong, T. Torng, and P.-K. Wang, "Perpendicular spin transfer torque magnetic random access memories with high spin torque efficiency and thermal stability for embedded applications (invited)" *J. Appl. Phys.* **115**, 172615 (2014).

[156] P.-J. Hsu, A. Kubetzka, A. Finco, N. Romming, K. von Bergmann, and R. Wiesendanger, "Electric-field-driven switching of individual magnetic skyrmions" *Nat. Nanotech.* **12**, 123–126 (2017).

[157] F. Büttner, I. Lemesh, M. Schneider, B. Pfau, C. M. Günther, P. Hessing, J. Geilhufe, L. Caretta, D. Engel, B. Krüger, J. Viefhaus, S. Eisebitt, and G. S. D. Beach, "Field-free deterministic ultrafast creation of magnetic skyrmions by spin–orbit torques" *Nat. Nanotech.* **12**, 1040–1044 (2017).

[158] S. Woo, K. M. Song, X. Zhang, M. Ezawa, Y. Zhou, X. Liu, M. Weigand, S. Finizio, J. Raabe, M.-C. Park, K.-Y. Lee, J. W. Choi, B.-C. Min, H. C. Koo, and J. Chang, "Deterministic creation and deletion of a single magnetic skyrmion observed by direct time-resolved X-ray microscopy" *Nat. Electron.* **1**, 288–296 (2018).

[159] J. M. Iwata-Harms, G. Jan, H. Liu, S. Serrano-Guisan, J. Zhu, L. Thomas, R.-Y. Tong, V. Sundar, and P.-K. Wang, "High-temperature thermal stability driven by magnetization dilution in CoFeB free layers for spin-transfer-torque magnetic random access memory" *Sci. Rep.* **8**, 14409 (2018).

[160] H. Oike, A. Kikkawa, N. Kanazawa, Y. Taguchi, M. Kawasaki, Y. Tokura, and F. Kagawa, "Interplay between topological and thermodynamic stability in a metastable magnetic skyrmion lattice" *Nat. Phys.* **12**, 62–66 (2015).

[161] K. Everschor-Sitte, M. Sitte, T. Valet, A. Abanov, and J. Sinova, "Skyrmion production on demand by homogeneous DC currents" *New J. Phys.* **19**, 092001 (2017).

[162] A. Brataas, A. D. Kent, and H. Ohno, "Current-induced torques in magnetic materials" *Nat. Mater.* **11**, 372–381 (2012).

[163] P. Gambardella and I. M. Miron, "Current-induced spin-orbit torques" *Phil. Trans. R. Soc. A* **369**, 3175–3197 (2011).

[164] A. Brataas and K. M. D. Hals, "Spin–orbit torques in action" *Nat. Nanotech.* **9**, 86–88 (2014).

[165] J. E. Hirsch, "Spin Hall Effect" *Phys. Rev. Lett.* **83**, 1834–1837 (1999).

[166] V. P. Amin and M. D. Stiles, "Spin transport at interfaces with spin-orbit coupling: Formalism" *Phys. Rev. B* **94**, 104419 (2016).

[167] V. P. Amin and M. D. Stiles, "Spin transport at interfaces with spin-orbit coupling: Phenomenology" *Phys. Rev. B* **94**, 104420 (2016).

[168] V. P. Amin, J. Zemen, and M. D. Stiles, "Interface-Generated Spin Currents" *Phys. Rev. Lett.* **121**, 136805 (2018).

[169] J.-C. Rojas-Sánchez, N. Reyren, P. Laczkowski, W. Savero, J.-P. Attané, C. Deranlot, M. Jamet, J.-M. George, L. Vila, and H. Jaffrès, "Spin Pumping and Inverse Spin Hall Effect in Platinum: The Essential Role of Spin-Memory Loss at Metallic Interfaces" *Phys. Rev. Lett.* **112**, 106602 (2014).

[170] W. Zhang, W. Han, X. Jiang, S.-H. Yang, and S. S. P. Parkin, "Role of transparency of platinum-ferromagnet interfaces in determining the intrinsic magnitude of the spin Hall effect" *Nat. Phys.* **11**, 496–502 (2015).

[171] C.-F. Pai, Y. Ou, L. H. Vilela-Leão, D. C. Ralph, and R. A. Buhrman, "Dependence of the efficiency of spin Hall torque on the transparency of Pt/ferromagnetic layer interfaces" *Phys. Rev. B* **92**, 064426 (2015).

[172] L. Liu, O. J. Lee, T. J. Gudmundsen, D. C. Ralph, and R. A. Buhrman, "Current-Induced Switching of Perpendicularly Magnetized Magnetic Layers Using Spin Torque from the Spin Hall Effect" *Phys. Rev. Lett.* **109**, 096602 (2012).

[173] K. Garello, I. M. Miron, C. O. Avci, F. Freimuth, Y. Mokrousov, S. Blügel, S. Auffret, O. Boulle, G. Gaudin, and P. Gambardella, "Symmetry and magnitude of spin-orbit torques in ferromagnetic heterostructures" *Nat. Nanotech.* **8**, 587–593 (2013).

[174] L. Liu, C.-F. Pai, Y. Li, H. W. Tseng, D. C. Ralph, and R. A. Buhrman, "Spin-Torque Switching with the Giant Spin Hall Effect of Tantalum" *Science* **336**, 555–558 (2012).

[175] C.-F. Pai, L. Liu, Y. Li, H. W. Tseng, D. C. Ralph, and R. A. Buhrman, "Spin transfer torque devices utilizing the giant spin Hall effect of tungsten" *Appl. Phys. Lett.* **101**, 122404 (2012).

[176] R. Ramaswamy, X. Qiu, T. Dutta, S. D. Pollard, and H. Yang, "Hf thickness dependence of spin-orbit torques in Hf/CoFeB/MgO heterostructures" *Appl. Phys. Lett.* **108**, 202406 (2016).

[177] J. Iwasaki, W. Koshibae, and N. Nagaosa, "Colossal spin transfer torque effect on skyrmion along the edge" *Nano Lett.* **14**, 4432–4437 (2014).

[178] M.-W. Yoo, V. Cros, and J.-V. Kim, "Current-driven skyrmion expulsion from magnetic nanostrips" *Phys. Rev. B* **95**, 184423 (2017).

[179] W. Legrand, D. Maccariello, N. Reyren, K. Garcia, C. Moutafis, C. Moreau-Luchaire, S. Collin, K. Bouzehouane, V. Cros, and A. Fert, "Room-Temperature Current-Induced Generation and Motion of sub-100 nm Skyrmions" *Nano Lett.* **17**, 2703–2712 (2017).

[180] K. Zeissler, S. Finizio, K. Shahbazi, J. Massey, F. A. Ma'Mari, D. M. Bracher, A. Kleibert, M. C. Rosamond, E. H. Linfield, T. A. Moore, J. Raabe, G. Burnell, and C. H. Marrows, "Discrete hall resistivity contribution from néel skyrmions in multilayer nanodiscs" *Nature Nanotechnology* **13**, 1161–1166 (2018).

[181] G. Yu, P. Upadhyaya, Q. Shao, H. Wu, G. Yin, X. Li, C. He, W. Jiang, X. Han, P. K. Amiri, and K. L. Wang, "Room-Temperature Skyrmion Shift Device for Memory Application" *Nano Lett.* **17**, 261–268 (2017).

[182] S. Lemerle, J. Ferré, C. Chappert, V. Mathet, T. Giamarchi, and P. Le Doussal, "Domain Wall Creep in an Ising Ultrathin Magnetic Film" *Phys. Rev. Lett.* **80**, 849–852 (1998).

[183] V. Jeudy, A. Mougin, S. Bustingorry, W. Savero Torres, J. Gorchon, A. B. Kolton, A. Lemaître, and J.-P. Jamet, "Universal Pinning Energy Barrier for Driven Domain Walls in Thin Ferromagnetic Films" *Phys. Rev. Lett.* **117**, 057201 (2016).

[184] M. Baćani, M. A. Marioni, J. Schwenk, and H. J. Hug, "How to measure the local Dzyaloshinskii-Moriya Interaction in Skyrmion Thin-Film Multilayers" *Sci. Rep.* **9**, 3114 (2019).

[185] C. Reichhardt, D. Ray, and C. J. O. Reichhardt, "Collective Transport Properties of Driven Skyrmions with Random Disorder" *Phys. Rev. Lett.* **114**, 217202 (2015).

[186] C. Reichhardt and C. J. Olson Reichhardt, "Noise fluctuations and drive dependence of the skyrmion Hall effect in disordered systems" *New J. Phys.* **18**, 095005 (2016).

[187] J.-V. Kim and M.-W. Yoo, "Current-driven skyrmion dynamics in disordered films" *Appl. Phys. Lett.* **110**, 132404 (2017).

[188] A. Hrabec, J. Sampaio, M. Belmeguenai, I. Gross, R. Weil, S. M. Chérif, A. Stashkevich, V. Jacques, A. Thiaville, and S. Rohart, "Current-induced skyrmion generation and dynamics in symmetric bilayers" *Nat. Commun.* **8**, 15765 (2017).

[189] L. Liu, T. Moriyama, D. C. Ralph, and R. A. Buhrman, "Spin-Torque Ferromagnetic Resonance Induced by the Spin Hall Effect" *Phys. Rev. Lett.* **106**, 036601 (2011).

[190] S. Woo, M. Mann, A. J. Tan, L. Caretta, and G. S. D. Beach, "Enhanced spin-orbit torques in Pt/Co/Ta heterostructures" *Appl. Phys. Lett.* **105**, 212404 (2014).

[191] C. Hahn, G. de Loubens, O. Klein, M. Viret, V. V. Naletov, and J. B. Youssef, "Comparative measurements of inverse spin Hall effects and magnetoresistance in YIG/Pt and YIG/Ta" *Phys. Rev. B* **87**, 174417 (2013).

[192] J. Yu, X. Qiu, W. Legrand, and H. Yang, "Large spin-orbit torques in Pt/Co-Ni/W heterostructures" *Appl. Phys. Lett.* **109**, 042403 (2016).

[193] H. A. Dürr, E. Dudzik, S. S. Dhesi, J. B. Goedkoop, G. van der Laan, M. Belakhovsky, C. Mocuta, A. Marty, and Y. Samson, "Chiral Magnetic Domain Structures in Ultrathin FePd Films" *Science* **284**, 2166–2168 (1999).

[194] J.-Y. Chauleau, W. Legrand, N. Reyren, D. Maccariello, S. Collin, H. Popescu, K. Bouzehouane, V. Cros, N. Jaouen, and A. Fert, "Chirality in Magnetic Multilayers Probed by the Symmetry and the Amplitude of Dichroism in X-Ray Resonant Magnetic Scattering" *Phys. Rev. Lett.* **120**, 037202 (2018).

[195] I. Lemesh and G. S. D. Beach, "Twisted domain walls and skyrmions in perpendicularly magnetized multilayers" *Phys. Rev. B* **98**, 104402 (2018).

[196] S. Jaiswal, K. Litzius, I. Lemesh, F. Büttner, S. Finizio, J. Raabe, M. Weigand, K. Lee, J. Langer, B. Ocker, G. Jakob, G. S. D. Beach, and M. Kläui, "Investigation of the Dzyaloshinskii-Moriya interaction and room temperature skyrmions in W/CoFeB/MgO thin films and microwires" *Appl. Phys. Lett.* **111**, 022409 (2017).

[197] E. Sagasta, Y. Omori, S. Vélez, R. Llopis, C. Tollan, A. Chuvilin, L. E. Hueso, M. Gradhand, Y. Otani, and F. Casanova, "Unveiling the mechanisms of the spin Hall effect in Ta" *Phys. Rev. B* **98**, 060410 (2018).

[198] S. Woo, K. M. Song, X. Zhang, Y. Zhou, M. Ezawa, X. Liu, S. Finizio, J. Raabe, N. J. Lee, S.-I. Kim, S.-Y. Park, Y. Kim, J.-Y. Kim, D. Lee, O. Lee, J. W. Choi, B.-C. Min, H. C. Koo, and J. Chang, "Current-driven dynamics and inhibition of the skyrmion Hall effect of ferrimagnetic skyrmions in GdFeCo films" *Nat. Commun.* **9**, 959 (2018).

[199] K.-W. Kim, K.-W. Moon, N. Kerber, J. Nothhelfer, and K. Everschor-Sitte, "Asymmetric skyrmion Hall effect in systems with a hybrid Dzyaloshinskii-Moriya interaction" *Phys. Rev. B* **97**, 224427 (2018).

[200] P. Bloemen and W. de Jonge, "Magnetic anisotropy of Co/Ni/Co/Pt multilayers" *J. Magn. Magn. Mater.* **116**, L1–L6 (1992).

[201] R. Sbiaa, J. M. Shaw, H. T. Nembach, M. Al Bahri, M. Ranjbar, J. Åkerman, and S. N. Piramanayagam, "Ferromagnetic resonance measurements of (Co/Ni/Co/Pt) multilayers with perpendicular magnetic anisotropy" *J. Phys. D: Appl. Phys.* **49**, 425002 (2016).

[202] P. J. H. Bloemen, H. W. van Kesteren, H. J. M. Swagten, and W. J. M. de Jonge, "Oscillatory interlayer exchange coupling in Co/Ru multilayers and bilayers" *Phys. Rev. B* **50**, 13505–13514 (1994).

[203] J. Barker and O. A. Tretiakov, "Static and Dynamical Properties of Antiferromagnetic Skyrmions in the Presence of Applied Current and Temperature" *Phys. Rev. Lett.* **116**, 147203 (2016).

[204] L. Caretta, M. Mann, F. Büttner, K. Ueda, B. Pfau, C. M. Günther, P. Hessing, A. Churikova, C. Klose, M. Schneider, D. Engel, C. Marcus, D. Bono, K. Bagschik, S. Eisebitt, and G. S. D. Beach, "Fast current-driven domain walls and small skyrmions in a compensated ferrimagnet" *Nat. Nanotech.* **13**, 1154–1160 (2018).

[205] P. Bruno and C. Chappert, "Oscillatory coupling between ferromagnetic layers separated by a nonmagnetic metal spacer" *Phys. Rev. Lett.* **67**, 1602–1605 (1991).

[206] P. Bruno and C. Chappert, "Ruderman-Kittel theory of oscillatory interlayer exchange coupling" *Phys. Rev. B* **46**, 261–270 (1992).

[207] V. Baltz, B. Rodmacq, A. Bollero, J. Ferré, S. Landis, and B. Dieny, "Balancing interlayer dipolar interactions in multilevel patterned media with out-of-plane magnetic anisotropy" *Appl. Phys. Lett.* **94**, 052503 (2009).

[208] K. Yakushiji, T. Saruya, H. Kubota, A. Fukushima, T. Nagahama, S. Yuasa, and K. Ando, "Ultrathin Co/Pt and Co/Pd superlattice films for MgO-based perpendicular magnetic tunnel junctions" *Appl. Phys. Lett.* **97**, 232508 (2010).

[209] S. Bandiera, R. C. Sousa, S. Auffret, B. Rodmacq, and B. Dieny, "Enhancement of perpendicular magnetic anisotropy thanks to Pt insertions in synthetic antiferromagnets" *Appl. Phys. Lett.* **101**, 072410 (2012).

[210] R. Lavrijsen, A. Fernández-Pacheco, D. Petit, R. Mansell, J. H. Lee, and R. P. Cowburn, "Tuning the interlayer exchange coupling between single perpendicularly magnetized CoFeB layers" *Appl. Phys. Lett.* **100**, 052411 (2012).

[211] R. Lavrijsen, J.-H. Lee, A. Fernández-Pacheco, D. C. M. C. Petit, R. Mansell, and R. P. Cowburn, "Magnetic ratchet for three-dimensional spintronic memory and logic" *Nature* **493**, 647–650 (2013).

[212] M. Belmeguenai, H. Bouloussa, Y. Roussigné, M. S. Gabor, T. Petrisor, C. Tiusan, H. Yang, A. Stashkevich, and S. M. Chérif, "Interface Dzyaloshinskii-Moriya interaction in the interlayer antiferromagnetic-exchange coupled Pt/CoFeB/Ru/CoFeB systems" *Phys. Rev. B* **96**, 144402 (2017).

[213] B. Dieny, J.-P. Gavigan, and J. Rebouillat, "Magnetisation processes, hysteresis and finite-size effects in model multilayer systems of cubic or uniaxial anisotropy with antiferromagnetic coupling between adjacent ferromagnetic layers" *J. Phys.: Condens. Matter* **2**, 159–185 (1990).

[214] M. Hervé, B. Dupé, R. Lopes, M. Böttcher, M. D. Martins, T. Balashov, L. Gerhard, J. Sinova, and W. Wulfhekel, "Stabilizing spin spirals and isolated skyrmions at low magnetic field exploiting vanishing magnetic anisotropy" *Nat. Commun.* **9**, 1015 (2018).

[215] O. Hellwig, T. L. Kirk, J. B. Kortright, A. Berger, and E. E. Fullerton, "A new phase diagram for layered antiferromagnetic films" *Nat. Mater.* **2**, 112–116 (2003).

[216] O. Hellwig, A. Berger, J. B. Kortright, and E. E. Fullerton, "Domain structure and magnetization reversal of antiferromagnetically coupled perpendicular anisotropy films" *J. Magn. Magn. Mater.* **319**, 13–55 (2007).

[217] N. S. Kiselev, U. K. Rößler, A. N. Bogdanov, and O. Hellwig, "Topological defects in antiferromagnetically coupled multilayers with perpendicular anisotropy" *Appl. Phys. Lett.* **93**, 162502 (2008).

[218] N. S. Kiselev, C. Bran, U. Wolff, L. Schultz, A. N. Bogdanov, O. Hellwig, V. Neu, and U. K. Rößler, "Metamagnetic domains in antiferromagnetically coupled multilayers with perpendicular anisotropy" *Phys. Rev. B* **81**, 054409 (2010).

[219] S.-Z. Lin, "Edge instability in a chiral stripe domain under an electric current and skyrmion generation" *Phys. Rev. B* **94**, 020402 (2016).

[220] X. Zhang, Y. Zhou, and M. Ezawa, "Magnetic bilayer-skyrmions without skyrmion Hall effect" *Nat. Commun.* **7**, 10293 (2016).

[221] X. Zhang, M. Ezawa, and Y. Zhou, "Thermally stable magnetic skyrmions in multilayer synthetic antiferromagnetic racetracks" *Phys. Rev. B* **94**, 064406 (2016).

[222] J. Zázvorka, F. Jakobs, D. Heinze, N. Keil, S. Kromin, S. Jaiswal, K. Litzius, G. Jakob, P. Virnau, D. Pinna, K. Everschor-Sitte, A. Donges, U. Nowak, and M. Kläui, "Thermal skyrmion diffusion applied in probabilistic computing" *arXiv:1805.05924* (2018).

[223] X. Qiu, W. Legrand, P. He, Y. Wu, J. Yu, R. Ramaswamy, A. Manchon, and H. Yang, "Enhanced Spin-Orbit Torque via Modulation of Spin Current Absorption" *Phys. Rev. Lett.* **117**, 217206 (2016).

[224] D.-s. Han, K. Lee, J.-P. Hanke, Y. Mokrousov, W. Yoo, T.-W. Kim, R. Lavijsen, C.-Y. You, H. J. M. Swagten, M.-H. Jung, and M. Kläui, "Chiral magnetic interlayer coupling in synthetic antiferromagnets" *arXiv:1809.01080* (2018).

[225] A. Fernández-Pacheco, E. Vedmedenko, F. Ummelen, R. Mansell, D. Petit, and R. P. Cowburn, "Symmetry-Breaking Interlayer Dzyaloshinskii-Moriya Interactions in Synthetic Antiferromagnets" *arXiv:1810.01801* (2018).

[226] J. Yu, D. Bang, R. Mishra, R. Ramaswamy, J. H. Oh, H.-J. Park, Y. Jeong, P. V. Thach, D.-K. Lee, G. Go, S.-W. Lee, Y. Wang, S. Shi, X. Qiu, H. Awano, K.-J. Lee, and H. Yang, "Long spin coherence length and bulk-like spin–orbit torque in ferrimagnetic multilayers" *Nat. Mater.* **18**, 29–34 (2019).

[227] P. Omelchenko, B. Heinrich, and E. Girt, "Measurements of interlayer exchange coupling of Pt in Py|Pt|Py system" *Appl. Phys. Lett.* **113**, 142401 (2018).

[228] R. M. Rowan-Robinson, A. A. Stashkevich, Y. Roussigné, M. Belmeguenai, S.-M. Chérif, A. Thiaville, T. P. A. Hase, A. T. Hindmarch, and D. Atkinson, "The interfacial nature of proximity-induced magnetism and the Dzyaloshinskii-Moriya interaction at the Pt/Co interface" *Sci. Rep.* **7**, 16835 (2017).

[229] I. Lemesh, F. Büttner, and G. S. D. Beach, "Accurate model of the stripe domain phase of perpendicularly magnetized multilayers" *Phys. Rev. B* **95**, 174423 (2017).

[230] W. Legrand, J.-Y. Chauleau, D. Maccariello, N. Reyren, S. Collin, K. Bouzehouane, N. Jaouen, V. Cros, and A. Fert, "Hybrid chiral domain walls and skyrmions in magnetic multilayers" *Sci. Adv.* **4**, eaat0415 (2018).

[231] S. Maat, K. Takano, S. S. P. Parkin, and E. E. Fullerton, "Perpendicular Exchange Bias of Co/Pt Multilayers" *Phys. Rev. Lett.* **87**, 087202 (2001).

[232] J. Sort, V. Baltz, F. Garcia, B. Rodmacq, and B. Dieny, "Tailoring perpendicular exchange bias in [Pt/Co]-IrMn multilayers" *Phys. Rev. B* **71**, 054411 (2005).

[233] J. Moritz, F. Garcia, J. C. Toussaint, B. Dieny, and J. P. Nozières, "Orange peel coupling in multilayers with perpendicular magnetic anisotropy: Application to (Co/Pt)-based exchange-biased spin-valves" *Europhys. Lett.* **65**, 123–129 (2004).

Titre: Élaboration de skyrmions magnétiques à température ambiante : taille, stabilité et dynamique dans les multicouches

Mots clés: Magnétisme, Spintronique, Skyrmion, Interaction Dzyaloshinskii-Moriya, Multicouches magnétiques, Dynamique induite par courant

Résumé: Les skyrmions magnétiques sont des enroulements bi-dimensionnels et nanométriques de la configuration de spin, pouvant être stabilisés dans certains matériaux magnétiques soumis à l'interaction d'échange antisymétrique Dzyaloshinskii-Moriya. Ils présentent une topologie non triviale et s'annoncent peut-être comme étant les plus petites configurations magnétiques pouvant être réalisées. Très récemment, des skyrmions magnétiques ont pu être stabilisés à température ambiante grâce à la conception de multicouches magnétiques brisant la symétrie d'inversion selon la direction verticale. Suite à cette avancée, l'objectif central de cette thèse est la compréhension et la maîtrise des multiples propriétés physiques des skyrmions hébergés dans ces systèmes multicouches. Pour aborder cet objectif, un modèle original est décrit puis employé, permettant la prédiction des profils adoptés par les skyrmions multicouches. Ce modèle numérique est très générique, n'utilisant que la symétrie cylindrique des skyrmions afin de simplifier la détermination des interactions magnétostatiques. Ce modèle est ensuite étendu afin de pouvoir approximer la stabilité thermique des skyrmions, ce qui constitue un élément clé dans leur obtention expérimentale. Une seconde dimension de ce travail consiste en l'étude expérimentale de la manipulation électrique des skyrmions multicouches, démontrant la possibilité de trois fonctionnalités centrales que sont leur nucléation par courants locaux, leur déplacement sous courant de spin et leur détection électrique individuelle par tension transverse. Le troisième aspect de ma thèse est l'étude des propriétés physi-ques influençant le déplacement des skyrmions dans les multicouches magnétiques. Un comportement d'ancrage sur des défauts est mis en évidence expérimentalement et est analysé à l'aide d'une modélisation micromagnétique. Un des résultats importants de ce travail est aussi la prédiction d'une chiralité hybride dans les configurations magnétiques de certaines multicouches, qui est ensuite démontrée expérimentalement par des mesures au synchrotron. Les conséquences attendues de cette chiralité hybride sur le déplacement des skyrmions sont étudiées pour permettre l'optimisation des multicouches, aboutissant à l'observation expérimentale de la propagation de skyrmions de 50 nm de rayon à des vitesses atteignant environ 40 m/s. La dernière partie de cette thèse vise à mettre à profit ces avancées théoriques et expérimentales afin de parvenir à réduire la taille des skyrmions à température ambiante. Après avoir analysé l'impact des interactions dipolaires sur la stabilité des skyrmions, il est entrepris d'optimiser les matériaux et la périodicité des couches. Je m'intéresse aussi à la conception expérimentale de textures magnétiques dont l'aimantation est compensée au sein de structures multicouches appelées antiferromagnétiques synthétiques, dont je montre qu'elles peuvent héberger des skyrmions antiferromagnétiques à température ambiante. Ce résultat final ouvre de nouvelles perspectives vers l'obtention de skyrmions à la fois mesurant moins de 10 nm et très mobiles, qui pourraient être utilisés dans la conception de composants de calcul et de stockage d'information plus compacts et plus efficaces.

Title: Crafting magnetic skyrmions at room temperature: size, stability and dynamics in multilayers

Keywords: Magnetism, Spintronics, Skyrmion, Dzyaloshinskii-Moriya interaction, Magnetic multilayers, Current-induced dynamics

Abstract: Magnetic skyrmions are nanoscale two-dimensional windings in the spin configuration of some magnetic materials subject to the Dzyaloshinskii-Moriya antisymmetric exchange interaction. They feature a non-trivial topology and show promise to be the smallest achievable magnetic textures. Very recently, magnetic skyrmions have been successfully stabilised up to room temperature by leveraging on the design of magnetic multilayer systems breaking the vertical inversion symmetry. Following up on this achievement, the main objective of this thesis is the understanding and the control of the various physical properties of skyrmions hosted by such multilayer systems. As a first approach to this objective, an original model allowing to predict the profiles adopted by multilayer skyrmions is described and then employed. This numerical model is very generic, as it exploits only the cylindrical symmetry of multilayer skyrmions, in order to determine the magnetostatic interactions with less effort. This model is further extended in order to approximate the thermal stability of multilayer skyrmions, which is key to their experimental realisation. The next aspect of this thesis consists in the experimental study of the electrical manipulation of multilayer skyrmions, demonstrating three main functionalities that are nucleation by local currents, displacement under spin currents and individual detection by transverse voltage. The third aspect of my thesis is the study of the physical properties influencing the current-induced motion of skyrmions in magnetic multilayers. A pinning behaviour is evidenced experimentally and analysed relying on micromagnetic modelling. One of the important results of this work is also the prediction of hybrid chirality for some multilayer magnetic configurations, which is then demonstrated experimentally using a synchrotron technique. The impact of hybrid chirality on current-induced skyrmion motion is discussed and leads to the optimisation of the multilayer design, resulting in the experimental observation of motion for skyrmions below 50 nm in radius at velocities reaching around 40 m/s. The last part of this thesis aims at leveraging on these theoretical and experimental advances in order to reduce the size of skyrmions at room temperature. After the analysis of the impact of dipolar interactions on skyrmion stability, the engineering of the materials and of the layers periodicity is attempted. I also investigate experimentally the conception of magnetic textures with compensated magnetization in multilayer structures known as synthetic antiferromagnets, and show that they can host antiferromagnetic skyrmions at room temperature. This last result opens up new prospects for achieving room-temperature skyrmions combining size in the single-digit nm range and high mobility, potentially allowing applications towards energy-efficient computation and storage devices with a very dense integration.